Scanning

Recent Applications of Scanning Microscopy in Surface Engineering 2021

Lead Guest Editor: Guosong Wu
Guest Editors: Paul K. Chu, Gheorghe Dinescu, and Ying Zhao

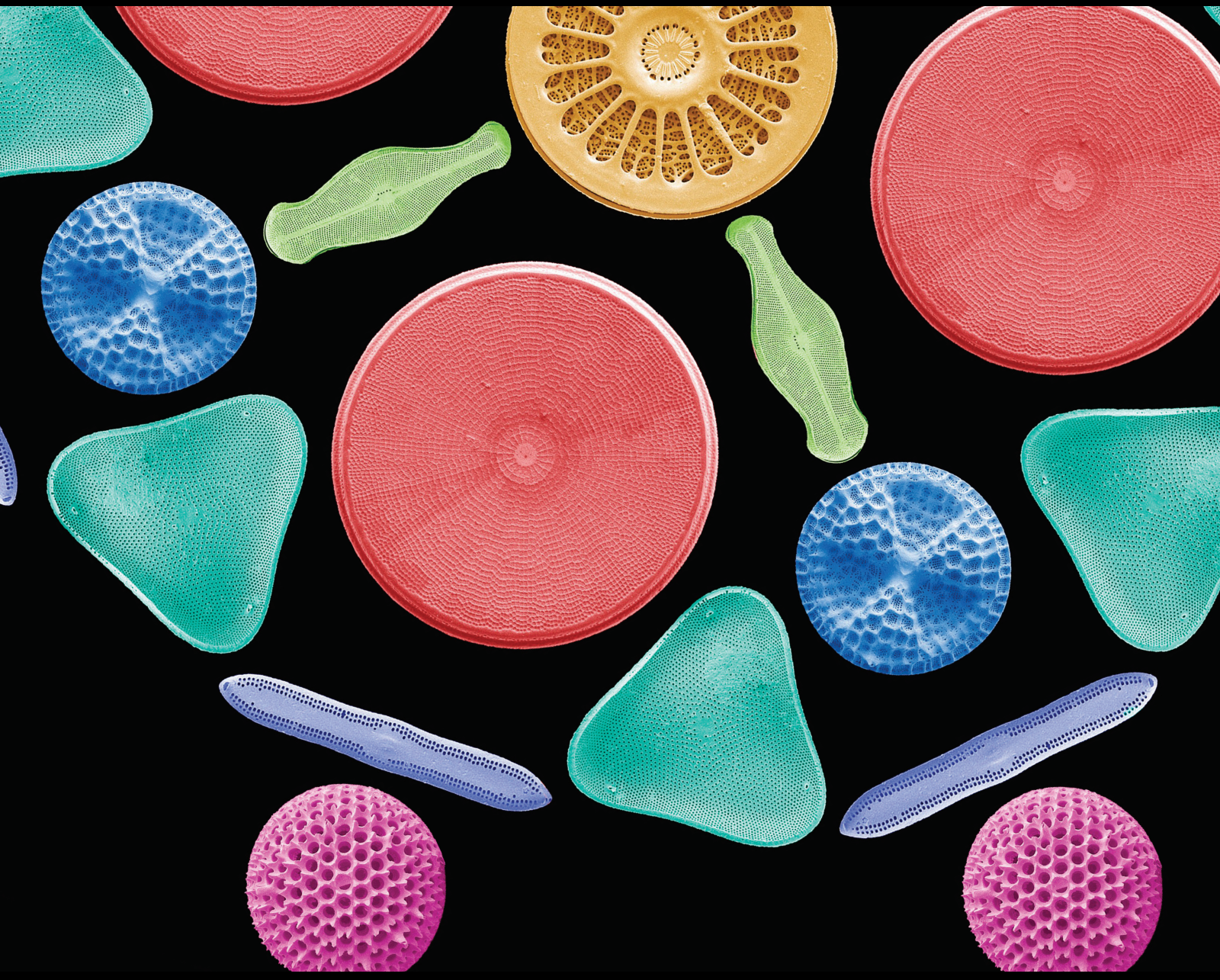

Recent Applications of Scanning Microscopy in Surface Engineering 2021

Scanning

Recent Applications of Scanning Microscopy in Surface Engineering 2021

Lead Guest Editor: Guosong Wu
Guest Editors: Paul K. Chu, Gheorghe Dinescu, and Ying Zhao

Contents

Hindawi
Scanning
Volume 2021, Article ID 4831387, 12 pages
https://doi.org/10.1155/2021/4831387

Research Article

Mechanical Properties and Degradation Behaviors of Zn-xMg Alloy Fine Wires for Biomedical Applications

Jing Bai,[1,2] **Yan Xu**,[1] **Qizhou Fan**,[1] **Ruihua Cao**,[1] **Xingxing Zhou**,[3] **Zhaojun Cheng**,[1,2] **Qiangsheng Dong**,[1,2] **and Feng Xue**[1,2]

[1]*Jiangsu Key Laboratory for Advanced Metallic Materials, School of Materials Science and Engineering, Southeast University, Nanjing 211189, China*
[2]*Institute of Medical Devices (Suzhou), Southeast University, Suzhou 215000, China*
[3]*Jiangsu Key Laboratory of Advanced Structural Materials and Application Technology, School of Materials Science and Engineering, Nanjing Institute of Technology, Nanjing 211167, China*

Correspondence should be addressed to Jing Bai; baijing@seu.edu.cn and Feng Xue; xuefeng@seu.edu.cn

Received 9 June 2021; Revised 16 July 2021; Accepted 30 November 2021; Published 24 December 2021

Academic Editor: Berndt Koslowski

Zn and Zn-based alloys exhibit biosafety and biodegradation, considered as candidates for biomedical implants. Zn-0.02 wt.% Mg (Zn-0.02 Mg), Zn-0.05 wt.% Mg (Zn-0.05 Mg), and Zn-0.2 wt.% Mg (Zn-0.2 Mg) wires (Φ 0.3 mm) were prepared for precision biomedical devices in this work. With the addition of Mg in Zn-xMg alloys, the grain size decreased along with the occurrence of Mg_2Zn_{11} at the grain boundaries. Hot extrusion, cold drawing, and annealing treatment were introduced to further refining the grain size. Besides, the hot extrusion and cold drawing improved the tensile strength of Zn-xMg alloys to 240-270 MPa while elongation also increased but remained under 10%. Annealing treatment could improve the elongation of Zn alloys to 12% -28%, but decrease the tensile strength. Furthermore, Zn-xMg wires displayed an increase in degradation rate with Mg addition. The findings might provide a potential possibility of Zn-xMg alloy wires for biomedical applications.

1. Introduction

Biomedical devices have been paid much attention since the living standard was improved during recent decades. Therefore, Mg-based, Zn-based, and Fe-based biodegradable metals (BMs) have become research hotspots owing to their acceptable mechanical properties, good biodegradability, and suitable biocompatibility for biomedical applications [1].

Fe-based alloys have higher mechanical properties similar to that of stainless-steel implants [2]. However, the degradation rates of Fe-based BMs were so slow in vivo that might hinder the bone healing process [3]. Besides, the ferromagnetism behaviors undermine the compatibility of magnetic resonance imaging (MRI) [4]. Besides, Mg-based alloys were investigated as BMs due to their excellent biocompatibility and suitable mechanical properties close to human bone [1, 2, 5, 6]. Mg ions play a positive role in promoting osteoblast proliferation and cell viability [7]. Nevertheless, an underlying problem is that a fast degradation rate destroys the mechanical integrity of implants during the healing of tissue [8, 9].

To explore suitable BMs with a moderate degradation rate and biomechanical compatibility, Zn and Zn alloys were investigated for biomedical applications [10–16]. Zn elements are also necessary microelements in the human body, which participate in life activities as major ingredients for vast macromolecules and enzymes in biomembrane formation [17, 18]. Besides, Zn has a standard electrode potential (vs standard hydrogen electrode) (-0.7618 V) between that of Mg (-2.372 V) and Fe (-0.447 V) [19], indicating a moderate degradation rate of Zn as BMs. Bowen et al. [20] studied pure Zn wires implanted in the artery of rats for 6 months and found that pure Zn wires had a proper degradation rate and favorable biocompatibility. However, the as-cast pure Zn has been reported limited elongation and tensile strength

Table 1: Chemical composition analyzed by OES.

Materials	Composition (wt.%)								
	Mg	Al	Cu	Pb	Sn	Fe	Mn	Ni	Zn
Zn	0.0012	0.0120	0.0013	0.0092	0.0064	0.0075	0.0010	0.0009	Balance
Zn-0.02 mg	0.0223	0.0018	0.0014	0.0100	0.0110	0.0070	0.0025	0.0017	Balance
Zn-0.05 mg	0.0488	0.0013	0.0013	0.0105	0.0127	0.0083	0.0027	0.0020	Balance
Zn-0.2 mg	0.193	0.0013	0.0014	0.0103	0.0142	0.0090	0.0043	0.0021	Balance

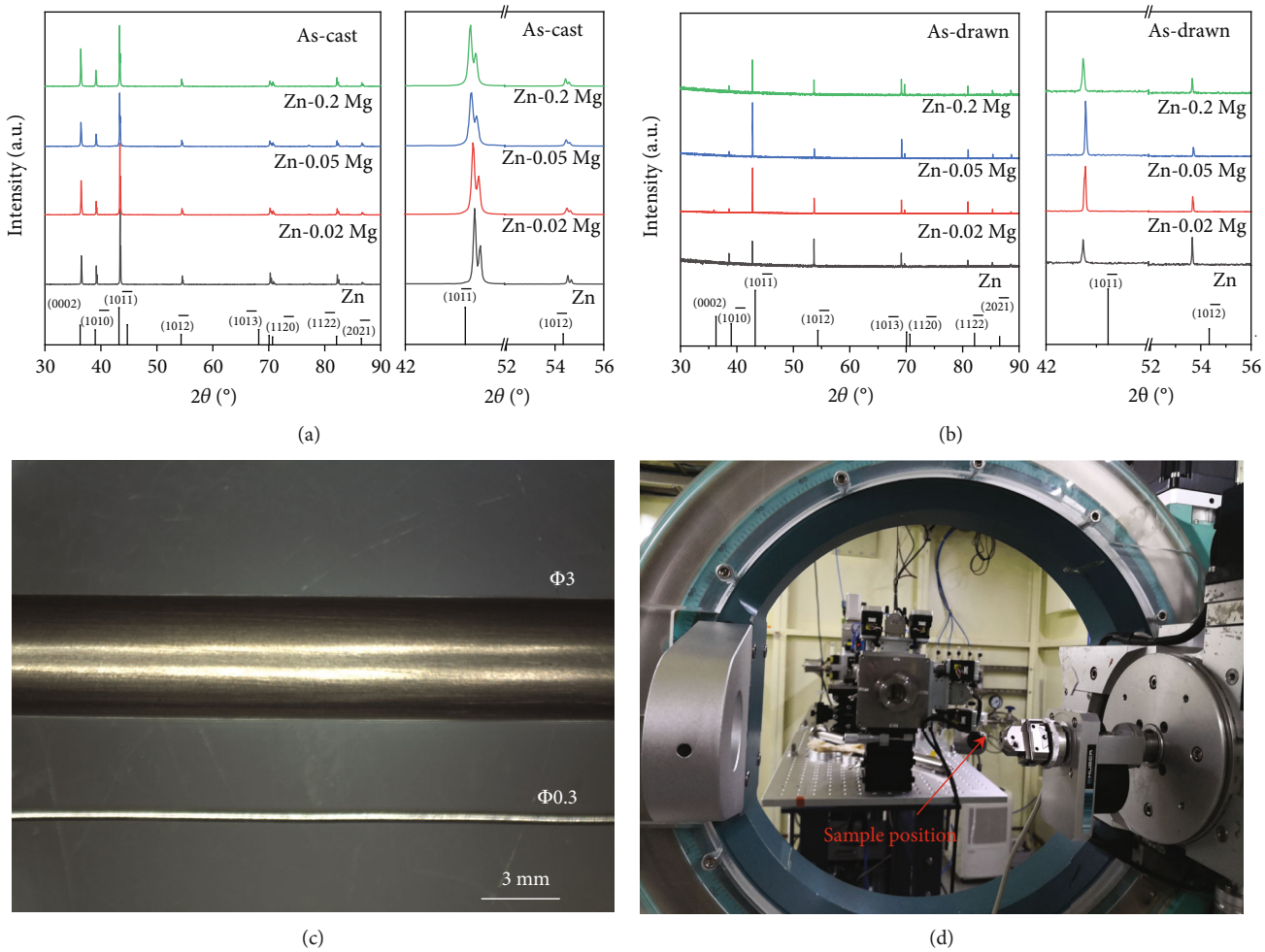

Figure 1: (a) XRD pattern of as-cast Zn-xMg alloys, (b) SR-XRD pattern of cold-drawn alloy wires, (c) optical morphology of alloy wires with 0.3 mm and 3 mm in diameter, and (d) synchronous radiator.

[21]. The drawbacks on undesirable plasticity and strength would be worthy of solving to expand clinical applications. The common metal materials are strengthened and plasticized through alloying and deformation combined with proper thermal treatment. Li et al. [22] reported that the mechanical properties of Zn alloys were improved by Mg, Ca, and Sr alloying and deformation process, resulting in that the ultimate tensile strength and elongation reached about 250 MPa and 7%, respectively. Zn-Mg alloys are widely studied among biodegradable Zn alloys [2]. Also, our research group prepared Zn-1.6% Mg alloy via multipass equal channel angular pressing and the optimal mechanical properties with the ultimate tensile strength of 423 MPa, the yield strength of 361 MPa, and the elongation of 5.2% [14]. In addition, Zn-Mg alloys have been reported good biocompatibility and osteogenesis in vivo and in vitro [22–24]. Therefore, Zn-Mg alloys are worthy of further investigation to explore wide biomedical applications.

Recently, BM wires have been paid much attention as temporary medical devices. Herein, BM sutures are potential biomedical applications owing to broadly accepted biodegradability, biocompatibility, and mechanical properties [25]. Our research group developed Mg alloy fine wire with a diameter of less than 0.4 mm [26]. Guo et al. [27] reported pure Zn wire for suture application. Zn-Mg alloys with a diameter of 0.6 mm have been developed for urinary tract

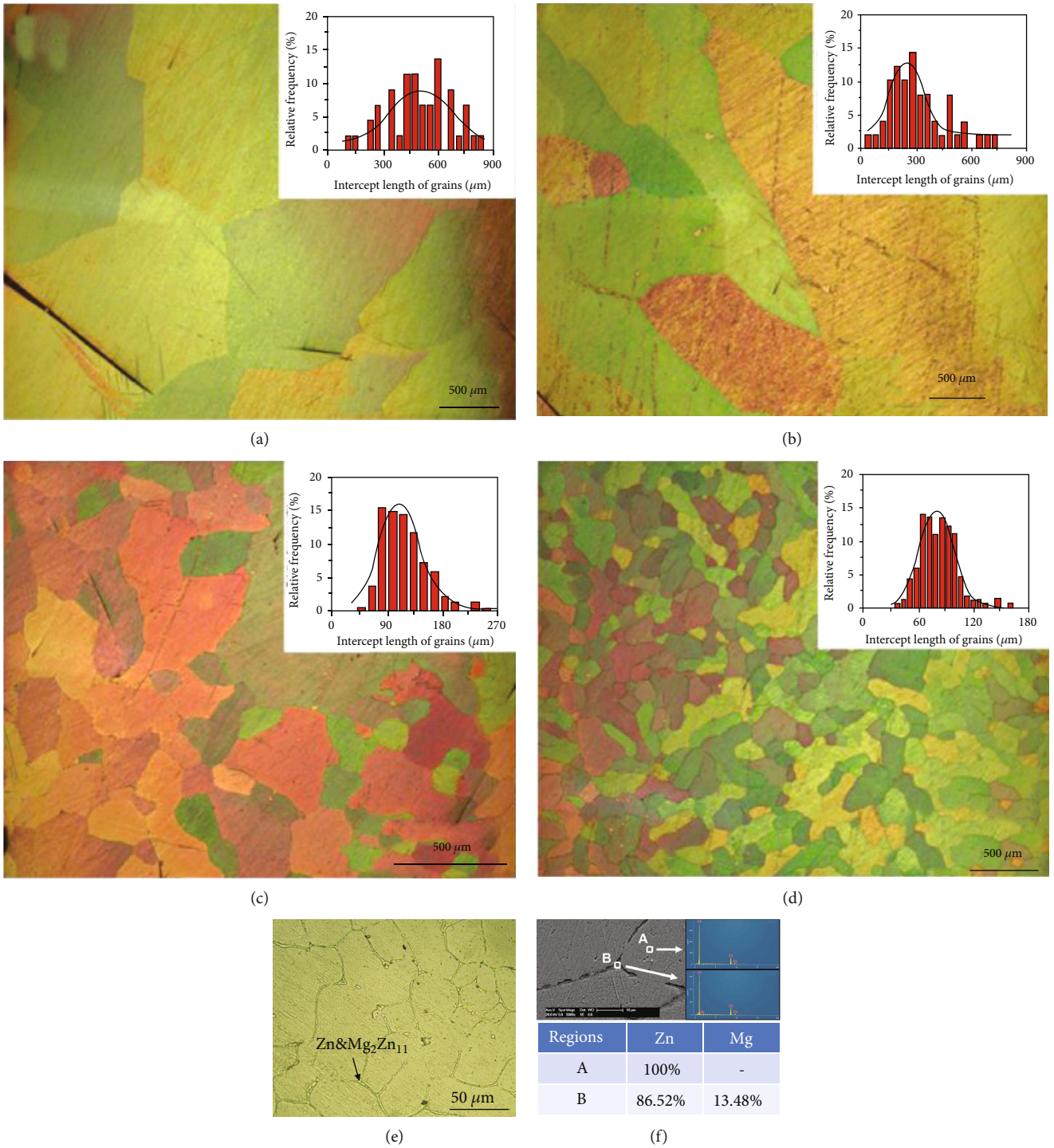

FIGURE 2: Microstructures of as-cast pure Zn (a), Zn-0.02 Mg (b), Zn-0.05 Mg (c) and Zn-0.2 Mg (d,e), and SEM and EDS for Zn-0.2 Mg (f).

surgeries [28]. BM fine wire with a diameter of less than 0.5 mm showed huge potentials in medical applications [26]. Zn alloy wires are appropriate for high strength sutures in hard tissue applications, which are required to have a long lifetime degradation of up to 2 years [25]. Furthermore, to explore precision medical implants with service performances, Zn-xMg ($x = 0.02$ wt.%, 0.05 wt.%, 0.2 wt.%) alloy fine wires (Φ 0.3 mm) were developed via hot extrusion, cold drawing, and annealing treatment. The microstructures and mechanical properties of different alloys through the whole process were analyzed and studied in detail. Besides, in *vitro* corrosion experiments were introduced to evaluate the corrosion properties of Zn-xMg alloy wires.

2. Materials and Methods

2.1. Material Preparation. The nutrient element Mg was selected as an alloying element for Zn-xMg alloys,

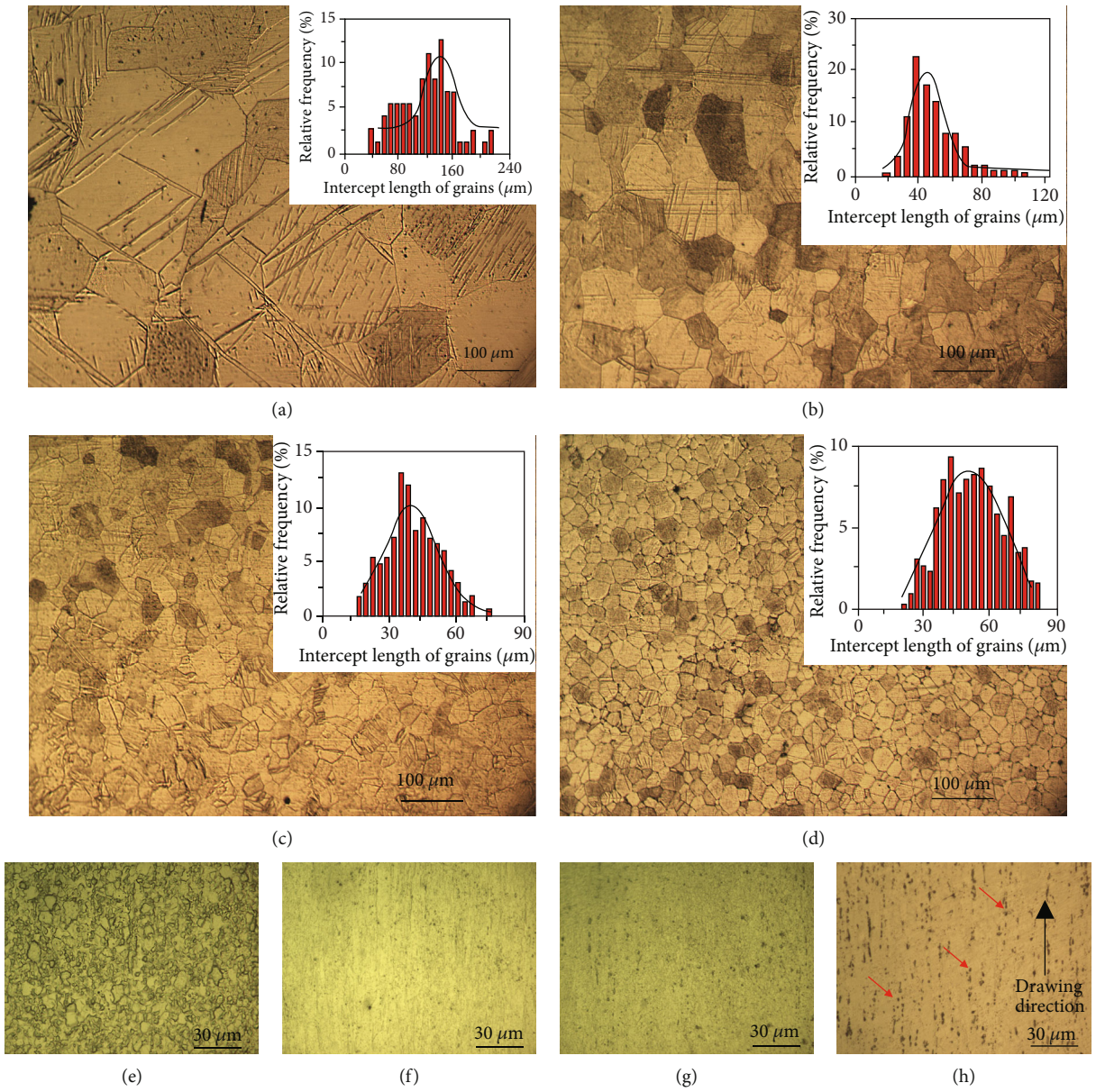

Figure 3: Microstructures of as-extruded Zn and Zn-xMg alloys: (a) Zn, (b) Zn-0.02 Mg, (c) Zn-0.05 Mg, and (d) Zn-0.2 Mg; microstructures of as-drawn Zn and Zn-xMg alloys: (e) Zn, (f) Zn-0.02 Mg, (g) Zn-0.05 Mg, and (h) Zn-0.2 Mg.

including Zn-0.02 wt% Mg (Zn-0.02 Mg), Zn-0.05 wt% Mg (Zn-0.05 Mg), and Zn-0.2 wt% Mg (Zn-0.2 Mg). Pure Zn and Zn-xMg alloys were prepared by melting pure Zn (99.95%) and pure Mg (99.95%) in an iron crucible shielded by mixed gas (CO_2 and SF_6) using a resistance furnace. The molten metal was cast into a water-cooled cylindrical coppery mold (Φ 60 mm) to obtain the as-cast Zn alloy ingots.

Zn-xMg alloy ingots were annealed at 350°C for 24 h to acquire uniform microstructures and then hot extruded at 200-300°C and an extrusion rate of 25 : 1. Next, the hot-extruded Zn-xMg alloy wires with a diameter of Φ 3 mm were cold-drawn to Φ 0.3 mm by a self-made drawing machine at room temperature (RT) [27]. If broken during cold drawing, the Zn-xMg alloys were annealed at 200°C for 5 min. Finally, Zn alloy wires (Φ 0.3 mm) were annealed at different temperatures (100°C, 150°C, 200°C, 250°C, 300°C) for different times (10 min, 30 min) to enhance the plasticity.

2.2. Microstructure Characterization. The metallographic microstructure paralleled to the deforming direction was detected and collected using an optical microscope (Olympus, Shinjuku, Tokyo, Japan). Before observation, the samples were ground and polished to mirror surface and then etched by a mixed solution of CrO_3 and Na_2SO_4 (10 g CrO_3, 0.75 g Na_2SO_4, and 50 mL H_2O) for 6-7 s at RT. The grain size was measured by the linear intercept technique [29]. Besides, the phases of the as-cast alloy were analyzed by an X-ray diffractometer (XRD, D8-Discover, German Bruker). The microstructures of cold-drawn alloy wires (Φ 0.3 mm) were characterized by synchrotron radiation X-ray diffractometer

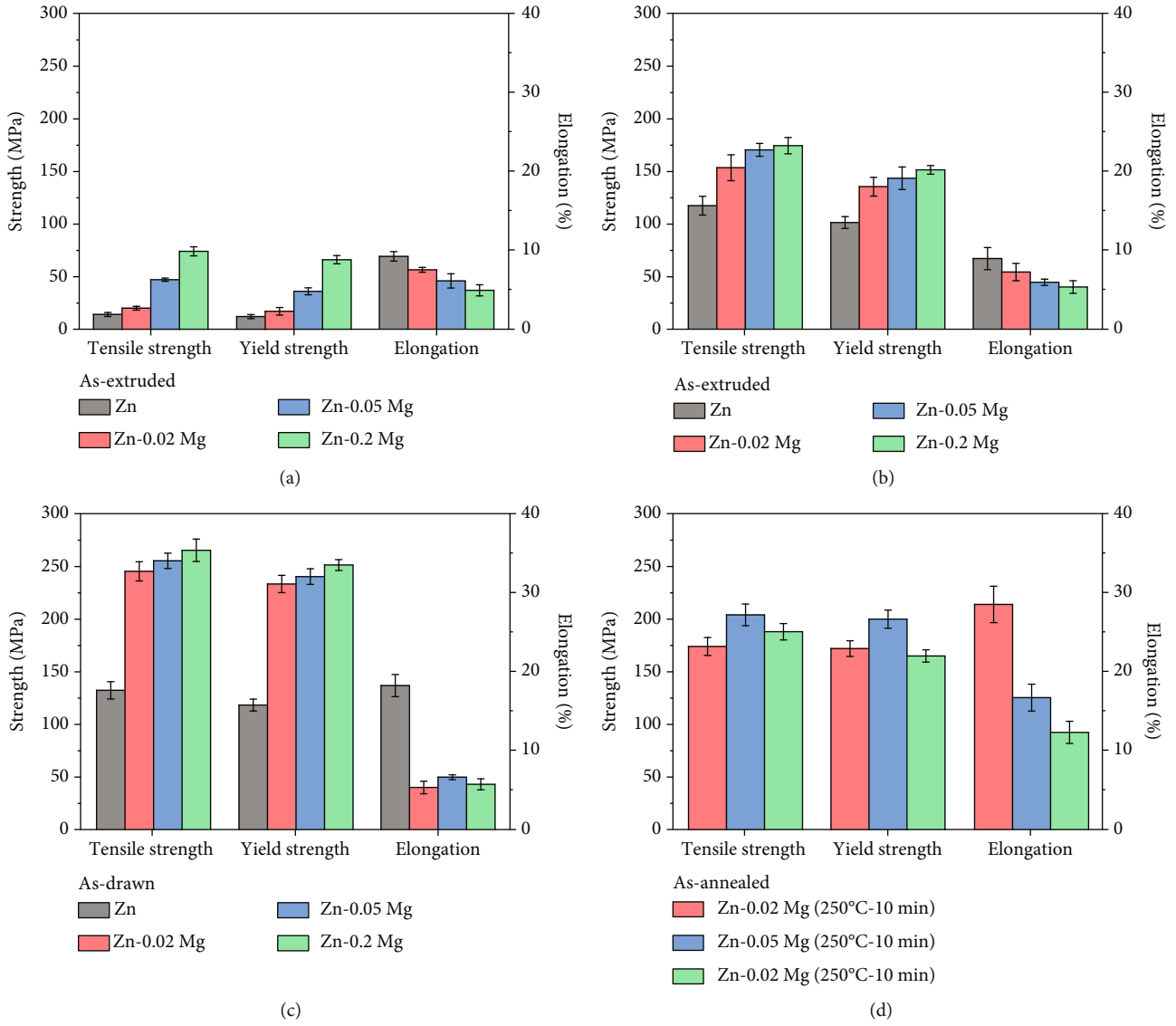

Figure 4: Mechanical properties of pure Zn and Zn-xMg alloys in different states: (a) as-cast, (b) as-extrude, (c) as-drawn, and (d) as-annealed.

(SR-XRD) at BL14B1 station, SSRF (Shanghai, China). Moreover, the second phases in Zn-Mg alloys were identified by a scanning electron microscope (SEM, Sirion 200) equipped with an energy dispersive spectrometer (EDS).

2.3. Mechanical Properties. Mechanical properties, including ultimate tensile strength (UTS), yield strength (YS), and elongation to fracture (EL), were measured by a universal material test machine (CTM4503). The wires with a gauge size of 50 mm in the center and a clamping size of 20 mm at both ends were designed as tensile samples. The mechanical tests for each sample were repeated three times at a constant tensile speed of 2 mm/min at RT.

The microhardness of the Zn alloy wires was measured using a microhardness tester (FM-700, Future-Tech, Japan) with a loading force of 100 gf. The hardness values of Zn alloy wires were collected and analyzed based on ten testing points of each sample.

2.4. Corrosion Behaviors. Corrosion behavior was measured by electrochemical methods and immersion tests in Hank's solution at 37 ± 0.5°C. In these electrochemical measurements, an electrochemical station (CHI660E) was carried out to collect open circuit potential (OCP) and potentiodynamic polarization (PP) curves. A classical three-electrode cell was applied for electrochemical measurements, in which the working electrode was Zn alloy wires with a fixed exposed area in Hank's solution, the platinum electrode was set as a counter electrode, and a saturated calomel electrode was acted as a reference electrode. Prior to electrochemical measurements, Zn alloy wires were acid cleaned in 1% nitric acid solution to remove surface oxide films. The wires were inserted vertically in Hank's solution for electrochemical measurements. The immersion length of the wires was recorded to calculate the exposed surface area. OCP curves were measured for 2400 s in Hank's solution. PP curves were scanned from -1.6 V vs SCE to -0.6 V vs. SCE at

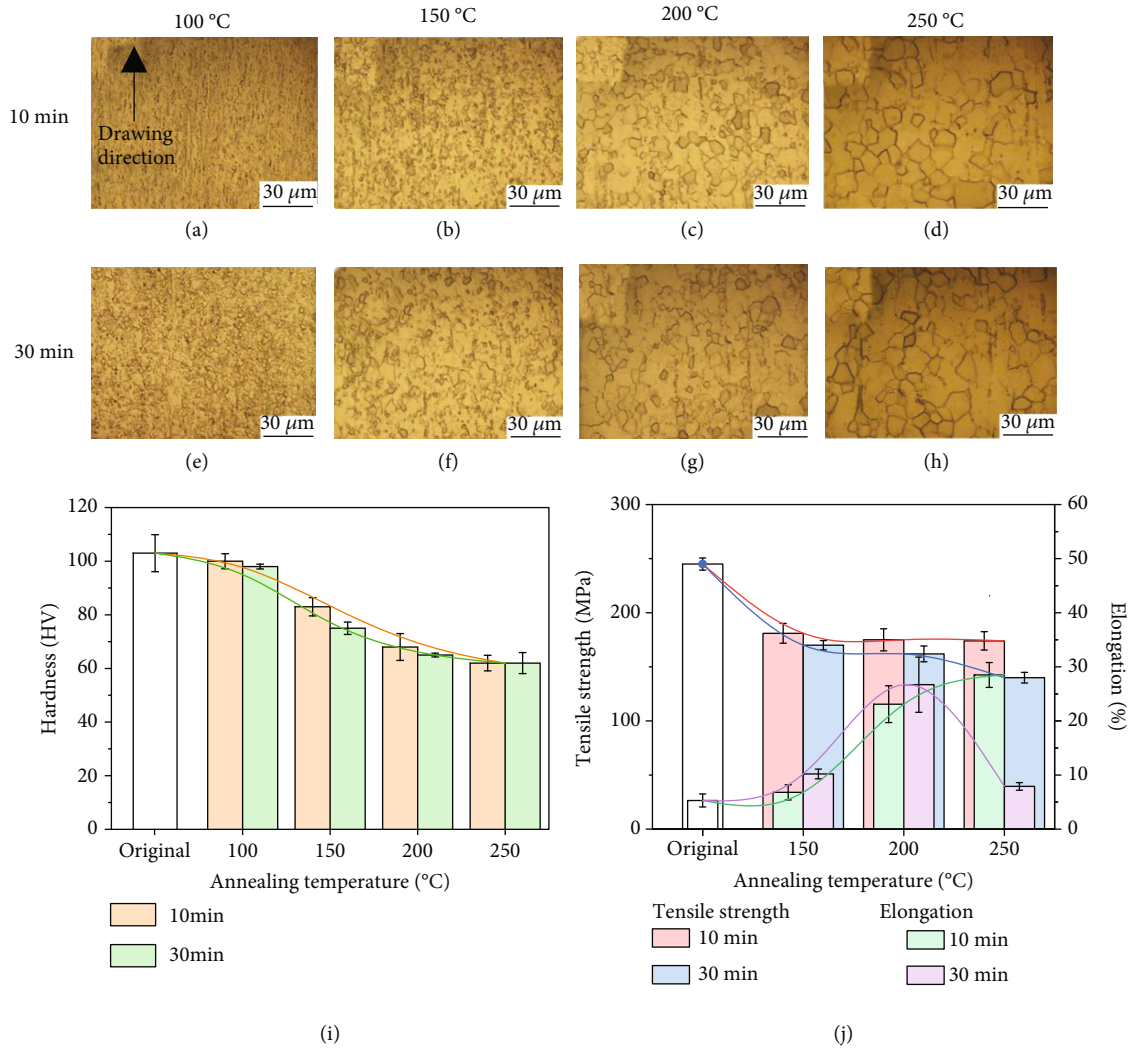

Figure 5: Microstructures and mechanical properties of Zn-0.02 Mg wire annealed under different conditions: (a) 100°C-10 min, (b) 150°C-10 min, (c) 200°C-10 min, (d) 250°C-10 min, (e) 100°C-30 min, (f) 150°C-30 min, (g) 200°C-30 min, (h) 250°C-30 min, (i) microhardness, and (j) tensile strength and elongation.

a scanning rate of 1 mV/s. In immersion tests, the wires were cleaned in 200 g/L CrO_3 solution at 80°C for corrosion product removal and dried before and after weighting. Corrosion rate (CR, mm/year) was calculated referring to Equation (1) [30], where m_0 is the initial weight of specimens, m_1 is the remaining weight of specimens after corrosion, ρ is the density of the alloy (7.138 g/cm^3 for Zn-0.02 Mg, 7.137 g/cm^3 for Zn-0.05 Mg, and 7.129 g/cm^3 for Zn-0.2 Mg), and t is the corrosion time. The corrosion morphology and products after 7 d and 14 d immersion were observed by SEM equipped with EDS.

$$\mathrm{CR} = \frac{3.65 \times (m_0 - m_1)}{\rho}. \quad (1)$$

3. Results and Discussion

The chemical concentration of as-cast Zn and its alloys was detected by an optical emission spectrometer (OES), as exhibited in Table 1. The OES results are fitting well with the designed compositions, and a little fluctuation in chemical composition might be caused by melting loss. Figures 1(a) and 1(b) are XRD patterns of as-cast and as-drawn Zn alloys. The as-drawn Zn alloy wires were analyzed by a synchronous radiator (Figure 1(d)), in which SR-XRD was performed for phase identifying of precision devices including Zn alloy fine wires. The Zn phase (JCPDF No. 04-0831) was identified in the as-cast and as-drawn Zn alloys while Mg-Zn second phase could not be found owing to the little Mg addition. Zn alloy wires with the dimension of Φ 3 mm and Φ 0.3 mm are displayed in Figure 1(c), and the surfaces show metallic color after cold drawing. Moreover, the comparison between XRD and SR-XRD patterns indicated that the texture evolution is induced by extrusion and cold drawing. There is a drastic decrease in the relative intensity of (0002) and (10$\bar{1}$0) planes, where the diffraction intensity of the (10$\bar{1}$2) plane increases in Zn-xMg alloys. By comparison, the (10$\bar{1}$2) plane of pure Zn is shifted to the strongest

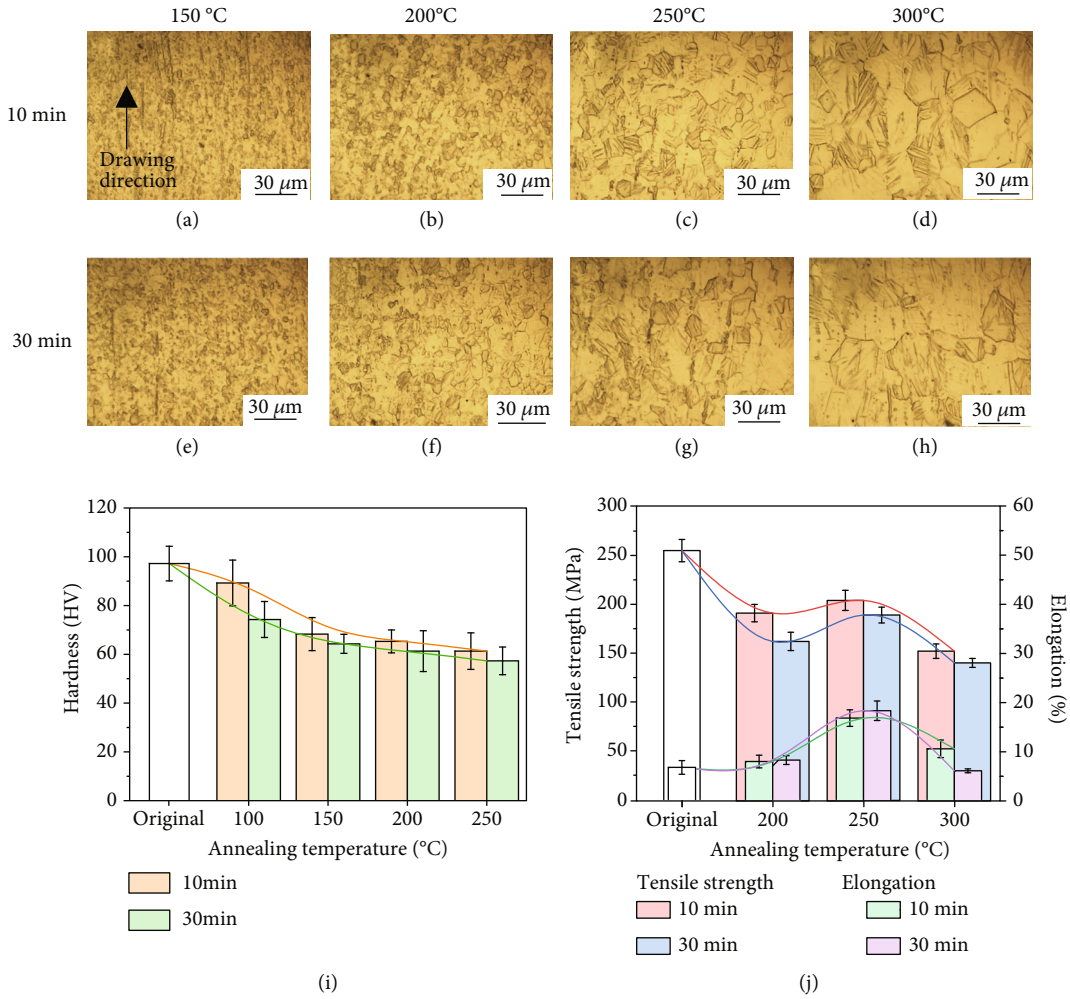

FIGURE 6: Microstructures and mechanical properties of Zn-0.05 Mg wire annealed in different parameters: (a) 150°C-10 min, (b) 200°C-10 min, (c) 250°C-10 min, (d) 300°C-10 min, (e) 150°C-30 min, (f) 200°C-30 min, (g) 250°C-30 min, (h) 300°C-30 min, (i) microhardness, and (j) tensile strength and elongation.

peak while Zn-xMg alloys still keep the $(10\bar{1}1)$ plane as the strongest peak, demonstrating that the Mg addition hinders the $(10\bar{1}2)$ plane. Also, the diffraction peaks of Zn and Zn-xMg alloys are shifted to a low diffraction angle, indicating the increase of d-spacing caused by deformation. As a consequence, Mg alloying in Zn alloys induces texture evolution during deformation.

Figure 2 exhibits the microstructures of as-cast Zn and Zn-xMg alloys. The average grain size of as-cast pure Zn is about 430 μm (in Figure 2(a)). The grain sizes of Zn-xMg alloys decrease with Mg addition, which are about 250 μm for Zn-0.02 Mg, 110 μm for Zn-0.05 Mg, and 80 μm for Zn-0.2 Mg (in Figure 2(b)–2(d)). According to the Zn-Mg binary phase diagram, the solubility of Mg in Zn at RT is 0.008%, and the maximum solubility is 0.16% at 364°C. Besides, the eutectic phases ($\alpha - Zn + Mg_2Zn_{11}$) are found with the Mg addition exceeding 0.15% [14]. As shown in Figure 2(e), the eutectic phases are distributed uniformly in Zn-0.2 Mg alloys. Herein, the EDS results (in Figure 2(f)) indicated that the Mg_2Zn_{11} phases are located in the grain boundary of Zn-0.2 Mg alloys.

Figure 3 illustrates the microstructures of Zn and Zn-xMg alloys after hot extrusion and cold drawing. The as-extruded grains are equiaxed in shape and with smaller size. The grain size distribution graphs are analyzed as inserted in Figures 3(a)–3(d). With Mg addition from 0.02 wt% to 0.2 wt%, the grain size and relevant distribution range are shrunk obviously. The average grain sizes of the as-extruded Zn alloys are about 130 μm for pure Zn, 60 μm for Zn-0.02 Mg, 40 μm for Zn-0.05 Mg, and 20 μm for Zn-0.2 Mg, respectively. Besides, after 54 passes cold drawing without annealing, the material starts dynamic recrystallization so that the fine and equiaxed grains result see in Figure 3(e), while the original equiaxed grains of as-extruded Zn-xMg are transformed into fibrous structures along the drawing direction. As indicated by red arrows in Figure 3(h), the intermediate phases are dispersed along the drawing direction in Zn-0.2 Mg alloys.

Figure 4 summarizes the mechanical properties of Zn and Zn-xMg alloys. In Figure 4(a), with Mg addition, the as-cast Zn and Zn-xMg alloys appear extremely brittle with reduced ELs and improved mechanical strength including

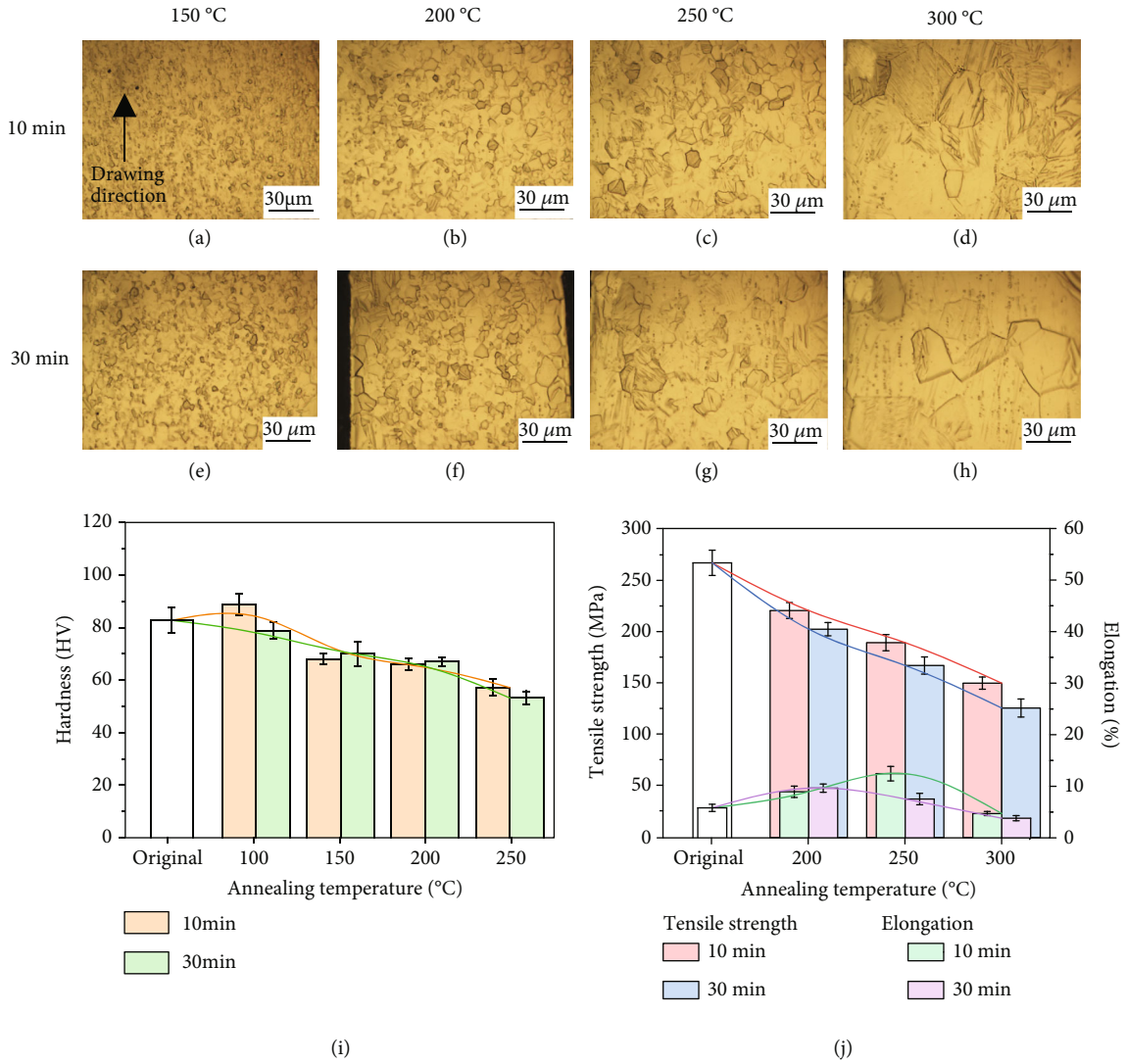

FIGURE 7: Microstructures and mechanical properties of Zn-0.2 Mg wire annealed in different parameters: (a) 150°C-10 min, (b) 200°C-10 min, (c) 250°C-10 min, (d) 300°C-10 min, (e) 150°C-30 min, (f) 200°C-30 min, (g) 250°C-30 min, (h) 300°C-30 min, (i) microhardness, and (j) tensile strength and elongation.

UTS and YS. The as-cast Zn has the lowest UTS of 14 MPa while UTS of Zn-0.2 Mg reaches the maximum of 74 MPa. The strengthening effect results from grain refinement and the formation of second phases. Figures 4(b) and 4(c) show the mechanical properties of pure Zn and Zn-xMg alloys after the deformation process. After hot extrusion, both the grain refinement and dispersed Mg_2Zn_{11} in Zn-xMg alloys contribute to an enhancement in mechanical properties, which UTS reaches 117 ± 8.9 MPa for pure Zn and 174 ± 7.7 MPa for Zn-0.2 Mg. The as-extruded Zn alloys have a grain size > 20 μm, in which grain boundary sliding can be activated. Thus, the as-extruded Zn alloys have limited ELs below 10%. As shown in Figure 4(c), there is an increasing trend in UTSs and YSs of as-drawn Zn and Zn alloys. UTSs increase with Mg addition: the as-drawn Zn wire has UTS of 130 MPa, and Zn-0.2 Mg wire shows an UTS of 270 MPa. By contrast, it is found that there are no changes in ELs of Zn-xMg alloys but an obvious increase in EL of pure Zn to 18.2%, which is attributed to the dynamic recrystallization at RT. Liu et al. reported the extraordinary plasticity of as-cast pure zinc is attributed to dynamic recrystallization [31]. However, the dynamic recrystallization might be restrained by the solid solution and second phase; so, the equiaxed crystals cannot be found in the as-drawn Zn-xMg alloys. Furthermore, the as-drawn Zn-xMg alloy wires are heat-treated at 250°C for 10 min, and the as-annealed Zn-xMg alloy wires exhibit comprehensive mechanical properties with combined strength and plasticity.

Moreover, the work also investigated the effect of annealing on microstructure and mechanical properties. Figure 5 exhibits the microstructures and mechanical properties of as-annealed Zn-0.02 Mg. Both, raising treatment temperature and prolonging time, coarsen microstructures regulate mechanical properties. In the recovery process at 100°C, the hardness seems to give no obvious sign of slowing down along with a slight increase in grain size. When the

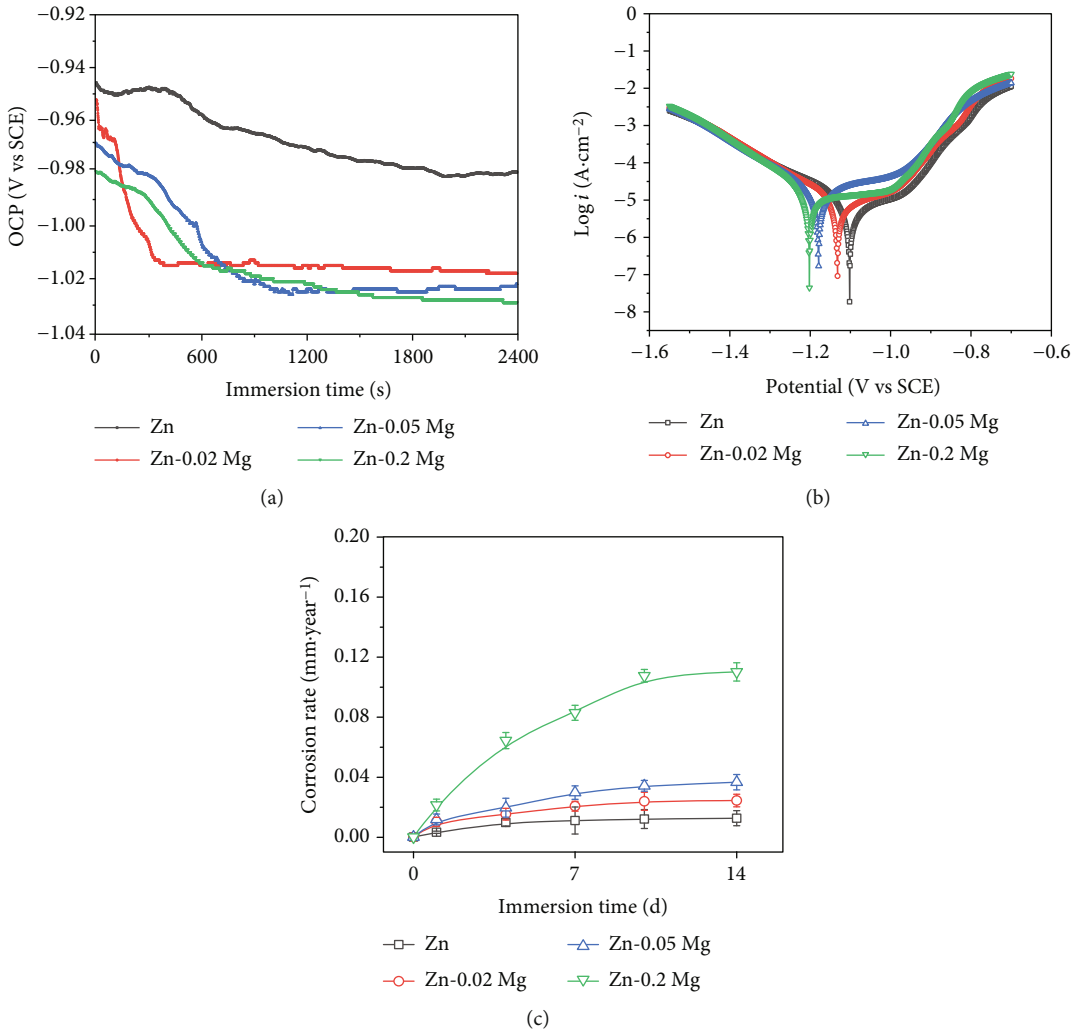

Figure 8: Corrosion measurements: (a) OCP curves, (b) PP curve, and (c) corrosion rate measured by weight loss.

Table 2: Corrosion rate calculated by electrochemical methods and weight loss measurements.

Alloy	Methods	Zn	Zn-0.02 mg	Zn-0.05 mg	Zn-0.2 mg
CR_1 (mm/year)	Electrochemical methods	0.019 ± 0.002	0.029 ± 0.003	0.040 ± 0.005	0.036 ± 0.010
CR_2 (mm/year)	Weight loss measurements	0.010 ± 0.001	0.020 ± 0.001	0.030 ± 0.002	0.104 ± 0.002

annealing temperature is above 100°C, the microhardness decreases sharply with the weakness of the inherited structure and occurrence of equiaxial grains, indicating the recrystallization process. The completed recrystallization might be performed at temperature above 200°C, in which the microhardness tends to be stable. Figure 5(j) shows the UTS and EL results of the as-annealed Zn-0.02 Mg. As the annealing temperature rises, UTS decreases in opposite to the increase of EL. Meanwhile, with annealing prolonged to 30 min, it is obvious that UTS decrease and EL increases. However, annealed at 250°C for 30 min, the excessive grain coarsening also makes damage to the improvement of EL. As mentioned above, the optimized parameter for annealing is at 250°C for 10 min, and the as-annealed Zn-0.02 Mg wire has an UTS of 172 MPa and EL of 28.5%. The short-time annealing at high temperature might complete recrystallization and retard excessive grain coarsening, leading to an increase in EL of the annealed Zn alloy wires.

Figures 6(a)–6(h) and 7(a)–7(h) display the microstructures of the annealed Zn-0.05 Mg and Zn-0.2 Mg alloy wires. An increase in Mg hinders the reversion and recrystallization, and a higher temperature is applied for annealing. The microstructure and microhardness evolution of Zn-0.05 Mg and Zn-0.2 Mg alloys are similar to that of the Zn-0.02 Mg alloy. The microstructure evolution process is composed of recovery, recrystallization, and coarsening stages. Figures 6(i), 6(j), 7(i), and 7(j) display the hardness and tensile test results. By comparison, the annealing temperature has more significant effects on microstructure and mechanical properties than the treatment time. In conclusion, Zn-

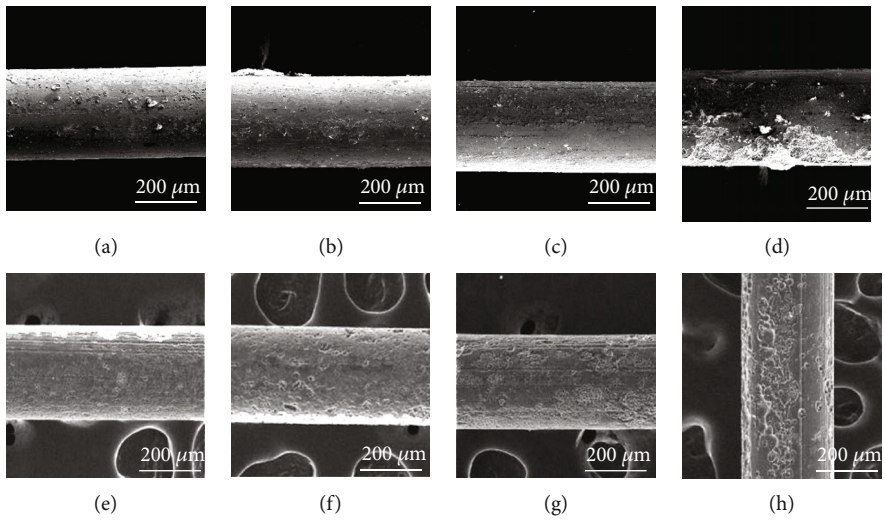

Figure 9: Morphologies of Zn-xMg wires immersed for 7 days: (a) pure Zn wire, (b) Zn-0.02 Mg wire, (c) Zn-0.05 Mgwire, and (d) Zn-0.2 Mg wire. Corrosion morphologies of Zn-xMg wires immersed for 14 days: (e) pure Zn wire, (f) Zn-0.02 Mg wire, (g) Zn-0.05 Mgwire, and (h) Zn-0.2 Mgwire.

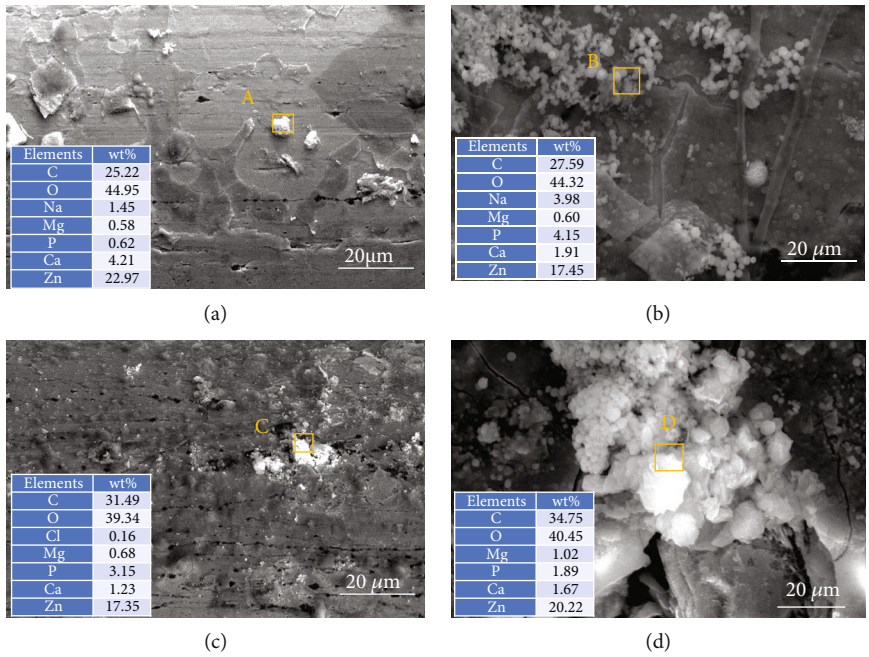

Figure 10: Morphologies and EDS of corrosion products on the surface of Zn-xMg wires immersed for 7 days: (a) pure Zn wire, (b) Zn-0.02 Mg wire, (c) Zn-0.05 Mg wire, and (d) Zn-0.2 Mg wire.

xMg alloy wires have a desirable microstructure and optimized mechanical properties after annealed at 250°C for 10 min. Annealed at the optimized parameter, the Zn-0.05 Mg alloy wire has an UTS of 204 MPa and EL of 16.7% while the Zn-0.2 Mg alloy wire has an UTS of 165 MPa and EL of 12.3%. Herein, the plasticity of Zn-0.2 Mg alloy wire was improved with limits owing to more intermediate phases.

Figure 8 exhibits the electrochemical results of cold-drawn Zn and annealed Zn-xMg alloy wires, and Table 2 lists the corrosion rate (CR) calculated by electrochemical methods and weight loss measurements. After the initial immersion in Hank's solution, OCP values (in Figure 8(a)) are stable to about -0.98 V (vs SCE) for pure Zn, -1.02 V (vs SCE) for Zn-0.02 Mg, -1.02 V (vs SCE) for Zn-0.05 Mg, and -1.03 V (vs SCE) for Zn-0.2 Mg, respectively. Mg addition for Zn alloys increases the tendency towards corrosion. In PP curves, Zn-xMg alloy wires exhibit larger corrosion current density (i_{corr}) with Mg addition. The i_{corr} is a major evaluation criterion of corrosion rate [32]. The corrosion rate is calculated from the electrochemical results, as shown in Figure 8(b). Zn-0.05 Mg and Zn-0.2 Mg alloy wires display rapid degradation rates. Moreover, the long-time immersion

tests directly reflect the degradation behavior of the Zn alloys after implantation. Figure 8(c) shows the corrosion rate curves based on weight loss tests. Zn-0.2 Mg alloy wire is degraded at a relatively higher rate while pure Zn wire has the lowest degradation rate. The mentioned above reflects that Mg alloying is conducive to improving the biodegradability of Zn alloys for biomedical applications.

In order to further evaluate the degradation behavior, the surface morphologies of Zn and Zn-xMg alloy wires after immersion are exhibited in Figures 9(a)–9(h). Few corrosion pits are found in Zn wires after 7 d and 14 d immersion. Zn-xMg alloy wires are seriously corroded with Mg addition. Besides, the corrosion product morphologies are shown in Figures 10(a)–10(d). Zn-0.2 Mg alloy wire is covered by a mass of corrosion products, which is attributed to the rapid degradation of Mg-rich second phases. Besides, the rapid formation of corrosion products might temporarily slow down the corrosion rate during PP measurements after the initial immersion of 30 min. Thus, for Zn-0.2 Mg alloy wire, the corrosion rate calculated by PP seems to mismatch with that one measured by weight loss. Based on EDS analysis, the corrosion products of Zn alloys in Hank's solution are composed of Zn, O, and C elements as well as a few Mg, Ca, and P elements, indicating that the corrosion product is composed of complex Zn mineral phases [33], which might be ZnO, $Zn_5(CO_3)_2(OH)_6$, $Zn_3(PO_4)_2{\cdot}4H_2O$, and Ca-P compounds [34]. With immersion time prolonging to 14 d, many deeper and more intensive corrosion pits occur on Zn-xMg alloys, especially Zn-0.2 Mg alloys, as shown in Figures 9(e)–9(h). These results are corresponding to that ones in Figure 8.

4. Conclusions

In this study, Zn-xMg ($x = 0.02$, 0.05, 0.2 wt%) alloy wires were prepared and investigated for biomedical applications. For the as-cast Zn and Zn-xMg alloys, Mg alloying led to an obvious decrease in average grain size and improves the tensile properties. Hot extrusion and cold drawing can substantially enhance the UTSs of Zn-xMg alloy and increase the ELs (5-8%) to a limited degree. Deformation texture was formed during the production, especially for Zn alloys with Mg alloying. Annealing treatment refined the structures of Zn-xMg alloy which further improved the plasticity but slightly decreased strength. After the optimized annealing process, Zn-0.05 Mg had the desirable comprehensive mechanical properties with UTS and EL reaching 204 MPa and 16.7%, respectively. Moreover, based on electrochemical measurements and immersion tests, Mg alloying increased the degradation rates of Zn alloy wires in Hank's solution. The research explored Zn-xMg alloy fine wires for biomedical applications and investigated the effect of the preparation process on service performances of Zn-xMg alloy fine wires.

Data Availability

The data used to support findings of this study are included within the article.

Conflicts of Interest

The authors declare that there is no conflict of interest regarding the publication of this article.

Acknowledgments

The authors thank all staff members of station BL14B1 (SSRF, China) for SR-XRD analysis. This work was supported by the National Key Research and Development Program of China (No. 2016YFC1102402), the National Natural Science Foundation of China (No. 51971062), the Science and Technology Project of Jiangsu Province (No. BE2019679), the Technological Innovation of Key Industry of Suzhou (SYG201904), and the Open Research Fund of Jiangsu Key Laboratory for Advanced Metallic Materials (AMM2021A01).

References

[1] Y. F. Zheng, X. N. Gu, and F. Witte, "Biodegradable metals," *Materials Science and Engineering: R: Reports*, vol. 77, pp. 1–34, 2014.

[2] H. F. Li, Y. F. Zheng, and L. Qin, "Progress of biodegradable metals," *Progress in Natural Science: Materials International*, vol. 24, no. 5, pp. 414–422, 2014.

[3] M. Peuster, C. Hesse, T. Schloo, C. Fink, P. Beerbaum, and C. von Schnakenburg, "Long-term biocompatibility of a corrodible peripheral iron stent in the porcine descending aorta," *Biomaterials*, vol. 27, no. 28, pp. 4955–4962, 2006.

[4] H. Hermawan, H. Alamdari, D. Mantovani, and D. Dube, "Iron-manganese: new class of metallic degradable biomaterials prepared by powder metallurgy," *Powder Metallurgy*, vol. 51, no. 1, pp. 38–45, 2008.

[5] C. Liu, Z. Ren, Y. D. Xu, S. Pang, X. B. Zhao, and Y. Zhao, "Biodegradable magnesium alloys developed as bone repair materials: a review," *Scanning*, vol. 2018, Article ID 9216314, 15 pages, 2018.

[6] X. Z. Gao, C. Y. Dai, Q. Jia et al., "In vivo corrosion behavior of biodegradable magnesium alloy by MAF treatment," *Scanning*, vol. 2021, Article ID 5530788, 9 pages, 2021.

[7] M. P. Staiger, A. M. Pietak, J. Huadmai, and G. Dias, "Magnesium and its alloys as orthopedic biomaterials: a review," *Biomaterials*, vol. 27, no. 9, pp. 1728–1734, 2006.

[8] M. Esmaily, J. E. Svensson, S. Fajardo et al., "Fundamentals and advances in magnesium alloy corrosion," *Progress in Materials Science*, vol. 89, pp. 92–193, 2017.

[9] X. N. Gu, Y. F. Zheng, Y. Cheng, S. P. Zhong, and T. F. Xi, "In vitro corrosion and biocompatibility of binary magnesium alloys," *Biomaterials*, vol. 30, no. 4, pp. 484–498, 2009.

[10] K. Chen, Y. Lu, H. Y. Tang et al., "Effect of strain on degradation behaviors of WE43, Fe and Zn wires," *Acta Biomaterialia*, vol. 113, pp. 627–645, 2020.

[11] G. N. Li, S. M. Zhu, J. F. Nie, Y. F. Zheng, and Z. L. Sun, "Investigating the stress corrosion cracking of a biodegradable Zn-0.8 wt%Li alloy in simulated body fluid," *Bioactive Materials*, vol. 6, no. 5, pp. 1468–1478, 2021.

[12] H. T. Yang, B. Jia, Z. C. Zhang et al., "Alloying design of biodegradable zinc as promising bone implants for load- bearing applications," *Nature Communications*, vol. 11, no. 1, p. 401, 2020.

[13] G. N. Li, H. T. Yang, Y. F. Zheng et al., "Challenges in the use of zinc and its alloys as biodegradable metals: perspective from biomechanical compatibility," *Acta Biomaterialia*, vol. 97, pp. 23–45, 2019.

[14] H. Liu, H. Huang, Y. Zhang et al., "Evolution of Mg-Zn second phases during ECAP at different processing temperatures and its impact on mechanical properties of Zn-1.6Mg (wt.%) alloys," *Journal of Alloys and Compounds*, vol. 811, article 151987, 2019.

[15] C. Chen, R. Yue, J. Zhang, H. Huang, J. L. Niu, and G. Y. Yuan, "Biodegradable Zn-1.5Cu-1.5Ag alloy with anti-aging ability and strain hardening behavior for cardiovascular stents," *Materials Science and Engineering: C*, vol. 116, article 111172, 2020.

[16] R. Yue, J. L. Niu, Y. T. Li et al., "In vitro cytocompatibility, hemocompatibility and antibacterial properties of biodegradable Zn-Cu-Fe alloys for cardiovascular stents applications," *Materials Science and Engineering: C*, vol. 113, article 111007, 2020.

[17] K. M. Hambidge and N. F. Krebs, "Zinc deficiency: a special challenge," *The Journal of Nutrition*, vol. 137, no. 4, pp. 1101–1105, 2007.

[18] P. J. Aggett and J. T. Harries, "Current status of zinc in health and disease states," *Archives of Disease in Childhood*, vol. 54, no. 12, pp. 909–917, 1979.

[19] Y. Liu, Y. F. Zheng, X. H. Chen et al., "Fundamental theory of biodegradable metals-definition, criteria, and design," *Advanced Functional Materials*, vol. 29, no. 18, article 1805402, 2019.

[20] P. K. Bowen, J. Drelich, and J. Goldman, "Zinc exhibits ideal physiological corrosion behavior for bioabsorbable stents," *Advanced Materials*, vol. 25, no. 18, pp. 2577–2582, 2013.

[21] D. Vojtech, J. Kubasek, J. Serak, and P. Novak, "Mechanical and corrosion properties of newly developed biodegradable Zn-based alloys for bone fixation," *Acta Biomaterialia*, vol. 7, no. 9, pp. 3515–3522, 2011.

[22] H. F. Li, H. T. Yang, Y. F. Zheng, F. Y. Zhou, K. J. Qiu, and X. Wang, "Design and characterizations of novel biodegradable ternary Zn-based alloys with IIA nutrient alloying elements Mg, Ca and Sr," *Materials & Design*, vol. 83, pp. 95–102, 2015.

[23] C. Xiao, L. Q. Wang, Y. P. Ren et al., "Indirectly extruded biodegradable Zn-0.05wt%Mg alloy with improved strength and ductility: *In vitro* and *in vivo* studies," *Journal of Materials Science and Technology*, vol. 34, no. 9, pp. 1618–1627, 2018.

[24] H. F. Li, X. H. Xie, Y. F. Zheng et al., "Development of biodegradable Zn-1X binary alloys with nutrient alloying elements Mg, Ca and Sr," *Scientific Reports*, vol. 5, no. 1, article 10719, 2015.

[25] J. M. Seitz, M. Durisin, J. Goldman, and J. W. Drelich, "Recent advances in biodegradable metals for medical sutures: a critical review," *Advanced Healthcare Materials*, vol. 4, no. 13, pp. 1915–1936, 2015.

[26] J. Bai, L. L. Yin, Y. Lu et al., "Preparation, microstructure and degradation performance of biomedical magnesium alloy fine wires," *Progress in Natural Science: Materials International*, vol. 24, no. 5, pp. 523–530, 2014.

[27] H. Guo, R. H. Cao, Y. F. Zheng, J. Bai, F. Xue, and C. L. Chu, "Diameter-dependent _in vitro_ performance of biodegradable pure zinc wires for suture application," *Journal of Materials Science and Technology*, vol. 35, no. 8, pp. 1662–1670, 2019.

[28] Y. Okamura, N. Hinata, T. Hoshiba et al., "Development of bioabsorbable zinc-magnesium alloy wire and validation of its application to urinary tract surgeries," *World Journal of Urology*, vol. 39, no. 1, pp. 201–208, 2021.

[29] H. Abrams, "Grain size measurement by the intercept method," *Metallography*, vol. 4, no. 1, pp. 59–78, 1971.

[30] M. C. Zhao, P. Schmutz, S. Brunner, M. Liu, G. L. Song, and A. Atrens, "An exploratory study of the corrosion of Mg alloys during interrupted salt spray testing," *Corrosion Science*, vol. 51, no. 6, pp. 1277–1292, 2009.

[31] S. Y. Liu, D. Kent, H. Y. Zhan, N. Doan, M. Dargusch, and G. Wang, "Dynamic recrystallization of pure zinc during high strain-rate compression at ambient temperature," *Materials Science and Engineering: A*, vol. 784, article 139325, 2020.

[32] Q. S. Dong, X. X. Zhou, Y. J. Feng et al., "Insights into self-healing behavior and mechanism of dicalcium phosphate dihydrate coating on biomedical Mg," *Bioactive Materials*, vol. 6, no. 1, pp. 158–168, 2021.

[33] C. García-Mintegui, L. C. Córdoba, J. Buxadera-Palomero et al., "Zn-Mg and Zn-Cu alloys for stenting applications: From nanoscale mechanical characterization to _in vitro_ degradation and biocompatibility," *Bioactive Materials*, vol. 6, no. 12, pp. 4430–4446, 2021.

[34] X. Liu, W. Yuan, D. Shen, Y. Cheng, D. Chen, and Y. Zheng, "Exploring the biodegradation of pure Zn under simulated inflammatory condition," *Corrosion Science*, vol. 189, article 109606, 2021.

Hindawi
Scanning
Volume 2021, Article ID 3760592, 10 pages
https://doi.org/10.1155/2021/3760592

Research Article

Detection of Changes of Ancient Buildings from Terrestrial Laser Scanning and Hyperspectral Imaging

Xiao Zhang, Rongqing Ma, and Ruoyi Gao

College of Art, Taiyuan University of Technology, Jinzhong 030600, China

Correspondence should be addressed to Xiao Zhang; zhangxiao@tyut.edu.cn

Received 27 July 2021; Accepted 30 August 2021; Published 18 September 2021

Academic Editor: Guosong Wu

Ancient buildings have various geometric and material changes caused by the historical and natural factors, and their comprehensive detection has also been a more important challenge. This way, in this paper, a flexible, scientific approach from terrestrial laser scanning and hyperspectral imaging is provided for this issue. It is possible to flexibly and accurately detect some potential crisis, which cannot be found in some surface phenomena of historical buildings. Furthermore, one of the main characteristic of this method is that the time and place of the two data acquisition need not be limited, but they can be accurately fused. Another one of the main features is that the fusion data can synthetically detect geometric and material changes of historical buildings. This method was applied to the case study of the Beijing Tianningsi Tower, an extremely dazzling pearl of the Chinese Buddhist pagoda, on which the signs of deformation and restoration were found in the tower shape and in the tower-body sculpture. It was possible to assess the typical physical, chemical, and biological changes of historical buildings, to provide scientific basis for comprehensive research. The results demonstrate that this method is feasible and applicable for detecting changes of ancient buildings and is applied to similar research using more analytical methods for multisource data.

1. Introduction

The research of conservation, restoration, and humanities of ancient buildings has been an important topic for many years, specially detecting and quantifying the geometric deformation, material deterioration, and microbial growth mildew of ancient buildings caused by natural or human factors, which is helpful to further evaluate their status and plan possible intervention measures in the future [1, 2]. In recent years, due to their high flexibility and no damage to buildings compared with classical systems, the contactless and noninvasive techniques, such as terrestrial laser scanning [3, 4], infrared thermography (IRT) [5, 6], and Multispectral or Hyperspectral Technique [7, 8], were used to detected historical buildings. Particularly, the different types of terrestrial laser scanner comparing historical objects and infrared thermography detecting of building diagnostics have accelerated the protection and restoration of cultural heritage [9].

However, the changes of ancient buildings are usually caused by geometric, biological, chemical, and other reasons. In addition, some buildings have been repaired many times in history, and the building materials are different, although the surface observation is the same. Single technology can not accurately detect these changes, such as laser scanning detecting geometric deformation and digital images detecting color changes. If we use multiple devices and the integration of multiple technologies can extract more information from multiple angles, we can observe historical buildings more effectively [1]. At present, the most popular fusion method is the fusion of TLS and digital imaging. For example, Tangible cultural heritage is assessed by Point Cloud and Background Photographic Image [10]. And cultural heritage is surveyed to create a 3D multiscale database based on image and active sensor [11]. TLS data with digital images strengthen the recognition of interesting details and their precise geometrical localization in the space because of the high-resolution image information [12, 13].

(a) (b)

Figure 1: Data acquisition equipment.

Table 1: Hyperspectral camera parameters.

Name	Parameter	Name	Parameter
Spectrum range	400-1000 nm	Spectrometer entrance slit width	30 μm
Spectral resolution	2.8 nm	Spectrometer entrance slit length	11.84 mm
FOV	27.2°	Camera lens focal length	23 mm
Spatial resolution	1600 pixels	Spectral band numbers	840

Compared with digital images having only three band spectral information like red, green, and blue, the hyperspectral data have hundreds or even thousands of band spectral information, which can detect quickly light frequencies and relative intensities of building surface. However, the fusion of laser scanning and hyperspectral imaging is rarely used, due to the so complicated fusion method caused by the different sensors and imaging modalities. This paper proposes a method to detect changes of ancient buildings using laser scanning and hyperspectral imaging. That is, laser data and hyperspectral data are first fused, and then they are used to comprehensively and accurately detect and analyze the change and history of ancient buildings. In the fusion data, the laser information detected the geometric change like incline, convex, and concave by point cloud 3D coordinates, and the hyperspectral information detects the material change caused by corroding, weathering, and salt blooming. This method was applied to the case study of Tianningsi Tower in Beijing, China.

2. Materials and Methods

2.1. Data Acquisition Equipment. In this work, data acquisition depends on the terrestrial laser scanning system and the terrestrial sweep hyperspectral scanning system, respectively. In either the data acquisition time or location, these two systems work independently.

The laser scanning system used is Leica Scanstation C10, as shown in Figure 1(a). This scanner is based in the principle of flight of time and has a laser source that emits pulses with a wavelength of 532 nm. The maximal scanning rate is 50,000 points per second. The full scanning field angle is $360^\circ \times 270^\circ$. The signal intensity received by the sensor system is recorded in [0 255]. The software Leica Cyclone was used for the acquisition and the processing of the data.

The hyperspectral imaging system used is independently integrated by our laboratory, which consists of a hyperspectral camera, a turntable, a controller, and a computer, as shown in Figure 1(b). And the hyperspectral camera parameters are shown in Table 1. The software used for the

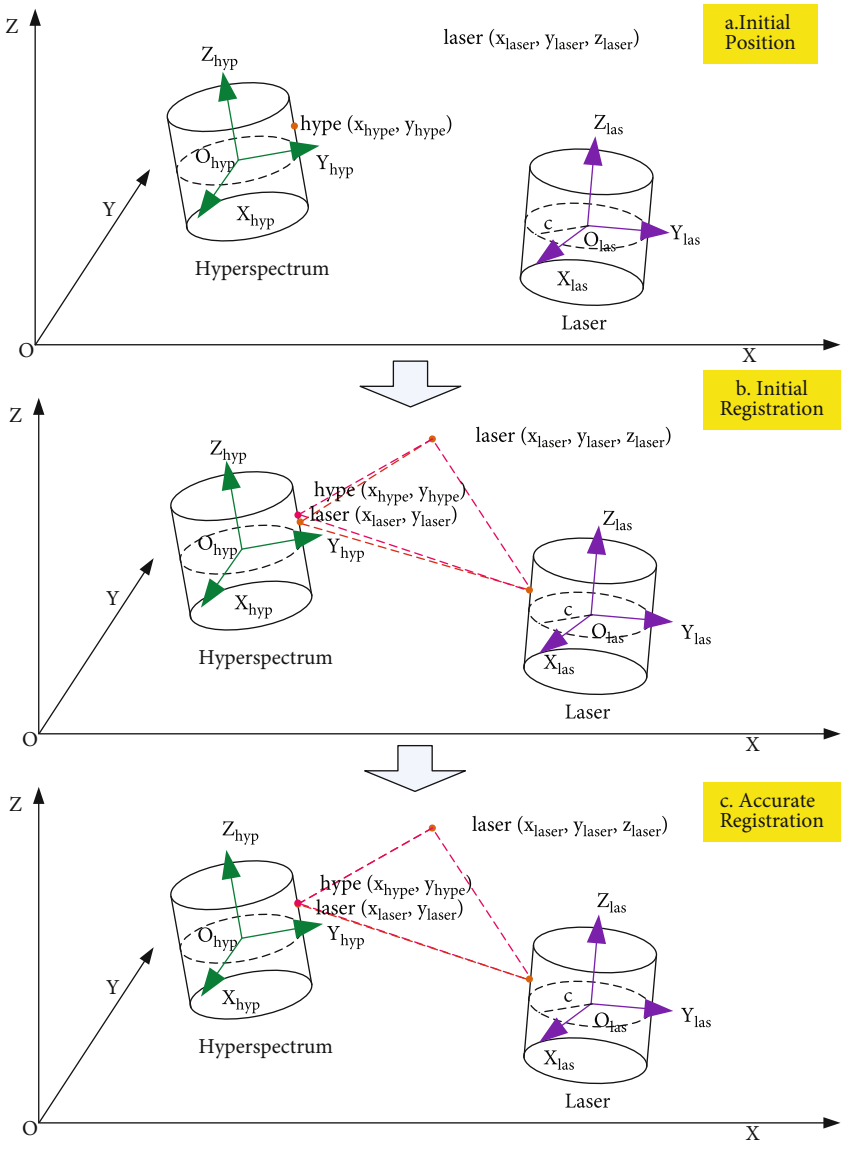

Figure 2: Registration model of laser data and hyperspectral data.

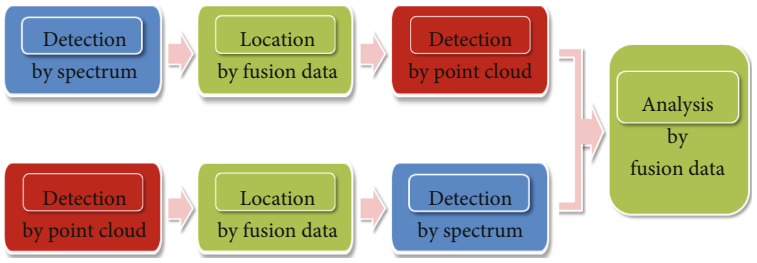

Figure 3: Detecting process of data fusion.

hyperspectral-data acquisition and processing is also developed by us.

2.2. Data Fusion. In this paper, the fusion of laser data and hyperspectral data is to attach hyperspectral Information to point cloud in the same target point. Let laser(x_{laser}, y_{laser}, z_{laser}, $x_1, \cdots, x_n$) be the point cloud information in any target point, where the 3D coordinate of laser is (x_{laser}, y_{laser}, z_{laser}), feature information of laser is ($x_1, \cdots, x_n$). Let hype(x_{hype}, y_{hype}, $y_1, \cdots, y_m$) be the hyperspectral information in same

target point, where the 2D coordinate of hype is $(x_{\text{hype}}, y_{\text{hype}})$ and spectral information of hype is $(y_1, \cdots, y_m)$. Then, the information of fusion data in this point is laser_hype$(x_{\text{laser}}, y_{\text{laser}}, z_{\text{laser}}, x_1, \cdots, x_n, y_1, \cdots, y_m)$.

The 3D laser scanning system and the hyperspectral imaging system have the different imaging models, which can generate, respectively, the multidimensional data with three-dimensional coordinates and the multidimensional data with two-dimensional coordinates, and therefore, the fusion between two kinds of data is very difficult. In this paper, "the fusion algorithm based on feature points" is constructed and used. In this algorithm, the point-cloud coordinates are regarded as the corresponding object coordinates of the hyperspectral coordinates, and the mapping relationship between them is constructed. Then, the one-to-one correspondence between point cloud and hyperspectral data is established to complete the registration of the two types of data.

The registration model of the algorithm is as follows: firstly, the corresponding feature points of point cloud and hyperspectral data are selected. According to the laser scanning system and hyperspectral imaging system, the position relation of the same target point is as shown in Figure 2(a), where laser$(x_{\text{laser}}, y_{\text{laser}}, z_{\text{laser}})$ is the point-cloud coordinate and hype$(x_{\text{hype}}, y_{\text{hype}})$ is the hyperspectral coordinate. Secondly, through the initial registration by collinear equation, the mapping model between point-cloud coordinate system and hyperspectral coordinate system is built, and laser$'(x_{\text{laser}'}, y_{\text{laser}'})$ is the corresponding coordinate of laser$(x_{\text{laser}}, y_{\text{laser}}, z_{\text{laser}})$ generated by the mapping relation. Theoretically, laser$'(x_{\text{laser}'}, y_{\text{laser}'})$ and hype$(x_{\text{hype}}, y_{\text{hype}})$ are the same point, but due to errors, there is a little deviation between them, as shown in Figure 2(b). Last distortion correction is used to reduce errors between them, and then the corresponding points of two systems coincide completely, as shown in Figure 2(c). Finally, hype$(y_1, \cdots, y_m)$ is attached to laser$(x_{\text{laser}}, y_{\text{laser}}, z_{\text{laser}}, x_1, \cdots, x_n)$ by the mapping relation, and laser_hype$(x_{\text{laser}}, y_{\text{laser}}, z_{\text{laser}}, x_1, \cdots, x_n, y_1, \cdots, y_m)$ is constructed.

The basic steps of the algorithm are as follows. Firstly, the corresponding feature points between point cloud and hyperspectral data are extracted from the points and clouds by our own algorithm. Secondly, according to the collinear equation, the initial correspondence relation is calculated using direct linear transformation. Thirdly, the accurate correspondence is established by the distortion correction through establishing the corrected values and eliminating the errors. Finally, the fusion between them is completed by the parameter of the accurate correspondence relation.

2.3. Fusion-Data Detection. In each case, the detection of the state of conservation and risk of historical buildings usually needs different methods. But generally, its steps may be divided into two categories, as shown in Figure 3.

In the first case, the material changes detect firstly the by the hyperspectral information of hyperspectral data. Then, the corresponding point-cloud regions of the detected-change hyperspectral data are located by the fusion data.

Figure 4: Tianningsi Tower.

Thirdly, the geometrical changes in the corresponding point-cloud region are detected by the geometrical and radiometric information of the corresponding point cloud. Finally, the architectural and constructive characteristics of historical buildings are analyzed thoroughly.

In the other case, it is vice versa, starting from detecting by point-cloud features, then locating the corresponding spectral information by the fusion data, and next detecting by spectral information, up to analyzing for the fusion data.

3. Experiment

In order to verify the feasibility and the applicability of this method, the part data of the Tianningsi Tower, as the research object, were selected. The laser data were acquired for the three-dimensional model construction of Tianningsi Tower. The hyperspectral data were collected for this experiment.

3.1. Tianningsi Tower. Beijing Tianningsi Tower is the oldest and highest building in Beijing (China), initially built from 1119 to 1120, located in Tianning Temple, Guanganmen, Xicheng District, Beijing, as shown in Figure 4. The tower is about 54.87 m high and is an octagonal-plane thirteen-layer solid-brick structure, composed of four parts such as tower-base, tower-body, tower-canopy, and tower-cap. All sides of the tower have many beautiful, well-proportioned brick-sculptures and clay-sculptures like Lotus, Loin, Bodhisattva, Muscleman, and so forth, which form a magnificent work of art and have the strong Buddhist meaning. Tianningsi Tower is one of the most representative Buddhist towers in China, a blending product of Indian Buddhist culture, foreign Western-Region culture, and traditional Chinese Central-Plain culture in the long-term development

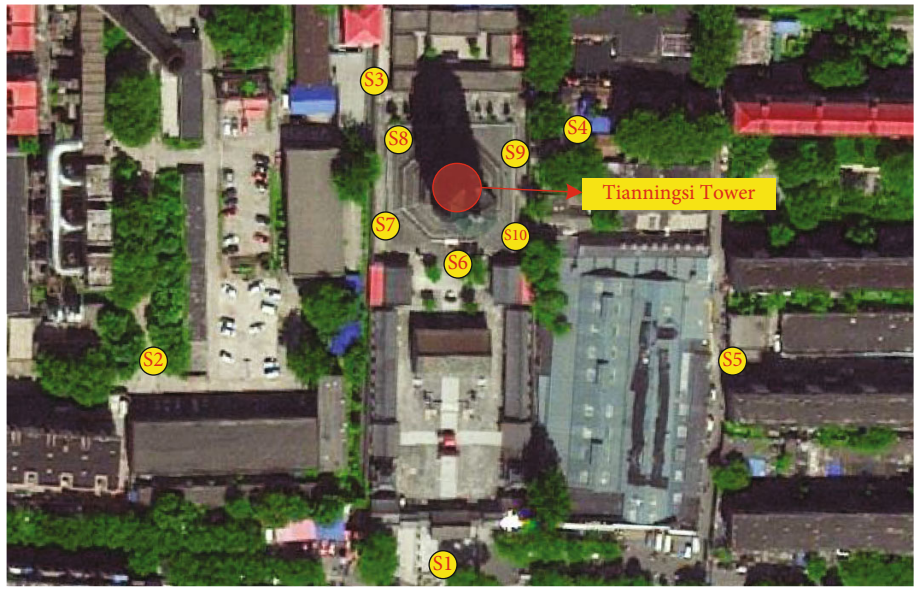

Figure 5: Data acquisition location map of Tianningsi Tower.

Figure 6: Hyperspectral fusion image in the south of Tianningsi Tower.

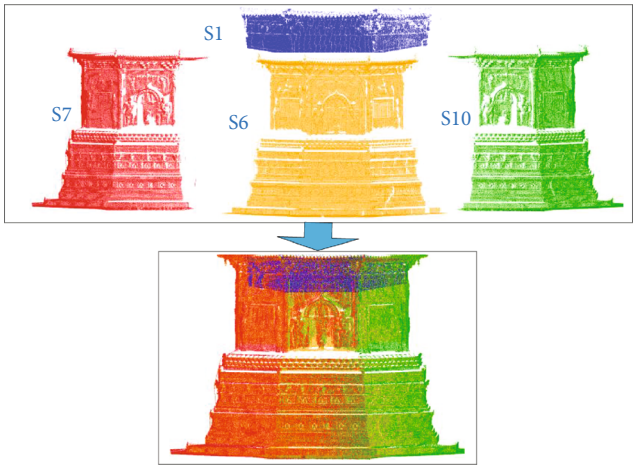

Figure 7: Southern fusion point cloud of Tianningsi Tower.

Table 2: Feature points of point cloud and hyperspectral data.

Hyperspectral data	Point cloud	Hyperspectral data	Point cloud
497, 29	-9.454, -11.619, 14.235	647, 169	-11.969, -9.519, 10.899
727, 32	-13.019, -8.228, 14.208	610, 74	-11.007, -9.727, 13.009
476, 265	-9.079, -11.743, 8.333	743, 273	-13.045, -7.953, 8.370

Figure 8: Southern fusion data of Tianningsi Tower.

Table 3: Single band hyperspectral image of Tianningsi Tower.

Wave band	1	44	54	64	84	114	145	191	204
Wavelength (nm)	390	449	463	477	505	548	592	660	679

process of colliding with each other. According to the historical data records, from the prime to the present, the tower has been damaged and repaired several times; moreover, it was influenced by natural conditions. Therefore, the tower height, the building material, and the sculpture modeling

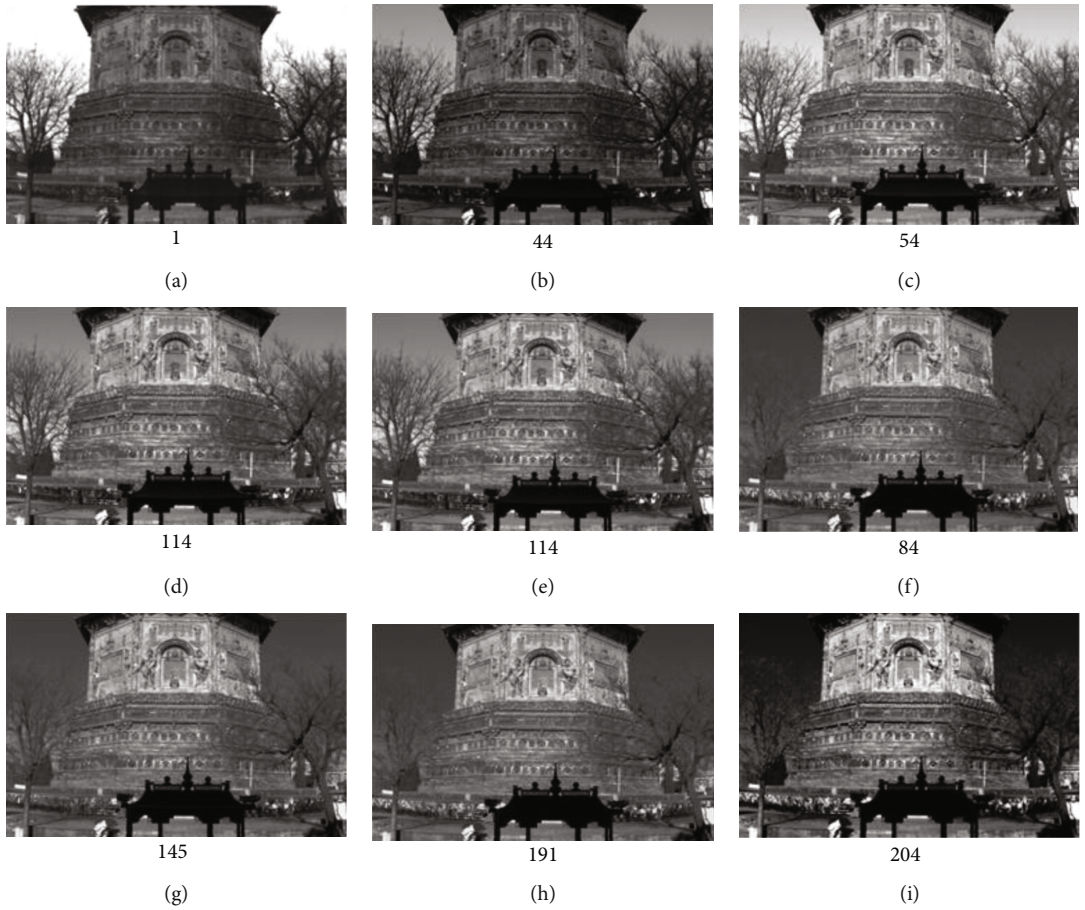

Figure 9: Single band hyperspectral image of Tianningsi Tower.

have also changed many times. It seems that the tower was initially about 57.8 m high, and it was about 55.38 m high in 1992 [14], but today, it has a height of about 54.87 m under this actual measurement.

3.2. Data Acquisition. Due to fact that Tianningsi Tower is located in the main city of Beijing, where the surrounding buildings are too many and the population is so dense, the acquiring data is more different, as shown in Figure 5. Our Research Group collects laser data and hyperspectral data two times. Laser data was acquired by Leica 3D Laser Scanner, and hyperspectral data was acquired by Sweep Hyperspectral Scanner. According to the tower height and the surrounding environment, the data were acquired by means of ten scans from ten different viewpoints distributed along the adjacent street around the prospect, as shown in Figure 5. Starting from the tower's south part in a clockwise direction, the initial laser scans in the tower upper side are acquired successively by five sites, such as S1, S2, S3, S4, and S5, which contain basic information of the tower's top part. And the initial laser scans in the tower lower side are acquired successively by five sites, such as S6, S7, S8, S9, and S10, which contain basic information of the tower's bottom part. The mean spot spacing was about 3 mm in the main part of the prospect. Moreover, the large overlapping area between adjacent scans can make the total point cloud denser.

Hyperspectral data in the south of Tianningsi Tower were acquired with 420 continuous wave bands and 390–1000 nm wave range. It is shown in Figure 6, which is the fusion image of the band R (191), G (118), and B (44).

3.3. Data Processing. The fusion experiment is the south part of Tianningsi Tower, according to the collected point cloud, partial data of four sites such as S1, S6, S7, and S10 need to be registered and integrated. In this process, the local registration algorithm uses the registration algorithm based on improved normal distribution transform, which is our previous research method [15]. And the global registration uses an automatic multiscan registration algorithm, which is also our previous research method [16, 17]. The fusion result of point cloud is shown in Figure 7.

Let 3D point-cloud into the 2D gray image, and RGB hyperspectral image into 2D gray image. The feature points of two 2D images are extracted and mapped into three-dimensional space to get the feature points of point cloud and hyperspectral data, and then the six-pair feature points are extracted, as shown in Table 2.

According to the six-pair feature points, the fusion data of point cloud and hyperspectral data are calculated using

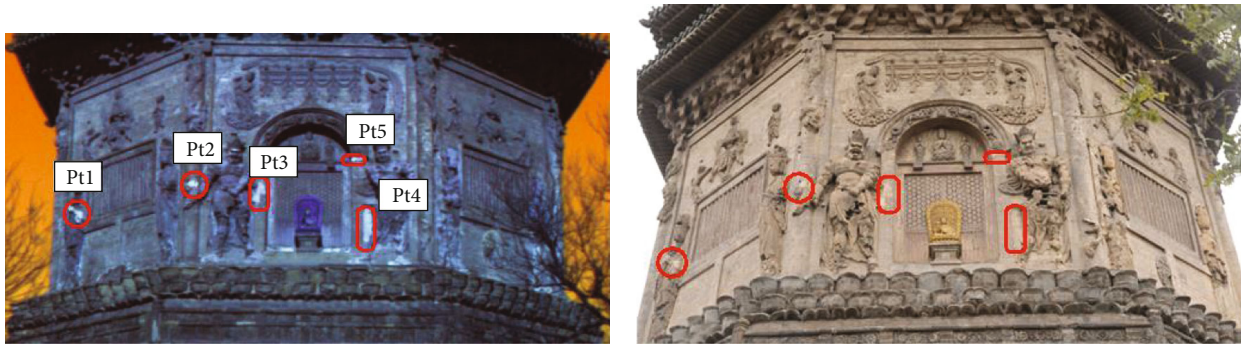

(a) (b)

Figure 10: Comparison of false-color high spectral image and digital image.

the fusion algorithm in above, as shown in Figure 8. Hyperspectral information of Tianningsi Tower is attached to the point cloud information; namely, the fusion data is the point cloud with the spectral information. If P is a point, at any point of Tianningsi fusion data, P can be expressed as $P(x, y, z, m_1, \cdots, m_k, n_1, \cdots, n_{420})$ containing three kinds of information, where $P(x, y, z)$ is the three-dimensional coordinate of fusion data, $P(m_1, \cdots, m_k)$ is the point-cloud attribute, and $P(n_1, \cdots, n_{420})$ is hyperspectral feature 8.

4. Discussion

Hyperspectral data contain hundreds or even thousands of spectral information, which can detect a lot of information undetected by visible light. Twelve single-band hyperspectral images are selected, in which there are some strange bright regions, as shown in Table 3 and Figure 9.

In order to make the highlighting regions more obvious, the three band images, 1, 6, and 204, which are selected from the tower-body, fused a false-color image, as shown in Figure 10(a). Then, five obvious feature regions are selected, labeled Pt1, Pt2, Pt3, Pt4, and Pt5, respectively, as shown in the red circle section of Figure 10(a). The same areas in digital image are no different with the surrounding areas, as shown in the red circle section of Figure 10(b). After field visiting, looking up historical data, and consulting experts, the highlight areas are the suspected repair-areas. Through hundreds of years of wind and sleet, Tianningsi Tower has been damaged, especially with serious clay damage, and it has been repaired many times. In view of the different repair materials in different periods and the material changes affected by weathering erosion, even if they have the same appearance, the material compositions have great difference.

In order to further make their difference, integral smoothing DN value spectra of seven areas, including five regions, one clay sculpture region, and one brick sculpture region, are analyzed, and the results are shown in Table 4 and Figure 11. The spectra of five regions, such as Pt1, Pt2, Pt3, Pt4, and Pt5, respectively, have the similar numerical waveforms. But the spectra of S1 and S2 have the great difference from the above five regions, which express clay sculpture region and brick sculpture region in the tower body.

Table 4: Correspondence of regions and DN value in Tianningsi Tower.

Area number	Pt1	Pt2	Pt3	Pt4	Pt5	S1	S2
Spectral color	Red	Green	Blue	Yellow	Navy	Purple	White

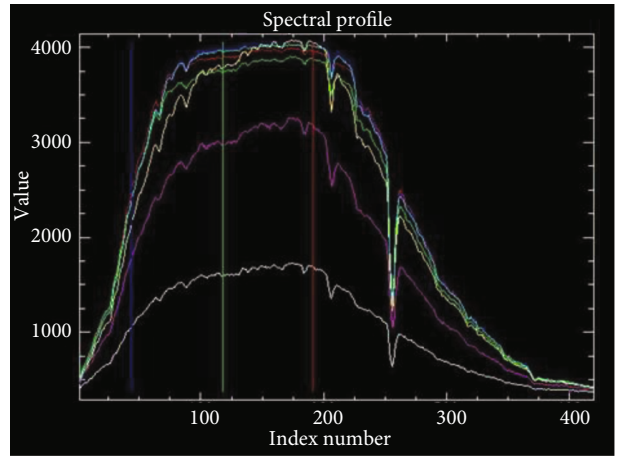

Figure 11: Seven regional DN value spectra in Tianningsi Tower.

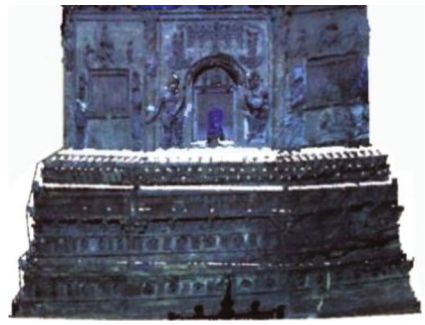

Figure 12: Fusion data of Tianningsi Tower.

This can be judged, although the appearance of the five regions and their surrounding sculptures looks so alike; in fact, the materials of the five areas may be the same, different from the surrounding. By the historical investigation and the temple inscription records, Tianningsi Tower has undergone

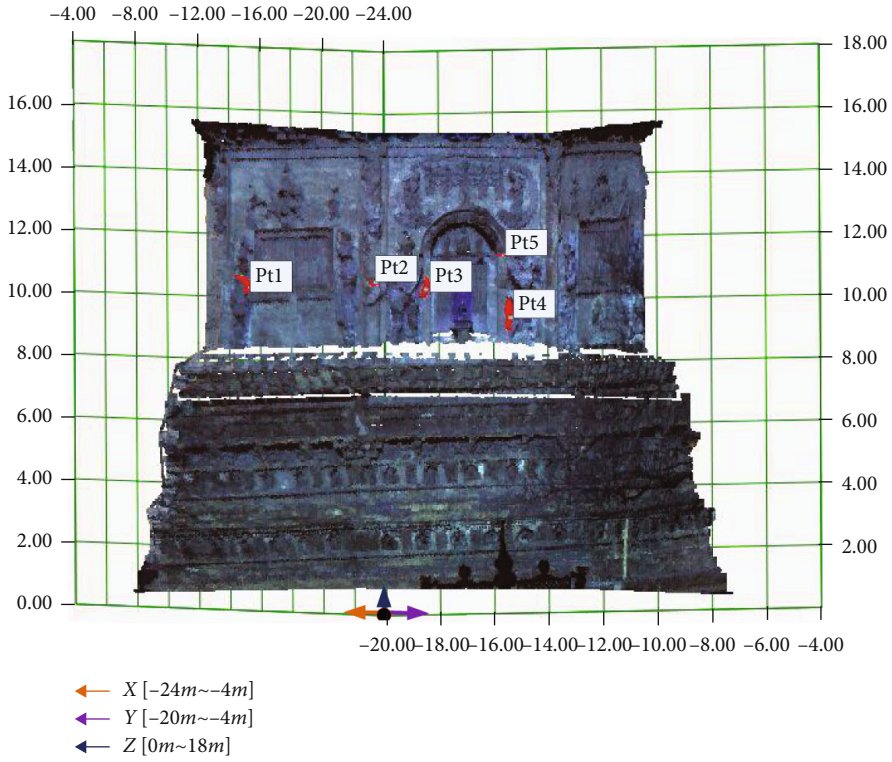

Figure 13: Fusion data of Tianningsi Tower in the grid coordinate.

Table 5: Suspected repair-region position of Tianningsi Tower (unit: m).

Suspected repair-region number	Suspected repair-region coordinate	Suspected repair-region position
Pt1	-8.880, -16.523, 10.258	16.880, 4.523, 10.258
Pt2	-8.889, -11.833, 10.198	16.889, 9.833, 10.198
Pt3	-10.255, -10.750, 10.060	14.255, 10.75, 10.060
Pt4	-12.302, -8.800, 9.343	12.302, 12.800, 9.343
Pt5	-12.129, -8.969, 11.147	12.127, 12.969, 11.147

many renovations, including several major overhauls, for example, in 1756 and 1782 of the Qing Dynasty, in 1937 and 1941–1943 of the Republic of China, and in 1991–1992 and 2002 of the People's Republic of China. Although the repair materials are still mixed with mud and sand, however, times of the production process and ingredients are different. Furthermore, weathering and erosion also have impact on the composition of the material. Therefore, it is again concluded that the five area materials belong to the same material and that the patches were highly likely available for the same period.

As mentioned above, the hyperspectral data can detect the potential spectral feature information to achieve damage detection, age judgment, and information recovery of ancient buildings caused by the different chemical composition, but not judged caused by the different geometric appearance. However, their fusion can also detect the geometric appearance to accurately determine the location of damage-area and repair-area. Therefore, their fusion can detect changes caused by material composition and geometric shape. The fusion data of Tianningsi Tower is shown in Figure 12, in which the repair areas of fusion data have obvious characteristics.

To further gain the repair-area information like location, shape, and size, according to the point-cloud coordinates, the grid coordinate is constructed, in which the fusion data is shown, where x-axis range is [−24 m,−4 m], y-axis range is [−20 m,−4 m], and z-axis range is [0 m, 18 m]; the grid size is 2 m, as shown in Figure 13. The red parts are the highlighted area detected by the hyperspectra, which have given the point cloud by fusion data. If the intermediate-point coordinates of the repair regions are regarded as the repair-region coordinates, the repair-region location relative to the coordinate system can be determined, as shown in Table 5.

Moreover, according to the highlight-region point clouds in fusion data, the Triangular mesh surfaces are constructed, whose shape is the repair-region shape and whose area is the repair-region area, as shown in Table 6 and Figure 14.

Table 6: Suspected repair-region area of Tianningsi Tower (unit: m^2).

Suspected repair-region number	Pt1	Pt2	Pt3	Pt4	Pt5
Suspected repair-region area	0.167	0.0433	0.234	0.324	0.013

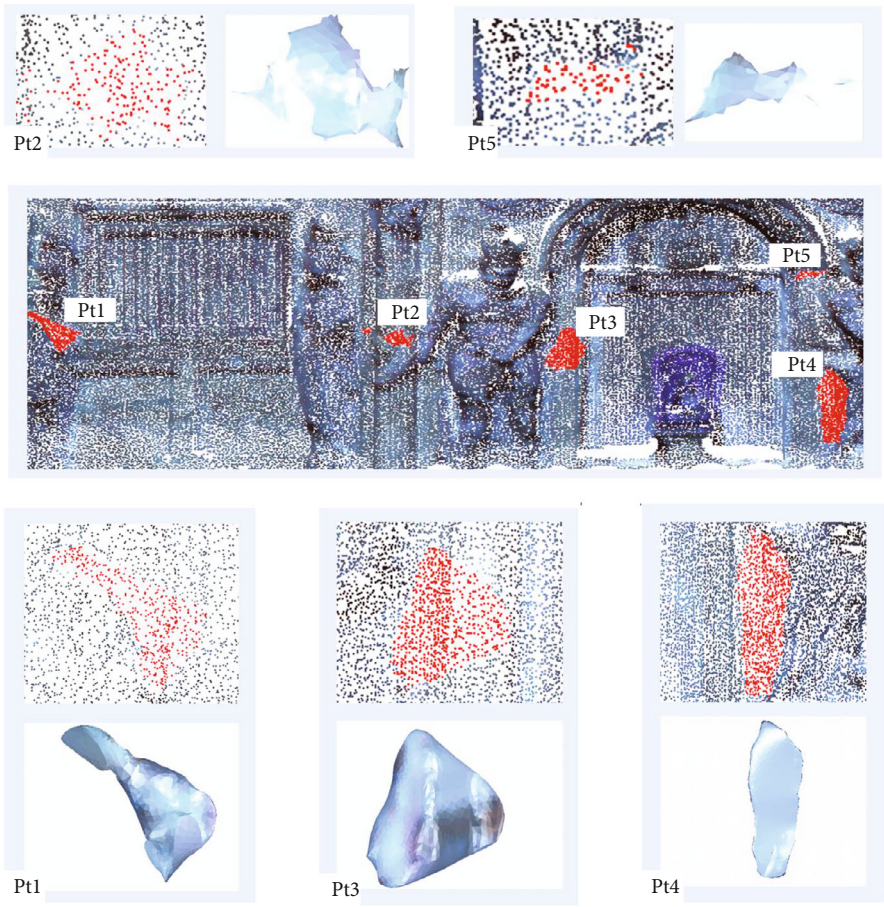

Figure 14: Suspected repair-region shape of Tianningsi Tower.

5. Conclusion

This paper reported the detected change methodology using terrestrial laser scanning and hyperspectral imaging in the conservation work on ancient buildings and attributed to Beijing Tianningsi Tower (17th century), China, the famous Buddhist pagoda. Firstly, laser data and hyperspectral data were acquired not on the same time or place. Secondly, two kinds of data were processed, respectively, and then they were registered and fused. Finally, the fusion data were applied to detect changes of historical buildings.

It is possible to assess that the fusion data of laser scanning and hyperspectral imaging offer an effective noncontact method to detect the surface changes without damaging the building. This multifusion, appropriately tested and verified, is an extremely precise and controlled method to detect geometrical and material changes in a selective and highly controlled modality.

All working steps were carefully documented by a multisource data detecting system that allowed for obtaining a comprehensive analysis on which all information gathered during the conservative procedure was inserted. In the field of conservation, the advantages to report the information in a single file linked to the object that, when necessary, can be used to update the more complete and accurate laser data and hyperspectral data, represent a valuable tool for documentation.

Data Availability

The datasets used and/or analyzed during the current study are available from the corresponding author on reasonable request.

Conflicts of Interest

There are no conflicts of interest.

Acknowledgments

The research was supported by the Key Research and Development Project of Shanxi, China "Research and Demonstration of Shanxi Ancient Stage Digital Protection and Cultural Tourism Service Platform Based on GIS" (201903D321042), and Soft Science Program of Shanxi, China "Research on the Integrated development of cultural heritage digital protection and tourism exploitation in Shanxi" (2018041015-5).

References

[1] A. Pesci, E. Bonali, C. Galli, and E. Boschi, "Laser scanning and digital imaging for the investigation of an ancient building: Palazzo d'Accursio study case (Bologna, Italy)," *Journal of Cultural Heritage*, vol. 13, no. 2, pp. 215–220, 2012.

[2] J. Armesto-González, B. Riveiro-Rodríguez, D. González-Aguilera, and M. T. Rivas-Brea, "Terrestrial laser scanning intensity data applied to damage detection for historical buildings," *Journal of Archaeological Science*, vol. 37, no. 12, pp. 3037–3047, 2010.

[3] M. Tsakiri, "Detection of geometric changes for an historic theatre by comparing surveying data of different chronological periods," *Journal of Cultural Heritage*, vol. 21, pp. 860–868, 2016.

[4] A. Pesci, G. Casula, and E. Boschi, "Laser scanning the Garisenda and Asinelli towers in Bologna (Italy): detailed deformation patterns of two ancient leaning buildings," *Journal of Cultural Heritage*, vol. 12, no. 2, pp. 117–127, 2011.

[5] A. Kylili, P. A. Fokaides, P. Christou, and S. A. Kalogirou, "Infrared thermography (IRT) applications for building diagnostics: a review," *Applied Energy*, vol. 134, pp. 531–549, 2014.

[6] F. Bisegna, D. Ambrosini, D. Paoletti, S. Sfarra, and F. Gugliermetti, "A qualitative method for combining thermal imprints to emerging weak points of ancient wall structures by passive infrared thermography - A case study," *Journal of Cultural Heritage*, vol. 15, no. 2, pp. 199–202, 2014.

[7] G. Bearman and C. V. Veen, "Hyperspectral imaging opens new perspectives in cultural heritage," *Laser Focus World*, vol. 51, no. 5, pp. 54–56, 2015.

[8] J. S. Pozo-Antonio, A. Ramil, M. P. Fiorucci, A. J. López, and T. Rivas, "The use of hyperspectral imaging technique to detect the most suitable graffiti-cleaning procedure," *Color Research & Application*, vol. 41, no. 3, pp. 308–312, 2016.

[9] A. Mulahusić, N. Tuno, N. Gajski, and J. Topoljak, "Comparison and analysis of results of 3D modelling of complex cultural and historical objects using different types of terrestrial laser scanner," *Survey review - Directorate of Overseas Surveys, Survey Review*, vol. 52, no. 371, pp. 107–114, 2020.

[10] L. Li, K. Hasegawa, I. Nii, and Tanaka, "Fused transparent visualization of point cloud data and background photographic image for tangible cultural heritage assets," *International Journal of Geo-Information*, vol. 8, no. 8, p. 343, 2019.

[11] S. Gubo, T. Kmet, A. Molnar, and O. Takac, "A multi-range approach for cultural heritage survey: a case study of a medieval church in Slovakia," in *2020 IEEE 18th World Symposium on Applied Machine Intelligence and Informatics (SAMI)*, Herlany, Slovakia, 2020.

[12] F. Nex and F. Rinaudo, "Digital photogrammetry and lidar: new ideas for cultural heritage metric surveys," *Stroke; a Journal of Cerebral Circulation*, vol. 45, no. 12, pp. 59–68, 2014.

[13] J. Markiewicz, P. Podlasiak, and D. Zawieska, "A new approach to the generation of orthoimages of cultural heritage objects—integrating TLS and image data," *Remote Sensing*, vol. 7, no. 12, pp. 16963–16985, 2015.

[14] Y. Wang and J. Wang, "Beijing Tianning Temple (III)," *Journal of Capital Normal University (Natural Science Edition)*, vol. 32, no. 6, pp. 78–88, 2011.

[15] X. Zhang, A. Zhang, and Z. Wang, "Point cloud registration based on improved normal distribution transform algorithm," *Laser & Optoelectronics Progress*, vol. 51, no. 4, pp. 96–105, 2014.

[16] X. Zhang and A. Zhang, "Automatic multi-scans registration of 3d point clouds based on improved normal distribution transform," *Journal of Information & Computational Science*, vol. 10, pp. 5559–5570, 2014.

[17] H. Sun, C. Gao, Z. Zhang, X. Liao, X. Wang, and J. Yang, "High-resolution anisotropic prestack Kirchhoff dynamic focused beam migration," *IEEE Sensors Journal*, vol. 20, no. 20, pp. 11753–11760, 2020.

Hindawi
Scanning
Volume 2021, Article ID 7846116, 8 pages
https://doi.org/10.1155/2021/7846116

Research Article

Microstructure and Properties of ER50-6 Steel Fabricated by Wire Arc Additive Manufacturing

Qingxian Hu,[1] **Junyan Miao**,[1] **Xiaoli Wang**,[1] **Chengtao Li**,[2] **and Kewei Fang**[2]

[1]*School of Materials Science and Engineering, Jiangsu University of Science and Technology, Zhenjiang 212003, China*
[2]*Suzhou Nuclear Power Research Institute, Suzhou 215004, China*

Correspondence should be addressed to Xiaoli Wang; xlwang@just.edu.cn

Received 31 May 2021; Revised 16 June 2021; Accepted 23 July 2021; Published 5 August 2021

Academic Editor: Guosong Wu

In this paper, ER50-6 steel was fabricated by wire arc additive manufacturing (WAAM) with an A-W GTAW system. The microstructure, mechanical properties, and corrosion behaviors of ER50-6 steel by WAAM were studied. The results showed that, with the GMAW current increased, from the bottom to the top of the sample, the microstructure was fine ferrite and granular pearlite, ferrite equiaxed grains with fine grains at grain boundaries, and columnar ferrite, respectively. The average hardness in the vertical direction of samples 1# and 2# was 146 and 153 HV, respectively. The hardness of sample 2# increased because of the refinement of grain. The pores in the sample increased as the bypass current increased. The higher bypass current also has a deterioration effect on the corrosion behavior of ER50-6 steel.

1. Introduction

Wire arc additive manufacturing (WAAM) becomes the core of the new industrial era. It has many advantages such as high deposition rate [1], low equipment cost, high material utilization, and environmental friendliness. It is a versatile and cost-effective method to fabricate complex parts and large-sized components [2]. It included three types of processes, namely, gas metal arc welding (GMAW), gas tungsten arc welding (GTAW), and plasma welding (PAW). In these processes, the arc is used as the heat source, and the wire is used as additive manufacturing materials. Compared to the process powder-based techniques, it has higher efficiency and lower production cost. As is known, there have been many research reports about WAAM, such as steel [3–5], Ti alloys [6], and steel and Al alloys [7, 8]. In the additive manufacturing, some defects, such as uncontrolled grain size, tensile residual stress, cracks, and delaminations [9], are very easy to produce. In order to widen the adoption of WAAM in diverse industries, some scientists studied how to eliminate the defects. Colegrove et al. [10] combined high-pressure rolling with WAAM and reported that peak residual stress was reduced and refined microstructure was obtained. Martina et al. [11] evaluated fatigue crack propagation behavior in WAAM Ti-6Al-4V using the numerical simulation method. In fact, during the process of WAAM, the main reason for various defects is due to excessive heat input. Therefore, how to maintain a high deposition rate, avoid excessive heat input, and maintain arc stability has become an urgent problem in the process of wire arc additive manufacturing. In order to reduce heat input, researchers used different processes for additive manufacturing. Li et al. [12] used cold metal transfer (CMT) to fabricate a higher and thinner layer by preheating the wire to reduce heat input. Based on compulsively constricted WAAM (CC-WAAM) proposed by Liu et al. [13], Rodrigues et al. [14] proposed a new process named ultracold-wire and arc additive manufacturing (UC-WAAM) that can reduce the process temperature, and it can create a hollow part without any support structure. However, it was not easy to control droplet transition during these processes.

Obviously, in addition to reducing heat input, the heat input should be controlled independently. As is known, gas metal arc welding (GMAW) has a high deposition rate. Gas

tungsten arc welding (GTAW) has low heat input, and it is stable and easy to operate. The advantages of GMAW and GTAW should be fully utilized. Zhang and his colleagues [15] have proposed an innovative arcing-wire gas tungsten welding (A-W GTAW). The schematic diagram of the A-W GTAW process is shown in Figure 1. In the A-W GTAW system, between the tungsten and the feeding wire, a side arc was inside the main GTAW. In their study paper, the process was described in detail to reduce heat input to the substrate. The feeding wire can be directly and quickly melted at high speeds. Compared with the traditional GMAW and GTAW, the A-W GTAW process makes full use of the advantages of GMAW and GTAW and achieves a high deposition rate, and it has a stable arc to be operated [15]. Therefore, it is very meaningful to attempt this process for additive manufacturing. ER50-6 wire is widely used for welding ordinary carbon steel, carbon structural steel for automobile manufacturing, and low alloy and high strength structural steel for hull and pressure vessel. This work attempted to use this process to fabricate ER50-6 steel thin wall, and the microstructure, mechanical properties, and corrosion resistance of the prepared parts were analyzed. This study will provide the research foundation for the wire arc additive manufacturing of the large components.

2. Experimental Details

The substrate was Q235. ER50-6 welding wire was used to additively manufacture samples. Table 1 shows the chemical composition of Q235 steel and ER50-6 welding wire. In order to remove the rust and oil on the surface of Q235, an angle grinder and acetone were used.

Based on Liu et al.'s study [13], Figure 2 shows the circuit diagram of the A-W GTAW additive manufacturing system. A special WSM-315C argon arc welding machine (Aotai, Shandong, China) and general GMAW-500P gas protection welding machine (Aotai, Shandong, China) are used to build the system of A-W GTAW. The tungsten electrode is connected to the negative power of the GTAW and GMAW welding machines. The positive electrode of GTAW and GMAW is connected to the substrate and the feeding wire, respectively.

In the process of additive manufacturing, with the increase of surfacing layers, the weld surplus height increased gradually. In order to control the consistency of welding gun height from the substrate, a high-precision lifting platform was used to adjust the height, and the adjustment range was 0-60 mm.

As shown in Figure 3, the distance marked h_1 between the substrate and the tungsten electrode tip was 9 mm. The feeding wire located directly below the tungsten electrode was 7.5 mm away from the additive manufacture layers. The horizontal distance marked d between the tungsten electrode and the feeding wire was 2 mm, and the angle between the GTAW electrode and the horizontal electrode was 35°. The protective gas was 99.99% pure argon. Single-pass multilayer surfacing welding was carried out on the Q234 substrate, and the time interval of each layer was 10 minutes. The deposition direction of each layer was the same. Based on many

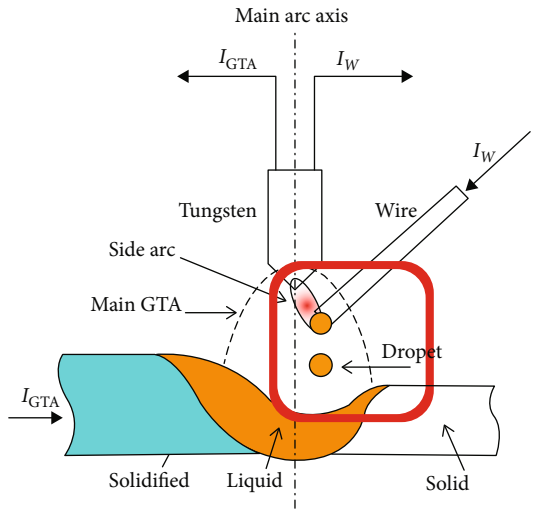

Figure 1: The schematic diagram of the A-W GTAW process [15].

experiments, two good samples (prepared by two different processes) were selected for comparative analysis of microstructure and properties. Table 2 shows the process parameters of additive manufacturing of ER50-6.

Figure 4 shows the macro morphology of additively manufactured ER50-6. The cross-sectional samples were obtained by wire cutting of the additively manufactured ER50-6, and samples for microstructure observation and performance test were prepared. First, the three samples were grinded with 200#, 600#, and 1000# sandpaper and polished with 2.5-mesh polishing paste. Samples prepared for microstructure observation were corroded with 4% nitric acid alcohol.

The microstructures of the two samples were observed using a Nikon Epiphot300 optical microscope (OM) (Nikon, Japan) and a scanning electron microscope with field emission (FESEM, SU-70, Hitachi, Japan). DHV-1000 model of hardness tester (Shanghai Shangcai Testermachine Co., LTD., China) was used to test the Vickers hardness of samples. The test load was 10 N, and the last time was 10 s. CSM NHT2 Nanoindenter (Anton Paar) was used to measure the elastic properties of samples 1# and 2# with 10 mN of the maximum load and 20 mN·min^{-1} of the loading/unloading rate. The depth recovery ratio (η_h) was used to characterize the elastic behavior of samples. The value of η_h was defined as follows [16, 17]:

$$\eta = \frac{h_{max} - h_r}{h_{max}}, \quad (1)$$

in which h_{max} was the maximum depth of penetration and h_r was the residual depth after unloading. The elastic modulus (EIT) of samples can be obtained directly by the test. The elastic modulus value was greater, which meant that the material deformation was not easy to happen, that is, it was more brittle.

Table 1: Chemical composition of Q235 steel and ER50-6 wire (wt.%).

Elements	Mn	Si	S	P	C	Cu	Fe
Q235	0.30	0.15	0.035	0.015	0.17	/	Bal.
ER50-6	1.40-1.85	0.80-1.15	≤0.035	≤0.035	0.06-0.15	≤0.50	Bal.

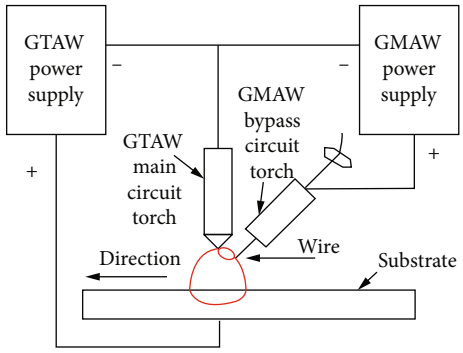

Figure 2: The circuit diagram of the A-W GTAW additive manufacturing system.

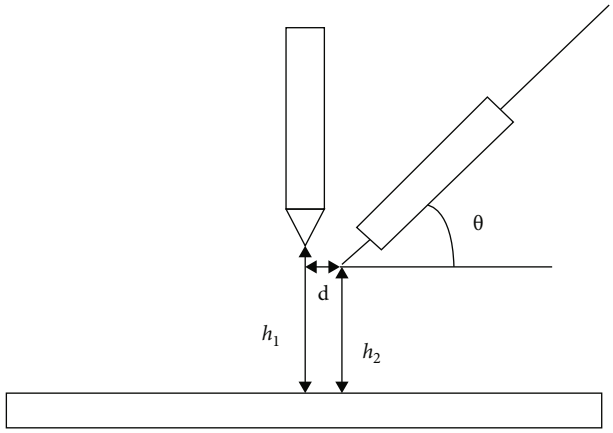

Figure 3: The position of the welding torch.

Table 2: Main technological parameters of additive manufacturing.

The process parameters	Sample 1#	Sample 2#
Main current I_1 (A)	150	150
Bypass current I_2 (A)	150	200
Tungsten electrode diameter (mm)	3	3
Angle of tungsten electrode θ (°)	50	50
Gas flow of GTAW (L·min^{-1})	15	15
Gas flow of GMAW (L·min^{-1})	12	12
Welding speed (mm·min^{-1})	160	160
Layer numbers	12	12

The tribocorrosion tests were performed in 3.5% NaCl solution at 25°C using an MSR-2T tribometer (Lanzhou Institute of Chemical Physics, Chinese Academy of Sciences, Lanzhou, China). In the present work, 25 × 15 mm^2 surface area of tested samples was in contact with the electrolyte throughout the tribocorrosion testing. The tribocorrosion test was conducted at a speed of 1 mm/s with a normal load of 20 N. The electrochemical behaviors of the tested specimen were conducted using a Reference 600+ electrochemical workstation (Gamry Instruments, Inc. USA) and a three-electrode electrochemical cell, with a saturated calomel electrode (SCE) as the reference electrode. Potentiodynamic polarization was measured after friction test was performed for 10 min and scanned at a constant rate of 1 mV/s from −400 mV below the corrosion potential and terminated when a current value of 10 mA was reached.

3. Results and Discussion

3.1. Macroscopic Morphology Observation. The morphology of the tested samples is shown in Figure 5. As is seen from Figure 5, the depth and height of the melting pool increased with the increase of GMAW current, indicating that the amount of the melted substrate increased [18]. It indicated that the deposition of arc additive was effectively improved by increasing GMAW current. On the other hand, the substrate deformation was more serious with the increase of GMAW current. In the following work, metallographic analysis and SEM observation experiments were carried out on samples 1# and 2#.

According to the deposition direction, samples were divided into three regions, top part, middle section, and bottom part, next to the fusion zone, as shown in Figure 5. The three regions were analyzed by optical microscopy and SEM in the paragraphs below.

3.2. Optical Microscopic (OM) Analysis. The microstructure transformation of ER50-6 steel can be divided into three types: ferrite phase transformation, pearlite phase transformation, and bainite phase transformation. Figure 6 shows the OM images of the different positions of samples 1# and 2#. It was seen that there was more strip pearlite in Figure 6(a) than in Figure 6(d). Because bypass current I_2 of sample 2# was larger than that of sample 1#, more heat input homogenizes the ingredients so that strip pearlite was not as obvious in Figure 6(d). The matrix of Figure 6(d) consisted of fine ferrite and granular pearlite. From Figures 6(b) and 6(e) in the middle of samples 1# and 2#, respectively, it can be seen that ferrite grains were equiaxed, especially on the grain boundary, and the grains in Figure 6(e) were smaller than those in Figure 6(b). During additive manufacturing, continuous thermal cycling resulted in recrystallization of grains. These grains can play a role in fine-grain strengthening. On the top of sample 1#,

Figure 4: The macro morphology of additively manufactured ER50-6.

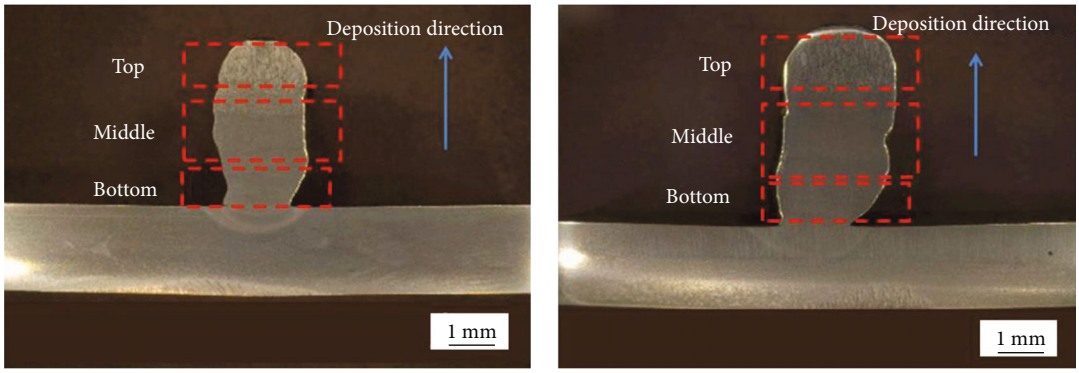

(a) (b)

Figure 5: OM of the additively manufactured samples (a) 1# and (b) 2#.

from Figure 6(c), it can be seen that there was columnar ferrite located at the grain boundary and acicular ferrite and pearlite located in grains. On the top of sample 2#, from Figure 6(f), it indicated that there was narrower columnar ferrite than that of sample 1#. It was that the different microstructures of the two samples would be leading to different mechanical properties, which was the result of rapid solidification [19].

3.3. SEM Analysis. The SEM images of samples 1# and 2# are shown in Figure 7. Figures 7(a) and 7(d), 7(b) and 7(e), and 7(c) and 7(f) are the images of the bottom, middle, and top section of samples 1# and 2#, respectively. As seen from Figures 7(a) and 7(d), there were regular circular pores. The defects of pores are often found in components fabricated by additive manufacturing [20]. It was mainly due to the evaporation of metal elements in the additive manufacturing process and the instability of the molten pool caused by the increase of bypass current I_2. The number of pores in sample 2# was significantly higher than that in sample 1#. From Figure 7(b), the lamellar structure of pearlite can be seen. However, in Figure 7(e), this structure cannot be seen because the pearlite became smaller than that in sample 1#. At the top of sample 2#, from Figures 7(c) and 7(f), it can be seen that the pores were bigger than those on the top of sample 1#. The increase in the number and volumes of these pores was mainly due to the increase of current density.

3.4. Mechanical Test

3.4.1. Hardness Test. Figure 8 presents the microhardness (HV) distribution of samples 1# and 2# in the cross section, as shown in Figure 5. Figure 8(a) shows the hardness curve of samples 1# and 2# from the center axis of the bottom to the top. The vertical direction is consistent with the deposition direction. The hardness of the two samples was similar to each other at the bottom and in the middle, while hardness curves at the top of samples varied. Figure 8(b) shows the average hardness in different areas of samples. The average hardness of sample 1# and sample 2#, at the bottom, in the middle, and at the top, was 153 and 156 HV, 145 and 150 HV, and 140 HV and 154 HV, respectively. It can be seen that the average hardness values of the bottom and middle of the two samples had little difference. Their difference was mainly reflected in the average hardness at the top of samples. The average hardness in the vertical direction of samples 1# and 2# was 146 and 153 HV, respectively. The hardness of sample 2# was higher than that of sample 1#. Combined with the analysis results in Figure 6, it can be concluded that the lowest hardness at the top of sample 1# was due to the presence of large columnar ferrite. Grain refinement in the middle and at the top of sample 2# was the reason why the hardness of sample 2# was higher than that of sample 1#. The analysis results were consistent with those in Figure 6.

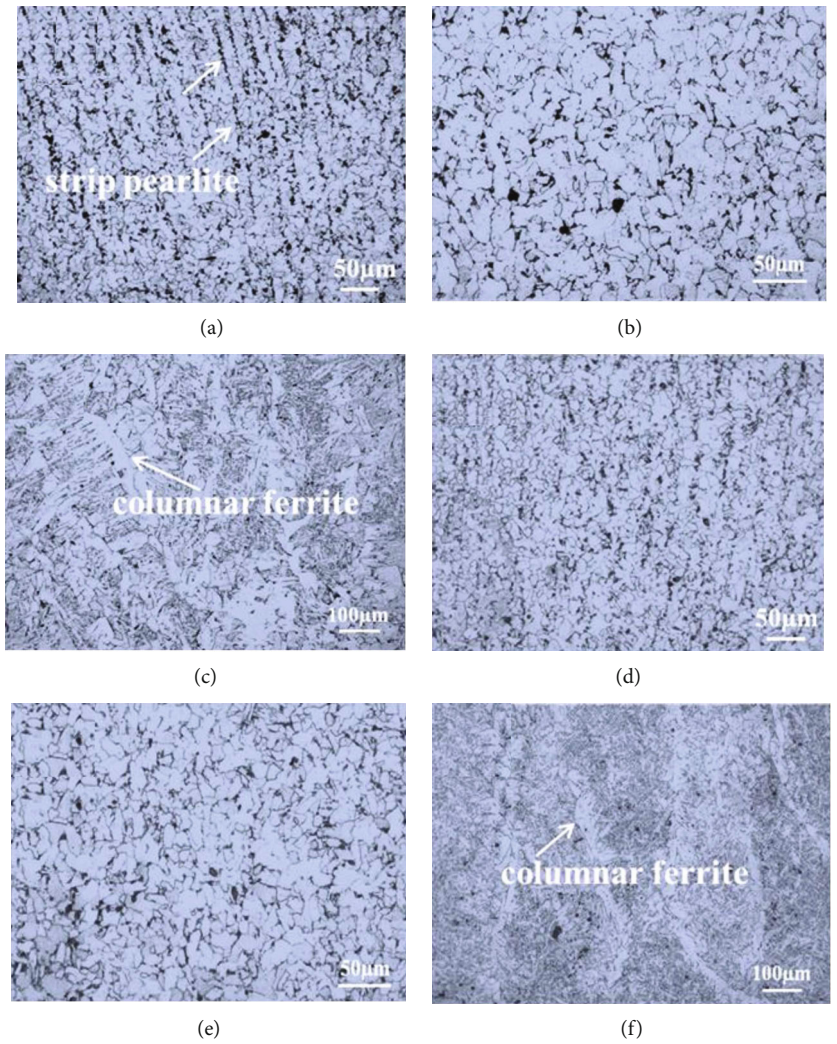

FIGURE 6: OM of the different positions of samples 1# and 2#. The images of the (a, d) bottom, (b, e) middle, and (c, f) top sections of samples 1# and 2#, respectively.

3.4.2. Nanoindentation Characterization. The nanoindentation curves of different parts for samples 1# and 2# are shown in Figure 9. The maximum depth (h_{max}) of indentation with 10 mN load of the middle of samples 1# and 2# was 358.86 nm and 331.16 nm, respectively. The values of the parameters, including the maximum depth (h_{max}), residual depth (h_r), depth recovery ratio (η_h), and elastic modulus (EIT) extracted from Figure 9, are presented in Table 3. h_{max} for sample 1# at the bottom, middle, and top was higher than that for sample 2#. It indicated that sample 1# had a higher resistance to plastic deformation than sample 2#.

The corrosion potentials (E_{corr}) of the tested samples measured under static and friction conditions in 3.5% NaCl solution are shown in Figure 10. During the measurements, the static and friction conditions were periodically switched. In the first static period of 30 min, E_{corr} of the two samples decreased continuously. When the friction started, E_{corr} sharply shifted to a more positive potential, followed by the slow shifting to a negative direction. Once the friction stopped, E_{corr} suddenly dropped. At the second static immersion period and friction period, the response of E_{corr} was identical to that of the first test cycle. Whether in static or friction conditions, E_{corr} of sample 1# was always higher than that of sample 2#. The stirring effect of friction can accelerate the diffusion of oxygen and lead to the increase of their active dissolution [18, 21–23].

Figure 11 shows the polarization curves for the two tested samples in 3.5% NaCl solution under friction conditions. As seen from Figure 11, both alloys exhibited the active corrosion behavior. The electrochemical response of the two samples is similar. The corrosion potential (E_{corr}) and corrosion current density (i_{corr}) obtained from Figure 11 are listed in Table 4. As is seen in Table 4, sample 2# exhibited a relatively higher corrosion current density. This suggested that a higher bypass current accelerated the corrosion rate of the specimens in 3.5% NaCl solution. One reason was that sample 2# had more defects than sample 1#, and the other was that the refinement of sample 2# provided more channels for corrosion [24–28].

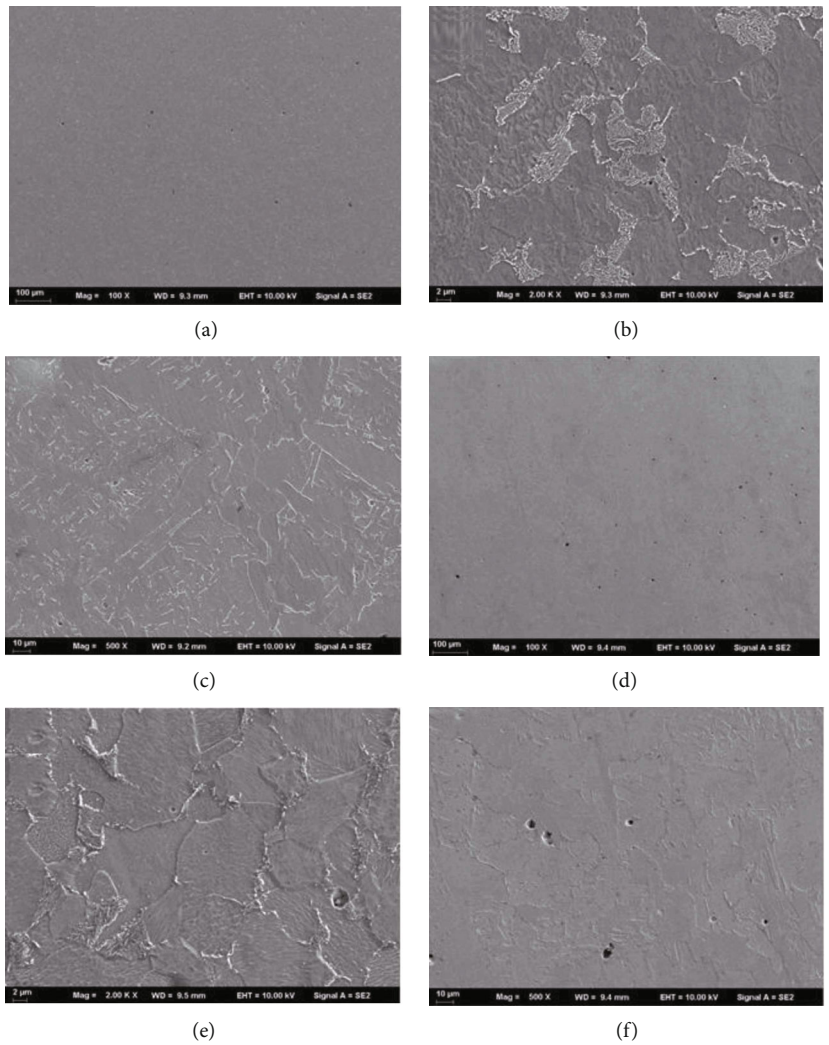

Figure 7: The SEM images of (a–c) sample 1# and (d–f) sample 2#. The images of the (a, d) bottom, (b, e) middle, and (c, f) top sections of samples 1# and 2#, respectively.

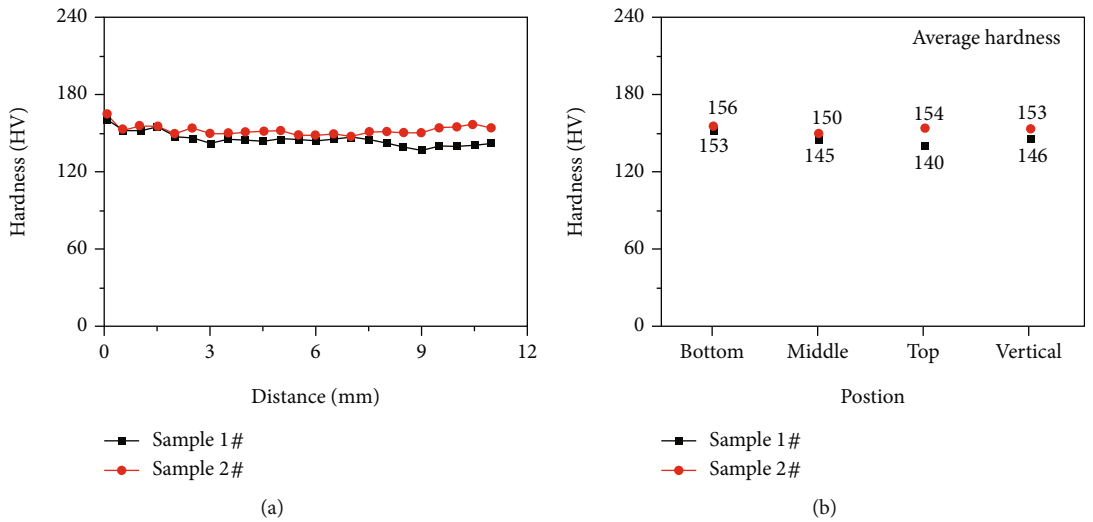

Figure 8: Hardness curves of samples 1# and 2#. (The horizontal distance was from the center axis of the fusion line to the top of samples.).

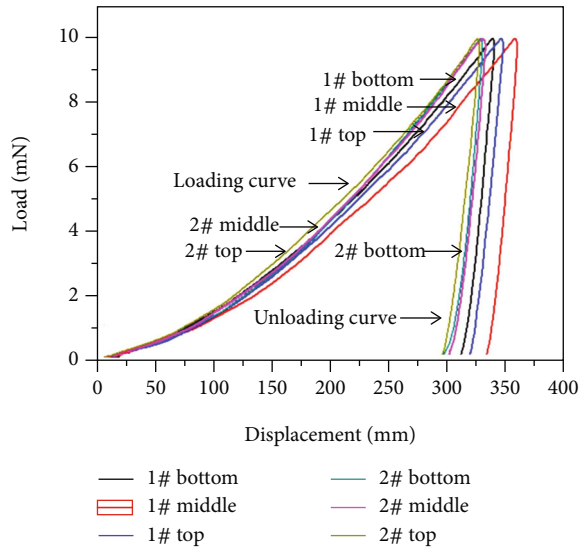

Figure 9: The load-displacement curves (P-h) of different parts for samples 1# and 2#.

Table 3: The parameters of indentation from the load-displacement curves in Figure 8.

Sample	Location	h_{max} (nm)	h_r (nm)	η_h	EIT (GPa)
1#	Bottom	339.02	316.07	0.08	258.22
	Middle	358.66	338.82	0.06	286.09
	Top	346.44	323.59	0.07	252.16
2#	Bottom	328.77	308.83	0.06	316.44
	Middle	331.16	311.21	0.06	312.9
	Top	326.26	302.83	0.07	262.61

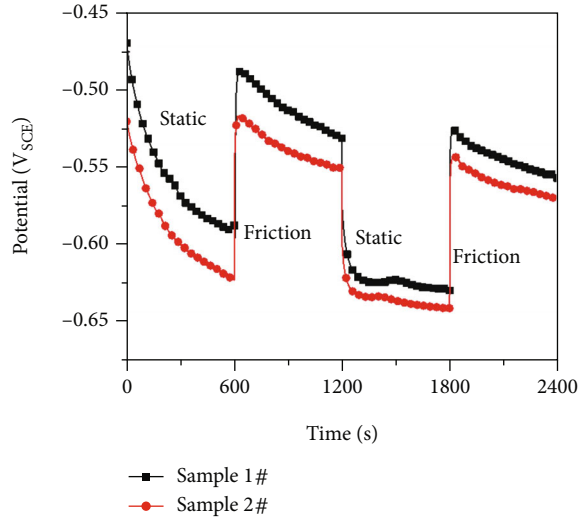

Figure 10: E_{corr} vs. time for the tested samples in 3.5% NaCl solution under static and friction conditions.

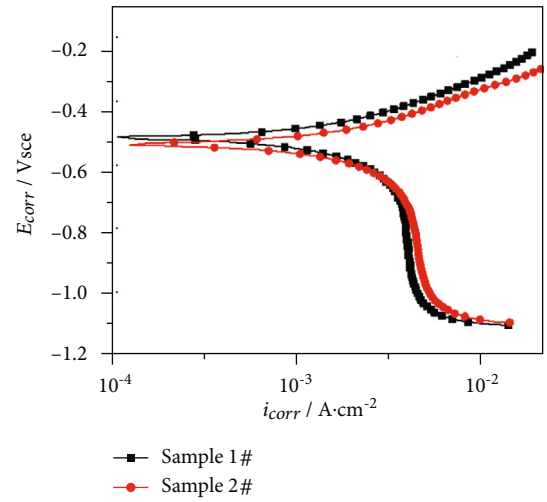

Figure 11: Potentiodynamic polarization curves for the two tested samples in 3.5% NaCl solution under friction condition.

Table 4: Electrochemical parameters extracted from potentiodynamic polarization curves (Figure 11).

	E_{corr} (mV_{SCE})	i_{corr} ($A{\cdot}cm^{-2}$)
Sample 1#	-543 ± 5	$1.13 \pm 0.04 \times 10^{-3}$
Sample 2#	-514 ± 6	$1.32 \pm 0.07 \times 10^{-3}$

4. Conclusions

The conclusions can be drawn as follows:

(1) ER50-6 steel was fabricated by wire + arc additive manufacturing based on the A-W GTAW system. The deposition rate of arc additive can be significantly improved by increasing bypass current through cross-sectional analysis of additive samples by an optical microscope

(2) The microstructure of the two samples in the middle was ferrite grains which were equiaxed. With the GMAW current increased, from the bottom to the top of the sample, the microstructure was fine ferrite and granular pearlite, ferrite equiaxed grains with fine grains at grain boundaries, and columnar ferrite, respectively. The average hardness in the vertical direction of samples 1# and 2# was 146 and 153 HV, respectively. The hardness of the sample increased because of the refinement of grains

(3) The higher bypass current had a deterioration effect on the corrosion behavior of ER50-6 steel because it can produce more defects and make grain refinement that provided more channels for corrosion

Data Availability

The data used to support the findings of this study are available from the corresponding author upon request.

Conflicts of Interest

The authors declare that they have no competing interests.

References

[1] J. Mazumder, D. Dutta, N. Kikuchi, and A. Ghosh, "Closed loop direct metal deposition: art to part," *Optics and Lasers in Engineering*, vol. 34, no. 4-6, pp. 397–414, 2000.

[2] J. G. Lopes, C. M. Machado, V. R. Duarte, T. A. Rodrigues, T. G. Santos, and J. P. Oliveira, "Effect of milling parameters on HSLA steel parts produced by wire and arc additive manufacturing (WAAM)," *Journal of Manufacturing Process*, vol. 59, pp. 739–749, 2020.

[3] P. Wanjara, M. Brochu, and M. Jahazi, "Electron beam free-forming of stainless steel using solid wire feed," *Materials & Design*, vol. 28, no. 8, pp. 2278–2286, 2007.

[4] A. Sreenathbabu, K. P. Karunakaran, and C. Amarnath, "Statistical process design for hybrid adaptive layer manufacturing," *Rapid Prototyping Journal*, vol. 11, no. 4, pp. 235–248, 2005.

[5] R. R. Unocic and J. N. DuPont, "Process efficiency measurements in the laser engineered net shaping process," *Metallurgical & Materials Transactions B*, vol. 35, no. 1, pp. 143–152, 2004.

[6] L.-E. Rännar, A. Glad, and C.-G. Gustafson, "Efficient cooling with tool inserts manufactured by electron beam melting," *Rapid prototyping Journal*, vol. 13, no. 3, pp. 128–135, 2007.

[7] L. E. Murr, S. M. Gaytan, D. A. Ramirez et al., "Metal fabrication by additive manufacturing using laser and electron beam melting technologies," *Journal of Materials Science & Technology*, vol. 28, no. 1, pp. 1–14, 2012.

[8] S. Li, L. J. Zhang, J. Ning et al., "Comparative study on the microstructures and properties of wire+arc additively manufactured 5356 aluminium alloy with argon and nitrogen as the shielding gas," *Additive Manufacturing*, vol. 34, p. 101206, 2020.

[9] J. Xiong, G. J. Zhang, Z. L. Qiu, and Y. Z. Li, "Vision-sensing and bead width control of a single-bead multi-layer part: material and energy savings in GMAW-based rapid manufacturing," *Journal of Cleaner Production*, vol. 41, pp. 82–88, 2013.

[10] P. A. Colegrove, H. E. Coules, J. Fairman et al., "Microstructure and residual stress improvement in wire and arc additively manufactured parts through high-pressure rolling," *Journal of Materials Processing Technology*, vol. 213, no. 10, pp. 1782–1791, 2013.

[11] F. Martina, J. Mehnen, S. W. Williams, P. Colegrove, and F. Wang, "Investigation of the benefits of plasma deposition for the additive layer manufacture of Ti-6Al-4V," *Journal of Materials Processing Technology*, vol. 212, no. 6, pp. 1377–1386, 2012.

[12] Z. X. Li, C. M. Liu, T. Q. Xu et al., "Reducing arc heat input and obtaining equiaxed grains by hot-wire method during arc additive manufacturing titanium alloy," *Material Science and Engineering: A*, vol. 742, pp. 287–294, 2019.

[13] W. Q. Liu, C. B. Jia, M. Guo, J. Q. Gao, and C. S. Wu, "Compulsively constricted WAAM with arc plasma and droplets ejected from a narrow space," *Additive Manufacturing*, vol. 27, pp. 109–117, 2019.

[14] T. A. Rodrigues, V. R. Duarte, R. M. MIRANDA, T. G. Santos, and J. P. Oliveira, "Ultracold-Wire and arc additive manufacturing (UC-WAAM)," *Journal of Materials Processing Technology*, vol. 296, p. 117196, 2021.

[15] J. S. Chen, Y. Lu, X. R. Li, and Y. M. Zhang, "Gas tungsten arc welding using an arcing wire," *Welding Journal*, vol. 91, pp. 261–269, 2012.

[16] Y. X. Qiao, J. Chen, H. L. Zhou et al., "Effect of solution treatment on cavitation erosion behavior of high-nitrogen austenitic stainless steel," *Wear*, vol. 424-425, pp. 70–77, 2019.

[17] Y. X. Qiao, S. L. Sheng, L. M. Zhang et al., "Friction and wear behaviors of a high nitrogen austenitic stainless steel Fe-19Cr-15Mn-0.66N," *Journal of Mining and Metallurgy, Section B: Metallurgy*, vol. 57, pp. 285–293, 2021.

[18] Z. X. Chen, H. X. Hu, Y. G. Zheng, and X. M. Guo, "Effect of groove microstructure on slurry erosion in the liquid-solid two- phase flow," *Wear*, vol. 466-467, p. 203561, 2021.

[19] A. Bordin, S. Bruschi, A. Ghiotti, F. Bucciotti, and L. Facchini, "Comparison between wrought and EBM Ti6Al4V machinability characteristics," *Key Engineering Materials*, vol. 611-612, pp. 1186–1193, 2014.

[20] S. Gorsse, C. Hutchinson, M. Gouné, and R. Banerjee, "Additive manufacturing of metals: a brief review of the characteristic microstructures and properties of steels, Ti-6Al-4V and high-entropy alloys," *Science and Technology of Advanced Materials*, vol. 18, no. 1, pp. 584–610, 2017.

[21] C. H. Qian, H. Z. Xu, and Q. Zhong, "The influence of process parameters on corrosion behavior of Ti6Al4V alloy processed by selective laser melting," *Journal Laser Applications*, vol. 32, no. 3, article 032010, 2020.

[22] L. M. Zhang, Z. X. Li, J. X. Hu et al., "Understanding the roles of deformation-induced martensite of 304 stainless steel in different stages of cavitation erosion," *Tribology International*, vol. 155, p. 106752, 2021.

[23] L. L. Li, Z. B. Wang, S. Y. He, and Y. G. Zheng, "Correlation between depassivation and repassivation processes determined by single particle impingement: its crucial role in the phenomenon of critical flow velocity for erosion-corrosion," *Journal of Materials Science & Technology*, vol. 89, pp. 158–166, 2021.

[24] K. X. Zheng, H. X. Hu, F. G. Chen, and Y. G. Zheng, "Failure analysis of the blackwater regulating valve in the coal chemical industry," *Engineering Failure Analysis*, vol. 125, p. 105442, 2021.

[25] D. P. Wang, H. T. Zhang, P. Y. Guo, B. A. Sun, and Y. X. Wang, "Nanoscale periodic distribution of energy dissipation at the shear band plane in a Zr-based metallic glass," *Scripta Materialia*, vol. 197, p. 113784, 2021.

[26] Z. G. Liu, X. H. Gao, M. Xiong et al., "Role of hot rolling procedure and solution treatment process on microstructure, strength and cryogenic toughness of high manganese austenitic steel," *Materials Science and Engineering: A*, vol. 807, p. 140881, 2021.

[27] Y. X. Qiao, Y. Chen, L. L. Li et al., "Corrosion behavior of a nickel-free high-nitrogen stainless steel with hydrogen charging," *JOM*, vol. 73, no. 4, pp. 1165–1172, 2021.

[28] B. J. Wang, D. K. Xu, X. Cai, Y. X. Qiao, and L. Y. Sheng, "Effect of rolling ratios on the microstructural evolution and corrosion performance of an as-rolled Mg-8 wt.%Li alloy," *Journal of Magnesium and Alloys*, vol. 9, no. 2, pp. 560–568, 2021.

Hindawi
Scanning
Volume 2021, Article ID 5535403, 13 pages
https://doi.org/10.1155/2021/5535403

Research Article

Bias Evaluation of the Accuracy of Two Extraoral Scanners and an Intraoral Scanner Based on ADA Standards

Naiyu Cui,[1] **Jiayin Wang**,[1] **Xingyu Hou**,[1] **Shixun Sun**,[1] **Qixuan Huang**,[1] **Ho-Kyung Lim**,[2] **HongXin Cai**,[1] **Qi Jia**,[1] **Eui-Seok Lee**,[2] **and Heng Bo Jiang**[1]

[1]*The Conversationalist Club, School of Stomatology, Shandong First Medical University & Shandong Academy of Medical Sciences, Tai'an, Shandong 271016, China*
[2]*Department of Oral and Maxillofacial Surgery, Graduate School of Clinical Dentistry, Korea University, Seoul 02841, Republic of Korea*

Correspondence should be addressed to Eui-Seok Lee; ees225@hanmail.net and Heng Bo Jiang; hengbojiang@hotmail.com

Received 18 January 2021; Revised 17 March 2021; Accepted 30 May 2021; Published 11 June 2021

Academic Editor: Lavinia C. Ardelean

The spread and application of computer-aided design/computer-aided manufacturing (CAD/CAM) technology have contributed to the rapid development of digitalization in dentistry. The accuracy of scan results is closely related to the devising subsequent treatment plans and outcomes. Professional standards for evaluating scanners are specified in the American National Standard/American Dental Association Standard 132 (ANSI/ADA No. 132). The aims of this study were to use the three samples mentioned in ANSI/ADA No. 132 and evaluate the accuracy and reproducibility of two extraoral scanners and an intraoral scanner based on the inspection standards recommended by ANSI/ADA No. 132. In this study, two trained operators used two extraoral scanners (E4, 3Shape, Denmark & SHINING DS100+, Shining, China) and an intraoral scanner (TRIOS SERIES3, 3Shape, Denmark) to perform 30 scans of each of the three samples at a temperature of 25 ± 2°C and export standard tessellation language files and used reverse engineering software to perform measurements and iterative nearest point matching experiments. The measured values obtained were compared with the reference values measured by a coordinate measuring machine (NC8107, Leader Metrology, USA). We performed a normal distribution test (Shapiro-Wilk test), the nonparametric Kruskal-Wallis test, and an independent-samples t-test to analyze the reproducibility of each scan for different models. The experimental results indicate that the trueness and precision of the two extraoral scanners and the intraoral scanner had a slight mean deviation. The trueness and precision of the three scanners on the curved surface and groove areas are poor. The accuracy and reproducibility of E4 outperformed SHINING and TRIOS. The iterative closest point matching experiment also showed good matching results. The two extraoral scanners and the intraoral scanner in this study can meet the basic clinical requirements in terms of accuracy, and we hope that digital technology will be more widely used in dentistry in the future.

1. Introduction

In dentistry, the use of digital methods such as computer-aided design/computer-aided manufacturing (CAD/CAM) is rapidly increasing [1–4]. It improves diagnostic ability and facilitates contact between doctors and patients by allowing the rapid acquisition of 3D diagnostic information and transmission of digital data, and along with the rapid development of CAD/CAM technology in the dental field, their use in clinical diagnosis and prosthodontics is becoming more widespread [5–15]. Studies have shown that intraoral scanners are more comfortable for the patient and reduce processing time, and their accuracy and precision are within clinically acceptable limits [10, 11, 16–24]. With the progress of digital technology in the dental field, the accuracy rating of oral scanners has become increasingly important. Extraoral scanners still have higher accuracy than intraoral scanners, and the trueness and precision of intraoral scanners have become an issue of concern.

The current study shows that differences in scanning systems and methods affect experimental results to an uncertain extent [25]. Oh et al. found that different scanning strategies

affect the accuracy of the results [26, 27], and a study by Giménez et al. found that operator proficiency also affects the accuracy of digital impression testing [28]. Furthermore, the accuracy of intraoral scanners changes with the length and distribution of the dental arch: the larger the scan area, the lower the accuracy with the maximum deviation of the scan in the posterior part of the dental arch [29]. The impact of external factors on the results of oral scanners has been the focus of attention, but the objective of evaluating the accuracy of oral scanners has been neglected. Therefore, it is important to objectively grade oral scanners using a more consistent scanning strategy for a standard sample.

In this study, we designed samples based on the American National Standard/American Dental Association Standard 132 (ANSI/ADA NO.132) [30] and measured the height of the crown and the radius of its top circle, the height of the inlay, and the radius of the top circle, and the distance between the reference points of the sphere. The aim of this study was to evaluate the accuracy of two extraoral scanners and an intraoral scanner by analyzing and comparing various data based on the inspection standards recommended by ANSI/ADA No. 132. Furthermore, we introduced CAD/-CAM technology because it is a proven technique for manufacturing samples and computer-designed stereo images based on absolute reference measurements in the form of a coordinate measuring machine (CMM) to perform iterative closest point matching experiments to further evaluate their accuracy [31]. Meanwhile, we conducted experiments to evaluate the reproducibility of the two extraoral scanners and an intraoral scanner.

2. Materials and Methods

2.1. Fabrication of Models. According to ANSI/ADA No. 132, this study designed three reference models. The theoretical values of the crown model radial of the top surface and height were set to 3.5 mm and 6.0 mm, respectively, the radial of the top surface and height of the inlay model were set to 4.0 and 6.0 mm, respectively, and the center distance of a sphere with a long-distance specimen model diameter of 8.0 mm is set as R1 = 35.0 mm, R2 = 59.5 mm, R3 = 55.0 mm, R4 = 59.5 mm, R5 = 40.0 mm, and R6 = 40.0 mm. The 3D views and optical images are shown in Figure 1. Models of the samples were first drawn using CAD software (AutoCAD 2018, Autodesk, USA) and then exported in standard tessellation language (STL) format for computer numerical control milling. Samples were fabricated from stainless steel according to the STL file and washed three times in an ultrasonic bath at 30°C for 5 min each time. Finally, all the samples were sandblasted with a powder size of 80 μm.

2.2. 3D Scanner. The oral scanners used in this experiment were an intraoral scanner (TRIOS SERIES3, 3Shape, Denmark) and two extraoral scanners (E4, 3Shape, Denmark & SHINING DS100+, Shining, China). The SHINING DS100 +, whose field of view is 100 mm × 100 mm × 75 mm, uses blue light and point cloud to capture and form the corresponding image. Similarly, the other extraoral scanner, E4, has the same light source and imaging type as SHINING DS 100+. By contrast, the light source of the intraoral scanner was white light, and the STL file was obtained by splicing the image. More details regarding these scanners are presented in Table 1. Because it is unlikely that the fabricated samples exactly match the software plotted results, CMM was used in this study to measure the relevant indexes of the samples, and the results obtained were used as reference values.

2.3. Sample Scanning and Data Acquisition. The fully trained operator performed 30 scans at 30 s intervals in strict accordance with the instructions for use under the same conditions to obtain a set named A ($N = 30$). The other operator performed 30 scans in a different environment to obtain a set named B ($N = 30$). Reverse engineering software (Geomagic Control X 2018; 3D SYSTEMS, USA) was used to measure a variety of indexes to complete the experiments (Figure 2).

Indexes marked in Figure 1 were measured, and then, data were compared and analyzed.

Using the principle of outlier elimination, if the difference between the data and the average value exceeds 1.96, standard deviations (i.e., outlier data) and the data are eliminated, and the scan and measurement are performed again. If there are more than two outliers, the experimental results will be canceled, and the experiment will be executed again.

2.4. Calculation of Trueness and Precision. Trueness and precision were quantified in terms of the relative error. Δd_M represents the trueness of the test results. The smaller the value of Δd_M, the higher the trueness of the scanner. $\Delta S(d_M)$ represents the precision of the test results. The smaller the $\Delta S(d_M)$, the higher is the precision of the scanner.

Calculate the relative error according to Equations (1) and (2). [30].

$$\Delta dM = \left| \frac{d_R - d_M}{d_R} \right|. \quad (1)$$

d_R represents the reference value of the sample, and d_M represents the measured value (including length, depth, height, and distance from the center).

$$\Delta S(dM) = \left| \frac{S}{d_R} \right|. \quad (2)$$

S represents the standard deviation and d_R represents the reference value of the sample.

The ANSI/ADA No. 132 professional standard considers the relative error of the indexes in samples 1 and 2. Less than 0.01 mm is the acceptable range in the dental requirements category, and a relative error of less than 0.0025 mm represents the distance between sphere reference points to ensure that the acceptable threshold value in the dental requirements category is used as the threshold value.

2.5. Reproducibility Analysis. The reproducibility is reflected by comparing the values of indexes measured from sets A and B. The closer the results of 30 scans of experimental

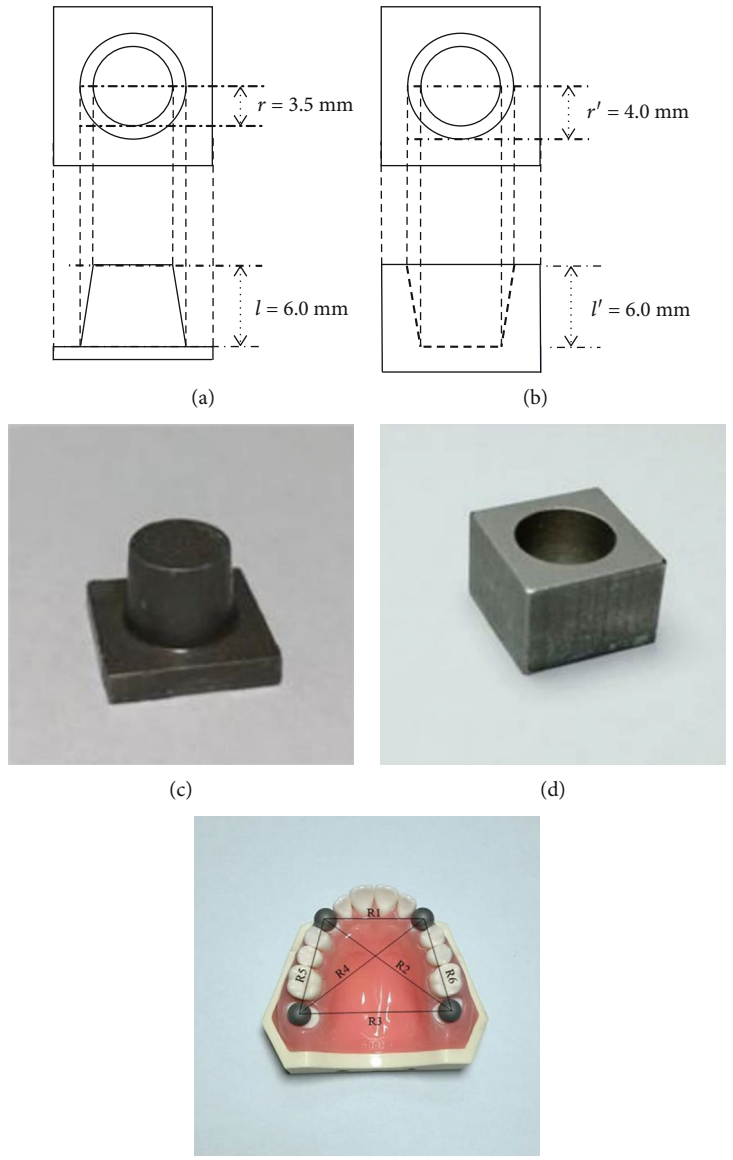

Figure 1: The sample observation drawn by CAD software. Top and side view of (a) sample 1 and (b) sample 2 which alphabetized the index. The manufactured (c) sample 1, (d) sample 2, and (e) sample 3 coated with alloy mentioned in ANSI/ADA No. 132. *"r" and "r'" are the radius of the circle on the top surface of samples 1 and 2. "l" and "l'" are the distance from the top to the bottom of samples 1 and 2. R1 is the distance from the center of the upper left sphere to the right. R2 is the distance from the center of the upper left sphere to the right. R3 is the distance from the center of the lower left sphere to the right. R4 is the distance from the center of the lower left sphere to the right. R5 is the distance from the center of the lower left sphere to the left. R6 is the distance from the center of the upper right sphere to the right. The indicators are consistent in the whole study.

Table 1: Product information of three oral scanners (SHINING, TROIS, E4) and coordinate measuring machine (CMM, NC8107).

Scanner	Manufacturer	Light source	Powder	Metal reflection	Output format	Imaging type
SHINING DS100+	Shining	Blue light	Free	Diffuse reflection	Proprietary or STL	Video (point cloud data)
TRIOS SERIES3	3Shape	White light	Free	Diffuse reflection	Proprietary or STL	Image
E4	3Shape	Blue light	Free	Diffuse reflection	Proprietary or STL	Video (point cloud data)
NC8107	Leader metrology	—	—	—	—	—

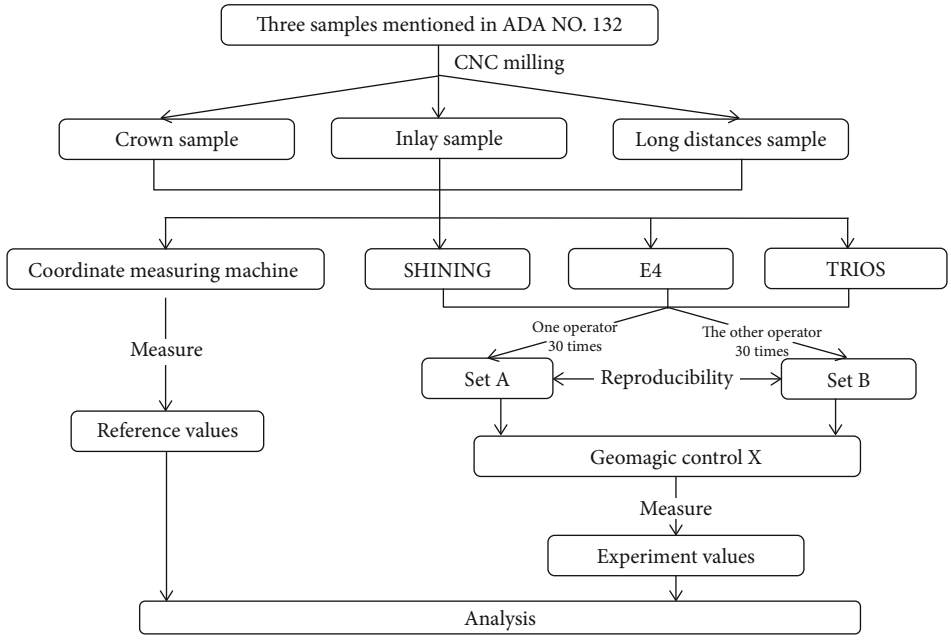

Figure 2: Specific processes of sample scanning and data acquisition based on repeatability and reproducibility experiments.

Table 2: Test protocol template for relative error Δd_M of crown, inlay sample, and long distance sample using three scanners (SHINING, E4, TROIS).

Test object	Δd_M (μm)		
	SHINING	E4	TRIOS
Crown sample			
l	1.75 ± 0.25	8.10 ± 0.05	1.91 ± 0.73
r	9.96 ± 4.88	13.99 ± 7.96	20.60 ± 6.73
Inlay sample			
l'	1.82 ± 0.22	0.10 ± 0.36	3.54 ± 1.52
r'	44.83 ± 8.19	13.99 ± 5.09	16.70 ± 6.51
Long distance sample			
R1	0.46 ± 0.12	0.02 ± 0.02	0.97 ± 0.64
R2	0.39 ± 0.12	0.02 ± 0.02	1.63 ± 1.10
R3	0.48 ± 0.12	0.03 + 0.03	3.31 ± 2.46
R4	0.47 ± 0.11	0.02 ± 0.02	1.26 ± 0.89
R5	0.40 ± 0.11	0.03 ± 0.02	0.64 ± 0.57
R6	0.35 ± 0.11	0.04 ± 0.03	0.55 ± 0.43

group B to that of experimental group A, the greater the reproducibility.

2.6. Statistical Analysis. Each set of data used the Shapiro-Wilk test for normality, which uses SPSS v.24.0 (IBM, USA) to determine the correlation between the scans from the different scanners in the experiment. The nonparametric Kruskal-Wallis test was used to analyze the differences in parameters. We then performed an independent samples t -test to analyze the reproducibility of each scan for different models.

2.7. Iterative Closest Point Matching Experiments. The values calculated from the scan images of the experiment were used to chart the accuracy and repeatability of the oral scanner. However, in addition to the overall detection indexes of the scanning image, the scanning effect of different scanners for the same part of the sample is also different, which cannot be reflected by the detection indexes. Therefore, it is necessary to perform matching experiments to intuitively compare the scanning differences among the three scanners for the same sample.

Each scanned STL file from one scanner was imported into Geomagic Control X to perform iterative closest point matching experiments with corresponding STL file obtained with another scanner. Before the matching experiments, excess parts of the STL file were removed for better results. Thereafter, the initial alignment is carried out, and then, the best-fit alignment between scan data is obtained by the least-squares method. Finally, 3D comparisons were conducted to obtain color images for the visual observation of the difference between the scanners. The average deviation of all points on the surface between two scanners scans is also calculated.

Because the scanned results were well distributed, the results of the iterative closest point matching experiments were also similar. A representative image was selected to represent the experimental results.

3. Results

3.1. Trueness. The results of scanning the indexes of each sample with two extraoral scanners and an intraoral scanner are shown in Table 2, and the relative errors (Δd_M) of the samples were compared with the ANSI/ADA No. 132 specified value. Figure 3 is a box plot of trueness values. Figures 4–6 show the measurements and reference values for sample 1

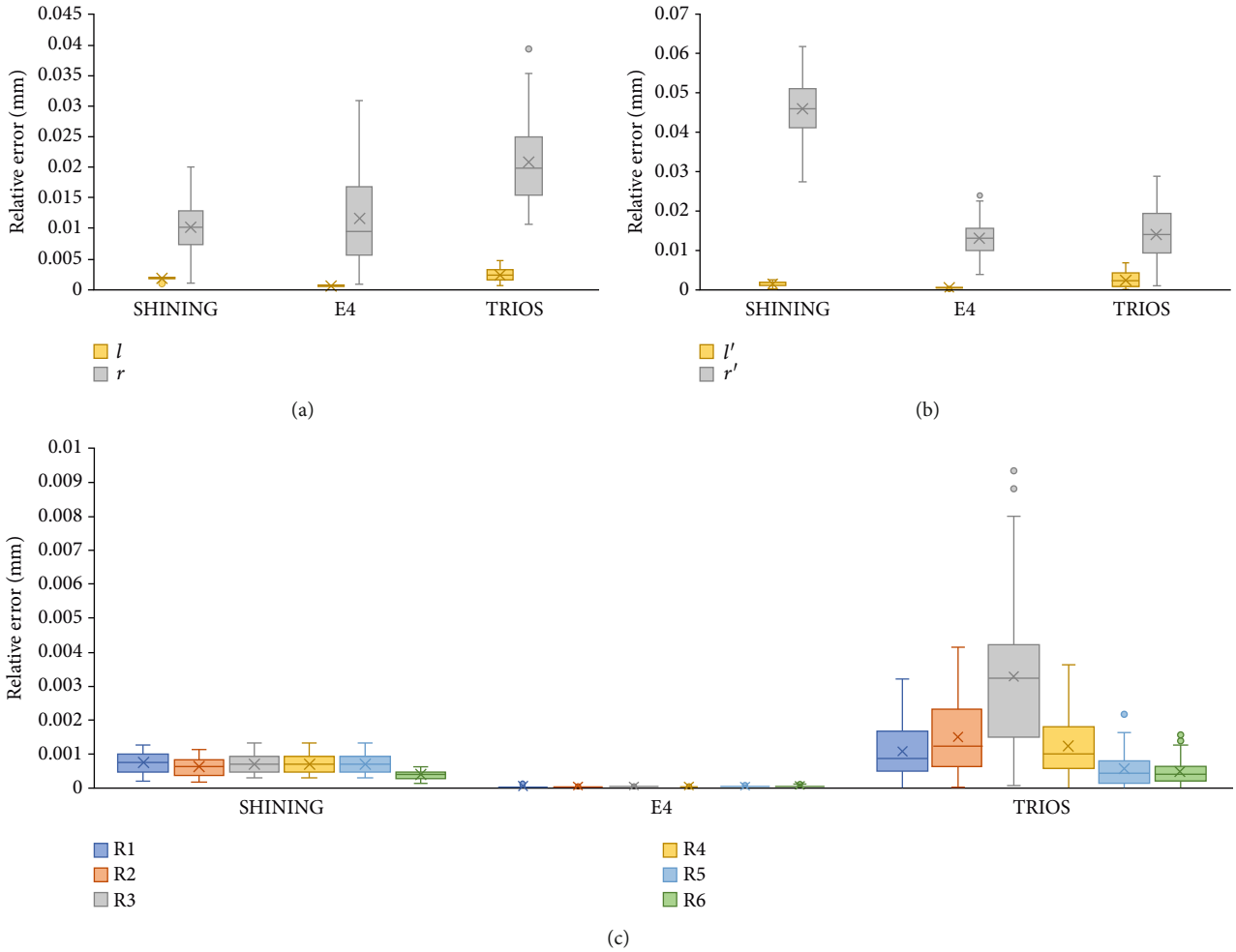

FIGURE 3: Boxplots of absolute mean trueness of crown, inlay sample, and long distance sample. Plot for the comparisons of (a) the crown, (b) the inlay, and (c) the long distance sample between SHINING, E4, and TRIOS.

(crown), sample 2 (inlay), and sample 3 scanned by SHINING, E4, and TRIOS scanners.

TRIOS had a large deviation in measuring R3, which exceeded the acceptable range in the dental requirement category. For sample 2, the SHINING scans showed larger relative errors than E4 and TRIOS, while for sample 1, the relative errors for E4 and TRIOS were larger than those for SHINING. Although the scanning data deviated from the reference value, the deviation was controlled between 0.001 and 0.184 mm. The E4 scan value was closest to the reference value.

There were significant differences in SHINING, E4, and TRIOS. The statistical differences between the three scanners are summarized in Table 3.

3.2. Precision. The results of scanning the indexes of each sample with two extraoral scanners and an intraoral scanner are shown in Table 4, and the relative errors ($\Delta S(d_M)$) of the samples were compared with the ANSI/ADA No. 132 specified value. The results of SHINING, E4, and TRIOS scanning crowns and inlays were accepted by ANSI/ADA No. 132. The $\Delta S(d_M)$ of E4 was the lowest of all three samples, showing the highest precision. SHINING, E4, and TRIOS have a large deviation from the reference value when scanning the inlay radius. The difference between repeated measurements of TRIOS is the largest, especially the distance between the datum points of the spheres.

3.3. Repeatability and Reproducibility of Samples. Regarding repeatability and reproducibility, most of the results tested by the two operators were statistically different (Table 5).

In the SHINING group, there was no statistically significant difference between groups A and B in the radius of the repeatedly scanned crowns and inlays. In the E4 group, there was no statistically significant difference between groups A and B in the radius of the scanned inlays. In the Trios group, there was no statistically significant difference between groups A and B in the radius of the repeatedly scanned crowns.

3.4. Iterative Closest Point Matching of Samples. The color bar represents qualitative information analysis. These differences between scanners are shown in the color bar [32]. While the color bar depicts deviations between -1 and 1 mm, acceptable errors between -0.01 and 0.01 mm are marked in green, better reflecting the differences between two scanners while

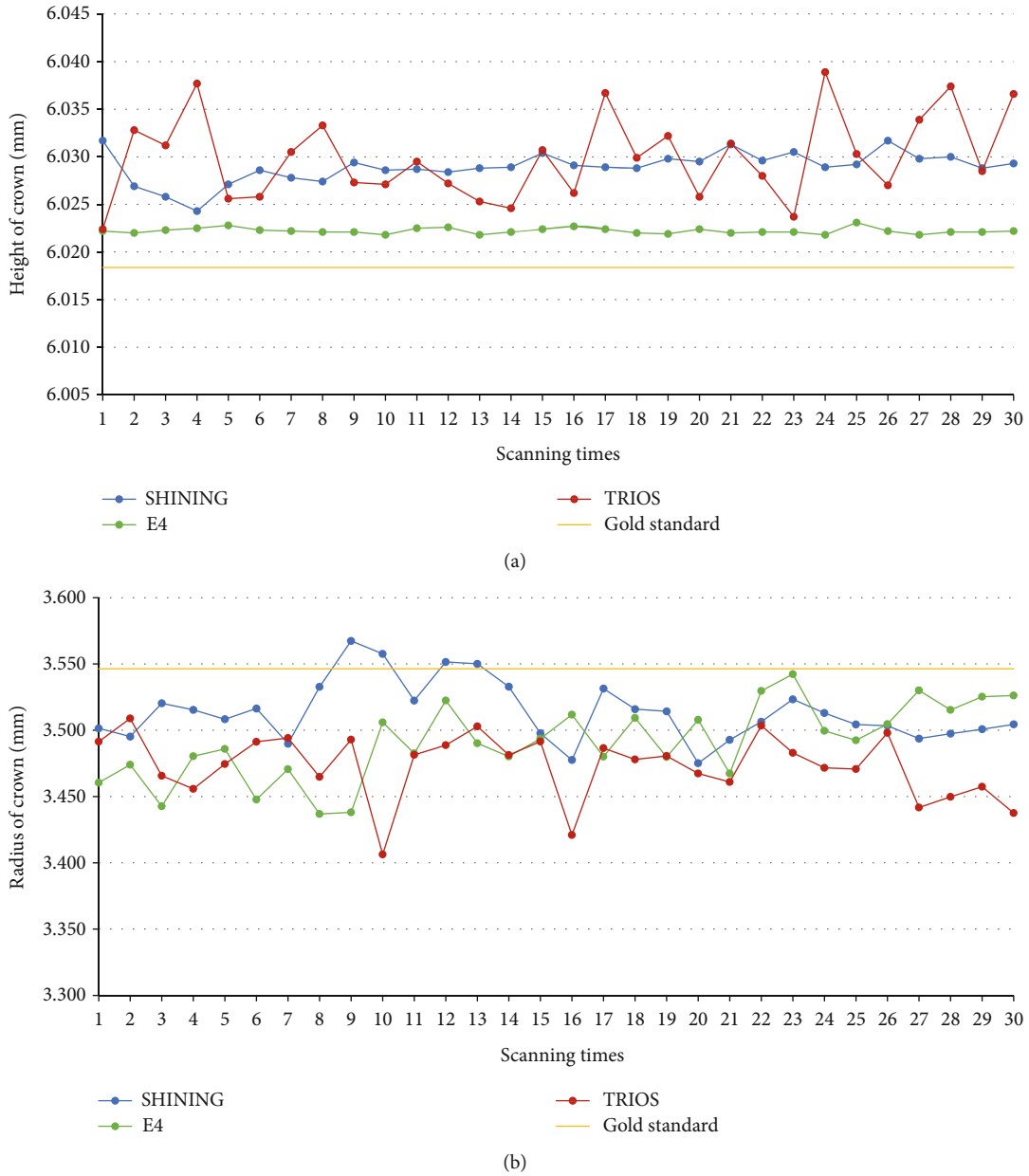

Figure 4: Plots for the comparisons of indexes between SHINING, E4, and TRIOS based on the results of the repeated measures. Plot for the comparisons of (a) the height of crown and (b) the radius of crown between SHINING, E4, and TRIOS.

scanning the same sample. A positive difference from yellow to red indicates a higher deviation from the reference model, and a negative difference from azure to dark blue indicates a lower deviation from the reference model.

Figures 7 and 8 show that the local deviation between the two scanners occurs on the curved surface and deep areas. Table 6 shows the RMS values between the two scanners, and the RMS values between the scanners is within 1.0 mm.

4. Discussion

The oral scanner is evaluated based on the "trueness" and "precision" specified in ISO 5725-1 [33], where trueness is defined as the consistency between the test result and the acceptable reference value. Precision is defined as the closeness of the independent test results obtained under the specified conditions. The accuracy of the scanner was verified by a combined evaluation of trueness and precision.

This study is aimed at evaluating the trueness and precision of three oral scanners based on three samples provided by ANSI/ADA No. 132. The CMM was used to measure the data obtained from the original sample as a reference value, and the results were compared with those of the three scanners. Experiments were conducted to further analyze the accuracy and reproducibility of the scanners [28, 34–38]. At the same time, some pits generated in the scanning process are introduced into the interactive closest point matching to reflect the differences among the three scanners.

The calculated Δd_M and $\Delta S(d_M)$ indicate that although there were a few large numerical errors (e.g., the average

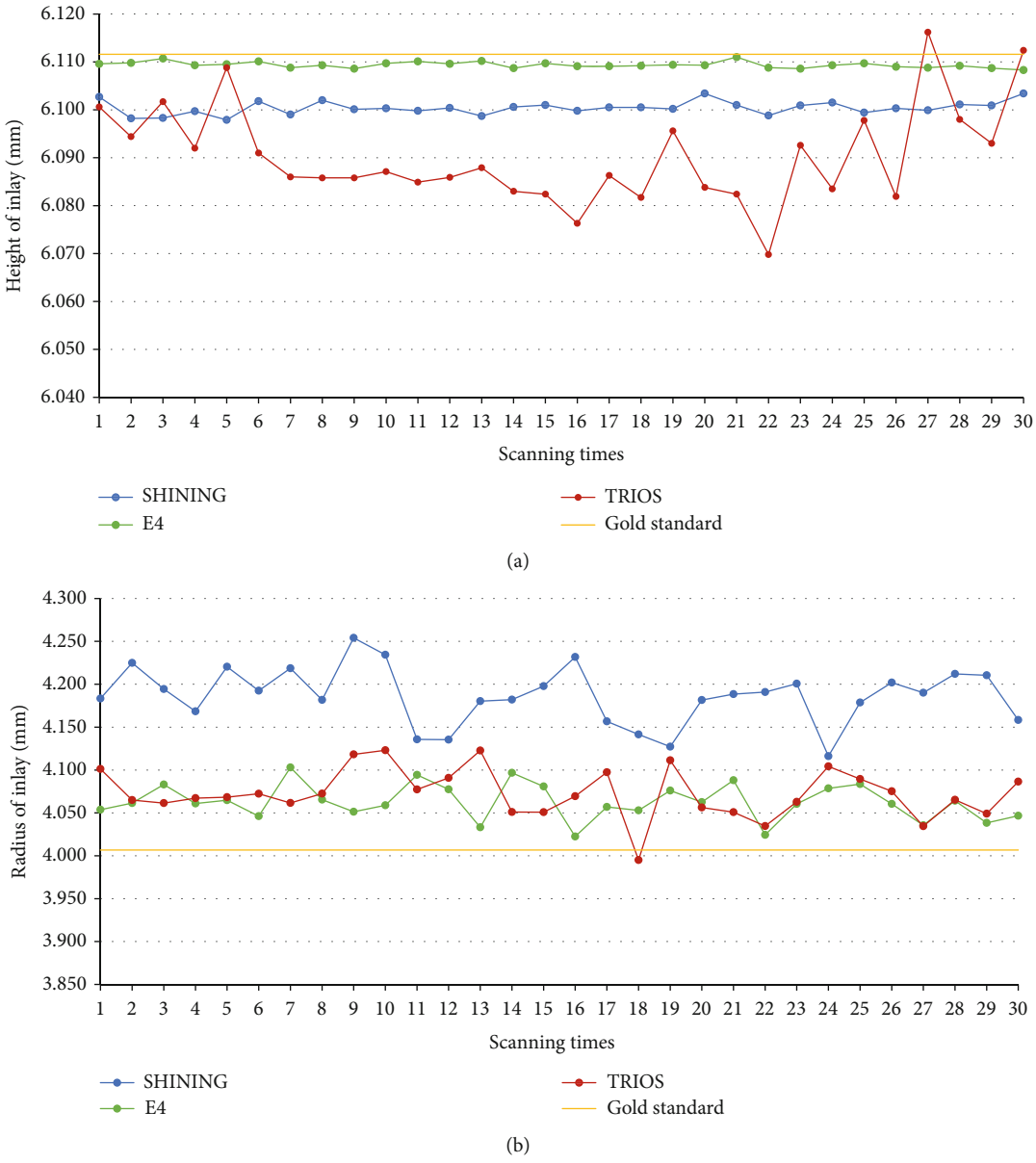

Figure 5: Plots for the comparisons of indexes between SHINING, E4, and TRIOS based on the results of the repeated measures. Plot for the comparisons of (a) the height of inlay and (b) the radius of inlay between SHINING, E4, and TRIOS.

value of the relative error of TRIOS for the radius of sample 1 is 0.0260 mm, and the average value of the relative error of SHINING for the radius of sample 2 is 0.0448), most of the trueness and precision were acceptable, and the accuracy was within the acceptable range. The accuracy of E4 was better than that of SHINING and TRIOS. In terms of reproducibility, most of the results tested by the two operators were statistically different.

As in previous studies [28, 34–39], the CMM measurement sample was used to obtain more accurate standard values. It should be noted that there is always an error between the results of the mechanical scan and the actual values of the sample. However, the CMM used in this study has high accuracy, and using CMM measurement samples as the reference value is also allowed in ANSI/ADA No. 132 [20, 40–42]. Inevitably, many errors were still present during the experiment.

The results of the repeated measures of TRIOS have a large fluctuation range. The high relative error of TRIOS may be related to the image acquisition method of the scanner and the operation of the operator. The extraoral scanner can construct the shape of the object effectively based on the point cloud obtained in the 3D point coordinate system, while the intraoral scanner uses the best-fitting algorithm to stitch the scanned images together. When the surface shape of the scanned object is complex, image alignment is easier, but when the scanned object is flat and smooth (such as edentulous jaws), images are more prone to errors, causing distortion of the STL file [43]. The farther away from the start scanning point and the greater the splicing times, the lower

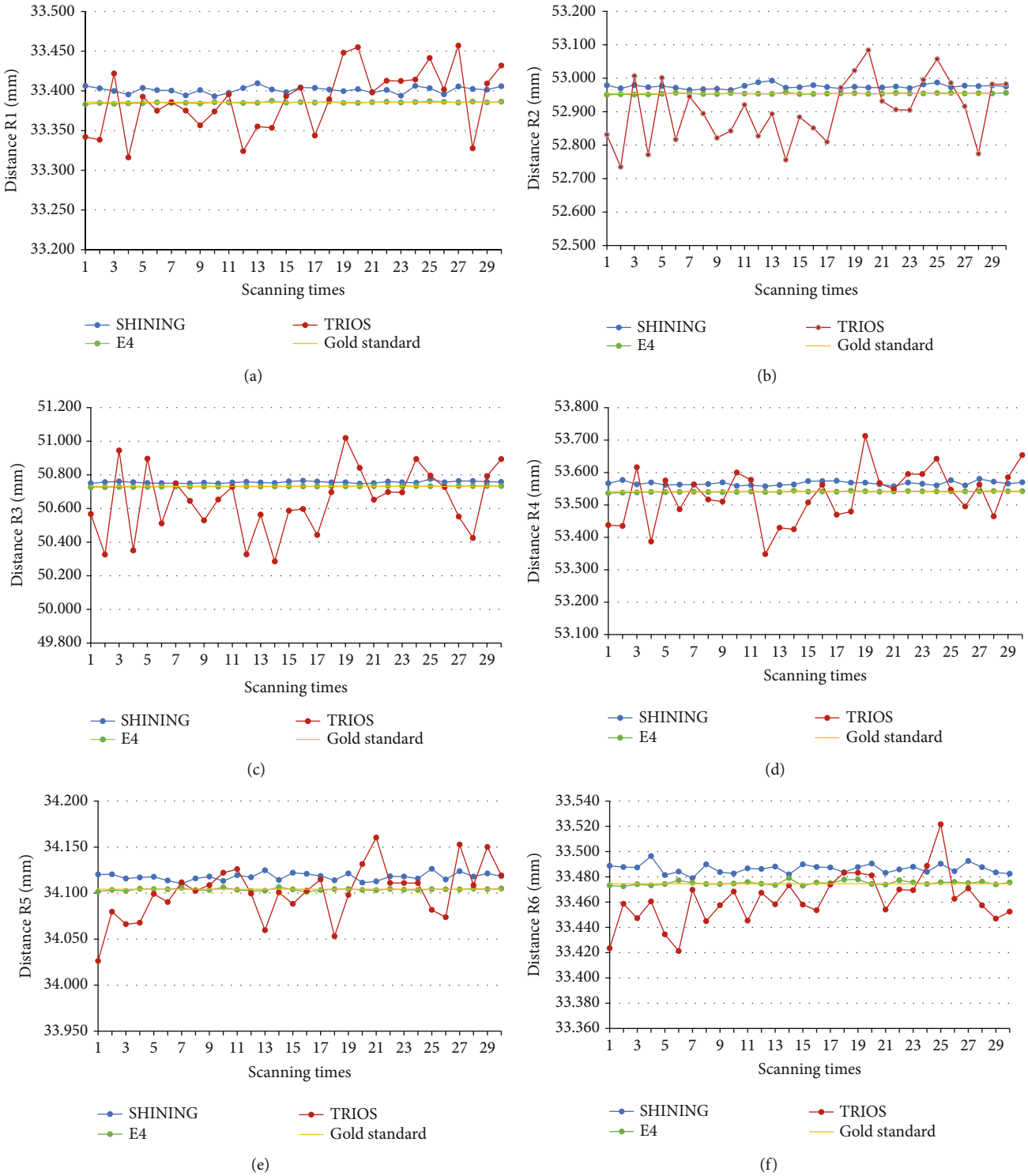

Figure 6: Plots for the comparisons of indexes between SHINING, E4, and TRIOS based on the results of the repeated measures. Plot for the comparisons of distance (a) R1, (b) R2, (c) R3, (d) R4, (e) R5, and (f) R6 between the datum points of spheres between SHINING, E4, and TRIOS.

the accuracy of the data. Therefore, some studies suggested placing complex geometry near the edentulous area to improve scanning accuracy when using an intraoral scanner [43–45]. At the same time, previous studies have shown that the posterior dental arch exhibits greater errors during intraoral scanning [10, 44, 46]. Moreover, the handheld intraoral scanner oscillates during scanning and needs to constantly change the coordinates [26]. Therefore, each time the image of the scanner is stitched, the processing and fitting errors increase, resulting in inaccurate measurement and

Table 3: Analysis of the difference in the SHINING, E4, and TROIS.

Test object	*P* value		
	SHINING-E4	SHINING-TRIOS	E4-TRIOS
Crown sample			
l	<.01**	.06	<.01**
r	1.00	<.01**	<.01**
Inlay sample			
l'	<.01**	1.00	<.01**
r'	<.01**	<.01**	1.00
Long distance sample			
R1	<.01**	.04	<.01**
R2	<.01**	<.01**	1.00
R3	<.01**	<.01**	1.00
R4	<.01**	<.01**	<.01**
R5	<.01**	<.01**	.17
R6	<.01**	<.01**	.35

* indicates a difference at the significance level of 0.05; ** indicates a difference at the significance level of 0.01. The normal distribution test (Shapiro-Wilk test) and an independent-samples Kruskal-Wallis test.

Table 4: Test protocol template for relative error $\Delta S(d_M)$ of crown, inlay sample, and long distance sample using three scanners (SHINING, E4, and TROIS).

Test object	$\Delta S(d_M)$ (μm)		
	SHINING	E4	TRIOS
Crown sample			
l	0.26	0.10	0.73
r	6.21	7.96	6.74
Inlay sample			
l'	0.22	0.10	1.66
r'	0.82	5.09	6.99
Long distance sample			
R1	0.12	0.27	1.16
R2	0.12	0.03	1.76
R3	0.12	0.04	3.77**
R4	0.11	0.03	1.53
R5	0.11	0.03	0.85
R6	0.11	0.05	0.58

*Greater than 10 μm; **greater than 2.5 μm.

image distortion [47]. Therefore, as the complexity and geometry of tooth preparation increases, intraoral scans become inaccurate [25, 38, 39, 48]. Michaeli et al. suggested alleviating the experimental error by increasing the scanning angle and scanning times [49]. The extraoral scanner automatically scans the fixed model at different angles to reduce the influence of the operator on the scanning process. Therefore, the operator's impact on the extraoral scanner is much less than that on the intraoral scanner [38]. However, the two extraoral scanners and the intraoral scanner in this study showed poor reproducibility. The authors speculate that this may be related to scanning in different environments.

The best match alignments between scanners were conducted using the best-fit algorithm of Geomagic Control X. Each point in the source point cloud was best aligned with the closest point in the reference point cloud. The offset between digital models obtained from every two scanners was visualized by color mapping. Geomagic Control X can efficiently detect the differences between irregular shapes, which is especially suitable for analyzing oral models. However, because the scanning offset reflected by Geomagic Control X is not applicable to the evaluation of sphere spacing, iterative closest point matching is not considered for the sphere sample in this study.

In Tables 2 and 4, the relative errors of E4, SHINING, and TRIOS in the scan model radius exceeded the acceptable range in the dental requirement category. In Figure 7, scanners showed relatively large differences when scanning curved surfaces and deep area. This may be caused by the energy lost by the light source because of the reflection when the surface of the scanned sample moves, which affects scanned by the scanner, and the curved surface is more likely to cause light reflection [50]. In Figure 8, comparing between each other, three scanners showed obvious deviation when scanning the bottom of the inlay, which may also be related to the fact that the scanner light source cannot perform detailed scanning at the bottom. Different light sources also affect the accuracy of the scanner [10, 51]. Araki et al. scanned under different light sources and evaluated the results. They found that the most suitable lighting conditions for digital impression scanning were 3900 K and 500 lux [52]. However, in the iterative closest point matching experiments, the deviations produced by the best matching process are all less than 0.01 mm.

In previous studies, different methods have been used to evaluate the accuracy of diverse oral scanners. Intraoral scanner systems were found to be less accurate than extraoral scanners, and the ability of extraoral scanners to scan the edges of the crown is also better than that of intraoral scanners [25, 39]. This is consistent with the results of our experiments. Cai et al. evaluated the accuracy of SHINING, CEREC, and TRIOS by scanning an international standard sphere model, and the results showed that the accuracy of the intraoral scanners was better than that of the extraoral scanner [53]. However, in this study, the accuracy of the extraoral scanner E4 was significantly better than that of the intraoral scanner TRIOS.

This study has some limitations, as it was conducted in vitro and did not simulate actual clinical conditions. The effects of temperature and humidity of the oral environment, saliva and blood, soft tissues, patient movement, oral cavity, and scanning laser angle of incidence were not considered [10, 54, 55]. At the same time, many items in the oral cavity, such as implants (ceramics, metals, and composite resins), dentin, enamel, oral soft tissue, and different materials and geometric shapes, also affect the accuracy of scanning. The scanned samples presented in this study have different light effects from the soft tissue around the oral cavity [26, 56]; therefore, there are some limitations. In future studies, we

Table 5: Repeatability and reproducibility in the SHINING, E4, and TROIS.

Test object	SHINING Mean ± SD A (mm)	SHINING Mean ± SD B (mm)	*P*	E4 Mean ± SD A (mm)	E4 Mean ± SD B (mm)	*P*	TRIOS Mean ± SD A (mm)	TRIOS Mean ± SD B (mm)	*P*
Crown sample									
L	6.03 ± 0.00	6.03 ± 0.00	.027*	6.02 ± 0.00	6.02 ± 0.00	.000**	6.03 ± 0.00	6.04 ± 0.01	.000**
R	3.51 ± 0.02	3.51 ± 0.01	.231	3.49 ± 0.03	3.52 ± 0.02	.000**	3.47 ± 0.02	3.47 ± 0.02	.724
Inlay sample									
l'	6.10 ± 0.00	6.10 ± 0.00	.000**	6.11 ± 0.00	6.11 ± 0.00	.000**	6.09 ± 0.01	6.10 ± 0.01	.000**
r'	4.19 ± 0.03	4.20 ± 0.03	.237	4.06 ± 0.02	4.06 ± 0.01	.109	4.07 ± 0.03	4.06 ± 0.03	.017*
Long distance sample									
R1	33.40 ± 0.00	33.42 ± 0.00	.000**	33.39 ± 0.00	33.39 ± 0.00	.003**	33.39 ± 0.04	33.42 ± 0.03	.002**
R2	52.98 ± 0.01	53.00 ± 0.01	.000**	52.95 ± 0.00	52.96 ± 0.00	.017*	52.90 ± 0.09	52.95 ± 0.09	.037*
R3	50.76 ± 0.01	50.78 ± 0.01	.000**	50.73 ± 0.00	50.73 ± 0.00	.000 **	50.65 ± 0.19	50.71 ± 0.19	.231
R4	53.57 ± 0.01	53.58 ± 0.01	.000**	53.54 ± 0.00	53.54 ± 0.00	.051	53.53 ± 0.08	53.56 ± 0.08	.138
R5	34.12 ± 0.00	34.12 ± 0.00	.000**	34.10 ± 0.00	34.10 ± 0.00	.015*	34.10 ± 0.03	34.11 ± 0.02	.159
R6	33.49 ± 0.00	33.49 ± 0.00	.006**	33.48 ± 0.00	33.47 ± 0.00	.012*	33.46 ± 0.02	33.47 ± 0.02	.022*

* indicates a difference at the significance level of 0.05; ** indicates a difference at the significance level of 0.01. The normal distribution test (Shapiro-Wilk test) and an independent-samples *t*-test.

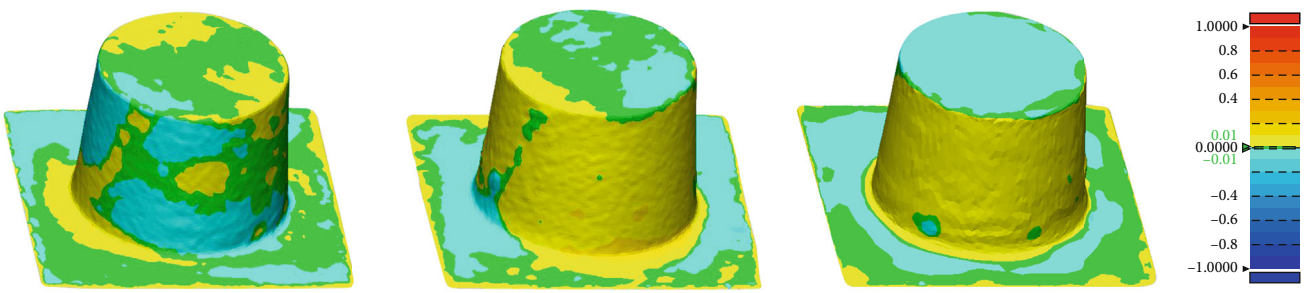

(a) (b) (c)

Figure 7: Selected representative crown scanned by SHINING, E4, and TRIOS for three-dimensional compare analysis. (a) E4 compares with TRIOS. (b) E4 compares with SHINING. (c) TRIOS compares with SHINING. ***Color bar depicting deviations with settings at nominal between -0.01 mm and 0.01 mm and critical between -1 and 1 mm.

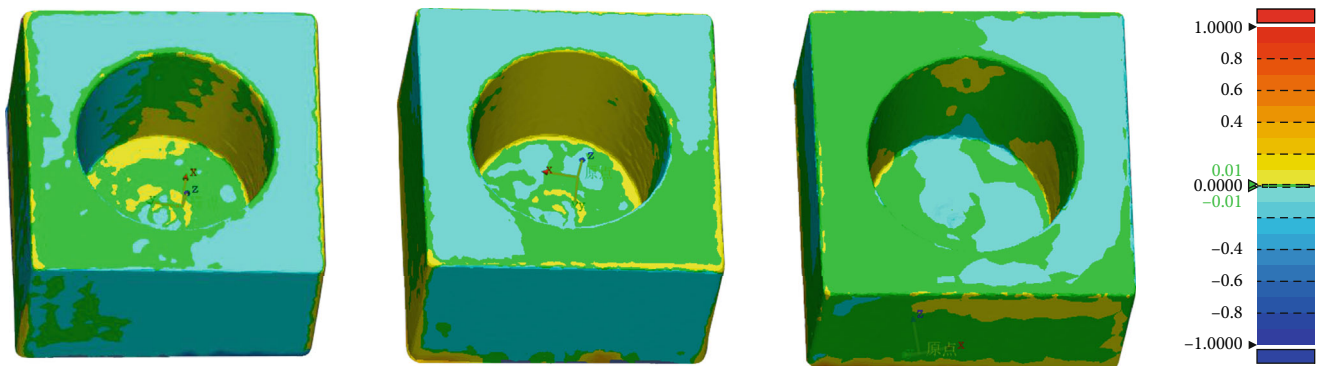

(a) (b) (c)

Figure 8: Selected representative inlay scanned by SHINING, E4, and TRIOS for three-dimensional compare analysis. (a) E4 compares with TRIOS. (b) E4 compares with SHINING. (c) TRIOS compares with SHINING. ***Color bar depicting deviations with settings at nominal between -0.01 mm and 0.01 mm and critical between -1 and 1 mm.

Table 6: RMS values for the 3D-fitting results.

Test group	RMS	
	Crown (mm)	Inlay (mm)
E4-TRIOS	0.0559	0.0669
E4-SHINING	0.0592	0.044
TRIOS-SHINING	0.0408	0.1345

will simulate a clinical setting and increase the number of scanning groups to further evaluate the accuracy of different scanners.

5. Conclusion

This study evaluated the accuracy of the three scanners by measuring ANSI/ADA No. 132 provided reference models.

(1) There was significant difference between the scanning results of the three scanners, with E4 showing the best reproducibility

(2) Whether scanning crown, inlay, or arch, the extraoral scanner showed fewer distortions than the intraoral scanner, with E4 showing the least error

(3) Most of the scanning errors of the extraoral and intraoral scanners were within the acceptable range of the ADA standard. However, the effect of scanning the sample radius is poor

(4) Relatively large differences between scanners occurred when scanning curved surfaces and the deep areas of the inlay

Data Availability

The data used to support the findings of this study are included in this article.

Conflicts of Interest

We declare that we have no financial or personal relationships with other people or organizations that can inappropriately influence our work.

Authors' Contributions

Naiyu Cui, Jiayin Wang, and Xingyu Hou contributed equally to this work. Naiyu Cui and Jiayin Wang are responsible for the conceptualization, methodology, formal analysis, investigation, and writing—original draft; Xingyu Hou for the methodology, validation, writing—review and editing, and visualization; ShiXun Sun and Qixuan Huang for the validation, data curation, and writing—review and editing; Ho-Kyung Lim for the writing—review and editing, and visualization; HongXin Cai and Qi Jia for the validation, resources, writing—review and editing, and supervision; and Eui-Seok Lee and Heng Bo Jiang for the validation, resources, supervision, project administration, and funding acquisition.

References

[1] M. B. Blatz and J. Conejo, "The current state of chairside digital dentistry and materials," *Dental Clinics of North America*, vol. 63, no. 2, pp. 175–197, 2019.

[2] G. Cervino, L. Fiorillo, A. V. Arzukanyan, G. Spagnuolo, and M. Cicciu, "Dental restorative digital workflow: digital smile design from aesthetic to function," *Dentistry Journal*, vol. 7, no. 2, p. 30, 2019.

[3] E. Blackwell, M. Nesbit, and H. Petridis, "Survey on the use of CAD-CAM technology by UK and Irish dental technicians," *British Dental Journal*, vol. 222, no. 9, pp. 689–693, 2017.

[4] D. Tran, M. Nesbit, and H. Petridis, "Survey of UK dentists regarding the use of CAD/CAM technology," *British Dental Journal*, vol. 221, no. 10, pp. 639–644, 2016.

[5] C. B. Martin, E. V. Chalmers, G. T. McIntyre, H. Cochrane, and P. A. Mossey, "Orthodontic scanners: what's available?," *Journal of Orthodontics*, vol. 42, pp. 136–143, 2015.

[6] O. de Waard, F. A. Rangel, P. S. Fudalej, E. M. Bronkhorst, A. M. Kuijpers-Jagtman, and K. H. Breuning, "Reproducibility and accuracy of linear measurements on dental models derived from cone-beam computed tomography compared with digital dental casts," *American Journal of Orthodontics and Dentofacial Orthopedics*, vol. 146, no. 3, pp. 328–336, 2014.

[7] P. S. Fleming, V. Marinho, and A. Johal, "Orthodontic measurements on digital study models compared with plaster models: a systematic review," *Orthodontics & Craniofacial Research*, vol. 14, no. 1, pp. 1–16, 2011.

[8] S. Amin, H. P. Weber, M. Finkelman, K. el Rafie, Y. Kudara, and P. Papaspyridakos, "Digital vs. conventional full-arch implant impressions: a comparative study," *Clinical Oral Implants Research*, vol. 28, no. 11, pp. 1360–1367, 2017.

[9] L. Lin, Y. Fang, Y. Liao, G. Chen, C. Gao, and P. Zhu, "3D printing and digital processing techniques in dentistry: a review of literature," *Advanced Engineering Materials*, vol. 21, p. 1801013, 2019.

[10] H. Kihara, W. Hatakeyama, F. Komine et al., "Accuracy and practicality of intraoral scanner in dentistry: a literature review," *Journal of Prosthodontic Research*, vol. 64, no. 2, pp. 109–113, 2020.

[11] K. Suese, "Progress in digital dentistry: the practical use of intraoral scanners," *Dental Materials Journal*, vol. 39, no. 1, pp. 52–56, 2020.

[12] F. Mangano, C. Mangano, B. Margiani, and O. Admakin, "Combining intraoral and face scans for the design and fabrication of computer-assisted design/computer-assisted manufacturing (CAD/CAM) polyether-ether-ketone (PEEK) implant-supported bars for maxillary overdentures," *Scanning*, vol. 2019, 4274714 pages, 2019.

[13] U. Schepke, H. J. Meijer, W. Kerdijk, G. M. Raghoebar, and M. Cune, "Stock versus CAD/CAM customized zirconia implant abutments - clinical and patient-based outcomes in a randomized controlled clinical trial," *Clinical Implant Dentistry and Related Research*, vol. 19, no. 1, pp. 74–84, 2017.

[14] E. Davidovich, B. Shay, E. Nuni, and E. Mijiritsky, "An innovative treatment approach using digital workflow and CAD-CAM part 1: the restoration of endodontically treated molars in children," *International Journal of Environmental Research and Public Health*, vol. 17, no. 4, p. 1364, 2020.

[15] T. Miyazaki, Y. Hotta, J. Kunii, S. Kuriyama, and Y. Tamaki, "A review of dental CAD/CAM: current status and future

perspectives from 20 years of experience," *Dental Materials Journal*, vol. 28, no. 1, pp. 44–56, 2009.

[16] A. M. R. Cuperus, M. C. Harms, F. A. Rangel, E. M. Bronkhorst, J. G. J. H. Schols, and K. H. Breuning, "Dental models made with an intraoral scanner: a validation study," *American Journal of Orthodontics and Dentofacial Orthopedics*, vol. 142, no. 3, pp. 308–313, 2012.

[17] D. Naidu and T. J. Freer, "Validity, reliability, and reproducibility of the iOC intraoral scanner: a comparison of tooth widths and Bolton ratios," *American Journal of Orthodontics and Dentofacial Orthopedics*, vol. 144, no. 2, pp. 304–310, 2013.

[18] M. G. Wiranto, W. P. Engelbrecht, H. E. Tutein Nolthenius, W. J. van der Meer, and Y. Ren, "Validity, reliability, and reproducibility of linear measurements on digital models obtained from intraoral and cone-beam computed tomography scans of alginate impressions," *American Journal of Orthodontics and Dentofacial Orthopedics*, vol. 143, no. 1, pp. 140–147, 2013.

[19] T. V. Flugge, W. Att, M. C. Metzger, and K. Nelson, "Precision of dental implant digitization using intraoral scanners," *The International Journal of Prosthodontics*, vol. 29, pp. 277–283, 2016.

[20] C. Keul and J. F. Guth, "Accuracy of full-arch digital impressions: an in vitro and in vivo comparison," *Clinical Oral Investigations*, vol. 24, no. 2, pp. 735–745, 2020.

[21] T. Grünheid, S. D. McCarthy, and B. E. Larson, "Clinical use of a direct chairside oral scanner: an assessment of accuracy, time, and patient acceptance," *American Journal of Orthodontics and Dentofacial Orthopedics*, vol. 146, no. 5, pp. 673–682, 2014.

[22] M. F. Sfondrini, P. Gandini, M. Malfatto, F. di Corato, F. Trovati, and A. Scribante, "Computerized casts for orthodontic purpose using powder-free intraoral scanners: accuracy, execution time, and patient feedback," *BioMed Research International*, vol. 2018, 8 pages, 2018.

[23] A. P. G. Sjögren, J. E. Lindgren, and J. Å. V. Huggare, "Orthodontic study cast analysis—reproducibility of recordings and agreement between conventional and 3D virtual measurements," *Journal of Digital Imaging*, vol. 23, pp. 482–492, 2010.

[24] A. Ender, M. Zimmermann, T. Attin, and A. Mehl, "In vivo precision of conventional and digital methods for obtaining quadrant dental impressions," *Clinical Oral Investigations*, vol. 20, no. 7, pp. 1495–1504, 2016.

[25] S. Shimizu, A. Shinya, S. Kuroda, and H. Gomi, "The accuracy of the CAD system using intraoral and extraoral scanners for designing of fixed dental prostheses," *Dental Materials Journal*, vol. 36, no. 4, pp. 402–407, 2017.

[26] C. Motel, E. Kirchner, W. Adler, M. Wichmann, and R. E. Matta, "Impact of different scan bodies and scan strategies on the accuracy of digital implant impressions assessed with an intraoral scanner: an in vitro study," *Journal of Prosthodontics*, vol. 29, pp. 309–314, 2020.

[27] K. C. Oh, J. M. Park, and H. S. Moon, "Effects of scanning strategy and scanner type on the accuracy of intraoral scans: a new approach for assessing the accuracy of scanned data," *Journal of Prosthodontics*, vol. 29, no. 6, pp. 518–523, 2020.

[28] B. Giménez, M. Özcan, F. Martínez-Rus, and G. Pradíes, "Accuracy of a digital impression system based on active wavefront sampling technology for implants considering operator experience, implant angulation, and depth," *Clinical Implant Dentistry and Related Research*, vol. 17, pp. e54–e64, 2015.

[29] J. H. Lee, J. H. Yun, J. S. Han, I. L. Yeo, and H. I. Yoon, "Repeatability of intraoral scanners for complete arch scan of partially edentulous dentitions: an in vitro study," *Journal of Clinical Medicine*, vol. 8, no. 8, p. 1187, 2019.

[30] "Scanning Accuracy of Dental Chairside and Laboratory CAD/CAM System," in *ADA/ANSI Standard No. 132*, American Dental Association, Chicago, IL, USA, 2015.

[31] K. Y. Wong, R. J. Esguerra, V. A. P. Chia, Y. H. Tan, and K. B. C. Tan, "Three-dimensional accuracy of digital static interocclusal registration by three intraoral scanner systems," *Journal of Prosthodontics*, vol. 27, no. 2, pp. 120–128, 2018.

[32] Y. Jang, J. Y. Sim, J. K. Park, W. C. Kim, H. Y. Kim, and J. H. Kim, "Evaluation of the marginal and internal fit of a single crown fabricated based on a three-dimensional printed model," *J Adv Prosthodont*, vol. 10, no. 5, pp. 367–373, 2018.

[33] "Accuracy (trueness and precision) of measurement methods and results — Part 1: General principles and definitions," *International Standard (ISO) 5725-1*, International Organization for Standardization, Geneva, Switzerland, 1994.

[34] B. Gimenez-Gonzalez, B. Hassan, M. Ozcan, and G. Pradies, "An in vitro study of factors influencing the performance of digital intraoral impressions operating on active wavefront sampling technology with multiple implants in the edentulous maxilla," *Journal of Prosthodontics*, vol. 26, no. 8, pp. 650–655, 2017.

[35] C. Vögtlin, G. Schulz, K. Jäger, and B. Müller, "Comparing the accuracy of master models based on digital intra-oral scanners with conventional plaster casts," *Physics in Medicine*, vol. 1, pp. 20–26, 2016.

[36] A. Di Fiore, R. Meneghello, L. Graiff et al., "Full arch digital scanning systems performances for implant-supported fixed dental prostheses: a comparative study of 8 intraoral scanners," *Journal of Prosthodontic Research*, vol. 63, no. 4, pp. 396–403, 2019.

[37] M. Bratos, J. M. Bergin, J. E. Rubenstein, and J. A. Sorensen, "Effect of simulated intraoral variables on the accuracy of a photogrammetric imaging technique for complete-arch implant prostheses," *The Journal of Prosthetic Dentistry*, vol. 120, no. 2, pp. 232–241, 2018.

[38] S. Fukazawa, C. Odaira, and H. Kondo, "Investigation of accuracy and reproducibility of abutment position by intraoral scanners," *Journal of Prosthodontic Research*, vol. 61, no. 4, pp. 450–459, 2017.

[39] J.-F. Güth, C. Runkel, F. Beuer, M. Stimmelmayr, D. Edelhoff, and C. Keul, "Accuracy of five intraoral scanners compared to indirect digitalization," *Clinical Oral Investigations*, vol. 21, no. 5, pp. 1445–1455, 2017.

[40] G.-H. Park, K. Son, and K.-B. Lee, "Feasibility of using an intraoral scanner for a complete-arch digital scan," *The Journal of Prosthetic Dentistry*, vol. 121, no. 5, pp. 803–810, 2019.

[41] J. Latham, M. Ludlow, A. Mennito, A. Kelly, Z. Evans, and W. Renne, "Effect of scan pattern on complete-arch scans with 4 digital scanners," *The Journal of Prosthetic Dentistry*, vol. 123, no. 1, pp. 85–95, 2020.

[42] R. N. Rotar, A. Jivanescu, C. Ille et al., "Trueness and precision of two intraoral scanners: a comparative in vitro study," *Scanning*, vol. 2019, 6 pages, 2019.

[43] M. Braian and A. Wennerberg, "Trueness and precision of 5 intraoral scanners for scanning edentulous and dentate complete-arch mandibular casts: a comparative in vitro study," *The Journal of Prosthetic Dentistry*, vol. 122, no. 2, pp. 129–136.e2, 2019.

[44] J.-E. Kim, A. Amelya, Y. Shin, and J.-S. Shim, "Accuracy of intraoral digital impressions using an artificial landmark," *The Journal of Prosthetic Dentistry*, vol. 117, no. 6, pp. 755–761, 2017.

[45] R. J. Kim, G. I. Benic, and J. M. Park, "Trueness of digital intraoral impression in reproducing multiple implant position," *PLoS One*, vol. 14, no. 11, article e0222070, 2019.

[46] B.-h. Kang, K. Son, and K.-b. Lee, "Accuracy of five intraoral scanners and two laboratory scanners for a complete arch: a comparative in vitro study," *Applied Sciences*, vol. 10, p. 74, 2020.

[47] R. J.-Y. Kim, J.-M. Park, and J. Shim, "Accuracy of 9 intraoral scanners for complete-arch image acquisition: a qualitative and quantitative evaluation," *The Journal of Prosthetic Dentistry*, vol. 120, 2018.

[48] R. G. Nedelcu and A. S. Persson, "Scanning accuracy and precision in 4 intraoral scanners: an in vitro comparison based on 3-dimensional analysis," *The Journal of Prosthetic Dentistry*, vol. 112, no. 6, pp. 1461–1471, 2014.

[49] J. G. Michaeli, M. C. DeGroff, and R. C. Roxas, "Error aggregation in the reengineering process from 3D scanning to printing," *Scanning*, vol. 2017, 1218548 pages, 2017.

[50] S. Akyalcin, B. E. Cozad, J. D. English, C. D. Colville, and S. Laman, "Diagnostic accuracy of impression-free digital models," *American Journal of Orthodontics and Dentofacial Orthopedics*, vol. 144, no. 6, pp. 916–922, 2013.

[51] M. Revilla-Leon, S. G. Subramanian, W. Att, and V. R. Krishnamurthy, "Analysis of different illuminance of the room lighting condition on the accuracy (trueness and precision) of an intraoral scanner," *Journal of Prosthodontics*, vol. 30, no. 2, pp. 157–162, 2021.

[52] T. Arakida, M. Kanazawa, M. Iwaki, T. Suzuki, and S. Minakuchi, "Evaluating the influence of ambient light on scanning trueness, precision, and time of intra oral scanner," *Journal of Prosthodontic Research*, vol. 62, no. 3, pp. 324–329, 2018.

[53] H. X. Cai, Q. Jia, H. Y. Shi et al., "Accuracy and precision evaluation of international standard spherical model by digital dental scanners," *Scanning*, vol. 2020, 6 pages, 2020.

[54] J. Song and M. Kim, "Accuracy on scanned images of full arch models with orthodontic brackets by various intraoral scanners in the presence of artificial saliva," *BioMed Research International*, vol. 2020, 2920808 pages, 2020.

[55] W. Renne, M. Ludlow, J. Fryml et al., "Evaluation of the accuracy of 7 digital scanners: an in vitro analysis based on 3-dimensional comparisons," *The Journal of Prosthetic Dentistry*, vol. 118, no. 1, pp. 36–42, 2017.

[56] F. Ferrini, G. Sannino, C. Chiola, P. Capparé, G. Gastaldi, and E. Gherlone, "Influence of intra-oral scanner (I.O.S.) on the marginal accuracy of CAD/CAM single crowns," *International Journal of Environmental Research and Public Health*, vol. 16, no. 4, p. 544, 2019.

Hindawi
Scanning
Volume 2021, Article ID 9976005, 8 pages
https://doi.org/10.1155/2021/9976005

Research Article

Preparation of Room Temperature Vulcanized Silicone Rubber Foam with Excellent Flame Retardancy

Weiqi Luo, Zhimin Li, Haihua Luo, Yuting Liu, Guojiang Xia, Hangtian Zhu, Jiayi Zhou, Ding Yu, Jianxin Zhang, Jianghang Song, Zhengzhou Duan, Yanxin Qiao, Jijun Tang, Yuxin Wang, and Chunfeng Meng

School of Material Science and Engineering, Jiangsu University of Science and Technology, Zhenjiang, Jiangsu 212003, China

Correspondence should be addressed to Chunfeng Meng; mchf@just.edu.cn

Received 4 March 2021; Revised 2 April 2021; Accepted 11 May 2021; Published 21 May 2021

Academic Editor: Guosong Wu

To retard the spread of fire in many cases with sealing materials is significant. A series of silicone rubber foam materials were prepared with room temperature vulcanization and foaming reactions. The morphology, chemical structure, cell structure, and thermal stability were investigated and results proved that the synthesis of silicone rubber was successful in a wide range of feed ratios. The fire-retardant tests were carried out to study the fire-proof property of the composite materials, and the excellent performance showed a promising prospect for wide application in sealing materials.

1. Introduction

Large-scale flames can spread through the holes and gaps around the pipes, and cable trenches, when an accidental fire occurs. The runoff of fire can lead to a devastating outcome. According to the data released by the Emergency Management Department Fire Rescue Bureau of China, a total of 196,000 fire accidents were reported from January to October, in the year 2020, causing 889 deaths, 583 injuries, and direct property losses up to 2.55 billion yuan. The chance of tragedies can be minimized only with particular precaution measures. Herein, to retard the spread of fire in buildings with sealing materials is significant and life-saving.

In the field of fire-retardant materials, industrialization production is busy due to the market demand. A series of polymer-based composite materials, such as styrene butadiene rubber [1–3], natural rubber [4, 5], and so on are often used as fire-proof sealing materials to retard flames [6], especially in nuclear power stations, railway traffic, through-the-wall cable channels, and other fields. Generally, the composite materials are categorized into two types according to the relation between the retardant and the polymer material, which are reaction-type and additive-type [7]. In recent years, silicone rubber foam has been one of the most successful commercialized additive-type fire-proof products [8, 9], due to the comparatively higher thermal stability of silicones than their polymer counterparts, the shielding effect provided by the residue silica ash formed in pyrolysis, excellent aging-resistant performance of polysilicone, outstanding smoke suppression ability, low mass density, nontoxicity, electrical insulating property, and so on [9]. Though silicone rubbers combust lower heat than other polymers, they are still flammable and ignitable. Therefore, inorganic flame retardants, such as $Al(OH)_3$, red phosphorus, Fe_2O_3, and SiO_2, are usually incorporated into silicone rubbers to fabricate fire-proof products [10, 11].

However, the synergetic effect between the polymer matrix and inorganic fire-retardant and the total performance of the composites are sometimes too intricate to evaluate. For example, some inorganic flame retardant additives themselves are controversial enough as the released toxic gas and smoke are extremely harmful despite the outstanding flame-retardant property [12]. Besides, the content of the inorganic filler as a function of fire retardant is limited by the chemical and physical property of the rubber matrix. Therefore, silane-modified polyether can be added to the

Table 1: Composition of raw materials (unit: g).

Sample	Vi-PDMS-Vi	PMVS	SMP	HO-PDMS-OH	Al(OH)3	Silica	Carbon black	Polymerization inhibitor	PMHS	Pt-catalyst
1	15	15	20	70	80	2	0.5	0.9	45	0.5
2	12.5	12.5	25	60	90	3	0.4	0.7	40	0.5
3	10	10	30	50	110	4	0.2	0.5	30	0.5
4	5	5	40	40	120	5	0.2	0.5	45	0.5

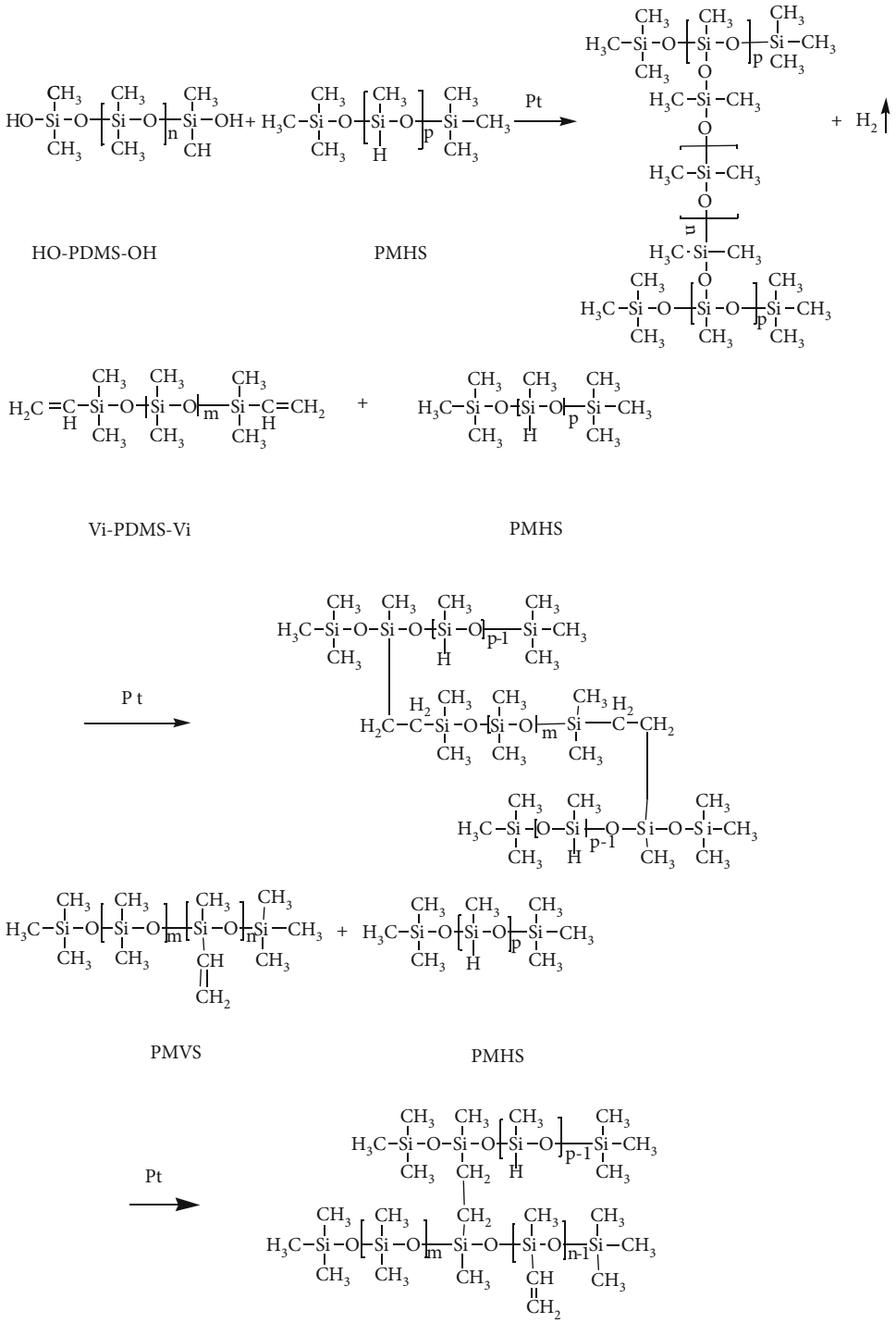

Figure 1: The foaming (up) and vulcanization reactions (middle and down).

rubber matrix, as the low viscosity makes it possible to add more flame retardant additives.

The solidification reaction is difficult to control when non-reactive components are doped in the material. Herein, in this work, we presented the synthesis of fire-retardant room-temperature-vulcanized silicone rubber foam by a facial way, and aluminum hydroxide was incorporated as a flame retardant. The experiments were carried in a wide range of feed ratios, and the flame retardancy, compression stress-strain properties of the silicone rubber foams were systematically studied. These nontoxic, smokeless, and halogen-free silicone rubber foams can be applied as excellent fire-proof sealing materials.

2. Experimental

2.1. Materials. α, ω-dihydroxypolydimethylsiloxane (HO-PDMS-OH, purity ≥98%, viscosity 750 mPa s, Shandong Dayi Chemical Co., Ltd.), divinylpolydimethylsiloxane (Vi-PDMS-Vi, purity ≥99%, viscosity 3500 mPa S, vinyl content wt% 0.43, Shandong Dayi Chemical Co., Ltd.), polymethylvinylsiloxane (PMVS, purity ≥99%, viscosity 3500 mPa s, vinyl content wt% 0.7, Shandong Dayi Chemical Co., Ltd.), polymethylhydrosiloxane (PMHS, purity ≥98%, viscosity 20 mPa s, active hydrogen content wt% ≥1.5, Shandong Dayi Chemical Co., Ltd.), and Silane modified polyether (SMP, viscosity 36000-42000 mPa s, Risun Polymer) were purchased and used directly. Aluminum hydroxide ($Al(OH)_3$, Zhengzhou Beifang Aluminum Co., Ltd.) Silica (Wacker International Group Co., Ltd), platinum catalyst (Shandong Dayi Chemical Co., Ltd), and carbon black (Anyang Tongsheng Carbon Black Co., Ltd.) were used as additives.

2.2. Preparation of Silicone Foam Materials. Vi-PDMS-Vi and PMVS with a weight ratio of 1 : 1 were mixed first, and then, HO-PDMS-OH, SMP, PMHS, catalyst, polymerization inhibitor, and other dopants were added and stirred to form a homogenous mixture, with weight ratios shown in Table 1. The viscous liquids were kept still at room temperature in a proper mold until complete vulcanization was reached, and silicone foam materials were obtained. The vulcanization and foaming reactions are shown in Figure 1.

2.3. Characterization. The apparent densities of the silicone rubber were calculated by Equation (1), referring to ISO 845-2006:

$$\rho = \frac{m}{V} \times 10^6, \tag{1}$$

where m is the mass of the sample in grams, V is the volume of the sample in cubic millimeters. Each sample was cut to a cubic with a size of 100 mm × 100 mm × 100 mm, and the apparent density of each sample was decided by the average value of five specimens. The expansion ratios were calculated by the volume ratios of the silicone rubbers after and before the vulcanization reaction, according to Equation (2)

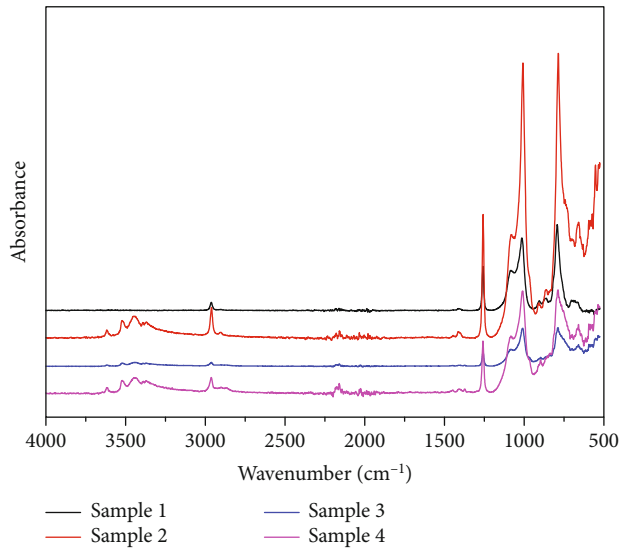

Figure 2: The ATR-FTIR spectra of the composite materials.

$$\frac{V_g - V_i}{V_g} \times 100, \tag{2}$$

where V_g is the geometrical volume of the test specimen, 10 mm × 10 mm × 10 mm, and V_i is the volume of the tested specimen into which water cannot get in or out. To measure V_i, a certain amount of water was put into a graduated cylinder and recorded as V_1. Then, the specimen with a size of 10 mm × 10 mm × 10 mm was put immersed, and the total volume was recorded as V_2, so the $V_i = V_2 - V_1$. The microstructure was studied with a field-emission scanning electron microscopy (ZEISS Merlin Compact).

The cell densities of the samples were tested with the following equation, referring to the literature [13, 14].

$$N_0 = \left[\frac{nM^2}{A}\right]^{\frac{3}{2}} \varphi, \tag{3}$$

where n, M, A, and ϕ represented the pore number in SEM image, the amplification factor, the area of SEM image, and the expansion ratio. The chemical structure of the silicone foams was investigated with ATR-FTIR, with a Nicolet IS 10 equipment in a wavenumber range of 4000-500 cm^{-1}. The thermal stability of silicone foams was studied with a thermogravimetric analysis device (PerkinElmer, Pyris Diamond TG-DTA), from room temperature to 900°C, at a ramp rate of 10°C min^{-1}, in the air. The stress-strain curves were measured with a universal testing machine (WAW/WEW-1000D, Jinanshidai Testing Machine Co., Ltd.) and recorded according to GB/T 8168-2008. The size of the specimen was 100 mm × 100 mm × 25 mm, and three specimens were tested for each sample with a preload of 2 N. The load of

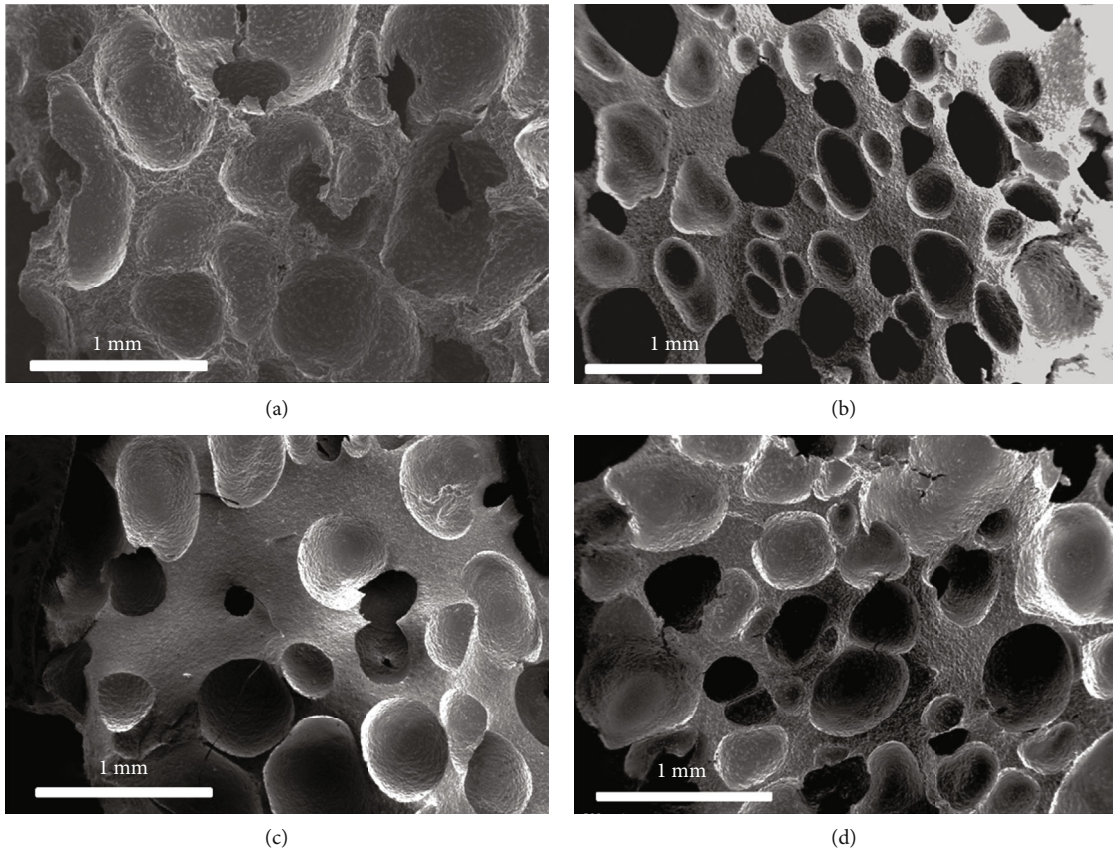

Figure 3: The SEM pictures of the composite materials. (a–d) Corresponding to Sample 1-4.

the compressing plate to the specimen was gradually increased along the thickness direction at a rate of 12 mm min^{-1} until the specimen was completely broken. The compressive strain was calculated by Equation (4)

$$\varepsilon_\alpha = \frac{T - T_i}{T}, \tag{4}$$

where ε_α is the compression deformation (%), T is the original height before compression, and T_i is the height after compression. And the compressive stress was calculated following the formula

$$\sigma = \frac{P}{A} \times 10^{-6}, \tag{5}$$

where σ is the press stress (Pa), P is the loaded force (N), and A is the base area of the specimen (mm^{-2}). The fire-retardancy property of the composites was studied with the vertical burning tests according to the UL-94 method [15, 16], and the materials are classified as V0, V1, or V2. The specimens with a size of 125 mm × 13 mm × 1.6 mm were ignited with methane. 10 seconds later, the methane was removed and the first afterflame time for the specimen was recorded as t_1. Once the first afterflame is extinguished, the specimen was ignited again for another 10 seconds, and the second afterflame time (t_2) and afterglow time (t_3) were noted. A piece of cotton was placed under the specimen, and if the cotton was ignited by the burning drops, the results should be recorded.

3. Results and Discussion

3.1. Preparation of the Composite Materials. Samples were synthesized with vulcanization and foaming reactions at room temperature. As shown in Figure 1, vulcanization reactions between Vi-PDMS-Vi, PMVS, and PMHS cross-linked to form the skeleton of the composite material, and the reaction between HO-PDMS-OH and PMHS caused the foaming structure. After 72 hours, all the samples were solidified.

ATR-FTIR was carried out to study the chemical structures of the samples, and the results were shown in Figure 2. The peak at 3620 cm^{-1} was the signal of Si-OH bond of residual HO-PDMS-OH, and the multiple peaks near 3500 cm^{-1} were the signals of Si-OH bonds. In all four samples, Si-CH = CH_2 bond around 1620 cm^{-1} was not detected, signifying the reactions were completed. The weak peak at 2150 cm^{-1} was the characteristic signal of Si-H, declaring the complete consumption of PMHS. The degree of vulcanization reaction affected the curing parameters of the rubber foam and the mechanical strength of the matrix. The strong peak at 1250 cm^{-1} was caused by the Si- CH_3, and the Si-O-C peaks appeared in the range of 1000 to 1080 cm^{-1}

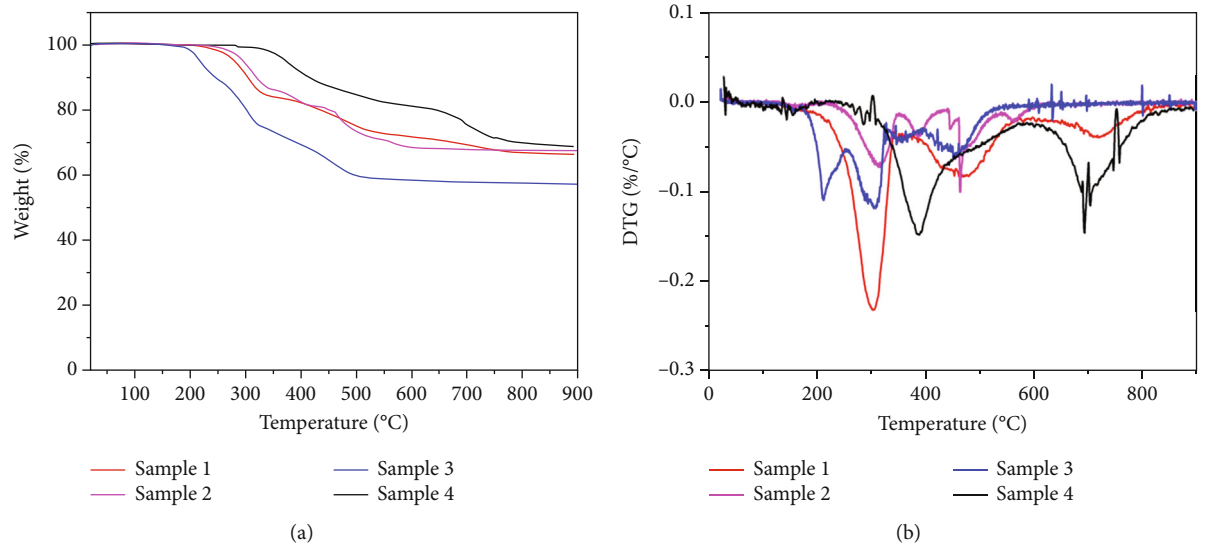

Figure 4: The thermogravimetry of the composite materials.

[17]. The ATR-FTIR results proved the samples were successfully synthesized.

The morphology of the prepared composite materials was recorded with SEM, as shown in Figure 3. The cell diameters of the four composite materials, formed in the foaming process, were close and in a range of 0.1-0.8 mm. The contained additives were dispersed uniformly in the silicone rubber and caused the roughness of the cell wall. The cell structure ensured the silicone rubber high expansion ratios after vulcanization, as well as good stress-strain capacity, which was good for effective sealing.

3.2. Thermal Stability of the Composite Materials. The thermal stability of fire-proof sealing materials is essential, and thermogravimetry was applied to investigate the four samples, as shown in Figures 4(a) and (b). All samples experienced multistep decomposition reactions. The decomposition process of Sample 1 started from 280°C, where the residual weight percent of Sample 1 was 95%. The thermal stability of Sample 2 was close to Sample 1. The thermal stability of sample 3 was relatively poorer than the other three analogs, as the decomposition process started from 200°C. The first degradation reaction of Sample 4 with a higher amount of $Al(OH)_3$ started from 380°C, which was 100°C higher than Sample 1. It can be found from the related TGA data (Figure 4(b)) that the peak temperatures of the first pyrolysis were 303 and 388°C for Sample 1 and Sample 4, respectively. The addition of $Al(OH)_3$ increased the thermal stability of the silicone rubber, which was helpful for fire-retardant materials. After decomposition, only SiO_2 and Al_2O_3 remained, and the left weight percentages of Sample 1-4 were 66%, 67%, 57%, and 69%, respectively. The left non-flammable SiO_2 and Al_2O_3 can act as shielding to stop the fire from spreading, which was the advantage of silicone rubber-based fire-retardant composite materials. The residue increment of Sample 2-4 comparing to Sample 1 was caused by the added amount of inorganic component $Al(OH)_3$.

Table 2: Properties of the prepared composite materials.

Sample	1	2	3	4
Apparent density ($g\,cm^{-3}$)	0.473	0.456	0.483	0.465
Expansion ratio	2.73	2.76	2.79	2.77
Porosity (%)	56.34	57.62	56.73	55.78

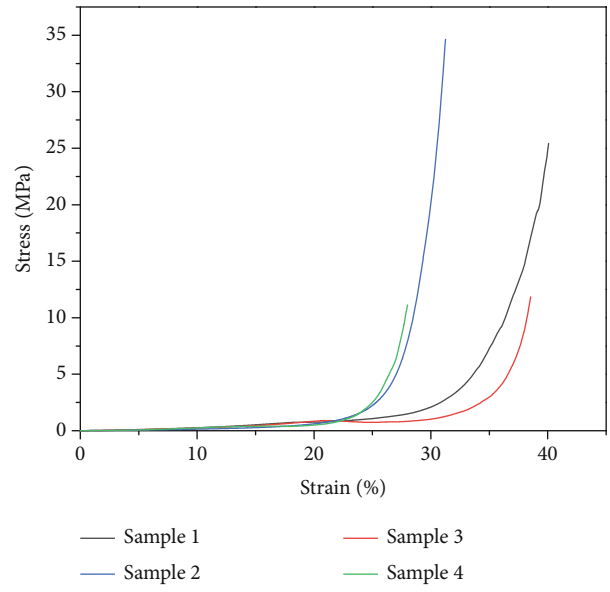

Figure 5: Stress-strain curves of the composite materials.

3.3. Mechanical Properties of the Composite Materials. The mechanical properties of the composite materials are crucial to the application of fire-retardant materials, and the apparent densities, expansion ratios, and porosities of the composite materials are shown in Table 2. The values of apparent

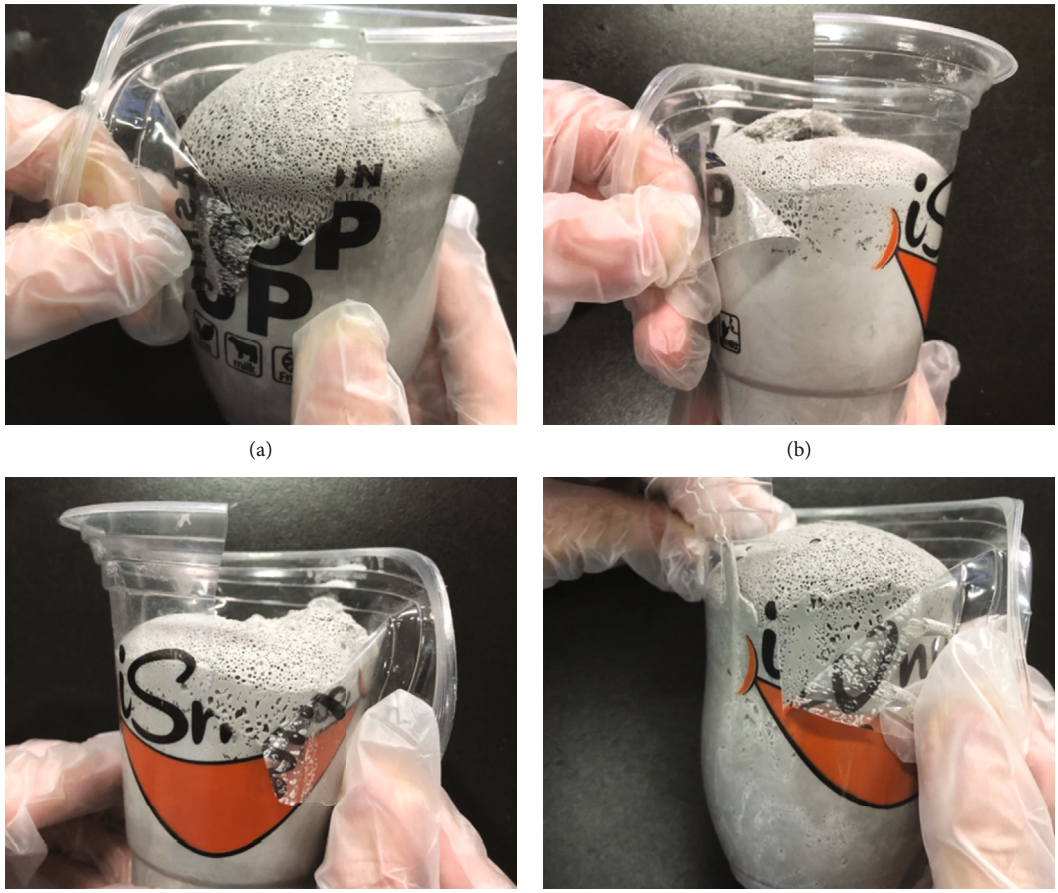

(a) (b) (c) (d)

Figure 6: Optical images of the composite materials.

densities ranged from 0.456 to 0.483 g cm^{-3}, and the discrepancy was inconspicuous. The measured expansion ratios were between 2.73 and 2.79, endowing the composites as sealing materials for the holes and cracks. The calculated cell densities of the four samples were 1.7×10^9, 2.9×10^9, 1.2×10^9, and 1.9×10^9 pores per cm^3. The size of pores was not evenly distributed. These data indicated that the silicone rubber foam can be successfully synthesized within a wide range of feed ratios.

The stress-strain curves of the composite materials were recorded with a universal testing machine, as presented in Figure 5. The results were consistent with the mode of conventional foams proposed by Gibson and Ashby [18, 19]. As the strain increased from zero to a certain value, the stress-strain relationships were approximately linear, and the rising trends of stress were gradual and smooth. The flat trends can be caused by the bending of cell walls or the minimum collapse of foam structure, corresponding to the compressive elastic region. Then, the stress increased sharply with the strain, due to the massive collapse of the cell structure. For Sample 1-4, the starting strains where the foam structure began to collapse were 28%, 23%, 32%, and 22%, respectively. The four samples displayed good endurance to the stress, which is useful since the foaming materials should resist the consequential mechanical stress of the heat runaway and blasts of airflow.

When the foaming composites are used as fireproof sealing materials, their adhesive performance to the surface of other materials is also essential, especially for the plastic materials. However, the surface energy of routine silicone rubber is low, so generally, the adhesion of routine silicone rubber is poor. In practical application, the sealing materials should adhere to the walls and gaps of plastic or metal pipes as long as possible. The adhesive performance of the samples to the surface of the commercial plastic cups is shown in Figure 6. After pealling off, the attachment remained on the inner walls of plastic walls, declaring the stickness of the composites to the plastic materials. Therefore, the samples are applicable for fireproof sealing materials.

3.4. Fire-Retardant Properties of the Composite Materials. The UL-94 tests of the composite materials are listed in Table 3. Firstly, the afterflame time (t_1 or t_2) for each individual specimen was less than 10 seconds. Secondly, the total afterflame time ($t_1 + t_2$) for any condition set for each specimen was less than 50 s. Thirdly, the afterflame plus afterglow time for each specimen after the second flame application was less than 30 s. Meanwhile, afterflame or afterglow of

Table 3: Flame retardant test results.

	Specimen	t_1	t_2	t_3	$t_1 + t_2$	$t_2 + t_3$	Afterflame or afterglow to the holding clamp	Cotton ignited by burning drops	UL-94 rate
Sample 1	1	5	4	15	9	19	No	No	V0
	2	5	5	14	10	19	No	No	
	3	6	4	15	10	19	No	No	
	4	5	3	14	8	17	No	No	
	5	6	5	14	11	19	No	No	
Sample 2	1	4	5	14	9	19	No	No	V0
	2	5	5	14	10	19	No	No	
	3	5	4	13	9	17	No	No	
	4	4	4	13	8	17	No	No	
	5	5	4	13	9	17	No	No	
Sample 3	1	4	4	13	8	17	No	No	V0
	2	5	4	13	9	17	No	No	
	3	4	4	12	8	16	No	No	
	4	4	4	13	8	17	No	No	
	5	4	5	11	9	16	No	No	
Sample 4	1	3	3	12	6	15	No	No	V0
	2	3	4	12	7	16	No	No	
	3	4	4	11	8	15	No	No	
	4	4	3	12	7	15	No	No	
	5	3	4	11	7	15	No	No	

any specimen up to the holding clamp was not observed, nor the cotton indicator was ignited by flaming particles or drops. Therefore, all samples were rating in V0 [15, 16, 20]. The excellent fire-retardant properties were endowed by the synergetic effect of silicone rubber and the fire-retardant additives and ensured the composite materials practical application foreground in fireproof sealing.

4. Conclusion

In this work, a series of silicone rubber foam was prepared through room temperature vulcanization and foaming. The characterization results proved that the composite materials had been successfully synthesized in a wide range of feed ratios, and the cell structures and other mechanical properties were suitable for fire-retarding application. The composite materials exhibited excellent thermal stability. Fire-retardant tests proved the outstanding fireproof property for all four samples. In summary, the composite materials displayed good overall performance as fire-retardant materials.

Data Availability

All data and models generated or used during the study appear in the submitted article.

Conflicts of Interest

The authors declare that they have no conflicts of interest.

References

[1] M. Imiela, R. Anyszka, D. M. Bieliński, M. Lipińska, P. Rybiński, and B. Syrek, "Synergistic effect of mica, glass frit, and melamine cyanurate for improving fire resistance of styrene-butadiene rubber composites destined for ceramizable coatings," *Coatings*, vol. 9, no. 3, p. 170, 2019.

[2] N. F. Attia and B. K. Saleh, "Novel synthesis of renewable and green flame-retardant, antibacterial and reinforcement material for styrene–butadiene rubber nanocomposites," *Journal of Thermal Analysis and Calorimetry*, vol. 139, no. 3, pp. 1817–1827, 2020.

[3] A. Abdel-Hakim, T. M. El-Basheer, and A. Abdelkhalik, "Mechanical, acoustical and flammability properties of SBR and SBR-PU foam layered structure," *Polymer Testing*, vol. 88, p. 106536, 2020.

[4] P. Intharapat, C. Nakason, and A. Kongnoo, "Preparation of boric acid supported natural rubber as a reactive flame retardant and its properties," *Polymer Degradation and Stability*, vol. 128, pp. 217–227, 2016.

[5] N. Wang, G. Xu, Y. Wu et al., "The influence of expandable graphite on double-layered microcapsules in intumescent flame-retardant natural rubber composites," *Journal of Thermal Analysis and Calorimetry*, vol. 123, no. 2, pp. 1239–1251, 2016.

[6] Z. E. Sun and Y. Zhou, "Discussion on fire-proof sealing technology and product," *Procedia Engineering*, vol. 135, pp. 644–648, 2016.

[7] G. Camino, L. Costa, and M. P. L. di Cortemiglia, "Overview of fire retardant mechanisms," *Polymer Degradation and Stability*, vol. 33, no. 2, pp. 131–154, 1991.

[8] C. Zhu, C. Deng, J. Y. Cao, and Y. Z. Wang, "An efficient flame retardant for silicone rubber: preparation and application," *Polymer Degradation and Stability*, vol. 121, pp. 42–50, 2015.

[9] F. Lou, W. Yan, W. Guo, T. Wei, and Q. Li, "Preparation and properties of ceramifiable flame-retarded silicone rubber composites," *Journal of Thermal Analysis and Calorimetry*, vol. 130, no. 2, pp. 813–821, 2017.

[10] A. U. R. Shah, M. N. Prabhakar, and J.-I. Song, "Current advances in the fire retardancy of natural fiber and bio-based composites – a review," *International Journal of Precision Engineering and Manufacturing-Green Technology*, vol. 4, no. 2, pp. 247–262, 2017.

[11] E. Gallo, B. Schartel, U. Braun, P. Russo, and D. Acierno, "Fire retardant synergisms between nanometric Fe2O3 and aluminum phosphinate in poly(butylene terephthalate)," *Polymers for Advanced Technologies*, vol. 22, no. 12, pp. 2382–2391, 2011.

[12] Y. Shi, B. Yu, Y. Zheng et al., "A combination of POSS and polyphosphazene for reducing fire hazards of epoxy resin," *Polymers for Advanced Technologies*, vol. 29, no. 4, pp. 1242–1254, 2018.

[13] D. Yin, J. Mi, H. Zhou, X. Wang, and H. Tian, "Fabrication of branching poly (butylene succinate)/cellulose nanocrystal foams with exceptional thermal insulation," *Carbohydrate Polymers*, vol. 247, p. 116708, 2020.

[14] Y. Li, D. Yin, W. Liu, H. Zhou, Y. Zhang, and X. Wang, "Fabrication of biodegradable poly (lactic acid)/carbon nanotube nanocomposite foams: significant improvement on rheological property and foamability," *International Journal of Biological Macromolecules*, vol. 163, pp. 1175–1186, 2020.

[15] M. A. de Freitas Rocha, A. Landesmann, S. P. da Silva Ribeiro, and R. C. Martins, "Enhancement of fire retardancy properties of glass fibre–reinforced polyesters composites," *Fire and Materials*, vol. 43, no. 6, pp. 734–746, 2019.

[16] *UL 94–Standard for Tests for Flammability of Plastic Materials for Parts in Devices and Appliances*, Underwriter Laboratories, 2013.

[17] Y. Tan, J. Yao, and H. Zhu, "Preparation of room temperature vulcanized silicone rubber foam/SiO2 nanocomposite and its fatigue buffering performance," *Journal of Macromolecular Science, Part A Pure and Applied Chemistry*, vol. 57, no. 12, pp. 844–853, 2020.

[18] B. Xiang, Y. Jia, Y. Lei et al., "Mechanical properties of microcellular and nanocellular silicone rubber foams obtained by supercritical carbon dioxide," *Polymer Journal*, vol. 51, no. 6, pp. 559–568, 2019.

[19] L. J. Gibson and M. F. Ashby, *Cellular Solids: Structure and Properties*, Cambridge University Press, Cambridge, UK, 1997.

[20] W. Chen, C. Xu, Y. Liu, Y. Liu, and Q. Wang, "Synthesis and properties of an intrinsic flame retardant silicone rubber containing phosphaphenanthrene structure," *RSC Advances*, vol. 7, no. 63, pp. 39786–39795, 2017.

Hindawi
Scanning
Volume 2021, Article ID 5574946, 11 pages
https://doi.org/10.1155/2021/5574946

Research Article

Corrosion Evaluation of Pure Mg Coated by Fluorination in 0.1 M Fluoride Electrolyte

Chun Yu Dai,[1] **Xinzhe Gao**,[1] **ChuanYao Zhai**,[1] **Qi Jia**,[1] **Bing Cheng Zhao**,[1] **HaoYu Shi**,[1] **Qingting Gao**,[2] **HongXin Cai**,[1] **Eui-Seok Lee**,[3] **and Heng Bo Jiang**[1]

[1]*The Conversationalist Club, School of Stomatology, Shandong First Medical University & Shandong Academy of Medical Sciences, Tai'an, Shandong 271016, China*
[2]*Department of Stomatology, The First Affiliated Hospital of Nanchang University, Nanchang, 330006 Jiangxi, China*
[3]*Department of Oral and Maxillofacial Surgery, Graduate School of Clinical Dentistry, Korea University, Seoul 02841, Republic of Korea*

Correspondence should be addressed to Eui-Seok Lee; ees225@hanmail.net and Heng Bo Jiang; hengbojiang@vip.qq.com

Received 26 January 2021; Revised 16 March 2021; Accepted 30 April 2021; Published 15 May 2021

Academic Editor: Guosong Wu

In the ongoing research on the application of biodegradable materials, surface treatment of is considered to be a relatively effective solution to the excessive degradation rates of Mg alloys. In this study, to further optimize the proven effective surface coatings of fluoride, a low-voltage preparation fluorination method was used to achieve coating effectiveness under safer conditions. Optical observation, scanning electron microscopy (SEM), X-ray diffraction (XRD), energy-dispersive spectroscopy (EDS), and potential dynamic polarization (PDP) experiments were used for the analysis and evaluation. The coating characteristics of the MgF_2 coatings treated in the 10–90 V voltage range, including the structure, chemical conformation, and electrochemical corrosion assessment, were fully defined. The anodic fluoridation results showed that a pore structure of 1–14 μm thickness was formed on the Mg alloy substrate, and the coating was composed of Mg fluoride. The results of immersion corrosion and electrochemical corrosion experiments showed that compared with pure Mg, anodic fluorinated samples below 40 V exhibited better corrosion resistance, the prepared MgF_2 coating was more uniform, and the surface mostly exhibited point corrosion. When the voltage reached or exceeded 60 V, the prepared coating exhibited poor corrosion resistance, fracture, and protrusions. After corrosion, it mostly exhibited surface corrosion. The results indicate that idealized coatings can be obtained at relatively low and safe voltage ranges. This finding may enable more economical, environmentally friendly, and safe preparation of coatings.

1. Introduction

Mg alloys have been continuously studied in the field of biodegradable materials, because Mg and Mg alloys are the most clinically useful restorative materials owing to their excellent dimensional stability and mechanical properties [1], as well as their reduced potential for stress shielding [2]. Previous studies have discussed both permanent and nonpermanent material designs. In this regard, potential complications and risks of reoperation can be avoided if nonpermanent materials, that is, biodegradable materials, are used [3, 4]. Thus, Mg has been applied in various fields, including biochemistry and materials science [5]. In addition, Mg functions as a cofactor of adenosine triphosphate, induces osteogenesis, and synergizes biocircadian expression, demonstrating its potential as an implant material [6, 7].

However, pure Mg has a limitation for its clinical application and research, which is the fast decomposition rate in humoral situations and the inappropriate corrosion processes that can produce some adverse effects [4, 8–10]. Thus, methods to modulate the dissolution rate of early Mg alloy anodes are required. Therefore, the main objective of our study was to reduce the degradation rate of Mg alloys in a simulated body fluid environment.

Typically, methods to coordinate the alloy corroding behavior include electroplating and surface passivation [11–13]. In addition, ceramic coatings are also effective [14, 15]. By analyzing existing studies, we chose to further optimize

the feasibility of the existing fluorination coating treatment [16]. In this treatment, the corrosion conditions and corrosion rates are regulated by insulating the metal from external influences through insoluble corrosion-resistant substances. The metal oxide film formed also has electronic properties such as semiconduction and insulation [17].

Anodization allows the thickness and structure of the prepared coating to be controlled by varying the voltage. However, the prepared Mg oxide coatings can be affected by surface fracture and corrosion resistance [18, 19]. Micro-arc fluorination (MAF) is a combination of anodic oxidation and fluorination, using high voltage to form a layer of MgF_2 coating on the sample surface in a fluorinated environment [19–23]. However, the preparation process generates large quantities of hydrogen fluoride gas, which is harmful to humans and causes environmental pollution. Conventional MAF methods generally use voltages above 100 V and high concentrations of hydrofluoric acid [24]. Therefore, this experiment attempted to use a solution with a low fluoride ion concentration as the electrolyte and conduct anodic fluorination (AF) in a lower voltage range. Low-pressure coatings are more environmentally friendly and economical than high-pressure coatings. This reduces the release of irritating fumes, pollution and environmental damage, and harm to humans. The AF process requires a short time. Uniformly dense films can be prepared during this process, and pores are formed. The density of the films is similar to that of bone tissue and has been proven to be highly biocompatible [18, 21–23]. Moreover, the thicknesses of the MgF_2 coatings prepared under different voltages are different, which is more conducive to cell attachment and subsequent preparation [25, 26]. MgF_2 has strong corrosion resistance in vitro and can maintain good clinical effects after implantation in the human body [18, 25, 27–29].

In this experiment, the AF technique was used to prepare MgF_2 ceramic coatings on Mg surfaces. In the fluoride electrolyte (0.1 mol/L NH_4HF_2), the coating preparation experiment was performed in the voltage range of 10–90 V. Scanning electron microscopy (SEM) was used to measure the surface morphology of the coating, and potential dynamic polarization (PDP) was used to measure the electrochemical corrosion. The fluorine content of the sample surface under different voltages was analyzed, and the corrosion resistance of the prepared sample in Hank's balanced salt solution (HBSS) was analyzed and evaluated.

2. Materials and Methods

2.1. Sample Preparation. Pure Mg (Dongguan FeiTai Metal Products Co., Ltd., China) was cut into pieces with dimensions of $20 \times 20 \times 3$ mm. The samples were polished with grade 1200 SiC paper in absolute ethyl alcohol. Then, they were rinsed with absolute ethyl alcohol and blow-dried.

2.2. Surface Modification. The samples were divided into eight groups and then separately placed in 10, 20, 30, 40, 50, 60, 70, 80, and 90 V electrolytic cells for 3 min as the anode, and a graphite rod was chosen as the cathode. A magnetic bar was chosen to stir the electrolytic solution, which was a solution of 0.1 mol/L NH_4HF_2. The progress of the AF is shown in Figure 1. The samples were then washed with distilled water and dried. The conditions of the surface treatment are listed in Table 1.

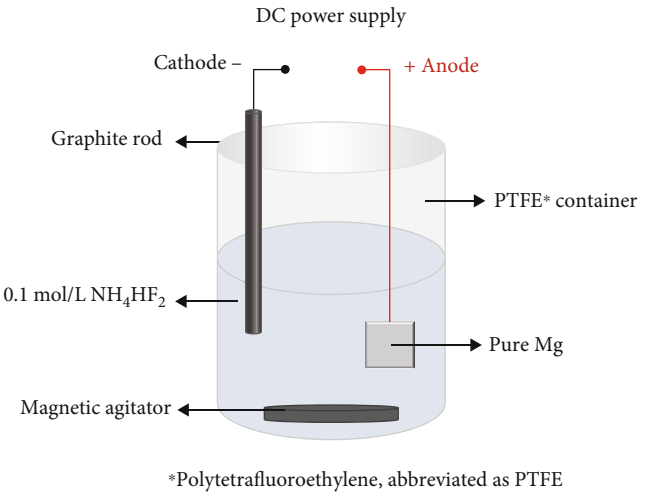

Figure 1: Diagram of AF of pure Mg.

Table 1: Sample codes and surface treatment conditions.

Sample code	Treatment conditions	Treatment time (min)
Pure Mg	/	/
AF10	Anodizing by DC* power supply in 10 V	3
AF20	Anodizing by DC power supply in 20 V	3
AF30	Anodizing by DC power supply in 30 V	3
AF40	Anodizing by DC power supply in 40 V	3
AF50	Anodizing by DC power supply in 50 V	3
AF60	Anodizing by DC power supply in 60 V	3
AF70	Anodizing by DC power supply in 70 V	3
AF80	Anodizing by DC power supply in 80 V	3
AF90	Anodizing by DC power supply in 90 V	3

*DC: direct current.

2.3. Surface Characterization. The surface morphologies of the samples and cross-sectional images were observed using a scanning electron microscope (JSM-67000). The elementary compositions were then determined by energy-dispersive spectroscopy (EDS). X-ray diffraction (XRD) measurements of the Mg phase on the surface of the MgF_2 sample were also performed at a scan rate of 1°/min at 40 kV and 30 mA.

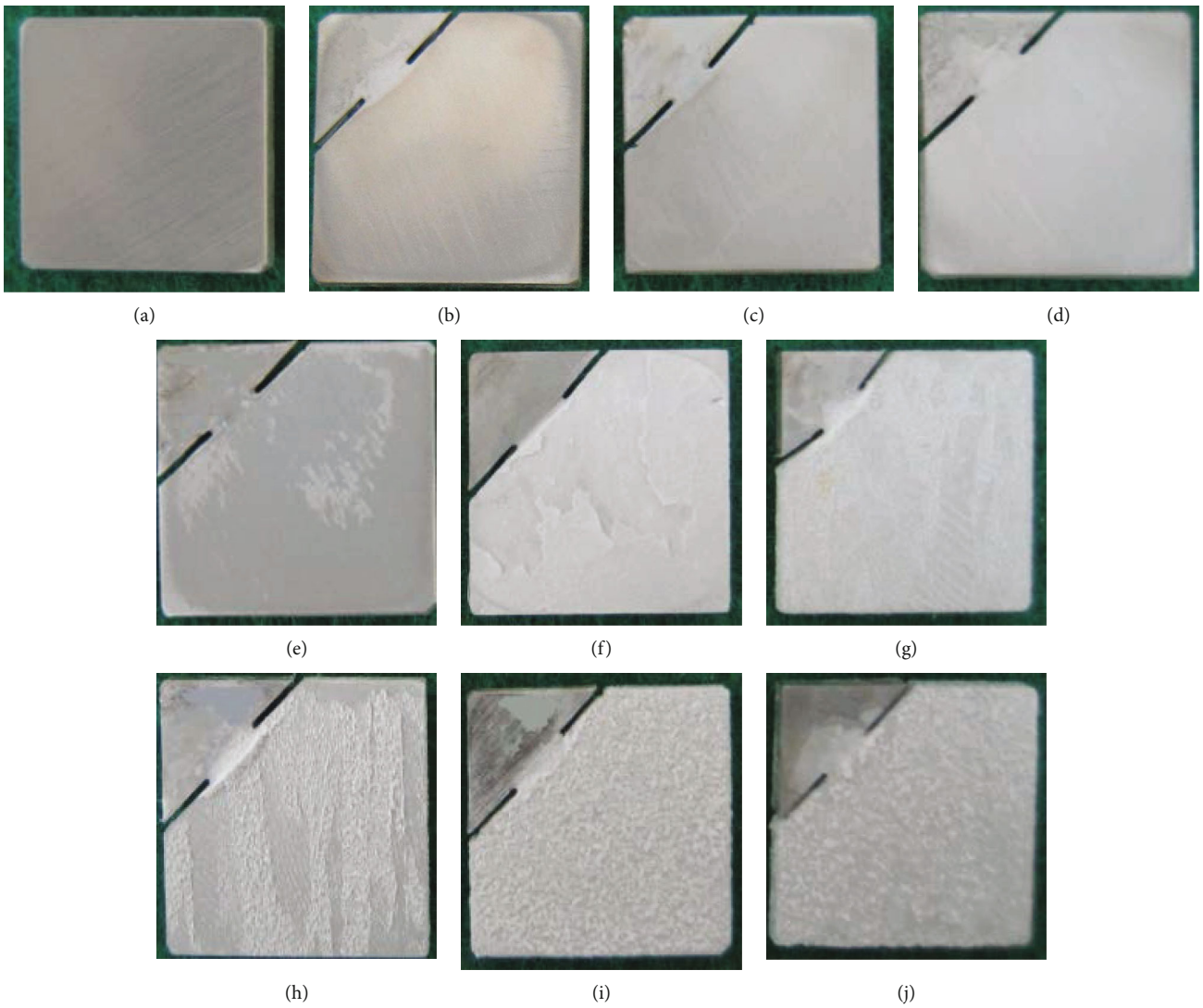

Figure 2: Optical observations of coated samples of (a) pure Mg, (b) AF10, (c) AF20, (d) AF30, (e) AF40, (f) AF50, (g) AF60, (h) AF70, (i) AF80, and (j) AF90.

2.4. Corrosion Resistance Test. In the immersion corrosion experiment, all processed samples were vertically immersed in the HBSS and kept at 37°C for seven days. For the sample surface area, the volume ratio of HBSS was 20 mL/cm^2, as per the ASTM standard G31. After seven days, the samples were rinsed with absolute ethanol and blow-dried, and electronic pictures were taken.

2.5. Electrochemical Corrosion Test. The exposed fluorinated Mg alloy surface was set to 1 cm^2. Electrochemical corrosion tests were performed using the PDP method with a constant potentiostat (VersaSTAT 3 : 300) and analyzed using a commercial software (VersaStudio 2.44.4). The classic three-electrode battery consisted of a working electrode for the test sample, a pure platinum rod electrode, and Ag/AgCl/Sat-KCL as the reference electrode (+197 mV compared with a standard hydrogen electrode). HBSS (1000 mL, WELGENE Inc., Korea) was used as an electrolyte and placed in a double-walled beaker, with the temperature maintained at 37 ± 1°C at all times. The scanning rate of the PDP measurements was 3 mV/s.

3. Results and Discussion

The surface condition of pure Mg coated by AF can be visually observed in Figure 2. The coating was more uniform before AF50, as shown in Figures 2(b)–2(f). However, there was a large area of coating shedding off the surface at AF50, and different degrees of coating flaring can be found at the shedding junction. The surface topography also became rougher with increasing voltage in the subsequent coating.

Figure 3 shows the varied microscopic surface morphologies of the samples treated at different voltages under SEM. The AF coating started to form at 10 V, and the coating exhibited a dot-like morphology. The AF20 coating appeared more uniformly covered, but the thickness of the coating was

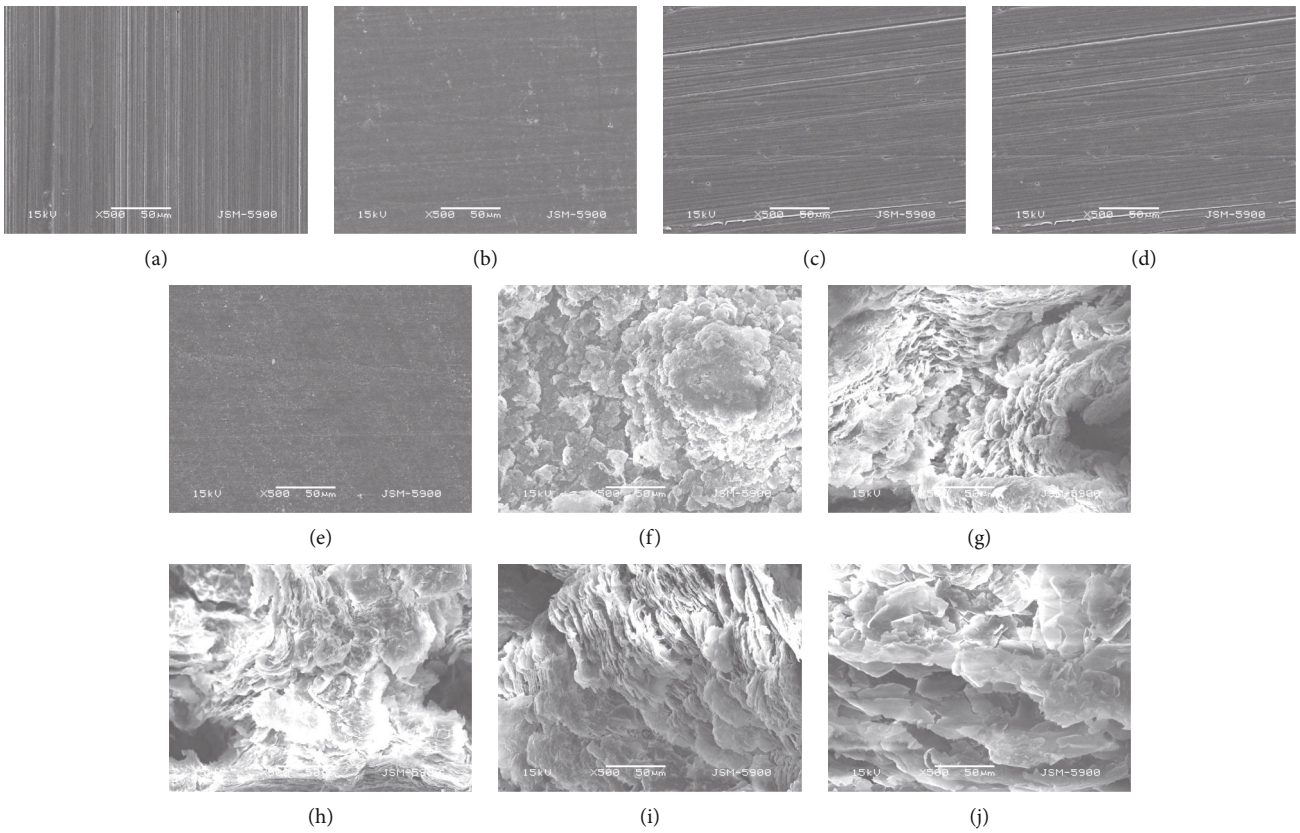

Figure 3: FE-SEM surface morphology of (a) pure Mg, (b) AF10, (c) AF20, (d) AF30, (e) AF40, (f) AF50, (g) AF60, (h) AF70, (i) AF80, and (j) AF90.

not large. The coatings of AF30 and AF40 gradually exhibited a homogeneous matte-like appearance. The coating of AF50 was more differentiated compared to those of AF40 and the previous treatment group. As shown in Figure 3(f), AF50 formed a coating with an inhomogeneous, nondense, and coral-like surface appearance. As the voltage increased, the coral-like shape became coarser and shale-like. The effect of voltage on surface morphology was evident. The surface microstructure was conducive to tissue attachment [30, 31]. The surface morphology of the fluorinated coating prepared in this experiment was slightly similar to that of the microarc oxidation coating, and we speculate that the microgaps and micropores produced on the surface were due to the plasma discharge and the involvement of a small amount of electrolyte particles in the electrolysis [19].

Figure 4 shows the fluoride coating produced on the surface of pure Mg analyzed by EDS. The results show that the F and Mg peaks appeared under different voltages. The main component of the surface coating on the AF sample was MgF_2. The percentage of elemental fluorine in the coating varied with voltage from pure Mg to 60 V treated samples. The increment in the elemental fluorine content peaked at the 60 V treatment condition, with a 48.28% increase compared to that of the AF10 voltage. The fluorine contents on the surfaces of AF70, AF80, and AF90 were 52.54%, 51.66%, and 53.12%, respectively.

Figure 5 shows the SEM cross-sectional morphology of the anodic fluorinated Mg, from which it can be seen that the thickness of the coatings thickened with increasing voltage [17]. The good adhesion of the coating to the Mg substrate without any separation boundary was due to the chemical transformation of the AF coating to the Mg substrate [19].

Figure 6 shows the relationships among the coating thickness, mass, atomic ratio, and voltages obtained from the EDS analysis plotted as a graph. The horizontal axis, left vertical axis, and right vertical axis are the voltage, coating thickness, and fluorine mass to atom ratio, respectively. From the figure, it can be clearly seen that the mass and atomic proportion curves show high consistency as the voltage increases. In the voltage range of 30–50 V, the mass and atomic proportion curves increased at the fastest speed and reached a maximum after 60 V. Because the coating thickness curve rapidly increased after 50 V, EDS X-rays were unable to penetrate the coating and scan for pure Mg, resulting in no significant increase in the mass curve of fluorine and atomic proportion curve. We speculate that the sudden decrease in the AF90 coating thickness may be due to the coating shedding that occurred during the coating preparation process. This also indicates that several microgaps and micropores formed inside the coating at 90 V, which caused the coating structure to be slightly loose and easy to peel off [19].

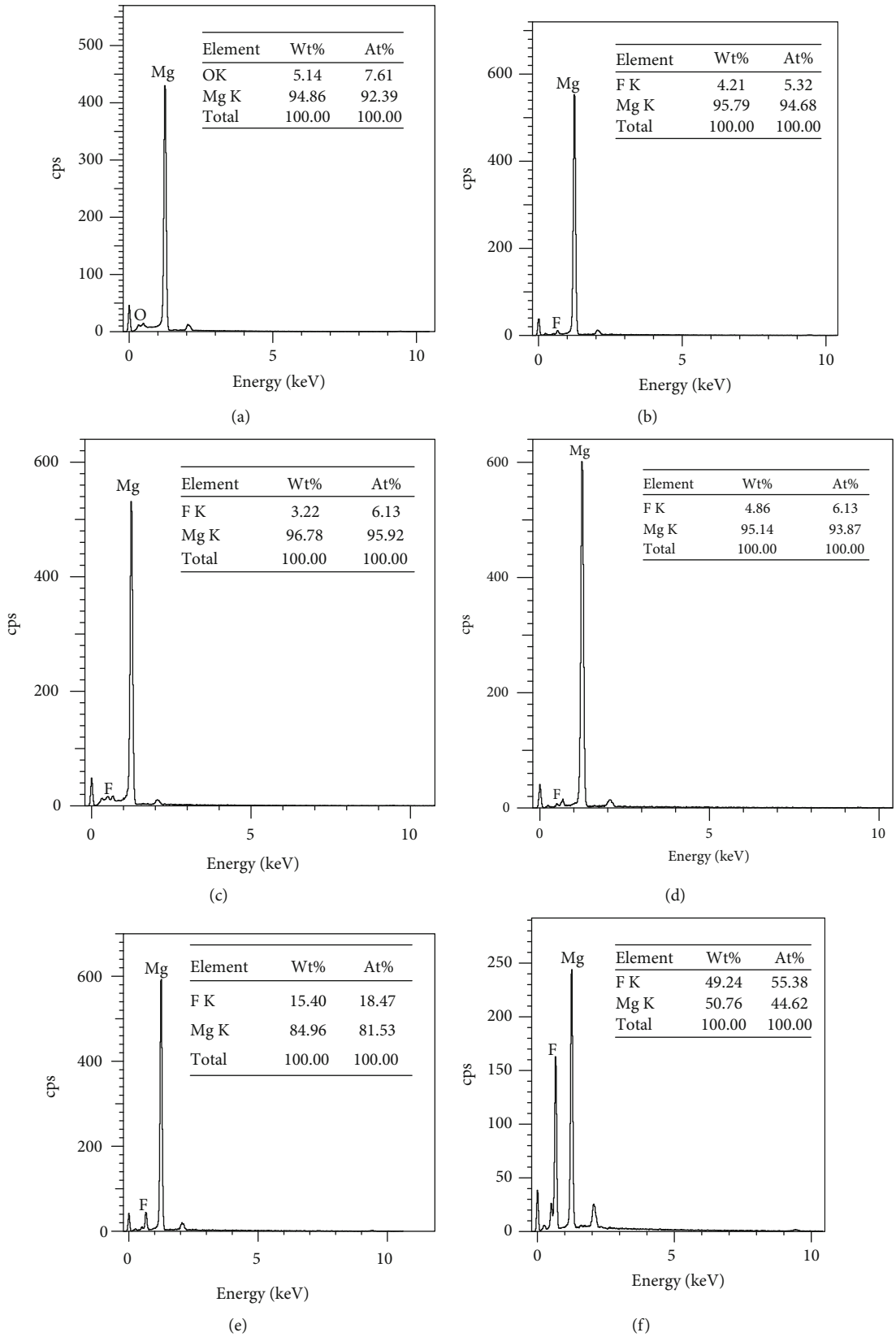

Figure 4: Continued.

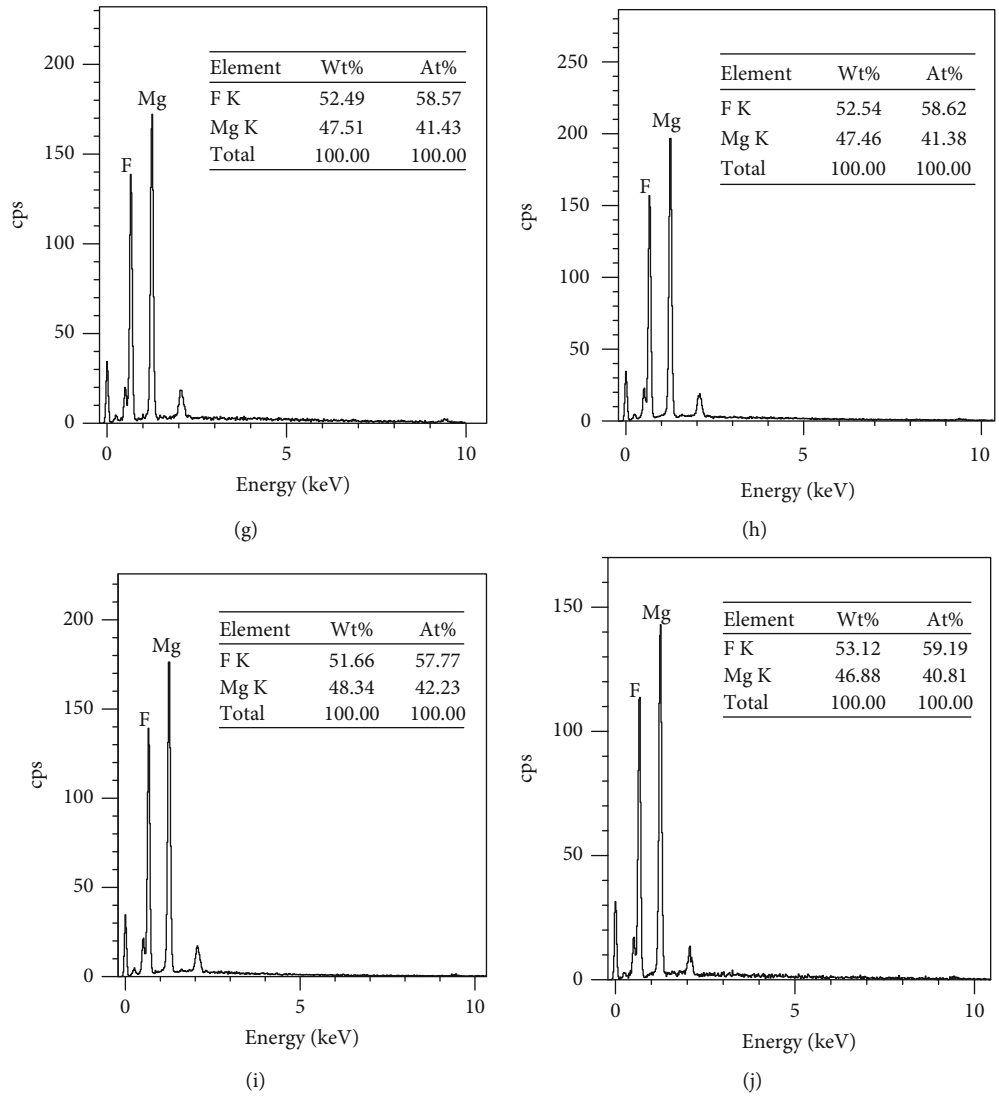

Figure 4: EDS analyses of (a) pure Mg, (b) AF10, (c) AF20, (d) AF30, (e) AF40, (f) AF50, (g) AF60, (h) AF70, (i) AF80, and (j) AF90.

Figure 7 shows the XRD patterns of the pure Mg and MgF_2 samples. Simultaneously, the crystal structure of the sample surface was analyzed. Compared to the untreated pure Mg, the diffraction pattern of Mg fluoride clearly showed the presence of MgF_2. As seen in the figure, AF10, AF20, AF30, and AF40 were basically the same in terms of the number of diffraction peaks, angular position, and shape of the diffraction peaks, whereas there were differences in the diffraction patterns of AF50, AF60, AF70, AF80, and AF90. This may be attributed to the change in coating thickness. However, there was only one crystalline phase from AF10 to AF90, which may be because the other crystalline phases were too small or amorphous, as reflected by the XRD analysis [32]. XRD requires a certain thickness of material to be measured to obtain a clear diffraction peak of the sample in the diffraction pattern.

To comprehensively and accurately evaluate the corrosion resistance of specimens, it is essential to conduct an electrochemical test on the fluoride-treated object and the control group (pure Mg) [11]. Figure 8 shows the Tafel curves of the samples. The polarization test is an electrochemical method that reflects the corrosion resistance properties by the metal corrosion potential (E_{corr}) and corrosion current density (I_d). More corrosion-resistant states occur at lower current densities and at relatively high corrosion voltages [2].

As shown in Figure 8, the pure samples exhibited normal corrosion conditions. Therefore, considering the pure Mg characteristics as the evaluation criterion (I_d pure Mg 2.25 $\times 10^{-5}$ A/cm^2), the electrochemical results were broadly divided into two groups. One group exhibited higher overall current density than the pure Mg (AF50–90, I_d values of 2.61×10^{-5}, 3.83×10^{-5}, 8.55×10^{-5}, 6.98×10^{-5}, and 7.72 $\times 10^{-5}$ A/cm^2, respectively), indicating poorer corrosion resistance, which suggests that the coating does not exhibit corrosion resistance effectiveness. On the contrary, the other

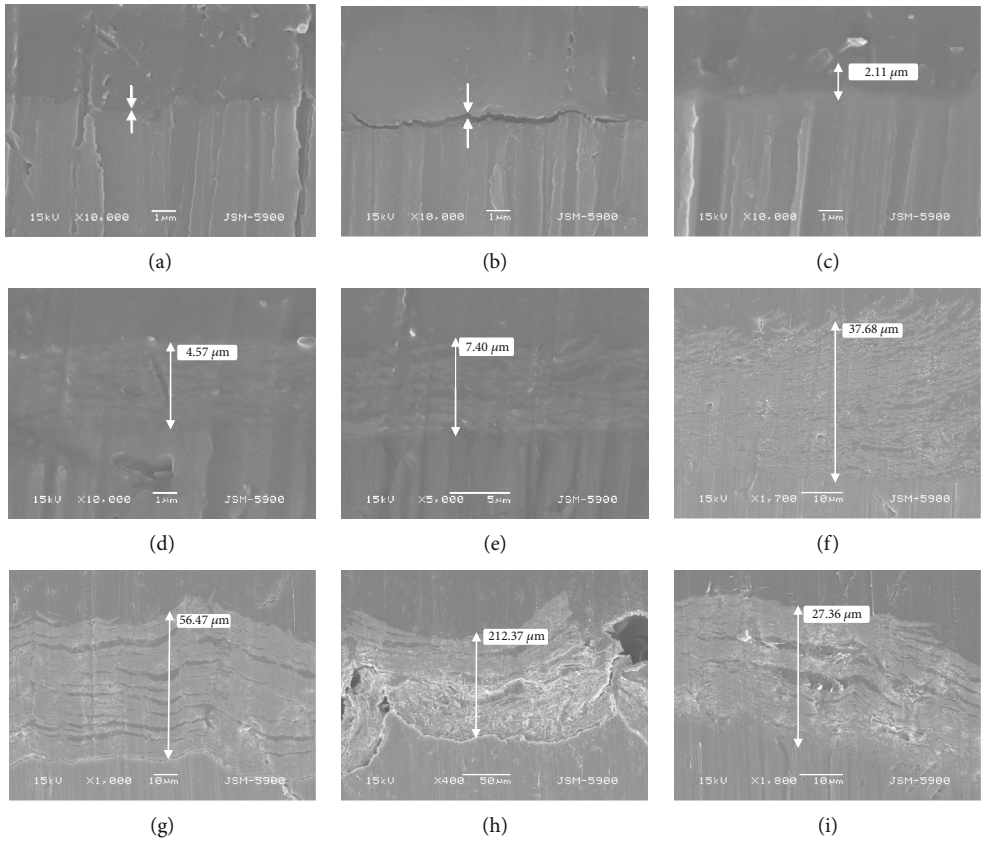

Figure 5: Cross-sectional SEM image of (a) AF10, (b) AF20, (c) AF30, (d) AF40, (e) AF50, (f) AF60, (g) AF70, (h) AF80, and (i) AF90 (the distance between the two arrows above A and B is the thickness of the coating).

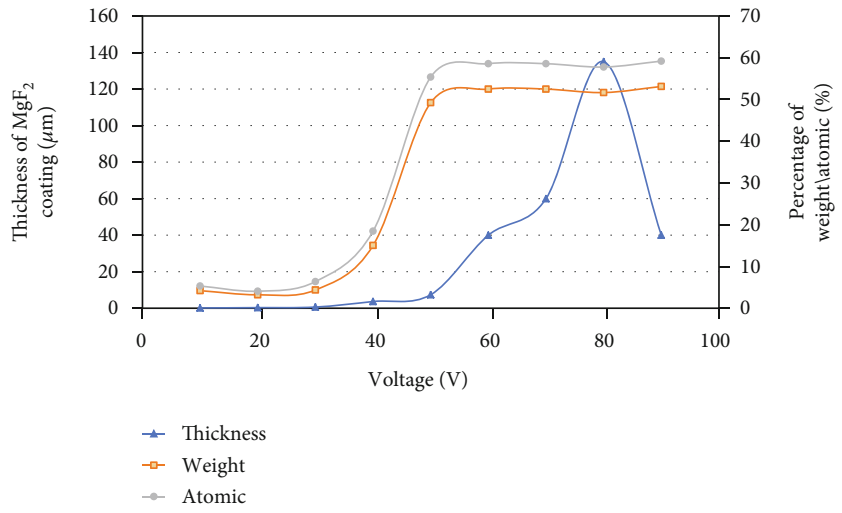

Figure 6: Variation of coating thickness and chemical compositions with processing voltage. In the figure, the blue triangle data point curve corresponds to the variation of coating thickness with the voltage (data from Figure 5). The curves of orange square data points and gray circular data points correspond to the changes of the mass and atomic proportion of fluorine with the increase of voltage, respectively (data from Figure 4).

group exhibited resistance against corrosion, with I_d values of AF20 4.13×10^{-6}, AF10 6.37×10^{-6}, and AF30 7.15×10^{-6} A/cm^2, respectively. Corrosion resistance properties were not obtained at 40 V and higher voltage treatments. However, lower voltages, for example 30 V and below, optimized the corrosion resistance of Mg.

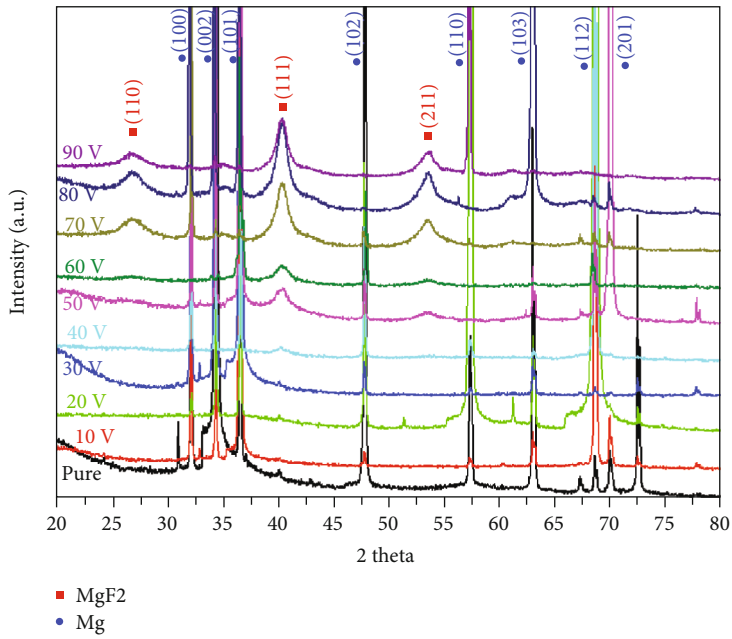

Figure 7: XRD patterns of pure Mg, AF10, AF20, AF30, AF40, AF50, AF60, AF70, AF80, and AF90.

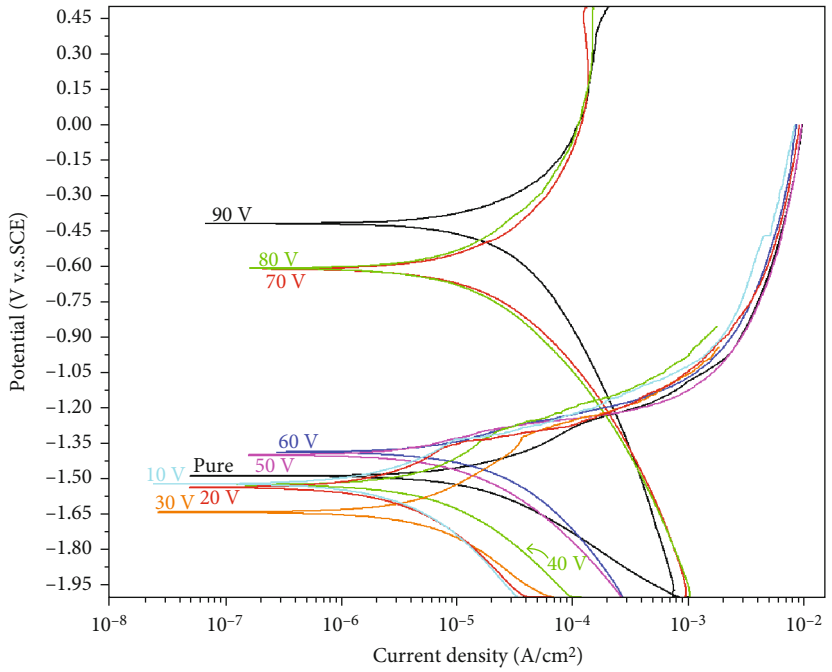

Figure 8: Electrochemical corrosion results: pure Mg, AF10, AF20, AF30, AF40, AF50, AF60, AF70, AF80, and AF90.

Therefore, a better coating impedance effect occurs in the relatively low-voltage experimental conditions, which is in agreement with the experimental expectations. Moreover, in the low-voltage treatment group, the corrosion resistance was more prominent for AF10, AF30, and AF20 (ranked from highest to lowest). A minimum current density and a relatively high corrosion voltage were obtained for the 10 V treatment sample.

Gu et al. [21] reported that the corrosion resistance of oxide coatings can be modulated by controlling the voltage applied during the coating preparation process. This was confirmed in the present study. In contrast to previous studies [16, 17], in the present experiments, reaction conditions in the safe voltage range were used to prepare coatings with tunable corrosion rates. This further confirms that the application of AF technology to Mg alloy coatings is still promising and valuable for research.

In combination with the SEM results, the fluoride coatings at 50 V and higher showed chipping or spalling, a phenomenon that may lead to uneven distribution under

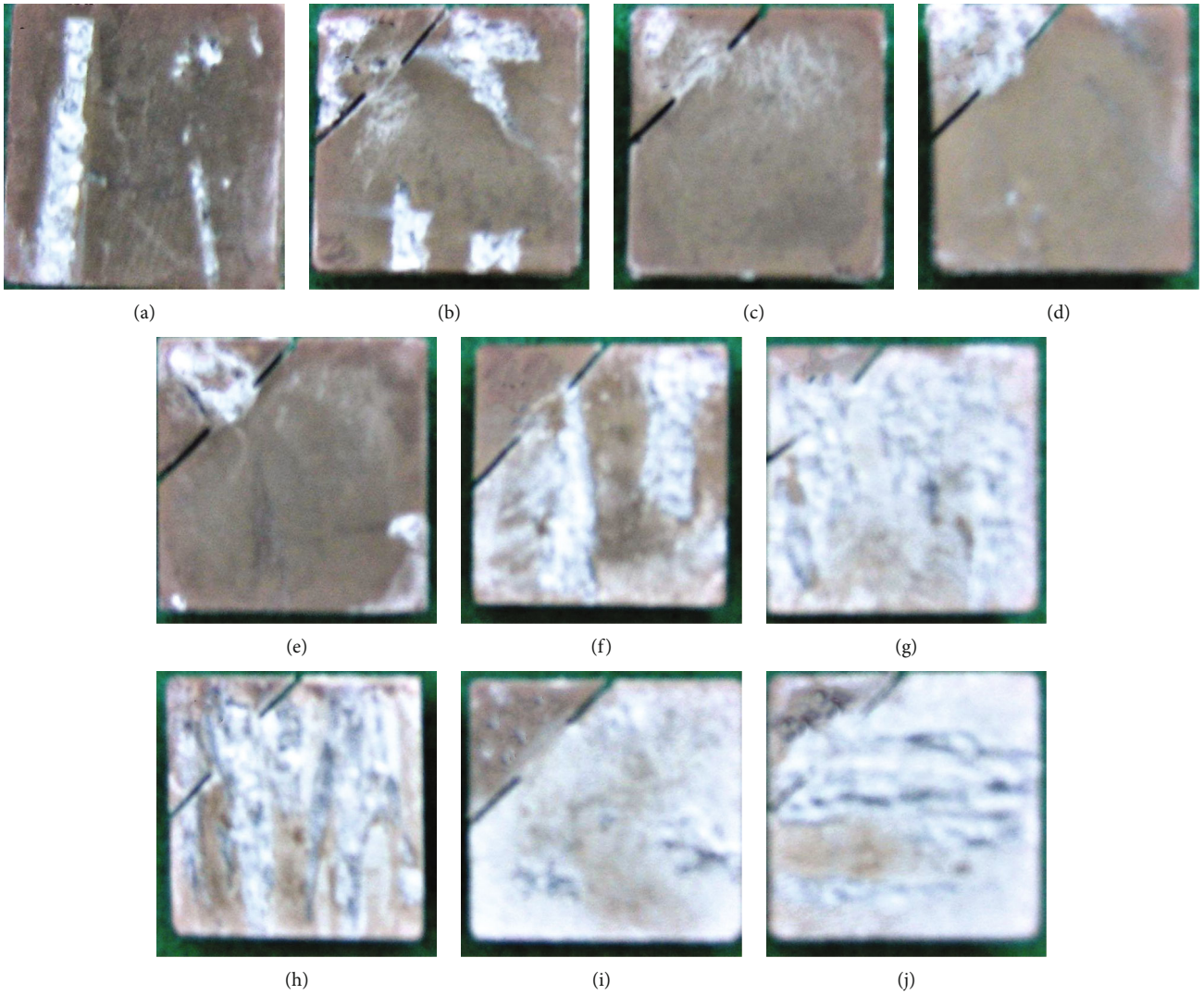

Figure 9: Optical observations of each group of samples after immersion experiments of (a) pure Mg, (b) AF10, (c) AF20, (d) AF30, (e) AF40, (f) AF50, (g) AF60, (h) AF70, (i) AF80, and (j) AF90.

optical observation. According to Hornberger et al., for coating samples, corrosion may start with some defects in the coating, which are nonuniform in nature [33, 34]. Figure 9 shows the optical observation of each group of samples after 7 days of HBSS immersion and etching. During the degradation of the coating, MgF_2 dissolved into F^- and Mg^{2+}, and the latter reacted with OH^- to produce $Mg(OH)_2$ deposits. A layer of $Mg(OH)_2$ degradation products covered the sample. Owing to the lower solubility of MgF_2, $Mg(OH)_2$ was generated at a slower rate, and the coating exhibited better corrosion resistance. As corrosion proceeded, H_2O and Cl^- penetrated the Mg alloy matrix, and the Mg alloy started to degrade to form $Mg(OH)_2$ and H_2 [35]. Owing to the absence of acid cleaning, grey-blue surface corrosion product deposits can be observed. Looking at the sediment distribution, we found more uniform observations and a smaller proportion of product distribution in AF20. AF50–AF90 exhibited large product deposits with similar moisture-shedding patterns.

4. Conclusion

In this study, under AF treatment, the following conclusions were drawn:

(1) After AF treatment, the surface formed coral-like and shale-like surface morphologies

(2) XRD and EDS analyses indicated that the main component of the surface coatings formed by AF was MgF_2

(3) Within a certain range, the thickness of the coating increased with an increase in voltage and reached a peak at AF60

(4) Compared with the untreated samples, the corrosion resistance of the treated samples was improved. The samples treated at 10 V were more resistant to corrosion

Data Availability

The data used to support findings of this study are included within the article.

Conflicts of Interest

We declare that we have no financial or personal relationships with other people or organizations that can inappropriately influence our work.

Authors' Contributions

Chun Yu Dai, and Xinzhe Gao did the conceptualization, methodology, formal analysis, investigation, and writing of original draft. ChuanYao Zhai did the methodology, validation, writing—review and editing, and visualization. Bing Cheng Zhao did the validation, data curation, writing—review and editing. Qi Jia and HaoYu Shi did the writing—review and editing and visualization. HongXin Cai and Qingting Gao did the validation, resources, writing—review and editing, and supervision. Eui-Seok Lee and Heng Bo Jiang did the validation, resources, supervision, project administration, and funding acquisition. Chun Yu Dai, Xinzhe Gao, and ChuanYao Zhai contributed equally to this work.

References

[1] Y. Su, J. Lin, Y. Su, W. Zai, G. Li, and C. Wen, "Investigation on composition, mechanical properties, and corrosion resistance of Mg-0.5Ca-X(Sr, Zr, Sn) biological alloy," *Scanning*, vol. 2018, Article ID 6519310, 10 pages, 2018.

[2] N. Hort, Y. Huang, D. Fechner et al., "Magnesium alloys as implant materials - principles of property design for Mg- RE alloys," *Acta Biomaterialia*, vol. 6, no. 5, pp. 1714–1725, 2010.

[3] G. Wang, X. Xiong, D. Xie et al., "A scalable approach for dendrite-free alkali metal anodes via room-temperature facile surface fluorination," *ACS Applied Materials & Interfaces*, vol. 11, no. 5, pp. 4962–4968, 2019.

[4] F. Witte, "The history of biodegradable magnesium implants: a review," *Acta Biomaterialia*, vol. 6, no. 5, pp. 1680–1692, 2010.

[5] C. Liu, Z. Ren, Y. Xu, S. Pang, X. Zhao, and Y. Zhao, "Biodegradable magnesium alloys developed as bone repair materials: a review," *Scanning*, vol. 2018, Article ID 9216314, 15 pages, 2018.

[6] K. A. Feeney, L. L. Hansen, M. Putker et al., "Daily magnesium fluxes regulate cellular timekeeping and energy balance," *Nature*, vol. 532, no. 7599, pp. 375–379, 2016.

[7] Z. J. Li, X. Gu, S. Lou, and Y. Zheng, "The development of binary Mg-Ca alloys for use as biodegradable materials within bone," *Biomaterials*, vol. 29, no. 10, pp. 1329–1344, 2008.

[8] R. C. Zeng, W. Dietzel, F. Witte, N. Hort, and C. Blawert, "Progress and challenge for magnesium alloys as biomaterials," *Advanced Engineering Materials*, vol. 10, no. 8, pp. B3–B14, 2008.

[9] Z. Zhen, X. Liu, T. Huang, T. F. Xi, and Y. Zheng, "Hemolysis and cytotoxicity mechanisms of biodegradable magnesium and its alloys," *Materials Science & Engineering C-Materials for Biological Applications*, vol. 46, pp. 202–206, 2015.

[10] J. Hofstetter, E. Martinelli, A. M. Weinberg et al., "Assessing the degradation performance of ultrahigh-purity magnesium _in vitro_ and _in vivo_," *Corrosion Science*, vol. 91, pp. 29–36, 2015.

[11] X. M. Xiong, Y. Yang, J. Li et al., "Research on the microstructure and properties of a multi-pass friction stir processed 6061Al coating for AZ31 mg alloy," *Journal of Magnesium and Alloys*, vol. 7, no. 4, pp. 696–706, 2019.

[12] T. S. N. Sankara Narayanan, I. S. Park, and M. H. Lee, "Strategies to improve the corrosion resistance of microarc oxidation (MAO) coated magnesium alloys for degradable implants: prospects and challenges," *Progress in Materials Science*, vol. 60, pp. 1–71, 2014.

[13] X. du, Y. Song, X. Xuan et al., "Characterization of a bioresorbable magnesium-reinforced PLA-integrated GTR/GBR membrane as dental applications," *Scanning*, vol. 2020, Article ID 6743195, 10 pages, 2020.

[14] X. L. Fan, Y. F. Huo, C. Y. Li et al., "Corrosion resistance of nanostructured magnesium hydroxide coating on magnesium alloy AZ31: influence of EDTA," *Rare Metals*, vol. 38, no. 6, article 1216, pp. 520–531, 2019.

[15] Y. Su, Y. Su, W. Zai, G. Li, and C. Wen, "In vitro degradation behaviors of manganese-calcium phosphate coatings on an Mg-Ca-Zn alloy," *Scanning*, vol. 2018, Article ID 6268579, 9 pages, 2018.

[16] H. B. Jiang, G. Wu, S. B. Lee, and K. M. Kim, "Achieving controllable degradation of a biomedical magnesium alloy by anodizing in molten ammonium bifluoride," *Surface & Coatings Technology*, vol. 313, pp. 282–287, 2017.

[17] H. B. Jiang, Y. K. Kim, J. H. Ji, I. S. Park, T. S. Bae, and M. H. Lee, "Surface modification of anodized Mg in ammonium hydrogen fluoride by various voltages," *Surface & Coatings Technology*, vol. 259, pp. 310–317, 2014.

[18] T. T. Yan, L. Tan, B. Zhang, and K. Yang, "Fluoride conversion coating on biodegradable AZ31B magnesium alloy," *Journal of Materials Science & Technology*, vol. 30, no. 7, pp. 666–674, 2014.

[19] Y. H. Gu, S. Bandopadhyay, C. F. Chen, C. Ning, and Y. Guo, "Long-term corrosion inhibition mechanism of microarc oxidation coated AZ31 Mg alloys for biomedical applications," *Materials & Design*, vol. 46, pp. 66–75, 2013.

[20] Q. M. Zhao, X. Guo, X. Dang, J. Hao, J. Lai, and K. Wang, "Preparation and properties of composite MAO/ECD coatings on magnesium alloy," *Colloids and Surfaces B-Biointerfaces*, vol. 102, pp. 321–326, 2013.

[21] X. N. Gu, N. Li, W. R. Zhou et al., "Corrosion resistance and surface biocompatibility of a microarc oxidation coating on a Mg-Ca alloy," *Acta Biomaterialia*, vol. 7, no. 4, pp. 1880–1889, 2011.

[22] H. X. Guo, Y. Ma, J. S. Wang, Y. S. Wang, H. R. Dong, and Y. HAO, "Corrosion behavior of micro-arc oxidation coating on AZ91D magnesium alloy in NaCl solutions with different concentrations," *Transactions of Nonferrous Metals Society of China*, vol. 22, no. 7, pp. 1786–1793, 2012.

[23] L. C. Zhao, C. Cui, Q. Wang, and S. Bu, "Growth characteristics and corrosion resistance of micro-arc oxidation coating on pure magnesium for biomedical applications," *Corrosion Science*, vol. 52, no. 7, pp. 2228–2234, 2010.

[24] L. Sun, B. C. Zhao, T. Wang et al., "Surface characterization and corrosion resistance of biomedical AZ31 Mg alloy treated by microarc fluorination," *Scanning*, vol. 2020, Article ID 5936789, 15 pages, 2020.

[25] L. Mao, G. Yuan, J. Niu, Y. Zong, and W. Ding, "In vitro degradation behavior and biocompatibility of Mg-Nd-Zn-Zr alloy by hydrofluoric acid treatment," *Materials Science & Engineering C-Materials for Biological Applications*, vol. 33, no. 1, pp. 242–250, 2013.

[26] X. L. Liu, Z. Zhen, J. Liu et al., "Multifunctional MgF_2/polydopamine coating on Mg alloy for vascular stent application," *Journal of Materials Science & Technology*, vol. 31, no. 7, pp. 733–743, 2015.

[27] T. T. Yan, L. Tan, D. Xiong, X. Liu, B. Zhang, and K. Yang, "Fluoride treatment and in vitro corrosion behavior of an AZ31B magnesium alloy," *Materials Science & Engineering C-Materials for Biological Applications*, vol. 30, no. 5, pp. 740–748, 2010.

[28] F. Witte, J. Fischer, J. Nellesen et al., "In vivo corrosion and corrosion protection of magnesium alloy LAE442," *Acta Biomaterialia*, vol. 6, no. 5, pp. 1792–1799, 2010.

[29] S. Fintová, J. Drábiková, F. Pastorek et al., "Improvement of electrochemical corrosion characteristics of AZ61 magnesium alloy with unconventional fluoride conversion coatings," *Surface & Coatings Technology*, vol. 357, pp. 638–650, 2019.

[30] W. W. Song, J. H. Heo, J. H. Lee, Y. M. Park, and Y. D. Kim, "Osseointegration of magnesium-incorporated sand-blasted acid-etched implant in the dog mandible: resonance frequency measurements and histomorphometric analysis," *Tissue Engineering and Regenerative Medicine*, vol. 13, no. 2, pp. 191–199, 2016.

[31] Y.-J. Lee, Y. Kim, J. Y. Kim, J. B. Huh, M. R. Kim, and S. J. Kim, "Effect of different concentrations of Escherichia Coli-derived rhBMP-2 coating on osseointegration of implants in dogs," *Tissue Engineering and Regenerative Medicine*, vol. 9, no. 4, pp. 209–215, 2012.

[32] K. Y. Chiu, M. H. Wong, F. T. Cheng, and H. C. Man, "Characterization and corrosion studies of fluoride conversion coating on degradable Mg implants," *Surface & Coatings Technology*, vol. 202, no. 3, pp. 590–598, 2007.

[33] H. Hornberger, S. Virtanen, and A. R. Boccaccini, "Biomedical coatings on magnesium alloys - a review," *Acta Biomaterialia*, vol. 8, no. 7, pp. 2442–2455, 2012.

[34] Q. Li, P. Zhu, S. Chen, B. Zhang, and K. Yang, "In vitro study on degradation of AZ31B magnesium alloy with fluoride conversion coating," *Materials Technology*, vol. 32, no. 7, pp. 409–414, 2016.

[35] Z. Z. Li, Z. Ba, T. Wang, J. Kuang, and Y. Jia, "Fabrication and characterization of Mg-Mn hydrotalcite films on pure Mg substrates," *Materials Research Express*, vol. 6, no. 11, p. 116440, 2019.

Hindawi
Scanning
Volume 2021, Article ID 5530788, 9 pages
https://doi.org/10.1155/2021/5530788

Research Article

In Vivo Corrosion Behavior of Biodegradable Magnesium Alloy by MAF Treatment

Xinzhe Gao,[1] **Chun Yu Dai**,[1] **Qi Jia**,[1] **ChuanYao Zhai**,[1] **HaoYu Shi**,[1] **Yifan Yang**,[1] **Bing Cheng Zhao**,[1] **HongXin Cai**,[1] **Eui-Seok Lee**,[2] **and Heng Bo Jiang**[1]

[1]*The Conversationalist Club, School of Stomatology, Shandong First Medical University & Shandong Academy of Medical Sciences, Tai'an, Shandong 271016, China*
[2]*Department of Oral and Maxillofacial Surgery, Graduate School of Clinical Dentistry, Korea University, Seoul 02841, Republic of Korea*

Correspondence should be addressed to Eui-Seok Lee; ees225@hanmail.net and Heng Bo Jiang; hengbojiang@vip.qq.com

Received 26 January 2021; Accepted 23 April 2021; Published 4 May 2021

Academic Editor: Lavinia C. Ardelean

Coating treatment plays an irreplaceable role in propelling the clinical application of magnesium alloys. This experiment was designed in order to observe the anticorrosion behavior of magnesium fluoride coating in rats. The MgF_2 layer was prepared on the surface of AZ31 magnesium alloy in saturated NH_4HF_2 solution by microarc fluorination (MAF) at 190 V. The cross-sectional SEM, EDS, and XRD analysis indicated that the alloy surface was covered with MgF_2. Meanwhile, SEM observation was used to compare the magnesium alloy samples before and after treatment, and it was found that the samples after coating were flatter and smoother. Two sets of experiments were carried out with the subjects, 6-week-old male rats. So that the untreated AZ31 samples and the microarc fluorinated AZ31 samples could be buried under the muscle layer individually. The volume changes and surface morphology of the corroded samples were monitored dynamically using micro-CT over a 16-week period *in vivo*. Comparison of results between the two sets of samples presented that the corrosion of the microarc fluoridated samples was much slower than that of the untreated ones. The MAF coating was shown to be effective in controlling the corrosion rate and progression of the magnesium alloy.

1. Introduction

As a biomaterial, magnesium (Mg) and magnesium alloys are promising for medical applications. Magnesium and magnesium alloys provide with high specific strength and desirable biocompatibility as implantable materials. Moreover, the density of magnesium and magnesium alloys is similar to that of the human bone [1, 2]. Nowadays, clinical practice commonly uses materials that primarily provide long-term structural stability, such as cobalt chromium alloys, titanium alloys, stainless steel, and other metals. However, because these materials are alien to the body, allergic or inflammatory reactions during treatment are also very common in subsequent recovery [3]. The process of bone remodeling will also be severely disrupted if a stress shielding effect occurs. Even secondary fractures could occur after implant removal surgery [4, 5]. It is worth noting that secondary surgeries after fracture healing will undoubtedly increase pain and medical costs. Magnesium materials, meanwhile, may avoid the aforementioned side effect. Consequently, magnesium alloy seems to be a more desirable option. Nevertheless, one outstanding drawback of magnesium materials is the rapid corrosion rate in human body. It will lead to problem such as an increase in the osmotic pressure of the local microenvironment, which may decrease the whole mechanical strength [1]. Therefore, it is a standing concern for scholars to control the corrosion rate of magnesium alloy.

The composition modification and alloy surface treatment can be used to slow down the corrosion progress of magnesium alloys. The former can improve its corrosion resistance and mechanical properties but not its bioactivity [6]. Currently, the commonly used surface modification

methods are ionic, carbon treatment, fluoride treatment, etc. At this stage of research, electrochemical corrosion analysis has demonstrated that the magnesium fluoride (MgF_2) layer can increase the polarization resistance of magnesium alloys [7–9]. In addition, in the existing studies to prove that the preparation of MgF_2 coating has a certain influence on the corrosion resistance [7, 10, 11]. In addition, the biocompatibility of the MgF_2 coatings has been shown to be positive in cytotoxicity experiments. The negative effects of the magnesium alloy on the degradation and precipitation of hydrogen gas in body fluids have been mitigated to some extent [8, 12, 13]. A point of interest is that the antimicrobial action of the magnesium fluoride coating is another property that has been found in previous studies [3]. In corrosion experiments, the Mg^{2+} and F^- ions produced during the degradation of the alloy are not only nontoxic to the surrounding tissues but also have a nutritional effect on the formation of the bone [6]. Fluorine in bone tissue mediates the metabolism of calcium and phosphorus and helps build bone strength [14]. Mg alloys coated with MgF_2 are highly resistant to corrosion *in vivo*. Additionally, its anticorrosive ability can may be controlled to meet the requirements for implant retention for an appropriate period of time. The sustainability of the MgF_2 coating is evident.

Experiments have been carried out to prepare MgF_2 coatings using the microarc fluorination (MAF) method [15–17]. A series of *in vitro* corrosion tests proved that the microarc fluoride treated magnesium alloy, compared to the untreated ones, has been significantly improved in anticorrosion properties. Moreover, the proliferation and adhesion rates of cells grown on the coating were advanced [15, 16]. This method is based on the principle of electrolysis. MgF_2 layers are prepared on magnesium or magnesium alloy substrates using a certain voltage as a reaction condition in a fluorinated solution [17, 18]. The MAF method was followed in this experiment. The purpose of this work is to observe the corrosion control by the MAF coating under the rat-body-fluid environment. A 190 V volt-treated MAF coating was prepared, and its dynamic changes and degradation behavior were recorded inside the experimental subjects. Its pre- and post-corrosion morphology, composition, and corrosion resistance were evaluated. This study complements the experiment system for the preparation of microarc fluorinated magnesium fluoride coatings by *in vivo* experiments.

2. Materials and Methods

2.1. Materials and Pretreatment. In this study, the size of the AZ31 (Dongguan FeiTai Metal Products Co., Ltd., China) was approximately 70.0 mm [3]. Then, polish the casted samples to 1000 grids. The AZ31 chemical composition is indicated in Table 1.

The testing samples were treated with microarc fluorination (MAF) method. Fluorinated coatings were prepared on samples in saturated NH_4HF_2 solution using 190 V constant voltage DC mode. A closed circuit was formed with AZ31 as anode and graphite rod as cathode during electrification. Clean all the samples with distilled water three times and dried thoroughly. The samples were divided into two groups labeled "Bare" and "MAF."

Table 1: Chemical composition of AZ31 (mass fraction, %).

Al	Zn	Mn	Si	Mg
2.87	0.85	0.38	0.1	Balance

2.2. Coating Observation. The morphology and cross-sectional images of each surface of the sample were observed by scanning electron microscopy (specific model reference: FE-SEM, JSM-67000). Then, the basic composition was determined by the energy spectrometer (EDS). The Mg phases on the surface of MgF_2 samples were measured at 40 kV and 30 mA by X-ray diffraction (XRD, Rigaku Ultima IV Japan), and the scan rate was 1/min.

2.3. Electrochemical Experiment. The Potential Dynamic Polarization (PDP) tests were performed with a constant potentiostat (VersaSTAT 3: 300) and commercial software (VersaStudio 2.44.). The electrochemical analysis cell included a classical three-electrode cell which contained the testing sample as a working electrode, a pure platinum rod electrode, and a reference electrode (Ag/AgCl/Sat-KCl+197 mV vs. standard hydrogen electrode). Here, 1000 mL of commercial Hank's Balanced Salt Solution (HBSS) solution (WELGENE Inc., Korea) was used as the electrolyte and placed in a double-walled beaker. Maintain the temperature of the electrolyte at 37 ± 1°C using a recirculating water heater. The scanning rate of PDP measurements was 3 mV/s.

2.4. Animal Experiments

2.4.1. Experimental Design. In vivo experiments were conducted with respect for animal ethics and animal protection guidelines. Six 6-week-old male rats (New Zealand) with an average weight of 180 g were randomly selected for this study. The rats were divided into two groups; one group was experimented with the Bare, and the other group was experimented with the MAF. After 16 weeks, the rats were euthanized, and the samples were removed.

2.4.2. Surgical Procedures. Firstly, the rats were anesthetized with isoflurane (Isolurane inhalation anesthetic solution; Pizer Japan Inc., Tokyo, Japan). Peel off the skin, fascia to expose the anterior tibial muscle. A sample was buried between the right tibial muscle and periosteum by dental round-bar and a nontaper tissue bar. Then, press the implant and flushed with saline, which can be seen in Figure 1. The wound was closed by suture needle (Nylon suture 5-0; Natsume seisakusho Co., Ltd.). After suturing the incision, put the rat on the pad until they recovered from the anesthetic state. For postoperative analgesia, 0.5 mL of transaminopurine hydrate (sulpyrine injection 250 mg NP; Nipro Pharma Corporation, Osaka, Japan) was added to in rats' drinking water as anti-inflammatory and analgesic for two weeks. At the end of the experiments, the rats were anesthetized with

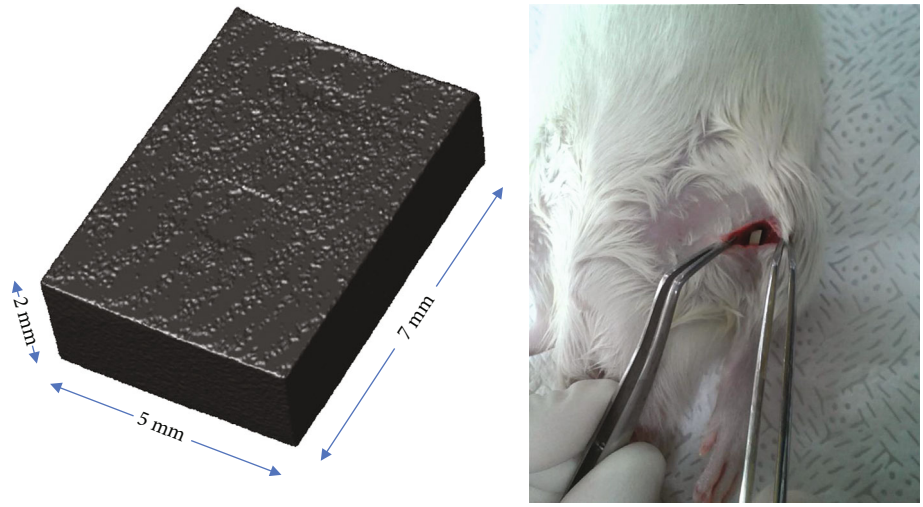

(a) (b)

Figure 1: In vivo corrosion control samples and intraoperative diagrams in rats. (a) Stereoscopic imaging of the sample and annotation of the sampling size. (b) Preparation of an in vivo corrosion model in rats and surgical burial of the sample.

isoflurane (Pizer Japan Inc.) and euthanized by inhalation of CO_2. The samples were removed from each rat.

2.5. Corrosion Analysis In Vivo. Samples from the fourth week were scanned by micro-CT (SkyScan1076, Bruker). The micro-CT scanner was set up with 100 kV voltage, 100 μA current, 360-degree rotation, and 17.6 μm pixel size. After the rats were anesthetized, the scan started 1 cm above the implant and ended 1 cm below it. After removal of the samples at week 16, the samples were scanned again. Both the images (2D and 3D) and the volume data were obtained by the program (CTAn-CTVol 1.10).

The volume loss percentages were calculated as:

$$\text{Volume loss\%} = \frac{V_1 - V_2}{V_1} \times 100\%. \quad (1)$$

V_1 is the volume before implantation, and V_2 is the volume after 16 weeks. In order to better visualize the *in vivo* morphology at week 16, the samples were washed in chromic acid (H_2CrO_3) and dried. The surface was observed by SEM.

3. Results

3.1. Specimen Surface Morphology. Figure 2 illustrates the surface morphology of the MAF group under scanning electron microscopy before it was placed in the body. The surface of MgF_2 coating was uneven and porous, coral-like.

Figure 3 presents the XRD curves of the Bare and the MAF sampling groups. Comparison of the untreated with the JCPDS standard card indicates that the coating of the treated sample consists of quadrilateral MgF_2 (JCPDS No. 41-1443) mainly. EDS analysis showed that the coating surface was dominated by F and Mg elements, which accounted for 61.04% and 38.41%, respectively, as shown in Figure 4.

Figure 5 gives the SEM scan of the cross-section of the MAF group. From Figure 5(a), it can be seen that a layer appeared between the Mg alloy substrate and PMMA, i.e., on the surface of the base. According to the EDS mapping analysis, F elements were only distributed in the upper layer of the samples (Figure 5(c)), averaging 4.26 μm thick. The middle part of the coating was more evenly spaced. The density of fluorine elements decreased as closer to the substrate, and the Mg elements in this depth were relatively sparsely distributed compared to the deeper part (Figure 5(d)). A combination of Figures 5(c) and 5(d) reveals a simultaneous distribution of Mg and F in this domain.

3.2. Corrosion Experiments. Figure 6 is the empirical result of the dynamic potential polarization (PDP) experiment. Resistance properties can be reflected by the corrosion potential of the samples (E_{corr}) and the current density (I_d). The Bare group showed a corrosion current density of approximately 4.0×10^{-5} A. The I_d of the MAF group was about 2.1×10^{-6} A, which was about 20 times lower than the former. Significantly better corrosion resistance of the treated specimens can be interpreted.

The surface images obtained by SEM (Figure 7) reveal that the Bare before implantation (Figure 7(a)) was a line shape produced by grinding, whereas the MAF (Figure 7(c)) had a smoother surface view. After removal at week 16, significant pitting was observed on the Bare surface (Figure 7(b)). Scan results displayed a corrosion range of approximately 0.94 mm in diameter. The MAF surface only appeared to be water-washed soil with a few occasional pitting holes, which can be read from Figure 7(d). The surfaces of the Bare were more uneven due to more localized corrosion in comparison.

3.3. Micro-CT Scanning. Figure 8 depicts the imaging of two groups of samples *in vivo* at week 4 using micro-CT. The large gas cavity was clearly visible in the Bare group at the location indicated (Figure 8(a)), and there were more small gas cavities around the sample, so that the color spots were

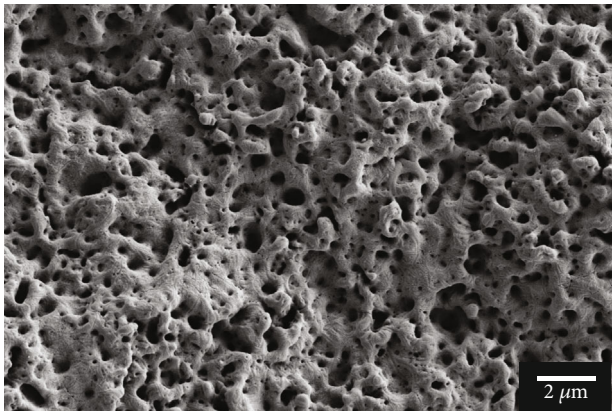

Figure 2: FE-SEM observing surface morphology after MAF coated.

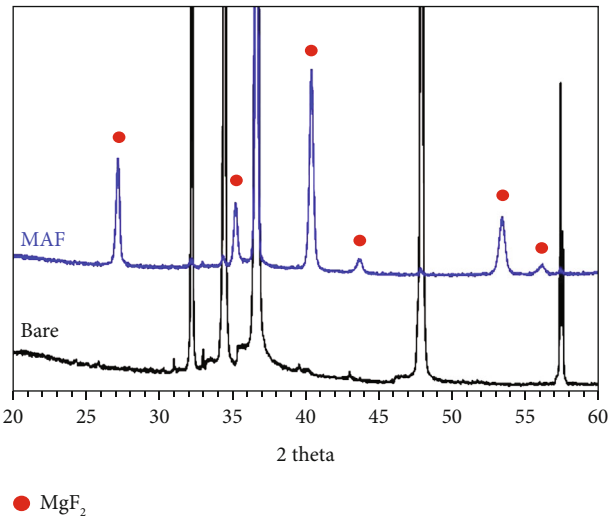

Figure 3: XRD patterns of the Bare and the MAF.

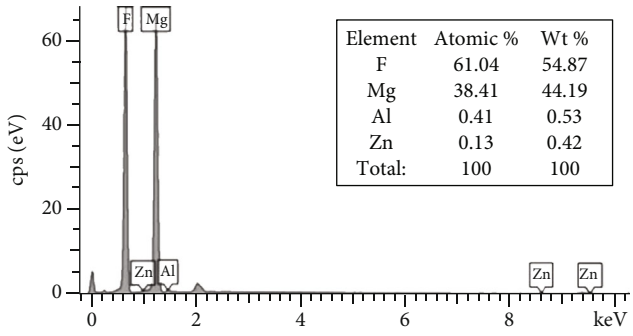

Figure 4: EDS spectra of the MAF coating and percentage of element composition.

sparse. The MAF group, on the other hand, had denser imaging around the sample, proving that the gas production was pretty slow.

Figure 9 contains the results of micro-CT imaging of the specimens at weeks 0, 4, and 16, respectively. At week 4, a corrosion pit appeared in the lower left corner of the Bare samples and tended to enlarge. At 16 weeks, the sampling from the Bare group had other corrosion pits in addition to the one in the lower left corner, the largest of which was nearly 1 mm in diameter. In addition to this, it can be noted that the rectangular form becomes incomplete. Nevertheless, the MAF group had only a few pitting-like indentations on the surface of the sample. Judging from the results of week 4 and week 16, the MAF group would be less corrosive than the Bare group no matter what.

Figure 10 is a histogram produced from the volume loss after sample removal. The volume loss in the Bare group was 14.9% compared to 3.2% in the MAF group. The Bare group was approximately 4.67 times more likely to be in the MAF group.

4. Discussion

Mg alloy, as a biodegradable biomaterial, is commonly used to provide short-term support during tissue recovery, and its potential for medical applications is recognized [19–22]. Nevertheless, it has been demonstrated in existing studies that the rapid degradation rate and localized corrosion behavior of magnesium alloys hinder their clinical application [23, 24]. The existing problems may lead to a mismatch between the support period and the tissue recovery process or even fracture damage to the implant due to stress concentration [8, 25, 26]. In order to solve the fundamental problem, controlling the corrosion rate of magnesium alloys in the electrolyte *in vivo* has become a more widely studied objective.

Surface coating treatment of magnesium alloys has been used in many studies, and effective corrosion rate mitigation results have been obtained. The surface modification treatment can also improve the biocompatibility of magnesium alloys as biomaterials [8]. It is worth mentioning that the coating treatment used should satisfy the following points: (I) strong adhesion to magnesium alloy substrate, (II) provide corrosion resistance, and (III) no cytotoxicity. In addition, for stable degradation of the material within the physiological environment, the corrosion products should also have good biocompatibility assessment results [27]. Li et al. [28] found that Mg fluoride coating in 3.5% NaCl solution improved the bioactivity of the samples. Chiu et al. [29] conducted experiments using HBSS solution and found that MgF_2 coating improved the corrosion resistance of the samples.

The corrosion tests in the *in vivo* environment were performed in combination with existing in vitro experiments on the MAF coating treatment. The composition, surface morphology, and electrochemistry of MAF-coated magnesium alloys have been evaluated to some extent by *in vitro* experiments in previous studies, with more satisfactory results [15–17]. In this experiment, the processed AZ31 samples were processed at 190 V constant voltage mode. Figure 2 shows the rough coral-like surface morphology of the microarc fluoride treated magnesium alloy, similar to previous MAF coatings at high voltages [15, 16, 30]. Figure 5(a) shows that the fluoride coating with a thickness of 4.26 μm is evenly distributed on top of the magnesium substrate. The distribution of oxygen elements throughout the section in Figure 5(b) is,

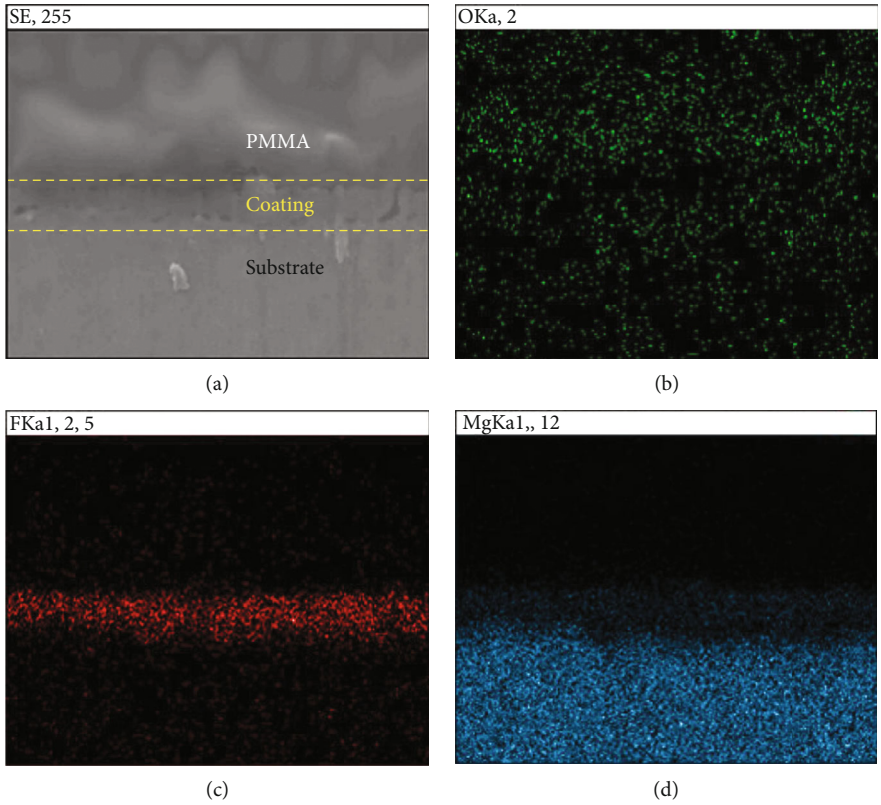

Figure 5: Cross-sectional electron microscopy images and energy diffraction spectra of the MAF coating. (a) Cross-sectional morphology observed under the SEM. Cross-sectional elemental mapping assay of the coating by EDS. (b–d) The results of the distribution of the three elements, oxygen, fluorine, and magnesium, respectively.

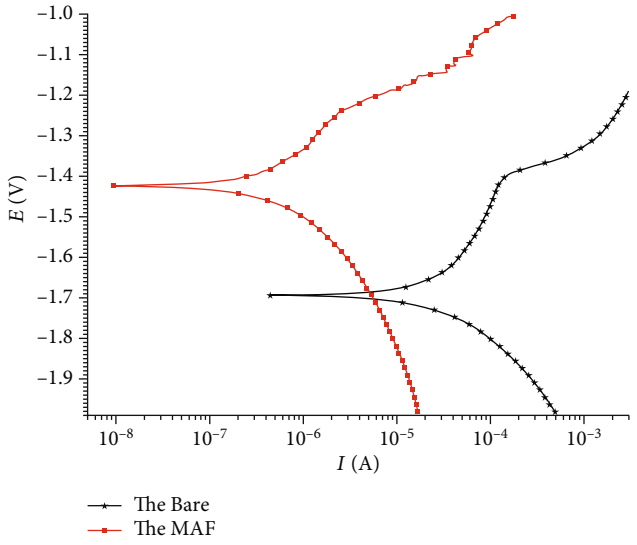

Figure 6: Potentiodynamic polarization curves of the Bare and the MAF samples.

we speculated, due to the internal magnesium exposure caused by the casting and grinding. Oxidation reactions with the air will form a thin oxide film. Because of the short reaction time, there is not much oxygen content. By the infiltrative distribution of fluorine elements in Figure 5(c), it can be assumed that the surface of the substrate is transformed into a fluorinated layer during the electrochemical process. As the fluoride layer grows inward and outward simultaneously, the geometry of the magnesium alloy slightly changes [5]. This also leads to a relative decrease in the distribution density of magnesium in the part of the coating in contact with the substrate. The chemical reaction leads to the combination of magnesium and fluorine atoms, which changes the original distribution of the elements. In addition, the corrosion current density and corrosion potential of the postcoated samples are analyzed by PDP experiments. A significant enhancement of the corrosion resistance can be observed.

Based on the above facts, it can be stated that the coating on the magnesium substrate is prepared completely and that the coating has a certain corrosion limitation. However, the corrosion resistance of MAF-treated coatings in the *in vivo* environment has not been studied previously [15–17]. In a study by Chan [31], the need for loss analysis of implantable materials, especially magnesium alloys, is raised. Fischerauer et al. [32] stated that the surface morphology can affect the corrosion rate to some extent. The use of micro-CT to monitor the corrosion characterization of samples in a body fluid environment is used to determine corrosion behavior and corrosion rate. This allows assessment of the effectiveness of the coating treatment. A certain degree of sample contact damage is avoided, ensuring the accuracy of the scan results.

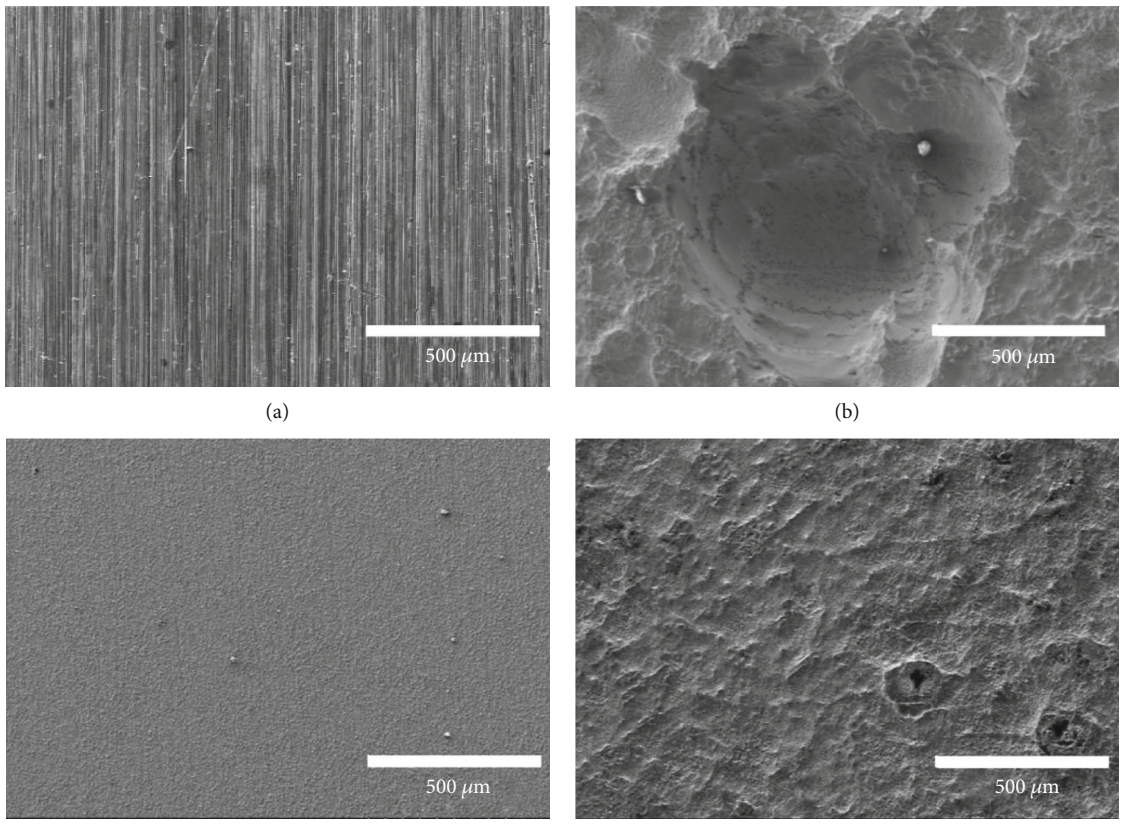

Figure 7: Observations of in vivo experimental samples before and after corrosion using FE-SEM. Surface morphology of (a) Bare, 0 week; (b) Bare, 16 weeks; (c) MAF, 0 week; and (d) MAF, 16 weeks.

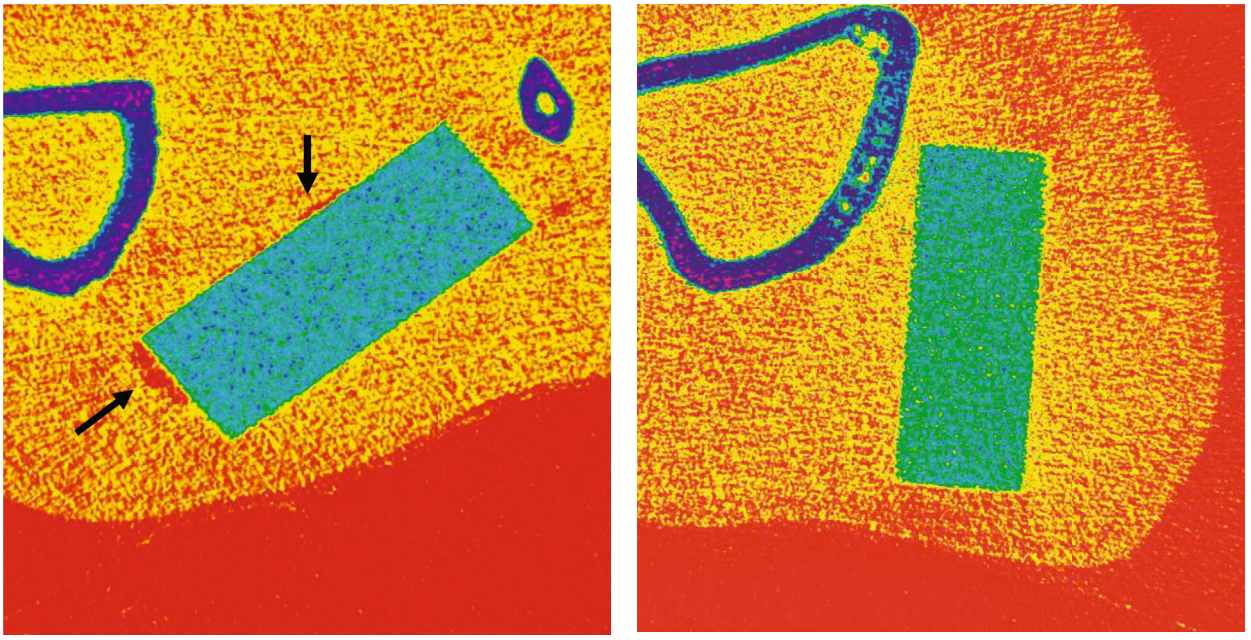

Figure 8: 2D results of the micro-CT scan of the sample (a) Bare and (b) MAF burial site at week four.

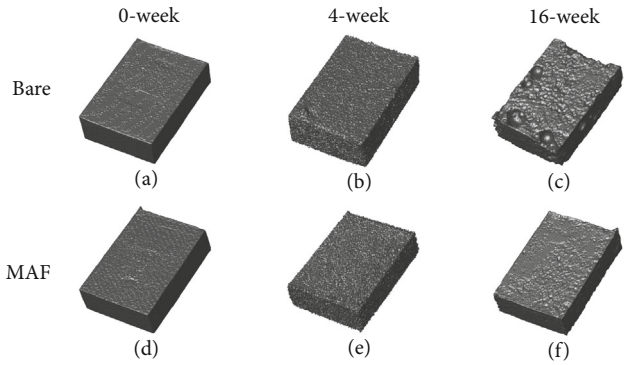

Figure 9: Micro-CT scans of samples from in vivo experimental procedures at selected time points, 3D images.

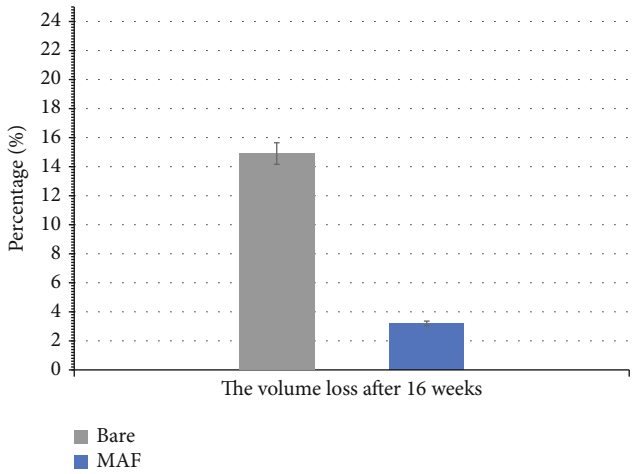

Figure 10: Volume change of in vivo experiments.

Magnesium alloys degrade rapidly in a body fluid environment, producing gases, composed mainly of hydrogen [23]. The process is influenced by the complex dynamics of the liquid environment in the organism. It has been shown that the presence of chloride ions (Cl^-) makes the surface of Mg alloys more likely to exhibit the rapid pitting corrosion. Because the body fluid contains a large amount of Cl^-, it can be converted into magnesium chloride ($MgCl_2$) by replacement reaction after contact with magnesium hydroxide formed on the surface of magnesium alloy [23, 33].

In summary, the chemical equation of the reaction is as follows:

$$\begin{aligned} Mg(s) + 2H_2O &\rightarrow Mg(OH)_2 + H_2(g) \\ Mg(s) + 2Cl^-(aq) &\rightarrow MgCl_2 \\ Mg(OH)_2(s) + 2Cl^- &\rightarrow MgCl_2 \end{aligned} \quad (2)$$

Obviously, there is a dynamic exchange of fluids between tissues, and their flow accelerates the corrosion process. It is worth mentioning that the damage of hydrogen bubbles to implants, such as causing a loss of mechanical integrity, has also been reported recently [34]. From the micro-CT imaging results (Figure 8(a)), it is evident that gas density belts appear around the untreated specimen. The presence of air cavities on the sample contact surface with body fluids represents the occurrence and product accumulation of the anodic dissolution process. This partly reflects the inappropriate degradation rate of magnesium alloys and the difficulty of wound healing due to bubbles. Although bubbles can adversely affect the implant, no further damage to the bone and surrounding tissues was observed, the same as in the subcutaneous magnesium implantation experiments of Kuhlmann et al. [35]. It has been shown that the hydrogen produced during the corrosion of magnesium-based materials can be removed and excreted to some extent [32, 36]. In a sense, the negative effects of corrosion behavior and bubbles can be minimized if the corrosion rate is kept within a safe range [25].

Fluorinated coatings have exhibited desirable properties in many previous studies. In addition to the most common aspects, its antimicrobial properties have been a noteworthy part of the research process since 1940 [37, 38]. Materials with bacterial resistance are highly desirable in medical implantation procedures [8, 39]. Scanning electron microscopy observation of the MAF coating in this experiment reveals similarities between the fluorinated coating and the previous study [15–17]. Therefore, we compared the results of the *in vivo* corrosion with the Hank's Balanced Salt Solution (HBSS) immersion experiments from previous studies. Similarities in the corrosion traces could be found [15–17]. Observation of Figure 9 SEM scan reveals an obvious corrosion pit, indicating localized corrosion of the uncoated magnesium alloy in a body fluid environment. This implies that corrosion does not develop uniformly at the interface between the alloy and the body fluid. Conversely, site-directed degradation corrosion has occurred at certain locations, and the corrosion process at that location is more advanced than at other planes at the same depth [40, 41]. When the rate of corrosion is greater than the carry-over excretion of body fluids, the gas accumulates and creates cavities. In other words, there is a high probability of gas localization at the location of the corrosion pits. This can also be demonstrated in conjunction with Figures 7(b) and 8(a). It can be inferred from the above facts that the presence of the MgF_2 coating not only reduces the contact area between the magnesium alloy and body fluids but also effectively inhibits the rate of H_2 production and reduces the damage of the implant material itself.

5. Conclusion

In this experiment, magnesium fluoride coatings were prepared on the surface of AZ31 magnesium alloy at 190 V constant voltages and evaluated for *in vivo* corrosion experiments, the following conclusions can be drawn.

(1) Homogeneous and dense magnesium fluoride coatings are prepared and bonded to the magnesium alloy substrate

(2) *In vitro* corrosion tests showed that the coating could significantly improve the corrosion resistance compared to bare magnesium alloy

(3) *In vivo* experiments in rats showed that the coating provided protection to the magnesium alloy and significantly reduced gas generation and accumulation during the corrosion process. 190 V MAF coating exhibits good corrosion resistance in an *in vivo* environment

The combined results demonstrate that the MgF_2 coating is effective in controlling the corrosion rate and progression of magnesium alloys, which shows its potential for medical implant material.

Data Availability

The data used to support findings of this study are included within the article.

Conflicts of Interest

We declare that we have no financial and personal relationships with other people or organizations that can inappropriately influence our work.

Authors' Contributions

Xinzhe Gao, Chun Yu Dai, and Qi Jia contributed equally to this work.

Acknowledgments

This study was funded by the Shandong Medicine & Health Science Technology Development Plan Project (2018WS125) and the Tai'an Science & Technology Development Plan Project (2019GX043).

References

[1] L. Y. Li, L. Y. Cui, R. C. Zeng et al., "Advances in functionalized polymer coatings on biodegradable magnesium alloys - a review," *Acta Biomaterialia*, vol. 79, pp. 23–36, 2018.

[2] Y. Su, J. Lin, Y. Su, W. Zai, G. Li, and C. Wen, "Investigation on composition, mechanical properties, and corrosion resistance of Mg-0.5Ca-X(Sr, Zr, Sn) biological alloy," *Scanning*, vol. 2018, Article ID 6519310, 10 pages, 2018.

[3] M. P. Staiger, A. M. Pietak, J. Huadmai, and G. Dias, "Magnesium and its alloys as orthopedic biomaterials: a review," *Biomaterials*, vol. 27, no. 9, pp. 1728–1734, 2006.

[4] J.-H. Kim, M.-S. Kook, S.-Y. Ryu, H.-K. Oh, and H.-J. Park, "A simple technique for the treatment of inferior orbital blow-out fracture: a transantral approach, open reduction, and internal fixation with miniplate and screws," *Journal of Oral and Maxillofacial Surgery*, vol. 66, no. 12, pp. 2488–2492, 2008.

[5] H. Hornberger, S. Virtanen, and A. R. Boccaccini, "Biomedical coatings on magnesium alloys – a review," *Acta Biomaterialia*, vol. 8, no. 7, pp. 2442–2455, 2012.

[6] H. Jiang, J. Wang, M. Chen, and D. Liu, "Biological activity evaluation of magnesium fluoride coated Mg-Zn-Zr alloy in vivo," *Materials Science & Engineering C: Materials for Biological Applications*, vol. 75, pp. 1068–1074, 2017.

[7] H. R. Bakhsheshi-Rad, M. H. Idris, and M. R. Abdul-Kadir, "Synthesis and in vitro degradation evaluation of the nano-HA/MgF2 and DCPD/MgF2 composite coating on biodegradable Mg–Ca–Zn alloy," *Surface & Coatings Technology*, vol. 222, pp. 79–89, 2013.

[8] T. Yan, L. Tan, B. Zhang, and K. Yang, "Fluoride conversion coating on biodegradable AZ31B magnesium alloy," *Journal of Materials Science & Technology*, vol. 30, no. 7, pp. 666–674, 2014.

[9] T. Yan, L. Tan, D. Xiong, X. Liu, B. Zhang, and K. Yang, "Fluoride treatment and in vitro corrosion behavior of an AZ31B magnesium alloy," *Materials Science and Engineering*, vol. 30, no. 5, pp. 740–748, 2010.

[10] M. Ren, S. Cai, T. Liu, K. Huang, and X. Wu, "Calcium phosphate glass/MgF2 double layered composite coating for improving the corrosion resistance of magnesium alloy," *Journal of Alloys and Compounds*, vol. 591, pp. 34–40, 2014.

[11] J. H. Jo, B. G. Kang, K. S. Shin et al., "Hydroxyapatite coating on magnesium with MgF2 interlayer for enhanced corrosion resistance and biocompatibility," *Journal of Materials Science Materials in Medicine*, vol. 22, no. 11, pp. 2437–2447, 2011.

[12] X. Liu, Z. Zhen, J. Liu et al., "Multifunctional MgF2/Polydopamine coating on Mg alloy for vascular stent application," *Journal of Materials Science & Technology*, vol. 31, no. 7, pp. 733–743, 2015.

[13] Z. Li, S. Shizhao, M. Chen, B. D. Fahlman, D. Liu, and H. Bi, "*In vitro* and *in vivo* corrosion, mechanical properties and biocompatibility evaluation of MgF_2-coated Mg-Zn-Zr alloy as cancellous screws," *Materials Science & Engineering C: Materials for Biogical Applications*, vol. 75, pp. 1268–1280, 2017.

[14] S. Liu, H. Zhou, H. Liu, H. Ji, W. Fei, and E. Luo, "Fluorine-contained hydroxyapatite suppresses bone resorption through inhibiting osteoclasts differentiation and function in vitro and in vivo," *Cell Proliferation*, vol. 52, no. 3, article e12613, 2019.

[15] H. B. Jiang, Y. K. Kim, J. H. Ji, I. S. Park, T. S. Bae, and M. H. Lee, "Surface modification of anodized Mg in ammonium hydrogen fluoride by various voltages," *Surface & Coatings Technology*, vol. 259, pp. 310–317, 2014.

[16] H. B. Jiang, G. Wu, S.-B. Lee, and K.-M. Kim, "Achieving controllable degradation of a biomedical magnesium alloy by anodizing in molten ammonium bifluoride," *Surface and Coatings Technology*, vol. 313, pp. 282–287, 2017.

[17] J. Sun, S. Jin, B. C. Zhao et al., "Enhanced corrosion resistance of biodegradable Mg alloys via ultrasonically treated fluoride coating," *Surface Topography: Metrology and Properties*, vol. 7, no. 2, article 025009, 2019.

[18] L. Sun, B. C. Zhao, T. Wang et al., "Surface characterization and corrosion resistance of biomedical AZ31 Mg alloy treated by microarc fluorination," *Scanning*, vol. 2020, Article ID 5936789, 15 pages, 2020.

[19] F. Witte, V. Kaese, H. Haferkamp et al., "In vivo corrosion of four magnesium alloys and the associated bone response," *Biomaterials*, vol. 26, no. 17, pp. 3557–3563, 2005.

[20] X. Guan, M. Xiong, F. Zeng et al., "Enhancement of osteogenesis and biodegradation control by brushite coating on Mg–Nd–Zn–Zr alloy for mandibular bone repair," *ACS Applied Materials & Interfaces*, vol. 6, no. 23, pp. 21525–21533, 2014.

[21] C. Castellani, R. A. Lindtner, P. Hausbrandt et al., "Bone–implant interface strength and osseointegration: biodegradable

magnesium alloy versus standard titanium control," *Acta Biomaterialia*, vol. 7, no. 1, pp. 432–440, 2011.

[22] L. Mao, L. Shen, J. Chen et al., "Enhanced bioactivity of Mg–Nd–Zn–Zr alloy achieved with nanoscale MgF2 surface for vascular stent application," *ACS Applied Materials & Interfaces*, vol. 7, no. 9, pp. 5320–5330, 2015.

[23] L. Mao, H. Zhou, L. Chen et al., "Enhanced biocompatibility and long-term durability in vivo of Mg-Nd-Zn-Zr alloy for vascular stent application," *Journal of Alloys and Compounds*, vol. 720, pp. 245–253, 2017.

[24] Y. Chen, Z. Xu, C. Smith, and J. Sankar, "Recent advances on the development of magnesium alloys for biodegradable implants," *Acta Biomaterialia*, vol. 10, no. 11, pp. 4561–4573, 2014.

[25] C. M. Weber, R. Eifler, J. M. Seitz et al., "Biocompatibility of MgF2-coated MgNd2 specimens in contact with mucosa of the nasal sinus – a long term study," *Acta Biomaterialia*, vol. 18, pp. 249–261, 2015.

[26] D. Ahmadkhaniha, A. Järvenpää, M. Jaskari et al., "Microstructural modification of pure Mg for improving mechanical and biocorrosion properties," *Journal of the Mechanical Behavior of Biomedical Materials*, vol. 61, pp. 360–370, 2016.

[27] T. N. Rezukhina, T. F. Sisoeva, L. I. Holokhonova, and E. G. Ippolitov, "The thermodynamic properties of some metal fluorides solid-electrolyte galvanic-cell studies," *The Journal of Chemical Thermodynamics*, vol. 6, no. 9, pp. 883–893, 1974.

[28] J. Li, J. Huang, Y. Tian, and C. Liu, "Corrosion action and passivation mechanism of magnesium alloy in fluoride solution," *Transactions of Nonferrous Metals Society of China*, vol. 19, no. 1, pp. 50–54, 2009.

[29] K. Y. Chiu, M. H. Wong, F. T. Cheng, and H. C. Man, "Characterization and corrosion studies of fluoride conversion coating on degradable Mg implants," *Surface and Coatings Technology*, vol. 202, no. 3, pp. 590–598, 2007.

[30] K. Saranya, M. Kalaiyarasan, S. Chatterjee, and N. Rajendran, "Dynamic electrochemical impedance study of fluoride conversion coating on AZ31 magnesium alloy to improve bioadaptability for orthopedic application," *Materials and Corrosion*, vol. 70, no. 4, pp. 698–710, 2019.

[31] L. C. Chan, K. M. Au, and K. M. Yu, "FEM–CT integrated design for multiscale damage analysis of hydroformed magnesium-based alloy tubular product," *NDT & E International*, vol. 56, pp. 38–47, 2013.

[32] S. F. Fischerauer, T. Kraus, X. Wu et al., "In vivo degradation performance of micro-arc-oxidized magnesium implants: a micro-CT study in rats," *Acta Biomaterialia*, vol. 9, no. 2, pp. 5411–5420, 2013.

[33] G. Song, A. Atrens, D. Stjohn, J. Nairn, and Y. Li, "The electrochemical corrosion of pure magnesium in 1 N NaCl," *Corrosion Science*, vol. 39, no. 5, pp. 855–875, 1997.

[34] K. Tesař and K. Balík, "Nucleation of corrosion products on H2 bubbles," *Materials Today*, vol. 35, pp. 195-196, 2020.

[35] J. Kuhlmann, I. Bartsch, E. Willbold et al., "Fast escape of hydrogen from gas cavities around corroding magnesium implants," *Acta Biomaterialia*, vol. 9, no. 10, pp. 8714–8721, 2013.

[36] T. Kraus, S. F. Fischerauer, A. C. Hänzi, P. J. Uggowitzer, J. F. Löffler, and A. M. Weinberg, "Magnesium alloys for temporary implants in osteosynthesis: in vivo studies of their degradation and interaction with bone," *Acta Biomaterialia*, vol. 8, no. 3, pp. 1230–1238, 2012.

[37] S. Naorungroj, H.-H. Wei, R. R. Arnold, E. J. Swift Jr., and R. Walter, "Antibacterial surface properties of fluoride-containing resin-based sealants," *Journal of Dentistry*, vol. 38, no. 5, pp. 387–391, 2010.

[38] J. Lellouche, A. Friedman, J.-P. Lellouche, A. Gedanken, and E. Banin, "Improved antibacterial and antibiofilm activity of magnesium fluoride nanoparticles obtained by water-based ultrasound chemistry," *Nanomedicine: Nanotechnology, Biology and Medicine*, vol. 8, no. 5, pp. 702–711, 2012.

[39] C. Liu, Z. Ren, Y. Xu, S. Pang, X. Zhao, and Y. Zhao, "Biodegradable magnesium alloys developed as bone repair materials: a review," *Scanning*, vol. 2018, Article ID 9216314, 15 pages, 2018.

[40] W. W. Song, J. H. Heo, J. H. Lee, Y. M. Park, and Y. D. Kim, "Osseointegration of magnesium-incorporated sand-blasted acid-etched implant in the dog mandible: resonance frequency measurements and histomorphometric analysis," *Tissue Engineering and Regenerative Medicine*, vol. 13, no. 2, pp. 191–199, 2016.

[41] Y.-J. Lee, Y. Kim, J. Y. Kim, J. B. Huh, M. R. Kim, and S. J. Kim, "Effect of different concentrations of Escherichia coli-derived rhBMP-2 coating on osseointegration of implants in dogs," *Tissue Engineering and Regenerative Medicine*, vol. 9, no. 4, pp. 209–215, 2012.

Hindawi
Scanning
Volume 2021, Article ID 5517567, 17 pages
https://doi.org/10.1155/2021/5517567

Review Article

Effects of Physical Stimulation in the Field of Oral Health

Yanxin Qi,[1] ShuXin Zhang,[1] Mi Zhang,[1] Zili Zhou,[1] Xinyi Zhang,[1] Wenhui Li,[1] HongXin Cai,[1] Bing Cheng Zhao,[1] Eui-Seok Lee,[2] and Heng Bo Jiang[1]

[1]*Stomatological Materials Laboratory, School of Stomatology, Shandong First Medical University & Shandong Academy of Medical Sciences, Tai'an, Shandong 271016, China*
[2]*Department of Oral and Maxillofacial Surgery, Graduate School of Clinical Dentistry, Korea University, Seoul 08308, Republic of Korea*

Correspondence should be addressed to Eui-Seok Lee; ees225@hanmail.net and Heng Bo Jiang; hengbojiang@vip.qq.com

Received 28 January 2021; Revised 11 March 2021; Accepted 19 March 2021; Published 8 April 2021

Academic Editor: Guosong Wu

Physical stimulation has been widely used in clinical medicine and healthcare due to its noninvasiveness. The main applications of physical stimulation in the oral cavity include laser, ultrasound, magnetic field, and vibration, which have photothermal, cavitation, magnetocaloric, and mechanical effects, respectively. In addition, the above four stimulations with their unique biological effects, which can play a role at the gene, protein, and cell levels, can provide new methods for the treatment and prevention of common oral diseases. These four physical stimulations have been used as important auxiliary treatment methods in the field of orthodontics, implants, periodontal, dental pulp, maxillofacial surgery, and oral mucosa. This paper systematically describes the application of physical stimulation as a therapeutic method in the field of stomatology to provide guidance for clinicians. In addition, some applications of physical stimulation in specific directions are still at the research stage, and the specific mechanism has not been fully elucidated. To encourage further research on the oral applications of physical stimulation, we elaborate the research results and development history of various physical stimuli in the field of oral health.

1. Introduction

Currently, the development of clinical therapies is mainly based on chemical achievements, and chemical achievements have been further utilized and expanded in the pharmaceutical industry. However, most drugs do not only affect the target tissue, but also affect the entire body, causing side effects in many cases. In contrast, general physical medicine, such as sound waves, magnetic fields, lasers, and mechanical vibrations, provides a noninvasive, safe, and easy-to-apply method to directly act on the injury site and to control the source of pain and inflammation [1]. Different physical stimulations have different effects on tissues and cells, although it can generally reduce inflammation, relieve pain, and improve immune function. It is a good mean to promote, to maintain, and to restore various functions of the human body [2].

In the oral cavity, treatment usually involves surgical procedures and drug therapy. Traditional surgery is the main method to treat oral diseases, although it requires strict indications and can cause trauma during treatment. Common surgical procedures such as root canal treatment, orthodontic treatment, and implants have problems such as incomplete root canal irrigation, long course of orthodontic treatment accompanied by pain, and an excessive implant healing cycle, respectively. In addition, drug therapy has always been the main method for the treatment of mucosal diseases, which is often universal and nonspecific, and can easily lead to bacterial resistance. With the intersection of physical therapy and the oral field, physical therapy is gradually applied to assist clinical treatment to achieve the purpose of reducing pain, thereby promoting healing, accelerating bone remodeling, and inhibiting inflammation and bacterial reproduction. This paper mainly describes the clinical application and development process of four kinds of physical stimulation in implant, orthodontic, dental pulp, periodontal, prosthodontic, mucosal, and maxillofacial surgery and describes its influence on oral treatment at the cellular, tissue, and individual levels.

2. Introduction to Physical Stimulation

2.1. Laser. Laser is the stimulated emission of light generated by a large number of particles excited by the coherent radiation field. According to the transmission form and wavelength, lasers can be divided into carbon dioxide (CO_2), Nd: YAG, Er: YAG, Er Cr: YSGG, diode lasers, and others. In the process of orthodontic treatment, it can accelerate tooth movement and reduce pain and periodontal inflammation during orthodontic treatment. In terms of implants, laser can improve the initial stability of implants and treat peri-implantitis. Besides, laser can be used to remove dental calculus and dental plaque, to promote wound healing and bone healing, and to remove hyperplastic gums in periodontal treatment. In terms of dental pulp, laser can be used for the treatment of dentin hypersensitivity and dental caries, and can also be used to assist root canal treatment. In addition, laser is used for the treatment of oral mucosal inflammation. It can reduce pain, promote wound healing, and shorten recovery time.

2.2. Magnetic Field. The magnetic field is generated by the moving charge or changing electric field and refers to the field that transmits the magnetic force between objects. Electromagnetic technology was developed by Maxwell in 1865, although in the 1980s, its role as a treatment attracted the interest of basic scientists and clinicians. According to the different generation methods, the magnetic field used in the oral cavity is mainly divided into pulsed electromagnetic field and static magnetic field generated by magnetic nanoparticles or magnetic materials. Currently, the magnetic field is used to regenerate the pulp and dentin, to promote mandibular fracture repair and implant bone healing, to shorten the orthodontic treatment course, and to relieve pain during the orthodontic process, and its magnetocaloric effect is used to target the oral mucosal squamous cell carcinoma.

2.3. Ultrasound. Ultrasound, as a form of high-frequency acoustic wave propagating energy through biological tissues, has been applied in several medical fields, and the safety of ultrasound used in long-term treatment has been improved. In the field of stomatology, ultrasonic stimulation is used for physical therapy, which can play an important role in periodontal, orthodontic, implant, and oral preventive health care. Ultrasound can eliminate dental plaque and calculus in periodontal tissues through the cavitation effect and acoustic microstreaming to achieve the anti-inflammatory, cleaning, and sterilization effect. In addition, the biological effect of ultrasound can promote bone remodeling to further accelerate the orthodontic movement speed and improve the survival rate and stability of implants by promoting bone healing. As a noninvasive technology, low-intensity pulsed ultrasound (LIPUS) is a new kind of physical stimulation that can help to treat injuries by emitting sound waves. It has been shown to play an important role in cell metabolism and tissue repair [3] and is widely used in medicine. In the dental field, LIPUS has entered the clinical stage in root canal flushing and plaque removal.

2.4. Mechanical Vibration. Vibration applied in stomatology is aimed at promoting bone remodeling in clinical practice, preventing osteoporosis, and accelerating orthodontic treatment. However, vibration can not only affect the alveolar bone but also affect the restoration of other periodontal tissues. Studies have shown that mechanical stress affects the cell shape and cytoskeletal structure, controlling many cellular behaviors critical to tissue development, including migration, growth, differentiation, apoptosis, and stem cell lineage transformation [4]. In clinical practice, vibration, as a noninvasive and physical means, has been applied to bone regeneration, joint ligament repair, and in the oral cavity and other fields [5]. Whole-body vibration has been shown to prevent osteoporosis and bone loss and to promote muscle formation. In orthodontic treatment, Mani et al. found that vibration can accelerate tooth movement and reduce post-orthodontic pain by promoting fibroblast repair and affecting bone tissue reconstruction [6, 7].

3. Application of Laser in the Oral Cavity

3.1. Shortened Orthodontic Treatment Course and Orthodontic Pain Relief. The therapeutic effects of laser on orthodontics mainly include three aspects: shortening the course of orthodontic treatment, reducing pain, and relieving periodontal inflammation caused by orthodontics. Delma et al. used GaAlAs lasers to conduct experiments on orthodontic patients and found that low-energy laser technology could greatly shorten the time of orthodontic treatment without damaging teeth and periodontal tissues [8]. The specific mechanisms include promoting vascular regeneration to provide nutrition for periodontal tissue reconstruction and promoting the proliferation of osteoclasts and periodontal ligament cells and formation of mineralized bone, which promote the reconstruction of periodontal tissue and accelerate tooth movement [9]. Ren et al. used 940 nm diodes (EZlase; Biolase Technology Inc.) to treat orthodontic patients and found that it can control the inflammation of periodontal tissue during orthodontic treatment. It controls the expression of factors such as cyclooxygenase-2, interleukin-1β (IL-β), platelet-derived growth factor, transforming growth factor-β, basic fibroblast growth factor, and other factors to control the orthodontic treatment of middle teeth inflammation of peripheral tissues. Besides, laser can reduce pain by reducing the increased levels of IL-β, prostaglandin E2 (PGE2), substance P, and other pain mediators; the patients' VAS score also confirmed this conclusion [10].

3.2. Improvement in the Success Rate of Dental Implants. Laser was first used in the second-stage exposure surgery of implants because of its good bleeding control effect, precise cutting effect, and local disinfection [11]. In addition, low-energy laser irradiation can promote osseointegration, improve the secondary stability of implants, and treat peri-implantitis; therefore, it is widely used in the field of oral implantation. Animal and cell experiments have showed that low-intensity laser irradiation can promote the proliferation and differentiation of osteoblasts by promoting the expression of BMP-2. Laser plays a role in accelerating bone

formation around the implant [11, 12] and promoting the stability of the implant [13]. In clinical trials, Mandić et al. performed low-intensity laser irradiation on the posterior maxillary teeth of 12 patients, and from Table 1, we found that the irradiated implant had higher stability, and the difference reached a significant level at the 5^{th} week after surgery [14].

Additionally, low-level laser therapy (LLLT) can also treat peri-implantitis, which is considered to be one of the main causes of implant failure. The accumulation of plaque on the surface of the implant is considered to be the initiating factor leading to the peri-implant inflammation. Bacteria can inhibit the growth of bone cells and stimulate osteoclasts to cause bone resorption. In Takasaki-treated dogs with Er: YAG laser-induced inflammation around the implant, good new bone formation was found on the surface of the implant and the implant-bone contact area increased [15]. Clinically, patients with peri-implantitis were irradiated with Er: YAG laser, and the plaque index, bleeding on probing, and gingival recession were all improved, which proved that the laser can promote bone formation and inhibit inflammation around implants to improve the success rate of the implant effectively [16].

Comparative analysis between the groups showed that the ISQ value of the experimental group was higher than that of the control group during the entire 6-week observation period, and the difference was statistically significant in the 5th week [14].

3.3. Treatment of Periodontal Disease. In terms of periodontal disease, laser can be used to remove dental calculus and plaque, to promote wound healing, and to promote the repair of bone defects. In addition, laser can also remove hyperplastic gums, to shorten the course of orthodontic treatment, and to treat orthodontic pain and oral mucosal inflammation.

3.4. Removal of Dental Calculus and Plaque. Dental calculus is an important pathogenic factor in the development of periodontal disease. After the calculus forms, it can compress the gums and affect blood circulation; besides, calculus contains a lot of water and inorganic substances, which is conducive to the growth of anaerobic bacteria, can easily cause bacterial infection of periodontal tissues, and form periodontal pockets. Therefore, removing calculus is the most critical step in the treatment of periodontitis. Er: YAG laser has good water absorbability. It can evaporate the water in the calculus to increase the pressure in the calculus, cause the calculus to burst, and remove the calculus. Clinically, 30 untreated mesial and distal tooth surfaces were treated with hand instruments and Er: YAG laser irradiation, respectively, which proved that the Er: YAG laser has the ability to remove calculus. Although its effectiveness is lower than mechanical cleaning, it can be improved by extending the course of treatment. Moreover, laser treatment has a better effect on cement preservation than handheld device treatment [17].

Dental plaque is an important factor in the occurrence and aggravation of periodontitis; thus, it is particularly important to control and to treat dental plaque. The most commonly used method now is mechanical treatment, although mechanical treatment is difficult to reach in areas such as the bifurcation of the roots and deep gingival sulcus in patients with periodontal disease, resulting in the recurrence of the disease. Drugs such as antibiotics alone usually cannot effectively remove dental plaque biofilm. Lasers can kill microorganisms on dental plaque, improve the environment of the root part, and facilitate the attachment and growth of periodontal ligament cells on cementum [18]. Reznick et al. showed that the shockwave technology generated by lasers can effectively disrupt *P. aeruginosa* biofilms *in vitro*, which changes the membrane permeability and eventually allows the antibiotic to penetrate into the bacterial cell and kill it. Therefore, the combination of lasers and antibiotics can result in synergies and then shows a better efficacy against *P. aeruginosa* [19]. Clinical studies have performed laser treatment on patients and found that laser has a significant therapeutic effect on patients' dental plaque and can reduce discomfort during treatment [20, 21].

3.5. Promotion of Wound Healing. Wound healing can be divided into three stages: inflammation, proliferation, and reconstruction [22]. Factors affecting wound healing include the proliferation of fibroblasts, collagen synthesis, macrophage stimulation, and extracellular matrix production. Pourzarandian et al. used pulsed Er: YAG lasers with different energy densities to irradiate cultured human gingival fibroblasts and found that the cell growth rate can be accelerated and that the optimal stimulation energy density was $3.37\,J/cm^2$ [23]. Laser promotes collagen synthesis in fibroblast cells by accelerating mRNA transcription rate of collagen gene and enhancing the activity of related enzymes [24]. Silveira et al. irradiated rats of the control group with laser and found that the laser could accelerate the wound healing process and promote the synthesis of collagen [25].

3.6. Promotion of Bone Defect Repair. Due to the fact that bone self-repair is slow, many people have done a lot of research on how to speed up bone healing. One of the most effective nonsurgical methods is LLLT. Cell studies have shown that low-level laser irradiation can enhance the activity of fibroblasts and osteoblasts and promote tissue healing, collagen metabolism, and granulation tissue formation [26, 27]. The possible mechanism of action is that laser stimulates the photoreceptors in the mitochondrial respiratory chain, converting light energy into chemical energy, and changes cellular ATP or cAMP levels [28]. Studies have used LLLT to irradiate the extraction socket of rats. After a period of time, it was found that Runx2, type 1 collagen, osteocalcin, platelet-derived growth factor-B, vascular endothelial growth factor, and other factors related to bone growth all increased [29]. Stein et al. used the He-Ne laser (632 nm) to irradiate human osteoblasts *in vitro* and found that the survival rate of osteoblasts increased, and from Figures 1 and 2, we can see that osteogenic markers increased significantly [30]. Korany et al. irradiated rats with a 75 MW, 830 nm GaAlAs laser and found that the percentage of trabecular bone increased [31]. Therefore, LLLT can promote the healing of tooth extraction sockets, and this effect has been confirmed even in ovariectomized and diabetic rats [32, 33]. In addition, LLLT plays an important role not only for extraction sockets but also in rat mandibular defects [31]. Pretel et al. used

Table 1: Differences in implant stability between irradiated (test) and nonirradiated (control) implants.

Time	Implant stability quotient ($x \pm$ SD)			P
	Test	Control	95% CI for MD	
Baseline	76.00 ± 3.52	72.89 ± 7.15	-0.78177 to 7.00399	0.110
1st week	74.88 ± 3.40	74.69 ± 4.80	-3.45378 to 3.82878	0.914
2nd week	74.22 ± 3.93	72.56 ± 5.67	-1.73616 to 5.06950	0.316
3rd week	72.67 ± 3.65	70.44 ± 6.16	-0.88360 to 5.32805	0.150
4th week	72.50 ± 4.18	69.22 ± 9.09	-0.72534 to 7.28089	0.102
5th week	72.94 ± 3.92	69.83 ± 7.03	0.34554 to 5.87668	0.030*
6th week	72.67 ± 3.69	70.61 ± 7.20	-0.60045 to 4.71157	0.121

MD: mean difference; *P values: statistically significant; CI: confidence interval.

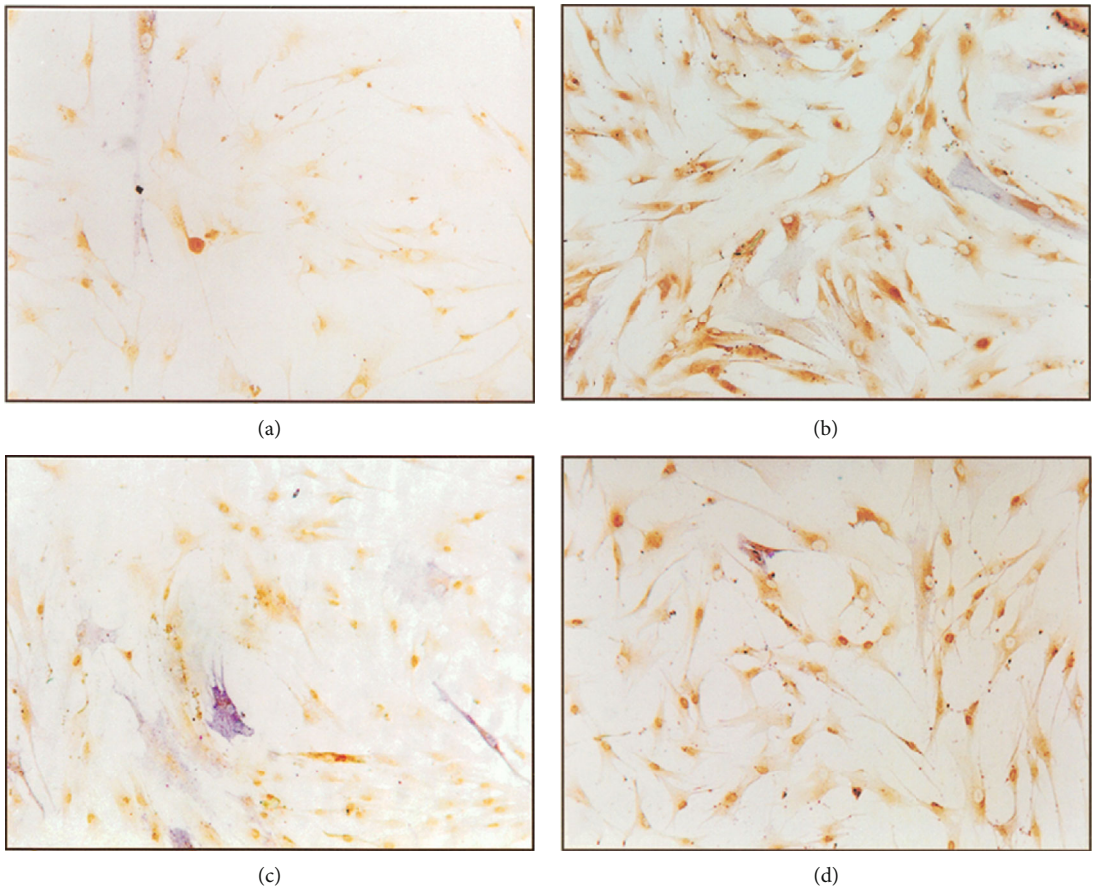

Figure 1: Light microscope micrograph of osteopontin expression in cultured human osteoblast cells 24 h (a) control nonirradiated cells and (b) laser irradiated cells and 48 h (c) control nonirradiated cells and (d) laser irradiated cells postsecond irradiation. Note very light positive staining in the control cells as compared with the significantly stronger positive staining in the irradiated cells (×200). The results showed that the expression of osteopontin in the irradiated cells was significantly increased compared with the unirradiated cells. Osteopontin is one of the osteogenic markers. This shows that laser irradiation in this experiment can promote the proliferation and maturation of human osteoblasts [30].

14 J/cm^2 GaAlAs laser (35 MW, 780 nm) to irradiate the mandibular defect in rats and found that the formation of new bone matrix developed rapidly in the 15-day and 45-day laser application groups [34].

4. Removal of Hyperplastic Gum Tissue

Gingival hyperplasia is a common feature of patients with periodontal disease. In clinical practice, gingival resection

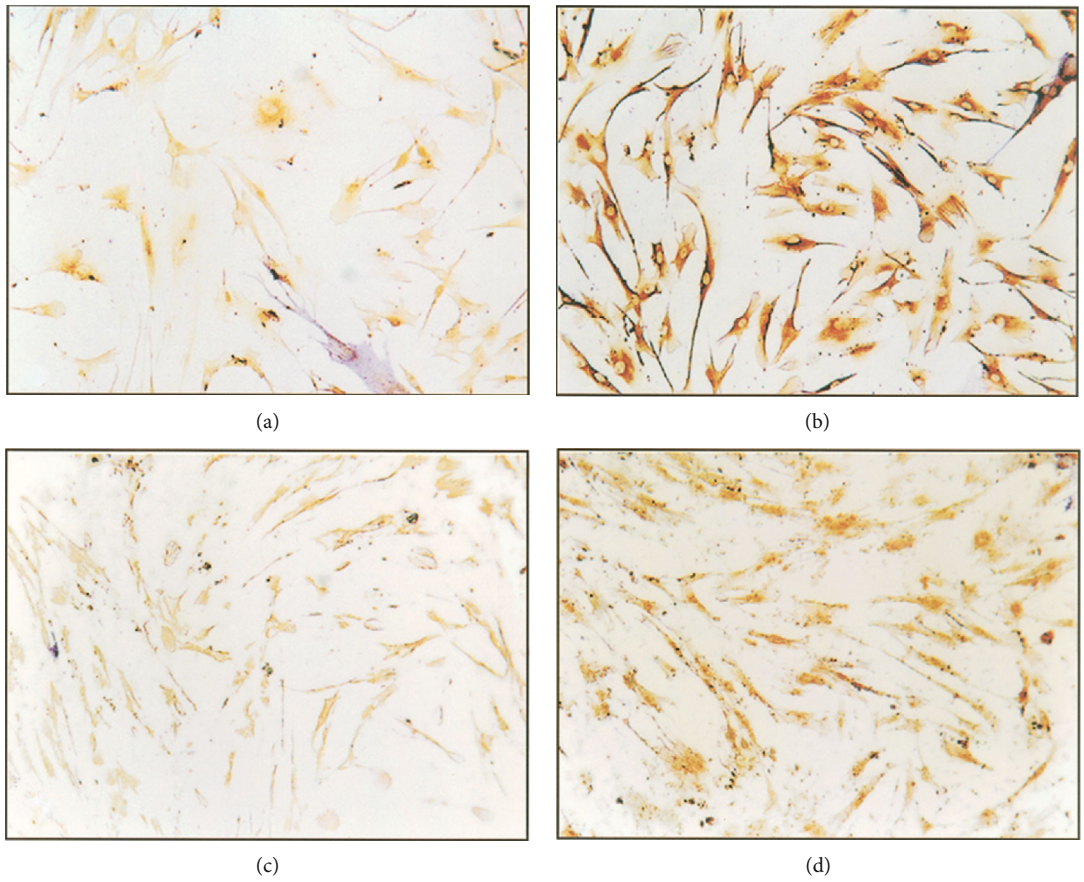

Figure 2: Light microscope micrograph of bone sialoprotein expression in cultured human osteoblast cells 24 h (a) control nonirradiated cells and (b) laser irradiated cells and 48 h (c) control nonirradiated cells and (d) laser irradiated cells postsecond irradiation. Note very light positive staining in the control cells as compared to the significantly stronger staining in the irradiated cells (×200). The results showed that, compared with the nonirradiated cells, bone sialoprotein expression in cells after irradiation significantly increased, and bone sialoprotein is a bone marker into one. Described laser irradiation may facilitate this human osteoblast proliferation and maturation experiment [30].

and angioplasty are usually performed with a scalpel or electric knife, although the comfort level of patients is poor. At present, the laser instruments commonly used for soft tissues include CO_2 and Nd: YAG lasers. Compared with traditional methods, removing gingival hyperplasia with laser has the advantages of less intraoperative bleeding, faster wound healing, and higher postoperative comfort. It has been applied in the field of clinical medicine [35].

4.1. Shortened Orthodontic Treatment Course and Orthodontic Pain Relief. Weichman used high-energy infrared laser to seal the orifice to the root canal for the first time, creating a new field of laser treatment in endodontics [36]. Laser can be used for the treatment of dentine hypersensitivity, dental caries, and root canal treatment. Dentin sensitivity is mainly caused by the wear of the tooth tissue and exposure of the dentin tubules. The external stimulation stimulates the pulp through the dental tubules. The photothermal effect of the laser is used to melt and to recrystallize the dentin surface to seal the dentin tubule opening, thereby isolating the external stimulus. To prevent damage to the root tip, the laser equipment uses low output power and provides enough water to cool the dentin surface and can limit the irradiation time to 10 s to avoid pulp irritation caused by overheating [37]. Kumar et al. confirmed that the Nd: YAG laser had a better effect on sealing dentin tubules than sodium fluoride, and the combination can achieve a better sealing effect [38].

Root canal treatment is the most important method for the treatment of pulp diseases. Bacteria in the root canal is an important pathogenic factor leading to periapical disease of dental pulp. The Nd: YAG laser can produce a photothermal effect; bacteria absorb the heat generated by the laser and then are killed [39, 40]. The laser can dissolve the dentin, and remove the residue and smear layer on the root canal wall. At the same time, the laser can remove the dentin on the root canal wall and enlarge the dentin tubules. Kokuzawa et al. used the Er: YAG laser to irradiate six isolated single human teeth. They found that the smear layer disappeared and the dentin tubules were opened. The Er: YAG laser vaporizes the water in the hard tissue and increases the internal pressure, thus causing the hard tissue to undergo a microexplosion to remove the damaged tissue [41]. Valério et al. treated 29 children with the Er: YAG laser for decayed first molars. It was found that the Er: YAG laser can effectively remove caries tissue and caries causing bacteria such as *Streptococcus mutans* and *Lactobacillus*, and can improve the safety and comfort of surgery [42].

4.2. Treatment of Oral Mucosal Inflammation. As a complication of various cancers, oral mucositis seriously affects the patient's treatment enthusiasm and clinical effect. The symptoms include dry mouth, altered taste, burning sensation, and difficulty swallowing. Compared with traditional surgery, laser surgery makes it easier to cut and shape the oral soft tissues, which can reduce bleeding, relieve patient pain, cause less tissue trauma, and heal faster, and is less likely to form scars. A simple laser surgery sometimes only requires surface anesthesia without local infiltration or block anesthesia. Usually, low-intensity laser treatment is used to promote wound healing (LLLT). The photoreceptor on the cell absorbs light energy, promotes the reduction of oxygen by the cytochrome c oxidase on the terminal enzyme of the mitochondrial respiratory chain, increases the synthesis of ATP in the body, and enhances energy metabolism [43]. At present, many experiments have confirmed the promoting effect of laser on the treatment of oral mucositis. Honarmand et al. found that semiconductor laser treatment shortened the recovery time and relieved the pain severity of RHL patients [44]. Sanchez et al. found that compared with acyclovir cream and tablets, laser treatment has fewer side effects and prolongs the recurrence time [45]. Amira et al. conducted follow-up treatment on a young patient with recurrent mucous cysts and also found that the use of 980 nm diode laser treatment can significantly reduce the recurrence rate of mucous cysts. The effect is significant, and diode laser treatment is an efficient, safe, and convenient treatment method [46].

5. Application of the Magnetic Field

5.1. Promotion of Dental Pulp and Dentin Regeneration. Pulp tissue is susceptible to infection and necrosis, and the pulp tissue after necrosis is difficult to regenerate due to a single blood supply. However, with the development of modern tissue engineering and the discovery of dental stem cells, the regeneration of dental pulp and dentin has been extensively studied [47]. The key to pulp regeneration is the selection of dental pulp stem cells and the establishment of three-dimensional scaffolds. Magnetite nanoparticles (MNPs) are superparamagnetic. The addition of MNPs can improve the mechanical properties of the scaffold and make the material show magnetic [48]. Hyung-mun et al. were the first to use magnetic scaffolds for pulp dentine regeneration. The results showed that magnetic scaffoldings could promote the odontogenic differentiation of dental pulp stem cells by increasing the activity of ALP and mRNA expression of odontogenic markers (DMP-1, DSPP, osteocalcin, and osteocalcin) and enhancing the adhesion and migration of PSCS [49]. These results indicate that magnetic scaffolds can provide good matrix conditions for dentine regeneration.

5.2. Treatment and Prevention of Periodontitis. The plaque attached to the gum and tooth surface has been considered as one of the predisposing factors of periodontal disease. Brushing has been widely accepted as the standard hygiene method for controlling scar formation on the gums and has greatly improved the periodontal health, although periodontal disease is still very common and causes huge medical care costs [50]. As a noninvasive physical stimulus, magnetic field can reduce the number of plaque bacteria, enhance the susceptibility of plaque biofilm to antibiotics, and inhibit the formation of plaque biofilm to treat periodontal disease.

Snezana et al. demonstrated the positive effect of magnetic fields on the reduction of plaque bacteria *in vitro*. During the first 24 h of exposure, the number of all isolated microbes was significantly reduced [51]. At present, there is still a controversy about the effect of electromagnetism on oral microbes. Morrow found that it does not have a significant impact on the growth and reproduction of the normal oral flora. Therefore, it is speculated that electromagnetism may only have an effect on disease-curing oral microorganisms, especially those that are involved in the formation of dental plaque. There is almost no effect on the normal oral flora, which further confirms its effectiveness and safety [52]. A reduction in the number of microbes was found under overdentures containing implanted magnets. This plays an important role in protecting the health of the periodontal tissue around the overdenture [53].

With the use of antibiotics, many bacteria have become resistant. As mentioned above, the effectiveness of magnetic fields in inhibiting bacterial proliferation has been confirmed. In addition, others have found that magnetic fields can also be used as an auxiliary means to use MNP/alternating magnetic fields through the magnetocaloric effect to increase part of the temperature, leading to an increase in the metabolic activity of *Staphylococcus aureus*, and promoting the absorption of antibiotics by the bacterial biofilm, thereby increasing the susceptibility of the bacterial biofilm to antibiotics, to reduce the amount of antibiotics and to assist in the purpose of antibiotics to kill resistant bacteria [54].

During the formation of the dental plaque, bacteria reach the tooth surface through electrostatic adsorption, and the magnetic effect may promote the deposition of bacteria and various ions in the dental plaque by reducing the activity of electrostatic ions. Johnson et al. appropriately combined a magnetic device with an oral irrigator to develop a magnetic water irrigator, which was applied to patients with periodontal disease, and found that it appears to greatly reduce the formation of supragingival tartar and its accompanying plaque. It can be reasonably assumed that this type of flushing device will produce great benefits for self-care or sanitation system [55].

5.3. Treatment of Oral Mucosal Lesions. Oral squamous cell carcinoma (OSCC) is one of the most common cancers in the world [56]. OSCC patients have a low survival rate and high metastasis rate. At present, the traditional treatment has not improved the prognosis in general, and the development of targeted therapy provides a new treatment for OSCC. OSCC magnetic nanomaterial-targeted treatment method involves coupling magnetic nanoparticles with antibodies targeting integrin (v$\alpha\beta$6). Due to the high expression of V 6 in SCC, the targeted localization of tumor cells can be realized. The heating properties of magnetic nanoparticles were used to induce thermal ablation of tumor cells in a changing magnetic field [57]. Magnetic nanomaterials have a good prospect of targeted therapy in the treatment of OSCC.

5.4. Production of Orthodontic Force and Shortened Orthodontic Treatment Course. Clinically, a long orthodontic time can cause a series of problems, such as dental caries, periodontal disease root resorption, and other problems, and increase the pain of patients; therefore, it is necessary to accelerate the orthodontic movement and shorten the orthodontic time [58].

At present, the orthodontic devices used in clinical practice cause oral friction to patients, increase the probability of mucosal disease, and aggravate the pain of patients. In addition, the traditional orthodontia cannot significantly improve the malocclusion; therefore, it is very necessary to develop a new orthodontic device. Currently, magnetic methods are used to treat maxillary teeth and class II and class III malocclusions. Compared with the traditional force transfer system, magnets have the following advantages: frictionless mechanics. When the magnet is in the state of attraction, its attraction is controllable and does not decay with time [2]. Animal experiments have shown that the application of 50 Hz ElF-EMF accelerates the movement of orthodontic teeth in rats [59]. In 1977, Kawata et al. designed the first ferrocobalt and chromium magnetic support, although the strength was insufficient and was subsequently replaced by a rare earth magnet, which produced enough orthodontic force. Rare earth magnets can generate a constant magnetic field in the mouth [60, 61]. Studies have shown that EMFs can regulate the proliferation and differentiation of osteoblasts by affecting cell metabolism, changing the structure and morphology of cytoskeleton, and play a role in promoting bone healing, accelerating bone formation, and further accelerating the remodeling of bone tissue associated with orthodontics. Zhao et al. developed a magnetic orthopedic appliance (MOA-III) and applied it to the children with class III malocclusions and found that it could correct the maxilla and mandible at the same time; Figure 3 shows that MOA-III had a good effect on moderate class III malocclusion [62]. In addition, magnets have obvious advantages in guiding the eruption of impacted teeth, such as less stimulation on palatal mucosa, stronger force control, and lower requirements on patient cooperation. These factors may be the main positive characteristics of this alternative therapy.

5.5. Improvement in the Implant Success Rate. Implants have become a solution to the epidemic of missing teeth with a high success rate [63]. The factors influencing the success of implants include the initial stability of the implant, bonding between the implant and bone, and number and density of the remaining alveolar bone. One of the key steps in implant healing is to establish osseous healing and osseointegration with the surrounding alveolar bone. Therefore, a variety of treatment methods were proposed to enhance and shorten the time of osseointegration. Pulsed magnetic field has been widely used in clinics to promote bone regeneration. The main principle of pulsed magnetic field is to affect cell differentiation and proliferation by affecting various metabolic pathways, promote angiogenesis and bone tissue formation, and thus promote fracture healing [2, 64]. PEMF was first applied to the oral implants of rabbits, and it was found that the amount of early osseointegration on the implants increased by three times, which verified the effectiveness of PEMF applied to implants for the first time [65]. A miniaturized electromagnetic device that can independently generate a magnetic field was developed to replace the standard healing abutment. It is equipped with a microelectronic module that can generate PEMF to improve bone formation after dental implant surgery. Shlomo et al. applied a miniaturized electromagnetic device (MED) to human oral implants for the first time and found that the initial stability of the implants was significantly improved in the early healing stage [66]. Nayak et al. also found that the average implant stability coefficient (ISQ) of the PEMF group increased by 6.8% in the first two weeks after applying MED, and the overall stability increased by 13%. The inflammatory factor TNF-concentration in the treatment group was significantly decreased in the first four weeks. PEMF stimulation may constitute a valuable new technique for early mastication of implants by promoting bone formation and accelerating bone integration. It can also increase the content of the remaining alveolar bone, thus greatly increasing the success rate of the implant and extending its service life. Some scholars have suggested that PEMF can improve the microenvironment around implants by influencing the level of cytokines [67]. It was shown that PEMF treatment had a positive effect on implant stability by regulating cytokine levels.

5.6. Promotion of Mandibular Fracture Healing. The mandible is the second most common site of facial fractures [68, 69]. The most prominent problem in the treatment process is that it requires a long time for fixation, and the subsequent rehabilitation work is delayed. Therefore, shortening the fixation time by accelerating fracture healing has been the subject of research. PEMF has been used as a simple noninvasive method to enhance bone healing. In 1976, Bassett et al. proved for the first time that inductively coupled electromagnetic fields can enhance the effect of bone repair. PEMF stimulation has a beneficial effect on bone healing. The effectiveness of PEMF has been confirmed, although the matrix that promotes bone formation is not fully understood. Some scholars have proposed that PEMF may promote the growth and expansion of blood vessels to promote the healing of tissues at the injured site [2]. Abdelrahim et al. used PEMF for the first time to stimulate patients with mandibular fractures and found that it significantly reduced pain in patients, due to its analgesic and anti-injury effects [70]. Many studies have reported the effectiveness of PEMF in relieving pain. However, Weintraub et al. found that PEMF is not effective in reducing diabetic neuropathic pain. These inconsistent results may be due to the use of fields of different intensities and frequencies [71]. In addition, PEMF reduced early (15 days) bone loss in patients with mandible fracture, and at 30 days postoperatively, possibly with enhanced osteogenesis, bone density was significantly increased in the experimental group [70]. Therefore, as a physical method, PEMF can promote mandibular fracture healing and relieve fracture pain; therefore, it can be used as a clinical auxiliary treatment method and has broad application prospects.

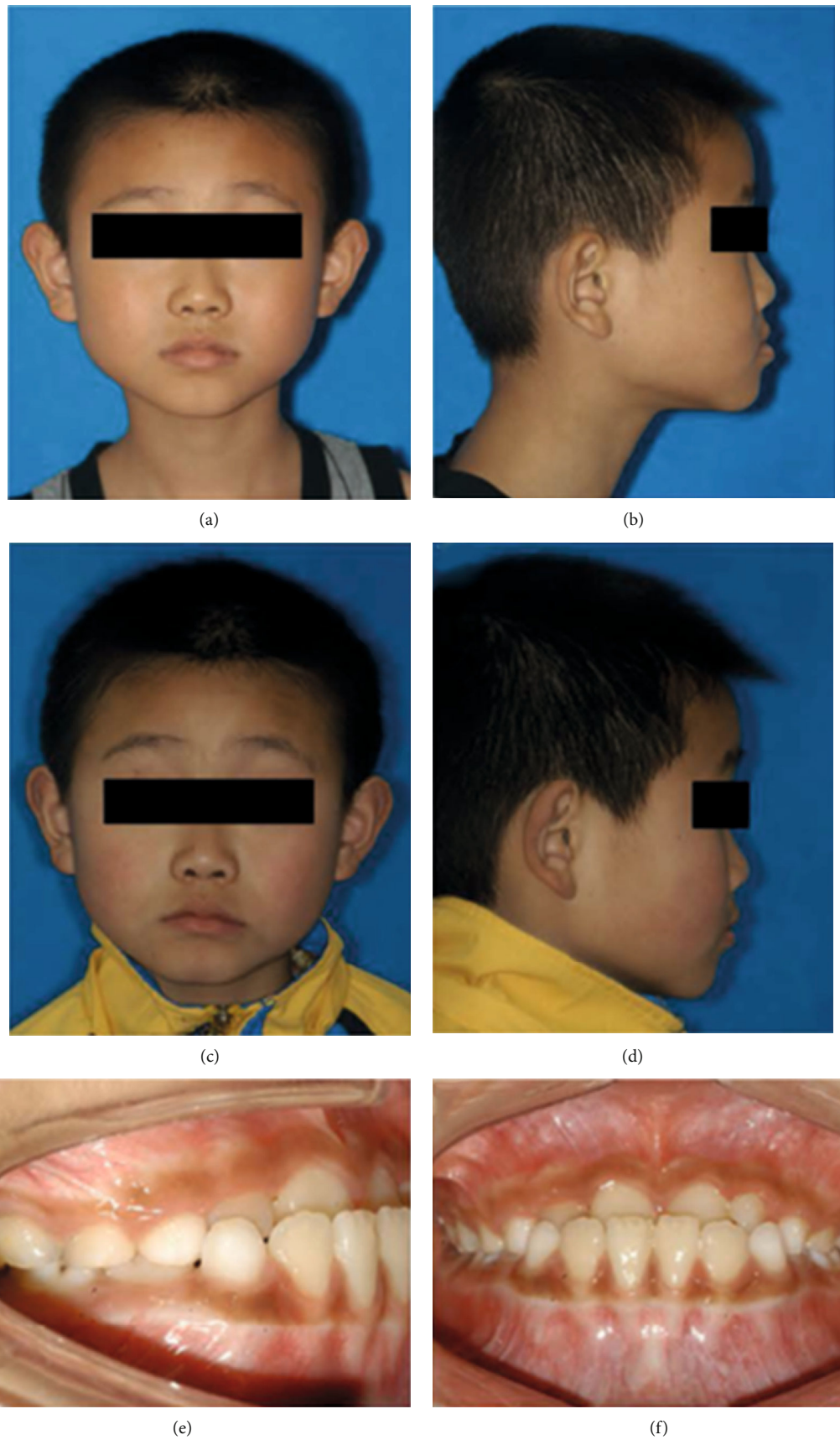

(a) (b) (c) (d) (e) (f)

Figure 3: Continued.

Figure 3: A case treated with MOA-III (comparison of pre- and posttreatment). Pretreatment: extraoral photos (a, b), intraoral photos (e–g), overbite/overjet (l). Posttreatment: extraoral photos (c, d), intraoral photos (h–j), overbite/overjet (m). Intreatment: intraoral photos (k) [62].

6. Application of Ultrasound in the Oral Cavity

6.1. Periodontal: Promotion of Periodontal Tissue Regeneration. The purpose of periodontal disease treatment is to prevent periodontal infection and maintain periodontal health. Removing a plaque and calculus is an important treatment and prevention method for periodontal disease. It is believed that the best way of periodontal treatment is to remove the pathogenic bacteria of the periodontal supragingival and subgingival tissues by a nonsurgical machinery. The irritants such as plaque and calculus on the tooth surface can be removed by ultrasound. Cavitation caused by ultrasound ruptures the attached sediments by producing shock waves. In addition, studies have shown that cavitation can enhance the permeability of bacterial cell membrane to antibiotics and can also promote some biochemical reactions in the cell, to be more conductive to the combination of antibiotics and targets and to help antibiotics to kill bacteria [72]. There are two basic types of ultrasonic devices in dentistry: magnetostrictive and piezoelectric devices. Magnetostrictive devices use flat metal strip or metal bars attached to the scaling tip. When the current is provided to the coil, a magnetic field will

be generated around the rod sensor, and an alternating magnetic field will be generated by the alternating current, making the tip of the vibrating blade move elliptically. In a piezoelectric element, when an electric current passes through the crystal surface, a change in the size of the crystal contained in the nose reactivates the piezoelectric element, and the resulting vibration leads to a tip motion that is mainly linear in direction and operates differently [73].

As a noninvasive physical stimulation, low-intensity pulsed ultrasound is widely used to promote bone healing and fracture healing by promoting the proliferation of osteoblasts and secretion of angiogenesis-related factors [74].

In the study of Kitano Lim et al., they used LIPUS to stimulate human alveolar bone-derived mesenchymal stem cells (hABMSCs) derived from the alveolar bone and found that the expression of alkaline phosphatase (ALP) and quantity of cell mineralized nodules was obviously increased after one week, proving that LIPUS promotes the proliferation and osteogenic differentiation of hABMSC [75]. In the experiment of Hu et al., LIPUS stimulation was performed on the periodontal ligament stem cells of adolescent premolars, and it was found that LIPUS could promote the mRNA expression of (ALP), osteocalcin, Runx-2, and integrin B1. Since (ALP) is an important marker of osteogenic differentiation, osteocalcin is used as a late marker of bone formation and osteogenic differentiation. RUNX-2 is an important transcription factor in the osteogenic pathway. Therefore, their study shows that LIPUS can promote the differentiation of bone stromal stem cells and thus enhance periodontal regeneration [76]. Imai et al. applied LIPUS to human mandibular fracture hematoma cells. They detected the expression levels of osteoblast-related gen 2 (Runx2). The expression levels of the osteoblast-related genes ALP, osteocalcin (OC), runt-related gene 2 (Runx2), osterix (OSX), osteopontin (OPN), and parathyroid hormone receptor 1 (PTHR1) were measured by real-time PCR. As shown in Figure 4, the expression levels of ALP, OC, Runx2, OSX, OPN, PTHR1, and mineralization genes were increased in the LIPUS group.

This finding demonstrates the significant influence of LIPUS on MHC osteogenic differentiation and provides important evidence for the potential usefulness of the clinical application of LIPUS in accelerating mandible fracture healing [78].

6.2. Improvement in the Implant Success Rate. Dental implants have become an important way to repair tooth loss and dentition defect, and it is the first choice for patients with tooth loss. The initial stability of the implant is an important basis for judging the effect of bone healing and determining the repair and loading time, and good initial stability is the key factor affecting the success rate. Scarano offers a way to place implants. Ultrasonic equipment was used to prepare the implant bed before root extraction. As shown in Figure 5, the preparations for osteotomy proceeded normally, and then, the insertion of each ultrasonic inserter was accompanied by osteotomy. It was found that the ISQ level of the control group was 49.9, which was much lower than the experimental group. Compared with traditional preparation, the advantage of this technology is that it is easy to operate and can improve the initial stability of the implant [79]. To shorten the time of bone healing, people have conducted further research on implant osseointegration. Ultrasound has been proven to be an effective method to promote bone healing. Under ultrasonic stimulation, the space between alveolar bone and implant can be filled with new bone trabecula more quickly, achieving the effect of implant binding with surrounding bone. Yakup et al. implanted dental implants into rabbits' femurs and found that the application of LIPUS on oral implants can promote peri-implant osseointegration and increase the bone area at the early stage of osseointegration [80]. Studies have shown that LIPUS can enhance the gene expression of COX-2 and thus enhance the synthesis of endogenous PGE2 in various osteoblastic cell lineages, which is of great significance for bone remodeling [3]. Therefore, ultrasonic stimulation can be an effective method to improve the success rate and stability of oral implants.

6.3. Shortened Orthodontic Treatment and Promotion of Root Restoration. Orthodontic tooth movement (OTM) is a complex bone remodeling process [81]. Therefore, accelerating alveolar bone remodeling has substantial benefits for patients [82]. Studies have reported that LIPUS promotes alveolar bone remodeling in a rat orthodontic tooth movement model by stimulating the HGF/Runx2/BMP-2 signaling pathway and RANKL expression, further demonstrating that LIPUS stimulation increases Runx2 and BMP-2 expression [83]. During orthodontic treatment, the activity of osteoblasts and osteoclasts around the alveolar bone is highly reactive; therefore, root resorption occurs to a certain extent more or less [84]. Orthodontic-induced inflammatory root resorption is one of the most common side effects of orthodontic treatment. The retention of the tooth body in the alveolar socket is mainly achieved by the cementum of the root, although after the root is damaged, the regeneration ability of the cementum will become very slow and weak. Therefore, a treatment method is needed to restore the damaged root to maintain the integrity of periodontal tissue. Inubushi et al. reported a study to investigate the effects of LIPUS stimulation on the proliferation and differentiation of cementoblast lineage cells. From Figure 6, we can find that compared with the control (untreated cells), LIPUS exposure had no significant effect on the proliferation. The number of cells with LIPUS exposure was almost similar to that in the control. Under the stimulation of LIPUS ($P < 0.01$), the expression level of ALP mRNA within 24 h was significantly increased, and the activity of ALP increased by 1.4 times compared with the control group, which induced the differentiation of human periodontal stem cells into osteoblasts, accelerating the repair of root resorption, and thus enabling the regeneration of periodontal tissue damaged by periodontal disease [85]. The noninvasive nature and safety of LIPUS make it valuable for clinical application [86].

7. Application of Mechanical Vibration in the Oral Cavity

7.1. The Impact of Vibration on the Periodontal Tissue. Vibration can be used to maintain the health of the periodontium

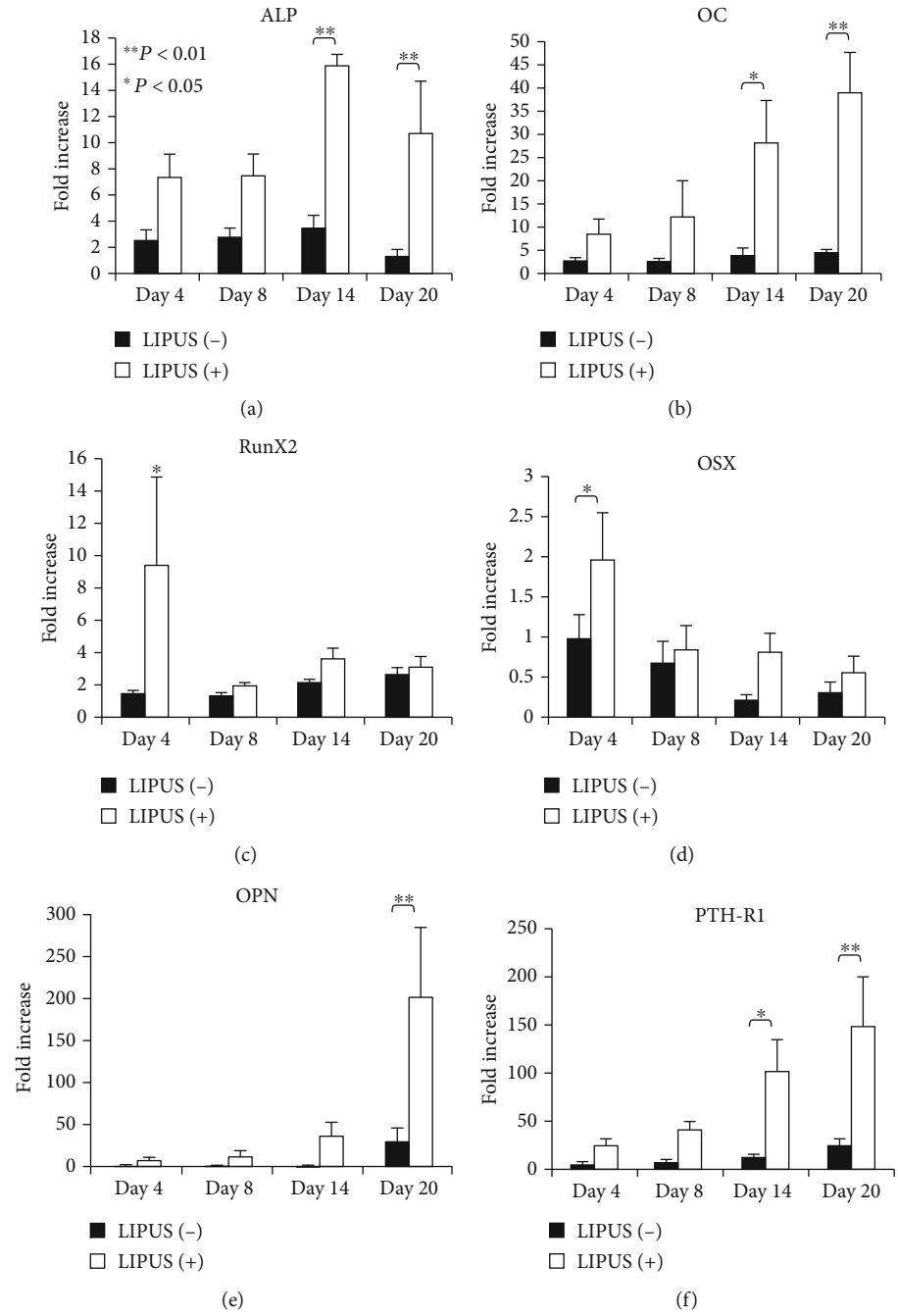

Figure 4: Histogram of real-time PCR gene expression analysis results of 5 cases in the LIPUS(+) group and LIPUS(-) group on the 4th, 8th, and 20th day. The results showed (a) alkaline phosphatase (ALP), (b) osteocalcin (OC), (c) runt-related gene2 (Runx2), (d) osteogenic protein (OSX), (e) bone-bridge Protein (OPN), and (f) parathyroid hormone receptor (PTH-R1). $*P$ and lt, 0.05; $**P$ and lt, 0.01 [77].

in three aspects: improving the activity of periodontal fibroblasts, promoting the osteogenic differentiation of periodontal stem cells, and maintaining the height of alveolar bone.

As the main component of periodontium, fibroblasts are the main repair cells for soft tissue injuries [87]. They migrate to the site of injury and proliferate, produce large amounts of collagen, and secret a variety of collagen cellulose hormone growth factors. Therefore, Lekic et al. believed that it is the engineer, builder, and manager of trauma repair [88]. Stefan et al. vibrated periodontal membrane fibroblasts through AcceleDent (30 Hz) and VPro5 (120 Hz) and found that both of them increased the secretion of FGF2 and CTGF in fibroblasts. However, FGF2 and CTGF levels after vibration of the VPro5 device were 30-40% higher than those in the AcceleDent group, suggesting that a vibration could promote the activity of fibroblasts, and fibroblast activities were more sensitive to high-frequency vibrations [89].

A large amount of evidence indicates that the best choice for periodontal tissue regeneration is periodontal ligament-(PDL-) derived stem cells/progenitors [90]. Such pluripotent

(a) (b) (c)

Figure 5: After the initial osteotomy, the implant is placed in the posterior mouth X-ray (a), and the guide pin (bur) is placed during the final osteotomy (b). Use ultrasound equipment in the interradicular bone for final osteotomy preparation (c) [75].

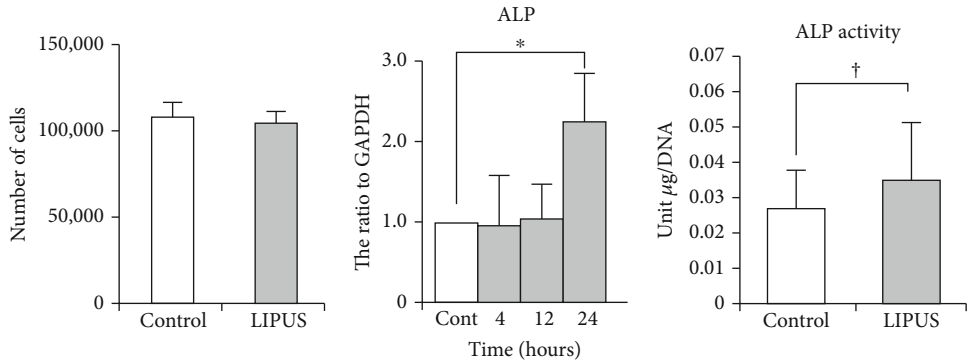

(a) (b) (c)

Figure 6: The number of HPL cells (mean ± SD) after being exposed to LIPUS. (a) There was no significant difference in the cell numbers between the control and LIPUS groups ($n = 5$ for each). Effect of LIPUS on the mRNA expression (b) and activity of alkaline phosphatase (c) in HPL cell culture ($n = 5$ for each). Cont: control. $^*P < 0.01$. Values are expressed as mean – SD. $^*P < 0.01$; $\dagger P < 0.0585$.

cells can respond to mechanical stimulation, send signals to surrounding cells during orthodontic tooth movement, and play an important role in the regulation of bone reconstruction. Therefore, it is necessary to study the effect of mechanical vibration on PDL. Benjakul S et al. found that mechanical vibration of LMHF promotes the osteogenic differentiation of PDLSC. Studies have shown that after vibration, the expression of PGE2, RANKL, and sRANKL related to osteogenesis and bone resorption role in periodontal ligament stem cells increased, which can promote the process of bone remodeling [91]. Zhang et al. proposed that vibration has a frequency dependent effect in determining the conversion rate of PDLSC to osteoblasts [92]. At the cellular level, a large number of studies have shown that vibration promotes the expression of ALP and type I collagen, which are markers of osteoblast differentiation, and upregulates the level of RUNX2 in osteoclasts and osteoblasts [89]. At the individual level, Alikhani et al. found that after applying a specific frequency 0.3 vibration (peak of acceleration 120 Hz) to the healthy alveolar bone site without stress stimulation of missing teeth but with osteogenesis, alveolar bone structure was preserved after tooth extraction [93, 94]. In the treatment of alveolar bone osteoporosis, Nishimura et al. found that the local application of vibration resulted in increased anabolism and reduced catabolism in alveolar bone in osteoporotic rats [95]. Therefore, vibration has a good prospect in preventing and treating alveolar bone loss caused by tooth loss or osteoporosis.

7.2. Effects of Vibration on Orthodontics: Acceleration of the Orthodontic Process and Pain Relief. In recent years, more and more attention has been paid to the application of vibration stimulation in orthodontic treatment. Its purpose is to accelerate the movement speed of orthodontic teeth by accelerating the reconstruction of periodontium and alveolar bone. The research of Nishimura et al. shows that vibration stimulation could accelerate the tooth movement speed of rats and causes no collateral damage to the periodontal tissues [96]. Many studies have reported that a short period of low-intensity high-frequency vibration combined with orthodontic force can increase the frequency of orthodontic tooth movement without causing additional damage to human tissues [97]. One of the studies claimed that a commercially available vibration device could increase the tooth movement distance by 2-3 mm per month and significantly improve the clinical patient acceptance and compliance [5]. Orthodontic force induces pressure on the PDL to cause vascular changes that lead to activation of cellular signaling

pathways and the release of proinflammatory molecules such as IL-1 β. The survival, fusion, and activation of osteoclasts are related to the level of IL-1β. IL-6 regulates alveolar bone remodeling, thereby affecting the amount of tooth movement during orthodontics [97]. Human studies have shown that IL-1β level in GCF significantly increases during orthodontic tooth movement. Therefore, vibration can accelerate the reconstruction of periodontal and alveolar bone, thus improving the movement speed of orthodontic teeth [98]. At present, the effectiveness of the vibrator currently used to shorten the course of orthodontic treatment has been confirmed and has been used in clinical practice. During the orthodontic process, due to the force of the tooth, its periodontal tissue will undergo a series of reactions: periodontal tissue is remodeled, and the periodontal ligament is compressed and ischemic, which can lead to the inflammatory response of the periodontal ligament. In addition, improper operation or the friction of the appliance itself on the mucous membrane can cause the patient's pain response. It is believed that temporary tooth displacement can relax the periodontal compression area (including nerve fibers and blocked blood vessels) and thus make the blood flow more easily. In this way, it may prevent the role of pain mediators in this area [99]. Therefore, a mechanical vibrator was proposed to relieve the pain caused by orthodontics. Marie et al. instructed their patients to use the device to vibrate immediately after placing the arch wire, each lasting 15 min, thinking that mechanical vibration may be an effective way to relieve pain [100]. There are few studies on mechanical vibration and the research conclusions are also inconsistent, which may be related to different people's pain sensitivity and different vibration methods. However, there is still a good prospect for improving the pain caused by orthodontic treatment.

8. Conclusions

In summary, physical factors play a crucial role in the development and maintenance of many tissues. Living things are always in a constantly changing physical environment and can react to it. Physical stimulation such as laser, magnetic field, sound wave, and vibration play an important role in the treatment and prevention of oral diseases and oral health care. In clinical practice, laser is used in oral soft tissue surgery, such as gingival resection, oral mucosal inflammation treatment, dental caries treatment, root canal preparation and disinfection, and dentin desensitization treatment. As a force source, magnetic field has been widely used in orthodontics and denture retention. Ultrasound can remove dental plaque, promote mandibular fracture healing, and rinse the root canal; vibration massage instrument which can accelerate orthodontic tooth movement has also been widely used in clinic. In addition, physical stimulation has a unique biological effect, which can assist antibiotics to kill oral microorganisms and to maintain oral hygiene. At present, a variety of physical stimulations have been extensively studied in promoting osseointegration of implants, and some of them have entered the stage of clinical experiment. Some of them are still in the research stage, and a large amount of experimental data is still needed to confirm its safety and effectiveness. Physical therapy provides a relatively noninvasive stimulation to promote tissue healing and repair and to relieve the pain of patients compared with the traditional treatment and provides a variety of choices for common oral treatment methods, which is a significant auxiliary means for oral clinicians.

Data Availability

All data, figures, and tables in this review paper are labeled with references.

Conflicts of Interest

We declare that we have no financial and personal relationships with other individuals or organizations that can inappropriately influence our work.

Authors' Contributions

Yanxin Qi, ShuXin Zhang, and Mi Zhang contributed equally to this work.

Acknowledgments

This study was funded by the National Undergraduate Innovation Training Program of China (201910439021).

References

[1] M. S. Markov, "Therapeutic application of static magnetic fields," *The Environmentalist*, vol. 27, no. 4, pp. 457–463, 2007.

[2] T. L. Smith, D. Wong-Gibbons, and J. Maultsby, "Microcirculatory effects of pulsed electromagnetic fields," *Journal of Orthopaedic Research*, vol. 22, no. 1, pp. 80–84, 2004.

[3] T. Kokubu, N. Matsui, H. Fujioka, M. Tsunoda, and K. Mizuno, "Low intensity pulsed ultrasound exposure increases prostaglandin E2 production via the induction of cyclooxygenase-2 mRNA in mouse osteoblasts," *Biochemical and Biophysical Research Communications*, vol. 256, no. 2, pp. 284–287, 1999.

[4] B. D. Matthews, D. R. Overby, R. Mannix, and D. E. Ingber, "Cellular adaptation to mechanical stress: role of integrins, rho, cytoskeletal tension and mechanosensitive ion channels," *Journal of Cell Science*, vol. 119, no. 3, pp. 508–518, 2006.

[5] C. H. Kau, "A radiographic analysis of tooth morphology following the use of a novel cyclical force device in orthodontics," *Head & Face Medicine*, vol. 7, no. 1, 2011.

[6] M. Alikhani, S. Alansari, M. A. Hamidaddin et al., "Vibration paradox in orthodontics: anabolic and catabolic effects," *PLoS One*, vol. 13, no. 5, article e0196540, 2018.

[7] F. Celebi, T. Turk, and A. A. Bicakci, "Effects of low-level laser therapy and mechanical vibration on orthodontic pain caused by initial archwire," *American Journal of Orthodontics and Dentofacial Orthopedics*, vol. 156, no. 1, pp. 87–93, 2019.

[8] D. R. Cruz, E. K. Kohara, M. S. Ribeiro, and N. U. Wetter, "Effects of low-intensity laser therapy on the orthodontic movement velocity of human teeth: a preliminary study,"

Lasers in Surgery and Medicine, vol. 35, no. 2, pp. 117–120, 2004.

[9] M. V. da Silva Sousa, M. A. Scanavini, E. K. Sannomiya, L. G. Velasco, and F. Angelieri, "Influence of low-level laser on the speed of orthodontic movement," *Photomedicine and Laser Surgery*, vol. 29, no. 3, pp. 191–196, 2011.

[10] C. Ren, C. McGrath, M. Gu et al., "Low-level laser-aided orthodontic treatment of periodontally compromised patients: a randomised controlled trial," *Lasers in Medical Science*, vol. 35, no. 3, pp. 729–739, 2020.

[11] N. Khandge, S. Pradhan, Y. Doshi, and A. Kulkarni, "Comparison of the effects of different laser wavelengths on implants surfaces," *International Journal of Laser Dentistry*, vol. 3, no. 1, pp. 14–18, 2013.

[12] S. Omasa, M. Motoyoshi, Y. Arai, K.-I. Ejima, and N. Shimizu, "Low-level laser therapy enhances the stability of orthodontic mini-implants via bone formation related to BMP-2 expression in a rat model," *Photomedicine and Laser Surgery*, vol. 30, no. 5, pp. 255–261, 2012.

[13] L. Mayer, F. Gomes, L. Carlsson, and M. Gerhardt-Oliveira, "Histologic and resonance frequency analysis of peri-implant bone healing after low-level laser therapy: an in vivo study," *International Journal of Oral & Maxillofacial Implants*, vol. 30, no. 5, pp. 1028–1035, 2015.

[14] B. Mandic, Z. Lazic, A. Markovic et al., "Influence of postoperative low-level laser therapy on the osseointegration of self-tapping implants in the posterior maxilla: a 6-week split-mouth clinical study," *Vojnosanitetski Pregled*, vol. 72, no. 3, pp. 233–240, 2015.

[15] A. A. Takasaki, A. Aoki, K. Mizutani, S. Kikuchi, S. Oda, and I. Ishikawa, "Er: YAG laser therapy for peri-implant infection: a histological study," *Lasers in Medical Science*, vol. 22, no. 3, pp. 143–157, 2007.

[16] F. Schwarz, A. Sculean, D. Rothamel, K. Schwenzer, T. Georg, and J. Becker, "Clinical evaluation of an Er: YAG laser for nonsurgical treatment of peri-implantitis: a pilot study," *Clinical Oral Implants Research*, vol. 16, no. 1, pp. 44–52, 2005.

[17] J. Eberhard, H. Ehlers, W. Falk, Y. Açil, H. K. Albers, and S. Jepsen, "Efficacy of subgingival calculus removal with Er: YAG laser compared to mechanical debridement: an in situ study," *Journal of Clinical Periodontology*, vol. 30, no. 6, pp. 511–518, 2003.

[18] B. O. Ozkaya, K. Gulsahi, M. Ungor, and J. S. Gocmen, "A comparison of Er:YAG laser with photon-initiated photoacoustic streaming, Nd:YAG laser, and conventional irrigation on the eradication of root dentinal tubule infection by Enterococcus faecalis biofilms: a scanning electron microscopy study," *Scanning*, vol. 2017, Article ID 6215482, 7 pages, 2017.

[19] Y. Reznick, E. Banin, A. Lipovsky, R. Lubart, and Z. Zalevsky, "Direct laser light enhancement of susceptibility of bacteria to gentamicin antibiotic," *Optics Communications*, vol. 284, no. 23, pp. 5501–5507, 2011.

[20] P. Ratka-Krüger, D. Mahl, D. Deimling et al., "Er: YAG laser treatment in supportive periodontal therapy," *Journal of Clinical Periodontology*, vol. 39, no. 5, pp. 483–489, 2012.

[21] A. Braun, S. Jepsen, D. Deimling, and P. Ratka-Krüger, "Subjective intensity of pain during supportive periodontal treatment using a sonic scaler or an Er: YAG laser," *Journal of Clinical Periodontology*, vol. 37, no. 4, pp. 340–345, 2010.

[22] W. Posten, D. A. Wrone, J. S. Dover, K. A. Arndt, S. Silapunt, and M. Alam, "Low-level laser therapy for wound healing: mechanism and efficacy," *Dermatologic Surgery*, vol. 31, no. 3, pp. 334–340, 2005.

[23] A. Pourzarandian, H. Watanabe, S. M. P. M. Ruwanpura, A. Aoki, and I. Ishikawa, "Effect of low-level Er: YAG laser irradiation on cultured human gingival fibroblasts," *Journal of Periodontology*, vol. 76, no. 2, pp. 187–193, 2005.

[24] S. Skinner, J. Gage, P. Wilce, and R. Shaw, "A preliminary study of the effects of laser radiation on collagen metabolism in cell culture," *Australian Dental Journal*, vol. 41, no. 3, pp. 188–192, 1996.

[25] P. C. L. Silveira, L. A. Silva, T. P. Freitas, A. Latini, and R. A. Pinho, "Effects of low-power laser irradiation (LPLI) at different wavelengths and doses on oxidative stress and fibrogenesis parameters in an animal model of wound healing," *Lasers in Medical Science*, vol. 26, no. 1, pp. 125–131, 2011.

[26] F. A. Al-Watban, X. Y. Zhang, and B. L. Andres, "Low-level laser therapy enhances wound healing in diabetic rats: a comparison of different lasers," *Photomedicine and Laser Surgery*, vol. 25, no. 2, pp. 72–77, 2007.

[27] F. G. Basso, T. N. Pansani, A. P. S. Turrioni, V. S. Bagnato, J. Hebling, and C. A. de Souza Costa, "In vitro wound healing improvement by low-level laser therapy application in cultured gingival fibroblasts," *International Journal of Dentistry*, vol. 2012, Article ID 719452, 6 pages, 2012.

[28] M. J. Conlan, J. W. Rapley, and C. M. Cobb, "Biostimulation of wound healing by low-energy laser irradiation a review," *Journal of Clinical Periodontology*, vol. 23, no. 5, pp. 492–496, 1996.

[29] J. B. Park, S. J. Ahn, Y. G. Kang, E. C. Kim, J. S. Heo, and K. L. Kang, "Effects of increased low-level diode laser irradiation time on extraction socket healing in rats," *Lasers in Medical Science*, vol. 30, no. 2, pp. 719–726, 2015.

[30] A. Stein, D. Benayahu, L. Maltz, and U. Oron, "Low-level laser irradiation promotes proliferation and differentiation of human osteoblasts in vitro," *Photomedicine and Laser Therapy*, vol. 23, no. 2, pp. 161–166, 2005.

[31] N. S. Korany, S. S. Mehanni, H. M. Hakam, and E. M. F. El-Maghraby, "Evaluation of socket healing in irradiated rats after diode laser exposure (histological and morphometric studies)," *Archives of Oral Biology*, vol. 57, no. 7, pp. 884–891, 2012.

[32] M. H. Aras, Z. Bozdag, T. Demir, R. Oksayan, S. Yanık, and O. Sökücü, "Effects of low-level laser therapy on changes in inflammation and in the activity of osteoblasts in the expanded premaxillary suture in an ovariectomized rat model," *Photomedicine and Laser Surgery*, vol. 33, no. 3, pp. 136–144, 2015.

[33] J. J. Park and K. L. Kang, "Effect of 980-nm GaAlAs diode laser irradiation on healing of extraction sockets in streptozotocin-induced diabetic rats: a pilot study," *Lasers in Medical Science*, vol. 27, no. 1, pp. 223–230, 2012.

[34] H. Pretel, R. F. Z. Lizarelli, and L. T. O. Ramalho, "Effect of low-level laser therapy on bone repair: histological study in rats," *Lasers in Surgery and Medicine*, vol. 39, no. 10, pp. 788–796, 2007.

[35] R. M. Pick, B. C. Pecaro, and C. J. Silberman, "The laser gingivectomy: the use of the CO2 laser for the removal of phenytoin hyperplasia," *Journal of Periodontology*, vol. 56, no. 8, pp. 492–496, 1985.

[36] J. A. Weichman and F. M. Johnson, "Laser use in endodontics," *Oral Surgery, Oral Medicine, Oral Pathology*, vol. 31, no. 3, pp. 416–420, 1971.

[37] W. Raucci-Neto, L. M. S. de Castro-Raucci, C. P. Lepri, J. J. Faraoni-Romano, J. M. G. da Silva, and R. G. Palma-Dibb, "Nd: YAG laser in occlusal caries prevention of primary teeth: a randomized clinical trial," *Lasers in Medical Science*, vol. 30, no. 2, pp. 761–768, 2015.

[38] N. G. Kumar and D. S. Mehta, "Short-term assessment of the Nd: YAG laser with and without sodium fluoride varnish in the treatment of dentin hypersensitivity–a clinical and scanning electron microscopy study," *Journal of Periodontology*, vol. 76, no. 7, pp. 1140–1147, 2005.

[39] M. A. Meire, T. Coenye, H. J. Nelis, and R. J. G. De Moor, "In vitro inactivation of endodontic pathogens with Nd: YAG and Er: YAG lasers," *Lasers in Medical Science*, vol. 27, no. 4, pp. 695–701, 2012.

[40] S. Pirnat, M. Lukac, and A. Ihan, "Study of the direct bactericidal effect of Nd: YAG and diode laser parameters used in endodontics on pigmented and nonpigmented bacteria," *Lasers in Medical Science*, vol. 26, no. 6, pp. 755–761, 2011.

[41] C. Kokuzawa, A. Ebihara, S. Watanabe et al., "Shaping of the root canal using Er: YAG laser irradiation," *Photomedicine and Laser Surgery*, vol. 30, no. 7, pp. 367–373, 2012.

[42] U. Keller, R. Hibst, W. Geurtsen et al., "Erbium:YAG laser application in caries therapy. Evaluation of patient perception and acceptance," *Journal of Dentistry*, vol. 26, no. 8, pp. 649–656, 1998.

[43] X. Wang, F. Tian, S. S. Soni, F. Gonzalez-Lima, and H. Liu, "Interplay between up-regulation of cytochrome-c-oxidase and hemoglobin oxygenation induced by near-infrared laser," *Scientific Reports*, vol. 6, no. 1, 2016.

[44] M. Honarmand, L. Farhadmollashahi, and E. Vosoughirahbar, "Comparing the effect of diode laser against acyclovir cream for the treatment of herpes labialis," *Journal of Clinical and Experimental Dentistry*, vol. 9, article e729, 2017.

[45] P. J. Muñoz Sanchez, J. L. Capote Femenías, A. Díaz Tejeda, and J. Tunér, "The effect of 670-nm low laser therapy on herpes simplex type 1," *Photomedicine and Laser Surgery*, vol. 30, no. 1, pp. 37–40, 2012.

[46] A. Besbes, Y. Elelmi, F. Khanfir, R. Belgacem, and H. Ghedira, "Case report recurrent oral mucocele management with diode laser," *Case Reports in Dentistry*, vol. 2020, 5 pages, 2020.

[47] G. M. Ahmed, E. A. Abouauf, N. AbuBakr, C. E. Dörfer, and K. F. El-Sayed, "Tissue engineering approaches for enamel, dentin, and pulp regeneration: an update," *Stem Cells International*, vol. 2020, 15 pages, 2020.

[48] S.-H. Jegal, J. H. Park, J. H. Kim et al., "Functional composite nanofibers of poly (lactide–co-caprolactone) containing gelatin–apatite bone mimetic precipitate for bone regeneration," *Acta Biomaterialia*, vol. 7, no. 4, pp. 1609–1617, 2011.

[49] H.-M. Yun, E. S. Lee, M. J. Kim et al., "Magnetic nanocomposite scaffold-induced stimulation of migration and odontogenesis of human dental pulp cells through integrin signaling pathways," *PLoS One*, vol. 10, no. 9, article e0138614, 2015.

[50] A. Sheiham, "Public health aspects of periodontal diseases in Europe," *Journal of Clinical Periodontology*, vol. 18, no. 6, pp. 362–369, 1991.

[51] S. Brkovic, S. Postic, and D. Ilic, "Influence of the magnetic field on microorganisms in the oral cavity," *Journal of Applied Oral Science*, vol. 23, no. 2, pp. 179–186, 2015.

[52] A. C. Morrow, R. H. Dunstan, B. V. King, and T. K. Roberts, "Metabolic effects of static magnetic fields on Streptococcus pyogenes," *Bioelectromagnetics*, vol. 28, no. 6, pp. 439–445, 2007.

[53] S. Brković-Popović, D. Stamenković, D. Stanišić-Sinobad, Z. Rakočević, and O. Zelić, "The influence of continuous magnetic field on periodontal tissues under overdentures," *Srpski Arhiv za Celokupno Lekarstvo*, vol. 137, no. 7-8, pp. 363–370, 2009.

[54] L. Alumutairi, B. Yu, M. Filka, J. Nayfach, and M.-H. Kim, "Mild magnetic nanoparticle hyperthermia enhances the susceptibility of Staphylococcus aureusbiofilm to antibiotics," *International journal of hyperthermia*, vol. 37, no. 1, pp. 66–75, 2020.

[55] K. E. Johnson, J. J. Sanders, R. G. Gellin, and Y. Y. Palesch, "The effectiveness of a magnetized water oral irrigator (Hydro Fioss®) on plaque, calculus and gingival health," *Journal of Clinical Periodontology*, vol. 25, no. 4, pp. 316–321, 1998.

[56] J. P. Shah and B. Singh, "Keynote comment: why the lack of progress for oral cancer?," *The Lancet Oncology*, vol. 7, no. 5, pp. 356-357, 2006.

[57] C. J. Legge, H. E. Colley, M. A. Lawson, and A. E. Rawlings, "Targeted magnetic nanoparticle hyperthermia for the treatment of oral cancer," *Journal of Oral Pathology & Medicine*, vol. 48, no. 9, pp. 803–809, 2019.

[58] A. Roykó, Z. Dénes, and G. Razouk, "The relationship between the length of orthodontic treatment and patient compliance," *Fogorvosi Szemle*, vol. 92, p. 79, 1999.

[59] M. Dogru, V. Akpolat, A. G. Dogru, B. Karadede, A. Akkurt, and M. I. Karadede, "Examination of extremely low frequency electromagnetic fields on orthodontic tooth movement in rats," *Biotechnology & Biotechnological Equipment*, vol. 28, no. 1, pp. 118–122, 2014.

[60] T. Kawata, M. Matsuga, N. Kitano, and H. Kishigami, "Further study of new orthodontic treatment with a magnetic appliance," *Journal of Dental Research*, vol. 57, 1978.

[61] T. Kawata and M. Matsuga, "Study of new orthodontic treatment by means of magnet," *Journal of Dental Research*, vol. 58, 1979.

[62] N. Zhao, J. Feng, Z. Hu, R. Chen, and G. Shen, "Effects of a novel magnetic orthopedic appliance (MOA-III) on the dentofacial complex in mild to moderate skeletal class III children," *Head & Face Medicine*, vol. 11, no. 1, p. 34, 2015.

[63] S. Compton, D. Clark, S. Chan, I. Kuc, B. Wubie, and L. Levin, "Dental implants in the elderly population: a long-term follow-up," *International Journal of Oral & Maxillofacial Implants*, vol. 32, no. 1, pp. 164–170, 2017.

[64] N. M. Shupak, F. S. Prato, and A. W. Thomas, "Therapeutic uses of pulsed magnetic-field exposure: a review," *URSI Radio Science Bulletin*, vol. 2003, no. 307, pp. 9–32, 2003.

[65] S. Barak, M. Neuman, G. Iezzi, A. Piattelli, V. Perrotti, and Y. Gabet, "A new device for improving dental implants anchorage: a histological and micro-computed tomography study in the rabbit," *Clinical Oral Implants Research*, vol. 27, no. 8, pp. 935–942, 2016.

[66] S. Barak, S. Matalon, O. Dolkart, B. Zavan, C. Mortellaro, and A. Piattelli, "Miniaturized electromagnetic device abutment

improves stability of the dental implants," *Journal of Craniofacial Surgery*, vol. 30, no. 4, pp. 1055–1057, 2019.

[67] B. P. Nayak, O. Dolkart, P. Satwalekar et al., "Effect of the pulsed electromagnetic field (PEMF) on dental implants stability: a randomized controlled clinical trial," *Materials*, vol. 13, no. 7, p. 1667, 2020.

[68] B. O. Ogundare, A. Bonnick, and N. Bayley, "Pattern of mandibular fractures in an urban major trauma center," *Journal of Oral and Maxillofacial Surgery*, vol. 61, no. 6, pp. 713–718, 2003.

[69] S. R. Thaller, "Management of mandibular fractures," *Archives of Otolaryngology–Head & Neck Surgery*, vol. 120, no. 1, pp. 44–48, 1994.

[70] A. Abdelrahim, H. R. Hassanein, and M. Dahaba, "Effect of pulsed electromagnetic field on healing of mandibular fracture: a preliminary clinical study," *Journal of Oral and Maxillofacial Surgery*, vol. 69, no. 6, pp. 1708–1717, 2011.

[71] M. I. Weintraub, D. N. Herrmann, A. G. Smith, M. M. Backonja, and S. P. Cole, "Pulsed electromagnetic fields to reduce diabetic neuropathic pain and stimulate neuronal repair: a randomized controlled trial," *Archives of Physical Medicine and Rehabilitation*, vol. 90, no. 7, pp. 1102–1109, 2009.

[72] H. Yu, S. Chen, and P. Cao, "Synergistic bactericidal effects and mechanisms of low intensity ultrasound and antibiotics against bacteria: a review," *Ultrasonics sonochemistry*, vol. 19, no. 3, pp. 377–382, 2012.

[73] T. Arabaci, Y. Cicek, and C. Canakci, "Sonic and ultrasonic scalers in periodontal treatment: a review," *International Journal of Dental Hygiene*, vol. 5, no. 1, pp. 2–12, 2007.

[74] J. Schortinghuis, A. L. J. J. Bronckers, B. Stegenga, G. M. Raghoebar, and L. G. M. de Bont, "Ultrasound to stimulate early bone formation in a distraction gap: a double blind randomised clinical pilot trial in the edentulous mandible," *Archives of Oral Biology*, vol. 50, no. 4, pp. 411–420, 2005.

[75] K. T. Lim, J. Kim, H. Seonwoo, S. H. Park, P.-H. Choung, and J. H. Chung, "In vitro effects of low-intensity pulsed ultrasound stimulation on the osteogenic differentiation of human alveolar bone-derived mesenchymal stem cells for tooth tissue engineering," *BioMed Research International*, vol. 2013, Article ID 269724, 15 pages, 2013.

[76] B. Hu, Y. Zhang, J. Zhou et al., "Low-intensity pulsed ultrasound stimulation facilitates osteogenic differentiation of human periodontal ligament cells," *PLoS One*, vol. 9, no. 4, article e95168, 2014.

[77] Y. Imai, T. Hasegawa, D. Takeda et al., "The osteogenic activity of human mandibular fracture haematoma-derived cells is stimulated by low-intensity pulsed ultrasound in vitro," *International Journal of Oral & Maxillofacial Surgery*, vol. 43, no. 3, pp. 367–372, 2014.

[78] A. Teo, A. Morshedi, J. C. Wang, Y. Zhou, and M. Lim, "Enhancement of cardiomyogenesis in murine stem cells by low-intensity ultrasound," *Journal of Ultrasound in Medicine*, vol. 36, no. 8, pp. 1693–1706, 2017.

[79] A. Scarano, "Traditional postextractive implant site preparation compared with pre-extractive interradicular implant bed preparation in the mandibular molar region, using an ultrasonic device: a randomized pilot study," *International Journal of Oral & Maxillofacial Implants*, vol. 32, no. 3, pp. 655–660, 2017.

[80] Y. Ustun, O. Erdogan, M. Kurkcu, T. Akova, and I. Damlar, "Effects of low-intensity pulsed ultrasound on dental implant osseointegration: a preliminary report," *European Journal of Dentistry*, vol. 2, p. 254, 2008.

[81] A. Van Schepdael, J. Vander Sloten, and L. Geris, "A mechanobiological model of orthodontic tooth movement," *Biomechanics and Modeling in Mechanobiology*, vol. 12, no. 2, pp. 249–265, 2013.

[82] T. Kohno, Y. Matsumoto, Z. Kanno, H. Warita, and K. Soma, "Experimental tooth movement under light orthodontic forces: rates of tooth movement and changes of the periodontium," *Journal of Orthodontics*, vol. 29, pp. 129–136, 2014.

[83] H. Xue, J. Zheng, Z. Cui et al., "Low-intensity pulsed ultrasound accelerates tooth movement via activation of the BMP-2 signaling pathway," *PLoS One*, vol. 8, no. 7, article e68926, 2013.

[84] D. M. Killiany, "Root resorption caused by orthodontictreatment: an evidence-based review of literature," *Seminars in orthodontics*, vol. 5, no. 2, pp. 128–133, 1999.

[85] T. Inubushi, E. Tanaka, E. B. Rego et al., "Effects of ultrasound on the proliferation and differentiation of cementoblast lineage cells," *Journal of Periodontology*, vol. 79, no. 10, pp. 1984–1990, 2008.

[86] K.-S. Leung, W.-S. Lee, H.-F. Tsui, P. P.-L. Liu, and W.-H. Cheung, "Complex tibial fracture outcomes following treatment with low-intensity pulsed ultrasound," *Ultrasound in Medicine & Biology*, vol. 30, no. 3, pp. 389–395, 2004.

[87] M. E. Grawish, L. M. Grawish, H. M. Grawish, M. M. Grawish, and S. A. El-Negoly, "Challenges of engineering biomimetic dental and paradental tissues," *Tissue Engineering and Regenerative Medicine*, vol. 17, no. 4, pp. 403–421, 2020.

[88] P. Lekic and C. A. G. McCulloch, "Periodontal ligament cell populations: the central role of fibroblasts in creating a unique tissue," *The Anatomical Record*, vol. 245, no. 2, pp. 327–341, 1996.

[89] S. Judex and S. Pongkitwitoon, "Differential efficacy of 2 vibrating orthodontic devices to alter the cellular response in osteoblasts, fibroblasts, and osteoclasts," *Dose-Response*, vol. 16, no. 3, 2018.

[90] Y.-H. Zhao, M. Zhang, N. X. Liu et al., "The combined use of cell sheet fragments of periodontal ligament stem cells and platelet-rich fibrin granules for avulsed tooth reimplantation," *Biomaterials*, vol. 34, no. 22, pp. 5506–5520, 2013.

[91] S. Benjakul, S. Jitpukdeebodintra, and C. Leethanakul, "Effects of low magnitude high frequency mechanical vibration combined with compressive force on human periodontal ligament cells in vitro," *European Journal of Orthodontics*, vol. 40, no. 4, pp. 356–363, 2018.

[92] C. Zhang, J. Li, L. Zhang et al., "Effects of mechanical vibration on proliferation and osteogenic differentiation of human periodontal ligament stem cells," *Archives of Oral Biology*, vol. 57, no. 10, pp. 1395–1407, 2012.

[93] M. Alikhani, E. Khoo, B. Alyami et al., "Osteogenic effect of high-frequency acceleration on alveolar bone," *Journal of Dental Research*, vol. 91, no. 4, pp. 413–419, 2012.

[94] M. Alikhani, J. A. Lopez, H. Alabdullah et al., "High-frequency acceleration," *Journal of Dental Research*, vol. 95, no. 3, pp. 311–318, 2015.

[95] M. Alikhani, M. Alikhani, S. Alansari et al., "Therapeutic effect of localized vibration on alveolar bone of osteoporotic rats," *PLoS One*, vol. 14, no. 1, article e0211004, 2019.

[96] M. Nishimura, M. Chiba, T. Ohashi et al., "Periodontal tissue activation by vibration: intermittent stimulation by

resonance vibration accelerates experimental tooth movement in rats," *American Journal of Orthodontics and Dentofacial Orthopedics*, vol. 133, no. 4, pp. 572–583, 2008.

[97] C. C. Teixeira, E. Khoo, J. Tran et al., "Cytokine expression and accelerated tooth movement," *Journal of Dental Research*, vol. 89, no. 10, pp. 1135–1141, 2010.

[98] L. R. Iwasaki, C. S. Gibson, L. D. Crouch, D. B. Marx, J. P. Pandey, and J. C. Nickel, "Speed of tooth movement is related to stress and IL-1 gene polymorphisms," *American Journal of Orthodontics and Dentofacial Orthopedics*, vol. 130, no. 6, pp. 698.e1–698.e9, 2006.

[99] M. Otasevic, F. B. Naini, D. S. Gill, and R. T. Lee, "Prospective randomized clinical trial comparing the effects of a masticatory bite wafer and avoidance of hard food on pain associated with initial orthodontic tooth movement," *American Journal of Orthodontics and Dentofacial Orthopedics*, vol. 130, no. 1, pp. 6.e9–6.e15, 2006.

[100] S. S. Marie, M. Powers, and J. J. Sheridan, "Vibratory stimulation as a method of reducing pain after orthodontic appliance adjustment," *Journal of Clinical Orthodontics*, vol. 37, pp. 205–208, 2003.